

CALIFORNIA PATH PROGRAM
INSTITUTE OF TRANSPORTATION STUDIES
UNIVERSITY OF CALIFORNIA, BERKELEY

Design, Field Implementation and Evaluation of Adaptive Ramp Metering Algorithms

**Roberto Horowitz, Adolf May, Alex Skabardonis, Pravin Varaiya,
Michael Zhang, Gabriel Gomes, Laura Muñoz, Xiaotian Sun,
Dengfeng Sun**

University of California, Berkeley

California PATH Research Report

UCB-ITS-PRR-2005-2

This work was performed as part of the California PATH Program of the University of California, in cooperation with the State of California Business, Transportation, and Housing Agency, Department of Transportation; and the United States Department of Transportation, Federal Highway Administration.

The contents of this report reflect the views of the authors who are responsible for the facts and the accuracy of the data presented herein. The contents do not necessarily reflect the official views or policies of the State of California. This report does not constitute a standard, specification, or regulation.

Final Report for Task Order 4136

January 2005

ISSN 1055-1425

TO 4136

Design, Field Implementation and Evaluation of
Adaptive Ramp Metering Algorithms

Final Report

Roberto Horowitz, Adolf May, Alex Skabardonis, Pravin Varaiya, Michael Zhang
Gabriel Gomes, Laura Muñoz, Xiaotian Sun, Dengfeng Sun

University of California, Berkeley

October 26, 2004

Abstract

TO 4136: Design, Field Implementation and Evaluation of Adaptive Ramp Metering Algorithms

**Roberto Horowitz, Adolf May, Alex Skabardonis, Pravin Varaiya, Michael Zhang
Gabriel Gomes, Laura Muñoz, Xiaotian Sun, Dengfeng Sun**

October 26, 2004

The main objectives of Task Order 4136 are (1) the design of improved freeway on-ramp metering strategies that make use of recent developments in traffic data collection, traffic simulation, and control theory, and (2) the testing of these methods on a 14-mile segment of Interstate 210 Westbound in southern California. To date, the major accomplishments of this project include (i) the development of a complete procedure for constructing and calibrating a microscopic freeway traffic model using the Vissim microsimulator, which was applied successfully to the full I-210 test site, (ii) a simulation study, using the calibrated Vissim I-210 model, comparing the fixed-rate, Percent Occupancy, and Alinea local ramp metering schemes, which showed that Alinea can improve freeway conditions when mainline occupancies are measured upstream of the on-ramp (as on I-210 and most California freeways), as well as when occupancy sensors are downstream of the on-ramp, (iii) development of computationally efficient macroscopic freeway traffic models, the Modified Cell Transmission Model (MCTM) and Switching-Mode Model (SMM), validation of these models on a 2-mile segment of I-210, and determination of observability and controllability properties of the SMM modes, (iv) design of a semi-automated method for calibrating the parameters of the MCTM and SMM, which, when applied to an MCTM representation of the full I-210 segment, was able to reproduce the approximate behavior of traffic congestion, yielding about 2% average error in the predicted Total Travel Time (TTT), and (v) development of a new technique for generating optimal coordinated ramp metering plans, which minimizes a TTT-like objective function. Simulation results for a macroscopic model of the 14-mile I-210 segment have shown that the optimal plan predicts an 8.4% savings in TTT, with queue constraints, over the 5-hour peak period.

Keywords: Ramp Metering, Traffic Flow, Advanced Traffic Management Systems, Control Algorithms, Computer Simulation, Freeways

Executive Summary

The central goal of this project is to incorporate recent advances in the areas of traffic data collection, traffic simulation, and control theory, into the design of new advanced onramp control methods, and to implement these methods on Interstate 210 Westbound in southern California. A section of I-210W, approximately 14 miles long, has been selected as a test site for several reasons, including the severity of the congestion problem during the morning commute, and the dedication of the District 7 Traffic Operations group to providing enhanced service to its highway users. However, the control techniques developed by this research will be general enough to be applied to other similar freeways.

The primary advancements achieved under T.O. 4136 include:

- *The development of a complete procedure for constructing and calibrating a microscopic freeway traffic model using the Vissim microsimulator.* This procedure was successfully applied to the I-210W test site. Two sources of traffic data were used in this study: the Performance Measurement System (PeMS), which collects loop detector data from freeways throughout California, and a manual survey of onramps and offramps. FREQ was used as an intermediate tool to generate a set of OD matrices from the assembled boundary flows. A qualitative set of goals was established for the calibration, and was met with relatively few modifications to Vissim's driver behavior parameters.
- *A simulation study, using the calibrated Vissim microscopic model of I-210, comparing several local ramp metering schemes.* The selected methods were fixed-rate metering, Percent Occupancy metering, and Alinea. Each of the metering methods was tested in Vissim using realistic traffic flow demands. One important result of this study is that Alinea can improve freeway conditions when mainline occupancies are measured upstream of the on-ramp (as is the case on I-210, and on most California freeways), as well as when occupancy is measured downstream of the on-ramp. In fact, the simulation results show that the upstream placement of the sensor is actually preferred during congestion.
- *Development of macroscopic freeway traffic models that are computationally efficient and suitable for use in real-time traffic monitoring and control applications.* The macroscopic Modified Cell Transmission Model (MCTM), based on Daganzo's CTM, is presented in this report. The MCTM has been piecewise-linearized to produce the Switching-Mode Model (SMM), a hybrid system. Both the SMM and MCTM have been simulated over a section of I-210W, using several days of loop detector data; the models produced density estimates that are both similar to one another and in good agreement with measured densities on I-210. The observability and controllability properties of the SMM modes have been determined, and shown to change depending on whether traffic flows freely or is congested.

- *Design of a semi-automated method for calibrating the parameters of the MCTM and SMM.* In this approach, free-flow speeds, congestion-wave speeds, and jam densities are determined for specified subsections of a freeway by applying a least-squares data fitting approach to loop detector data. Bottleneck capacities are estimated from measured mainline and on-ramp flows. The calibration method was tested on the 14-mile I-210W test site. The calibrated MCTM was able to reproduce observed bottleneck locations and the approximate behavior of traffic congestion, yielding approximately 2% average error in the predicted total travel time.

- *Development of a new technique for generating optimal coordinated ramp metering plans.* The design of this new predictive and coordinated strategy is based on avoiding the loss of travel time related to offramp blockage. In contrast to previous designs, the approach 1) produces a globally optimal solution to the nonlinear problem, 2) requires only to solve a single linear program, and 3) allows the enforcement of hard constraints on the on-ramp queue lengths. A numerical example, based on a macroscopic model of the full I-210W test site, has been used to demonstrate the technique. The example shows that the globally optimal metering plan predicts a 8.4% savings in Total Travel Time, with queue constraints, over the 5-hour peak period.

T.O. 4136 has yielded a number of advances which are directly applicable to solving the problem of traffic congestion on freeways. The calibrated macroscopic (cell-transmission-based) and microscopic (Vissim) models of I-210 are useful as intermediate testbeds for predicting the impact of traffic control strategies prior to setting up field tests. In addition, the calibration guidelines developed for the various models are sufficiently general to be applied to other freeways. The Vissim study of local ramp metering methods on I-210 confirmed that Alinea can yield improved traffic conditions in cases where, as on I-210, mainline detectors are located upstream of on-ramps, thus resolving a point of uncertainty that had existed before the start of the project. Of particular practical importance is the recently developed ramp-metering optimization method, since it is highly computationally efficient due to the linearity of the optimization problem, and predicts large savings in TTT under realistic conditions, i.e., a heavily congested freeway with constraints enforced on the on-ramp queue lengths.

Contents

1	Introduction	6
1.1	Research outline	7
1.1.1	Overview of Chapter 2	7
1.1.2	Overview of Chapter 3	8
1.1.3	Overview of Chapter 4	9
1.1.4	Overview of Chapter 5	9
1.1.5	Overview of Chapter 6	9
1.1.6	Overview of Chapter 7	10
2	Calibration of Vissim for a Congested Freeway	11
2.1	The test site - Sources of geometric information	12
2.2	Traffic data sources	14
2.3	PeMS data processing with Matlab	16
2.4	Loop-detector reliability	18
2.5	Ramp flows from the Caltrans D07 survey	20
2.6	Mainline flows from PeMS	20
2.7	Estimating OD matrices with the FREQ model	22
2.8	Identification of recurring bottlenecks	23
2.9	The VISSIM model	24
2.9.1	Overview of the program	24
2.9.2	Coding of the network geometry	26
2.9.3	Coding of traffic demands	27
2.9.4	VISSIM output	28
2.10	Changeable model parameters - default values	29
2.11	Variations of selected driver behavior parameters	30
2.12	Calibration goals - Final parameter selection	32
2.12.1	Onramp response	34
2.12.2	HOV lane response	34
2.12.3	Mixed-flow lane response	35
2.12.4	Random seed variations	35
2.13	Summary and Conclusions	36
3	Experiments with Vissim	37
3.1	Performance Measures	37
3.2	On-ramp configurations	39

3.3	The TMC and field controllers	40
3.4	Fixed-rate metering	43
3.5	Alinea control	51
3.6	Percent occupancy control	57
3.7	Conclusions	58
4	Macroscopic Traffic Simulation Models for Congested Freeways	61
4.1	Modified Cell Transmission Model	61
4.2	Switching-Mode Model	68
4.3	Observability and Controllability	74
4.3.1	General Results on Observability	77
4.3.2	General Results on Controllability	81
4.4	Density Estimation Results	83
4.5	Conclusions	88
5	Calibration Methodology for the Cell Transmission Model	90
5.1	Simplified Merge and Diverge Laws	90
5.2	Freeway Representation	91
5.3	Demand Reconstruction	93
5.4	Split Ratio Estimation	94
5.5	HOV Gate Flow Reconstruction	96
5.6	Calibration Methodology	98
5.7	Results	100
5.8	Conclusions	107
6	Simulation Software for Macroscopic Traffic Models	108
6.1	Data Processing and Simulation Software (Short Freeway Segments)	108
6.1.1	Processing Software for PeMS Data	108
6.1.2	MCTM and SMM Simulators in Matlab	109
6.2	MCTM Simulator in C++	109
6.2.1	Data Processing Software for MCTM C++ Simulator	117
7	Globally Optimal Solutions to the Onramp Metering Problem	120
7.1	Notation	121
7.2	Traffic Model	122
7.2.1	Theorem	123
7.3	Problem Formulation	124
7.4	The Cost Weights Synthesis Problem	126
7.4.1	The MWCC perturbation	126
7.4.2	Backstepping Numerical Method	128
7.5	A Simple Example	129
7.6	Modifications to the original formulation	129
7.6.1	Additional Assumptions	129
7.6.2	Dual Time Scales	131
7.7	Experiments and results	132

7.8	Conclusions	135
8	Conclusions and Future Work	137
	Bibliography	141
A	PeMS speed contours	145
B	Counts from the District 7 ramp survey	147
C	Final selection of boundary flows	153
D	Vehicle types	155
E	Intermediate Vissim results	158
F	Onramp response	159
G	Random seed variations	161
H	Historically-Averaged Split Ratios	163

Chapter 1

Introduction

The main objective of the research in T.O. 4136 and its continuation T.O. 5503 is to develop, validate and implement new traffic-responsive ramp metering strategies that will improve upon existing metering methods and reduce congestion along California freeways. These traffic-responsive ramp metering strategies are designed to achieve the following goals:

1. Maintain, for as long as possible, free-flow traffic conditions in all sections of the highway, while minimizing the occurrence of onramp queue spillover into adjacent arterial traffic.
2. When congestion occurs, minimize its negative effect on highway throughput, while bringing highway traffic to its free-flow state as quickly as possible.
3. Optimize highway throughput while employing ramp metering policies that are perceived to be fair by all travelers (i.e., no single onramp is unduly penalized).

A central goal of this project is to find ways to incorporate recent advances in the areas of traffic data collection (PeMS), traffic simulation, and control theory, into the design of new advanced onramp control methods, and to implement these methods on the Foothill Freeway (I-210) in Pasadena, California. I-210 was selected as the preferred test location, for simulation and possible eventual field-testing of adaptive and traffic responsive ramp metering control schemes for the following reasons:

- (a) I-210 has most of the necessary infrastructure for testing new ramp metering designs.
- (b) I-210 is a heavily used freeway that can benefit greatly from metering schemes that reduce congestion.
- (c) New ramp metering schemes, such as SWARM are currently being tested on I-210.
- (d) Caltrans D7 is a progressive district, which continues to support and explore innovative traffic management and monitoring techniques (e.g SWARM, PeMS). Moreover, there has been a good working relationship between D7 personnel and the PATH Performance Measurement System (PeMS) group, and Professor Dolf May's research group.

A recent study by the District 7 Traffic Operations group demonstrated that ramp metering can be used to alleviate the morning congestion on I-210 [1]. The study compared the traditional time-of-day (TOD) approach with 3 different modes of the SWARM strategy (1, 2b and 1/2b). It was concluded that only SWARM 1/2b resulted in an appreciable, although small improvement over TOD metering. The benefits of SWARM 1/2b were gauged with statistics such as Mainline Speed, which increased up to 44%, and Mainline Travel Time, which decreased by 14%. Both of these improved the highway operation at the expense of the waiting time in onramp queues, which increased on most onramps. Mainline Volume, an indicator that more correctly assesses the *overall* benefit of a ramp metering strategy, increased by only 1% with SWARM 1/2b. This result, we believe, demonstrates that there are still improvements that can be made in terms of the design and testing of ramp metering strategies for I-210. We believe that our approach of careful consideration of historical traffic data, formal controller design, and detailed modeling and simulation of expected outcomes, will result in better methods of onramp control.

1.1 Research outline

The research presented in this report can be separated into two major sections: research using microsimulation models and research using macrosimulation models.

The first section, which includes Chapters 2 and 3, documents the procedure that was followed to construct and calibrate a **microsimulation model**, using Vissim, of the westbound section of I-210 between Vernon and Fair Oaks, and describes an extensive computer simulation study that was conducted using this model to evaluate the performance of two local traffic-responsive metering strategies: Caltrans Percent Occupancy metering and Alinea. The purpose of the Vissim microsimulation model is to serve as a testbed for the evaluation of onramp metering strategies for congested freeways.

The second section, which includes Chapters 4, 5, 6 and 7, describes research that was performed in this project to construct a **macrosimulation model** of the same section of I-210, develop and test an automated calibration procedure for this model, and use this model, together with a linear programming optimizer, to develop a computationally efficient technique for determining globally optimal, coordinated ramp metering strategies for congested freeways which satisfy on-ramp queue constraints.

Below, we briefly describe each chapter of this report.

1.1.1 Overview of Chapter 2

In this chapter a procedure for calibrating Vissim, a microscopic freeway traffic model, is presented and applied to a 15-mile stretch of I-210 West in Pasadena, California. This test site provides several challenges for microscopic modeling: an HOV lane with an intermittent barrier, a heavy freeway-to-freeway connector, 20 metered onramps with and without HOV bypass lanes, and three interacting bottlenecks. Field data used as input to the model was compiled from two separate sources: loop detectors on the onramps and mainline (PeMS), and a manual survey of onramps and offramps. Gaps in both sources made it necessary to use a composite data set, constructed

from several typical days. FREQ was used as an intermediate tool to generate a set of OD matrices from the assembled boundary flows. The development of the Vissim-based model is described in detail. The model construction and calibration procedure consisted of: 1) analysis of the mainline data to identify recurring bottlenecks, 2) network coding, 3) traffic demands coding, and 4) iterated parameter variations based on observations from 1). A qualitative set of goals was established for the calibration. These were met with relatively few modifications to Vissim's driver behavior parameters (CC-parameters).

1.1.2 Overview of Chapter 3

In this chapter an extensive computer simulation study was conducted to compare the performance of several local traffic responsive ramp metering schemes, under realistic traffic flow demands, using a calibrated Vissim microsimulation model of I-210. Local traffic-responsive metering systems respond to changes in traffic volume and/or occupancy on the mainline, measured by loop detectors that are placed up- or down-stream of the on-ramp junction. The use of feedback from the mainline gives the system a degree of robustness, in the sense that it can perform well under a range of traffic conditions. The following two ramp-metering algorithms were selected for testing in this chapter:

Percent Occupancy metering (%-Occ)

This ramp metering strategy is extensively used by Caltrans. This scheme utilizes occupancy measurements *taken upstream of the on-ramp*, in order to set the ramp metering rate.

Alinea

Alinea is a local traffic responsive ramp metering scheme, which was developed by Markos Papageorgiou. It has been chosen as a starting point for our ramp metering design, due to its computational simplicity and successful performance in various European field studies. In 1990-91, Alinea was tested on a 6 km stretch of the Boulevard Peripherique in Paris, which included 3 metered on-ramps and 2 un-metered ramps. Alinea was shown to improve the traffic mean speed in the section, relative to the no-control case. A test comparing Alinea with the Dutch RWS strategy was carried out on the Amsterdam A10 West Motorway, in 1994. In this test, Alinea resulted in smaller delays (including delays incurred on the onramps as well as the mainline) and larger average traffic flows on the mainline.

The goal of the Alinea strategy is to sustain near maximum flow downstream of the on-ramp, by regulating the downstream occupancy to a target value, which is set a little below the critical occupancy at which congestion first appears. The Alinea control strategy uses an integral of occupancy error between the set point occupancy and the actual downstream occupancy to compute the desired ramp metering rate. In its original form, Alinea utilizes occupancy measurements that are located downstream of the ramp, and utilizes an integral action law with saturation.

It should be noted that I-210, as most California highways, does not have loop detectors located immediately downstream of the onramps. Thus, we have developed a version of Alinea, which utilizes the upstream detector, which has been tested using a Vissim simulation study. The simulation

results presented in this chapter show that the upstream placement of the sensor is actually preferred during congestion. These results are later corroborated in Chapter 4, where it is shown that upstream loop detectors are preferred over downstream detectors as the source of measurements during traffic congestion.

1.1.3 Overview of Chapter 4

This chapter deals with the development of macroscopic freeway traffic models that are computationally efficient and suitable for use in real-time traffic monitoring and control applications. Toward the fulfillment of this objective, a macroscopic traffic model, the Modified Cell Transmission Model (MCTM), which is based on Daganzo's CTM, is presented. The main differences with the basic CTM are that the MCTM uses cell densities as state variables instead of cell occupancies, and accepts nonuniform cell lengths, thus allowing greater flexibility in partitioning a freeway. Also in this chapter, the MCTM is piecewise-linearized to produce the Switching-Mode Model (SMM). The SMM is a hybrid system that switches among different sets of linear difference equations, or modes, depending on the mainline boundary data and the congestion status of the cells in a highway section. Using standard linear systems techniques, the observability and controllability properties of the SMM modes have been determined. Both the SMM and MCTM have been simulated over a section of I-210 West in Southern California, using several days of loop detector data collected during the morning rush-hour period. The simulation results show that the SMM and MCTM produce density estimates that are both similar to one another and in good agreement with measured densities on I-210. The mean percentage error averaged over all the test days was approximately 13% for both models.

1.1.4 Overview of Chapter 5

This chapter describes a semi-automated method for calibrating the parameters of the macroscopic modified cell transmission model, and switching-mode model, which were introduced in Chapter 4. A least-squares data fitting approach was applied to loop detector data to determine free-flow speeds, congestion-wave speeds, and jam densities for specified subsections of a freeway segment. Bottleneck capacities were estimated from measured mainline and on-ramp flows. The calibration method was tested on a 14-mile portion of Interstate 210 Westbound in southern California. The calibrated MCTM was able to reproduce observed bottleneck locations and the approximate behavior of traffic congestion, yielding approximately 2% average error in the predicted total travel time.

1.1.5 Overview of Chapter 6

Software developed for the macrosimulation studies of Chapters 4 and 5 is reviewed in this chapter. First, the Matlab-based software used in the MCTM/SMM validation study of Chapter 4 is described. Next, a more efficient, C++-based MCTM simulator is introduced, which can be applied to model a linear freeway segment of arbitrary length. Specifications for the input and output files of the simulator are given, along with instructions for encoding freeway geometries, configuring and running simulations, and generating simulated contour plots and performance measures.

1.1.6 Overview of Chapter 7

In this chapter a new technique for generating optimal coordinated ramp metering plans is developed. The design of this new *predictive* and *coordinated* strategy is based on avoiding the loss of travel time related to *offramp blockage* using an Asymmetric Cell Transmission Model (ACTM). The ACTM is similar to the default MCTM described in Chapter 4. The main difference resides in the treatment of merging flows. The MCTM merge model is *symmetric* in the sense that it makes no distinction between freeway mainline *through* flows and onramp *joining* flows. On the other hand, a clear distinction is made in the ACTM between through and joining flows at the merge. The advantage of using the ACTM for optimization is that its merge model involves a concave $\min\{\}$ function, as opposed to the non-convex/non-concave $\max\{\}$ function of the MCTM. This is shown to be tremendously beneficial to the numerical solution of the optimization problem.

With most predictive designs, the ramp metering rates are found as the solution to a nonlinear optimization problem. In contrast to previous designs, the approach presented in this chapter 1) produces a globally optimal solution to the nonlinear problem, 2) requires only to solve a single linear program, and 3) allows the enforcement of hard constraints on the on-ramp queue lengths. The price that is paid for these features is that the objective function being minimized is not Total Travel Time, but rather a member of a class of “TTT-like” objective functions. A TTT-like objective function is defined as a linear combination of mainline flows with weights that, similarly to the Total Travel Time cost weights, decrease linearly in time from some initial value to zero at the final time.

A numerical example, which is based on an ACTM model of the 15-mile stretch of I-210 West in Pasadena, California, is used to demonstrate the technique. The example shows that the globally optimal metering plan with respect to a TTT-like objective function also performs well in terms of Total Travel Time and predicts a 8.4% savings in Total Travel Time, with queue constraints, over the 5-hour peak period.

Chapter 2

Calibration of Vissim for a Congested Freeway

This chapter documents the procedure that was followed to construct and calibrate a detailed model of a freeway using VISSIM. The purpose of the model is to serve as a testbed for the design and evaluation of an improved onramp metering strategy for a congested freeway. The chosen test site is a stretch of Interstate 210 in Pasadena, California, under the jurisdiction of Caltrans District 07. This freeway sustains heavy congestion in the westbound direction, between around 5:30 and 10:30 am. District 07 Traffic Operations has actively sought to improve the performance of I-210 with onramp metering, and has tested several strategies including local traffic-responsive metering and SWARM, with positive results. They have agreed to consider implementing the control strategies developed by PATH T.O. 4136 if these can be shown in simulation to improve upon their current practices.

This chapter covers the entire model construction process, including data collection, data checking, VISSIM coding, and model calibration. I-210 presents several challenges to microscopic simulation: an HOV lane with an intermittent barrier, a heavy freeway connector, 20 metered onramps with and without HOV bypass lanes, and three interacting bottlenecks. Another complicating factor is the lack of reliable traffic counts from the ramps and mainline. As is demonstrated in Table 2.1, many of the loop detector stations on I-210 are unreliable and several ramps lack sensors altogether. These “real-world” obstacles were faced in ways that may be of interest to future practitioners wishing to construct detailed models of freeways.

The chapter is organized as follows:

Sections 2.1 through 2.6 describe the methods that were used to gather and process geometric and traffic information. Section 2.7 describes the translation of boundary flow data into a set of OD matrices (using FREQ). Section 2.8 presents a study of the mainline data which identifies three recurring bottlenecks and speculates on their causes. The VISSIM model is introduced in Section 2.9. Section 2.10 provides definitions of the model parameters that were varied in the calibration phase, and Sections 2.11 and 2.12 provide the calibration methodology and results.

2.1 The test site - Sources of geometric information

The site and time period chosen for the simulation study is the westbound direction of I-210 from Vernon St. to Fair Oaks (on SR-134, just beyond the 210/134 junction), between 5:30 am and 10:30 am (see Figure 2.1). These temporal and spatial ranges were chosen to ensure a freeflow state at the boundaries. This is a 15-mile stretch of freeway that sustains heavy congestion during the morning commute. Congestion usually begins around 6:00 am, peaks at 7:30 am, and finally dissipates at around 10:00 am. The site has 21 onramps, 20 of which are metered and equipped with a complete set of loop-detectors (all except the 605-NB/210-WB freeway connector). Each metered onramp has a corresponding mainline detector station for traffic-responsive control, and some, but not all, have HOV bypass lanes. There is a median-side HOV lane that spans the entire site, and is separated from the mixed-traffic lanes by an intermittent barrier (shown in Figure 2.1). The cut-off occupancy for the HOV lane is two or more passengers per vehicle, and is enforced at all times.

Simulation models require a detailed and complete description of the layout of the site in order to produce a realistic output. In VISSIM, the recommended method for entering the geometric data is to construct a scaled map, in bitmap format. This picture can be displayed as a background image in the program, allowing the user to easily trace the links and connectors that constitute the supply side of the model (see Figure 2.2). The topological features that were considered relevant to the description of I-210 are:

1. For the mainline:
 - (a) Width and numbers of lanes
 - (b) Locations of onramps and offramps
 - (c) Lane drops
 - (d) Auxiliary lanes
 - (e) Lane change zones
 - (f) Location of the HOV lane and gates
 - (g) Position of mainline loop-detector stations
2. For onramps and offramps
 - (a) Number of lanes at the gore of each onramp and offramp
 - (b) Existence of an HOV bypass lane on onramps
 - (c) Existence and position of metering lights on onramps
 - (d) Arrangement of loop-detectors on onramps and offramps. The position of the onramp queue detector with respect to the presence detector is especially important for experiments involving onramp control, since it determines the maximum storage of the onramp.

Three sources of geometric information were used for this study:

1. A set of photocopies of scaled aerial photographs obtained from Caltrans HQ. These photographs are black-and-white and printed on 11" × 17" paper, with a 1:2400 scale.

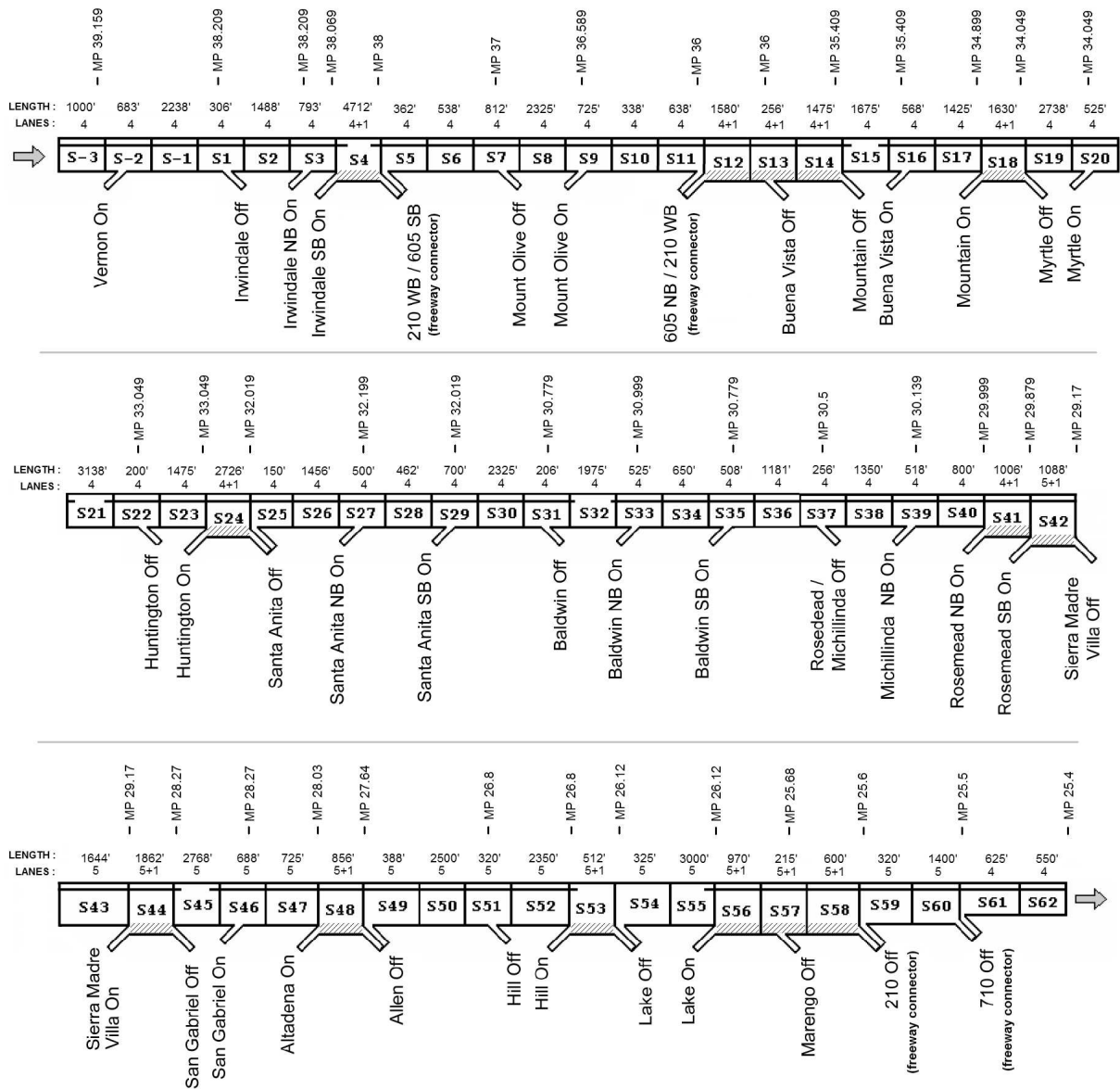


Figure 2.1: 65 sections in the test site. (MP = Mile Post)

2. A set of “as-built” maps indicating the arrangement of loop-detectors on onramps and the mainline. These were provided by the Caltrans District 07 Ramp Metering Group, headed by Mr. Hanh Pham.
3. Un-scaled aerial photographs in bitmap format downloaded from MapQuest (www.mapquest.com)

All of the geometric features were extracted from the aerial photographs (source 1), with the exception of items 1g, 2c, and 2d, which were measured from the as-built maps (source 2). Each of the important features was assigned a section in Figure 2.1. In total, the site was divided into 65 sections (the first three sections have negative indices because they were appended after the initial

numbering). Boundaries were chosen to isolate each of the important topological features. For example, section S29 contains a single lane change zone (item 1e) where traffic from the Santa Anita St. onramp merges with the mainline stream. Figure 2.1 also provides the lengths (in ft.) and the number of mixed-flow lanes in each section. This highway partition was transferred to the large overhead view compiled from source 3 (Figure 2.2), and thus encoded into VISSIM.

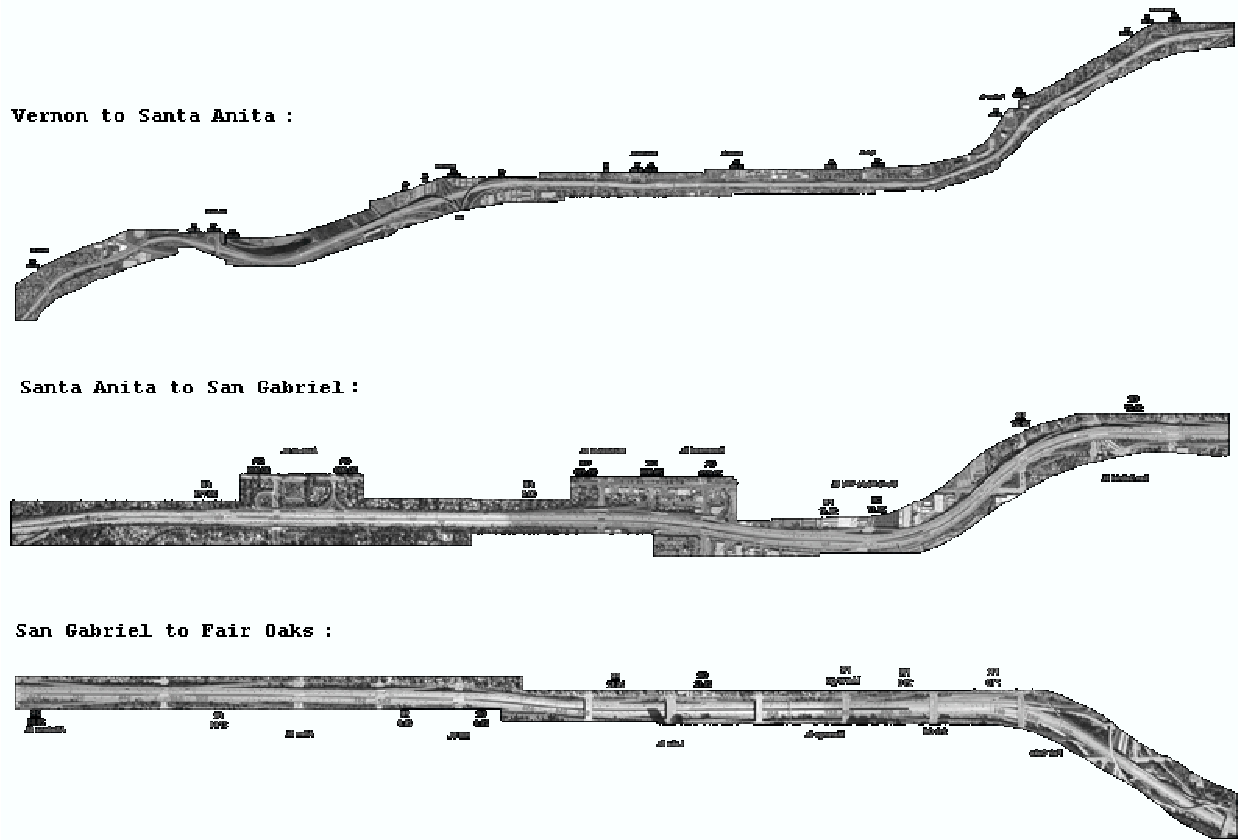


Figure 2.2: Assembled overhead view of I-210

2.2 Traffic data sources

The traffic demand can be defined in VISSIM as set of OD matrices, in which are specified the average numbers of vehicles going from every freeway origin to every destination, at 15-minute intervals. (This is one of two available methods. The alternative is to use aggregate vehicle sources, and to direct traffic using turning percentages.) This and the next few sections describe the procedure that was followed to gather and process traffic data for generating the OD matrices. The first step was to compile a complete and representative set of boundary flows, covering every onramp, offramp, and the two mainline boundaries. $FREQ^1$ was then used to translate the boundary flows into the required set of OD matrices.

¹ $FREQ$ is a macroscopic deterministic freeway corridor model for the development and evaluation of freeway operational strategies, developed by Adolf May and his colleagues at U.C. Berkeley [2].

Two sources of field data were used:

1. **PeMS:** The PeMS database gathers 30-second and 5-minute data from over 30,000 miles of freeway in California. This database was used to assemble a history of traffic measurements for every loop-detector station in the site. A Matlab-based data processing algorithm was created to filter, aggregate, and correct the PeMS data (Section 2.3). Three examples of speed contour maps generated from the processed PeMS mainline data can be found in Appendix A. These represent a heavy, a typical, and a light day of congestion on I-210. Speed contour plots such as these were used to characterize the three major bottlenecks in the system (Section 2.8), and played a significant role in the calibration effort.
2. **Manual counts:** The District 07 Traffic Operations group provided the results of a biennial survey of freeway ramp volumes conducted between 10/2001 and 1/2002. The collected data consists of 15-minute estimates of volumes on most of the onramps and offramps in the test site (all except Marengo St. and the 210 and 710 freeway connectors). The D07 survey did not include any mainline data.

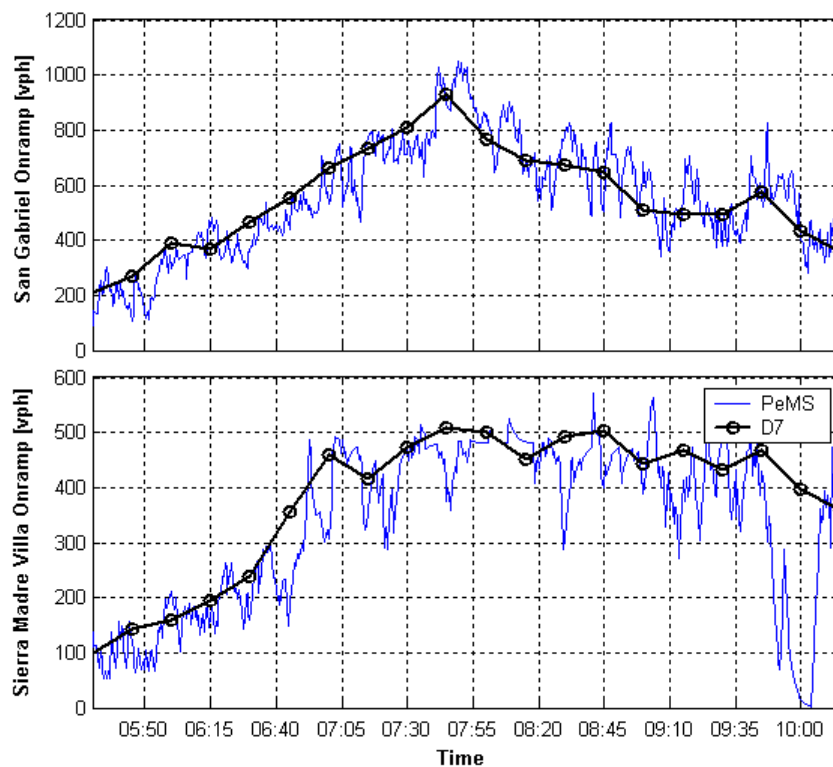


Figure 2.3: Comparison of PeMS 30-second data with the Caltrans D07 survey

A sample of flow values for the Sierra Madre Villa onramp (MP 29.17) from each of the two data sources is shown in Figure 2.3. As in this example, there is close agreement between the two sources in most cases. Instances where significant differences were noted were usually attributable to malfunctioning loop-detectors (i.e., errors in PeMS). Manual counts were generally favored over the PeMS loop-detector measurements for the ramps. PeMS data was used primarily where

mainline measurements were needed. That is, to determine the upstream and downstream mainline flows (needed to estimate the OD matrices in Section 2.7) and to construct the contour plots used for model calibration (Section 2.12).

2.3 PeMS data processing with Matlab

PeMS - the Performance Measurement System - has as its primary function to gather, analyze, and disseminate real-time traffic information for California highways. Its main user interface is a web page², where users can generate a number of plots and traffic performance indices. Additionally, the raw traffic data is stored in a database, and may be provided to interested groups, such as this one. We have used PeMS data in several areas of this project. First, it has served to identify the recurrent trends that characterize the morning commute on I-210. These trends include onramp demands and the normal patterns of congestion on the freeway. Interpretation of PeMS-derived flow and speed contour maps has yielded the critical traffic parameters (e.g. capacity, bottleneck locations) that were used to calibrate the VISSIM model. Secondly, the study of PeMS data has provided insight into the actual availability of reliable real-time data on I-210. Section 2.4 summarizes the conclusions that were reached in this respect. This section gives a brief overview of the filtering and aggregation algorithms that were applied to the raw PeMS data sources prior to their being used in VISSIM.

The PeMS database stores two levels of data resolution: 30 seconds and 5 minutes. The 5-minute data is generated from the 30-second feed, and is aggregated over time before storage. The traffic variables recorded in PeMS include occupancy, flow, speed, and g-factor (estimated effective vehicle length). These can be combined to compute an estimate of average density. All variables in the PeMS database are *per-loop* quantities. Samples of data sequences from PeMS are shown in Figure 2.4.

Figure 2.5 illustrates the stages of data processing that were applied to the raw PeMS feeds. All of these were implemented in Matlab. First, the raw 30-second data (R30) was put through a first-order low-pass filter, producing output S30. The smoothed and raw *per-loop* values (S30, R30 and R5) were then aggregated over lanes, to obtain values for cross-sections of the freeway at ramps and mainline locations (AS30, AR30 and AR5). In each case, the aggregation step was performed with:

$$\begin{aligned}
 occ^{agg}(i, k) &= \sum_j \gamma(i, j) occ(i, j, k) \\
 flow^{agg}(i, k) &= \sum_j \gamma(i, j) flow(i, j, k) \\
 speed^{agg}(i, k) &= \sum_j \gamma(i, j) speed(i, j, k)
 \end{aligned} \tag{2.1}$$

Here, the values on the left-hand-side are aggregated quantities. They are a linear combination of the *per-loop* values, with coefficients $\gamma(i, j)$. i denotes the detector station, j is an index for each loop-detector within a detector station, and k is the time interval. For onramps, the detector station may include *entrance*, *presence*, *passage*, *hov bypass*, and *queue* detectors. In this case,

²<http://pems.eecs.berkeley.edu>

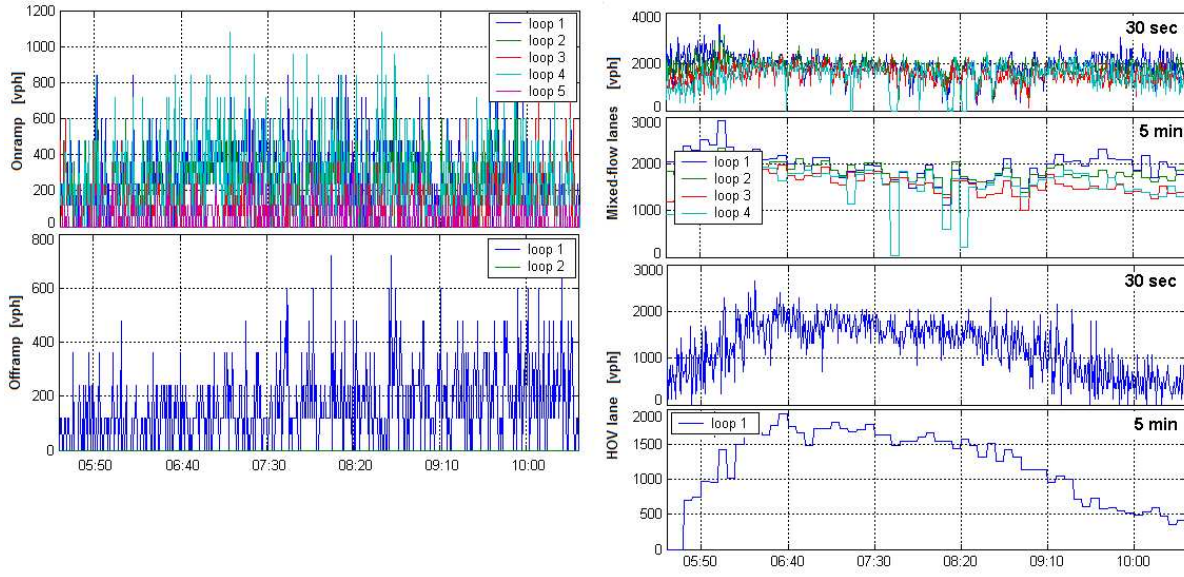


Figure 2.4: 30-second and 5-minute flows from PeMS (R30 and R5)

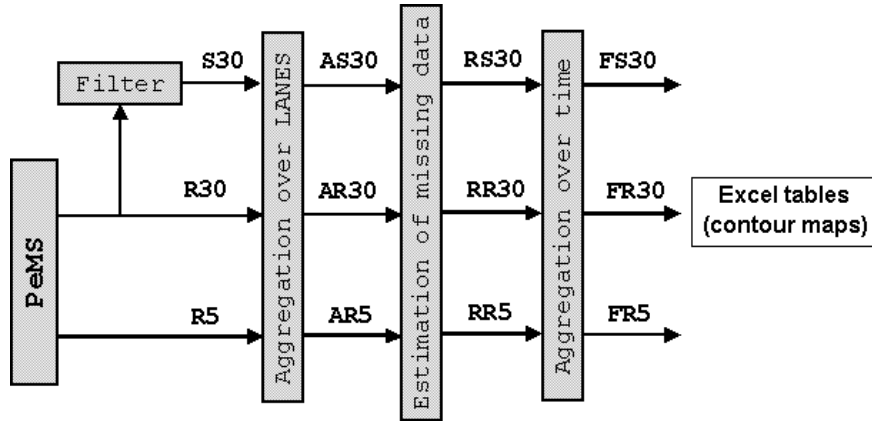


Figure 2.5: PeMS data processing

all $\gamma(i, j)$'s were set to zero, except for the one representing the *entrance* loop, which was set to 1.0. For mainline loop-detector stations, all $\gamma(i, j)$'s were set to 1.0. The $\gamma(i, j)$ coefficients were also used to perform crude data reconstruction for malfunctioning mainline loops. For instance, the detector on lane 2 of the Myrtle St. mainline station (MP 34.049) did not work on 11/6/2001. Its data was replaced with the average of lanes 1 and 3, by setting the γ 's on those lanes equal to 1.5.

Next, additional conservation-based data reconstruction methods were applied in cases where more severe data losses could not be compensated with the $\gamma(i, j)$ coefficients. Two examples of this situation that were encountered were the temporary loss of communication with an entire mainline station, and the permanent lack of loop-detectors on several offramps. The current reconstruction method is based on a static balance of flows on a small section of the freeway. Three reconstructed data sets resulted from this step: RS30, RR30, and RR5. These were fed to a

time-aggregation block which generated 15-minute tables. The contour plots of Appendix A are examples of the FR30 stage.

2.4 Loop-detector reliability

One of the difficulties of using detector data for model input and calibration (as well as for traffic-responsive control) is that in many cases adequate data is not available, due either to an incomplete sensor infrastructure or to failure of the existing system. The availability of large quantities of historical data from the PeMS database allowed us to assess the dependability of the existing loop-detector infrastructure on I-210.

Table 2.1 provides percentages of time during which each onramp, offramp and mainline station registered signal pulses. The percentage values in the table are the averages over all loops in a given station (onramp, offramp, or mainline/HOV station) of the ratio of the number of non-zero flow measurements to the total number of measurements. These are optimistic estimates since they do not consider whether the non-zero values were reasonable. The statistics were taken over 11 weeks of PeMS data, using weekdays only, and from 5:30 am to 10:30 am. It can be noted in the table that, in general, mainline and onramp detectors are more reliable than offramp detectors. Most remain on-line around 80% of the time. Two exceptions are the Michillinda NB (44%) and Sierra Madre Villa (60%) onramp and mainline stations. The only onramp lacking a set of loop-detectors is the freeway connector from 605 NB (MP 36). Offramps, on the other hand, are more problematic. Many lack sensors, or at least these are not included in the PeMS database (e.g. Buena Vista - MP 36). Others have sensors that appear to be permanently disconnected from the data collection system (e.g. Lake - MP 26.12).

Street Name	MP	% non-zero data		
		offramps	onramps	mainline/HOV
Vernon St On	39.159	-	81.0%	81.0%
Irwindale St. On/Off	38.209	0.0%	81.6%	81.6%
	38.069	-	81.2%	81.2%
605 SB Off	38	n.m.	-	-
Mt. Olive Off	37	n.m.	-	-
Mt. Olive On	36.589	-	81.4%	81.4%
605 NB On	36	-	n.m.	n.m.
Buena Vista Off	36	n.m.	-	-
Mountain Off	35.409	0.0%	-	-
Buena Vista On	35.409	-	72.1%	72.1%
Mountain On	34.899	-	65.9%	65.9%
Myrtle On/Off	34.049	79.1%	79.1%	79.1%
Huntington On/Off	33.049	79.9%	80.4%	80.4%
Santa Anita Off	32.019	76.5%	-	-
Santa Anita NB On	32.199	-	79.4%	79.4%
Santa Anita SB On	32.019	-	80.4%	80.4%
Baldwin Off	30.779	79.1%	-	-
Baldwin NB On	30.999	-	80.5%	80.5%
Baldwin SB On	30.779	-	79.1%	79.1%
Rosemead/Michillinda Off	30.5	n.m.	-	-
Michillinda NB On	30.139	-	44.0%	44.0%
Rosemead NB On	29.999	-	79.9%	79.9%
Rosemead SB On	29.879	-	62.7%	62.7%
Sierra Madre Villa On/Off	29.17	60.2%	60.2%	60.2%
San Gabriel On/Off	28.27	67.2%	81.5%	81.5%
Altadena On	28.03	-	81.5%	81.5%
Allen Off	27.64	74.0%	-	-
Hill On/Off	26.8	80.0%	80.0%	80.0%
Lake On/Off	26.12	0.0%	81.5%	81.5%
Marengo Off	25.68	81.5%	-	81.5%
210 connector Off	25.6	n.m.	-	-
710 connector Off	25.5	n.m.	-	-

Table 2.1: Percent non-zero flow measurements (n.m.=not measured, '-'=does not apply)

2.5 Ramp flows from the Caltrans D07 survey

The ramp counts collected by the District 07 biennial survey are provided in Appendix B. These measurements were gathered manually, by counting the number of vehicles that used every on-ramp and offramp, at 15-minute intervals, throughout the day. Each ramp was surveyed over a period of about 14 consecutive days. The surveyed days are highlighted in Tables B.1 and B.2 in Appendix B. This data set constituted a complete picture of the traffic demand entering and exiting the test site using the ramps, but it did not include any mainline data. Conversely, the PeMS database provided mainline measurements that were practically complete, but lacked information from several key ramps, including the heavy freeway connector from 605 NB (MP 36), and several offramps where loop-detectors had either failed or were missing.

The main difficulty encountered with the D07 boundary data was that there was no single day in which all ramps were surveyed simultaneously. This situation is common in real-world settings, since it is rare to find a complete and reliable sensor structure. As a consequence, it was necessary to assemble a single composite day using ramp counts from several different days considered as *typical*. The set of typical days was created by first discarding all Mondays, Fridays, weekends, and days that did not closely follow the normal (i.e. average) pattern. The remaining days are highlighted with bold grey lines in the time series plots of Figures B.3 through B.5. The variances in the counts for the reduced group are plotted in Figure 2.6. These values were computed as:

$$\text{var}(s) = \frac{1}{K \times D} \sum_{k=1}^K \sum_{d=1}^D \frac{(f_{s,k,d} - \bar{f}_{s,k})^2}{\bar{f}_{s,k}}$$

with

$$\bar{f}_{s,k} = \frac{1}{D} \sum_{d=1}^D f_{s,k,d}$$

$f_{s,k,d}$ is the k th 15-minute vehicle count in the 5:30 am to 10:30 am period ($K = 20$), on day d , from station s . D is the number of days in the reduced set. From this set, a single day was selected for each onramp and offramp. The selected day is marked with a ‘+’ sign in Tables B.1 and B.2, and also with ‘+’ markers in Figures B.3 through B.5.

2.6 Mainline flows from PeMS

Measurements for the two mainline boundaries (Vernon and Fair Oaks) were required to complete the specification of traffic demands for FREQ’s OD table estimation. These were obtained from PeMS. Figure 2.7 shows per-lane average flow measurements (AS30) for several days (Tuesdays, Wednesdays and Thursdays only) during the District 7 survey of freeway ramps. Notice that the flow pattern near Vernon St. does not resemble the expected inverted U shape for the morning period. Flows at this location start at an extremely high value, near 2200 vph per lane, and slowly decrease throughout the morning. This tendency is odd, but repeats itself from day to day.

Again, it was necessary to select a single typical day for the mainline boundary flows from a number of days. This selection was based on the following criteria:

1. completeness of the data set,

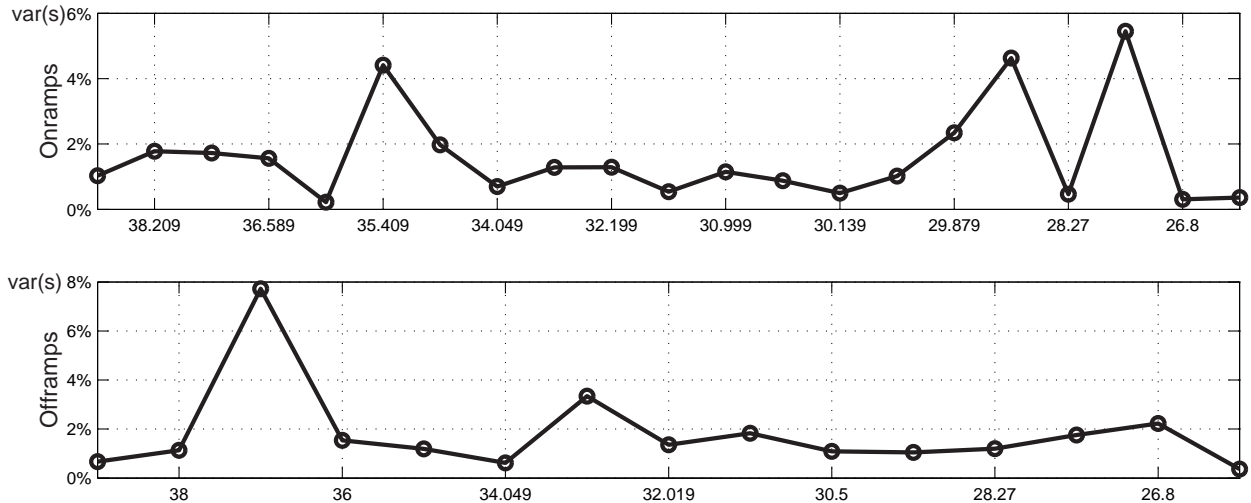


Figure 2.6: Percent variance in selected ramp counts from the Caltrans D07 survey

2. how well the flow data followed the day-to-day trend,
3. resulting “scale factor”.

Scale factors are defined as the ratio, for each 15-minute period, of the total number of vehicles entering the system to the total number of vehicles that exit. They are computed in *FREQ* as a first step to finding the OD matrices (Section 2.7). They can also be used to identify possible problems in the data set, since they are expected to fall within 10% of 1.00, for a normal (incident-less) traffic scenario, and their average over a 5-hour period should be very close to 1.00. The scale factors resulting from the final selection of ramp and mainline flows are shown in Figure 2.8. The aggregate scale factor for the 5 hour period is 1.02.

Two tables with the final selection of ramp flows can be found in Appendix C.

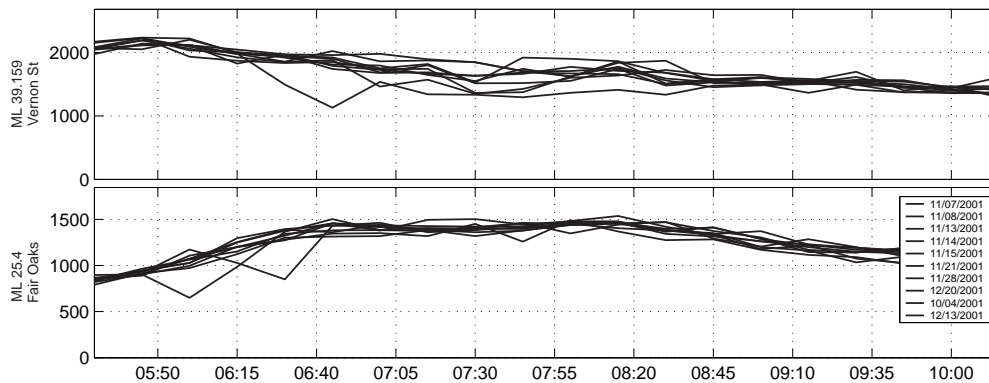


Figure 2.7: Mainline boundary flows

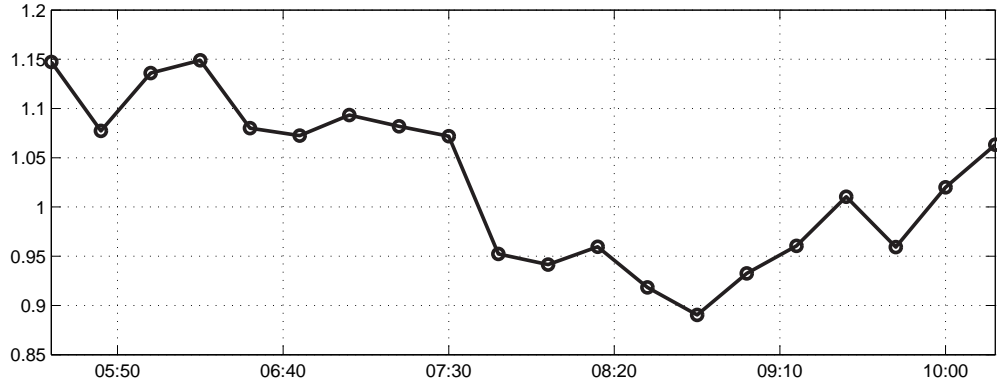


Figure 2.8: Scale factors with final input flow selection

2.7 Estimating OD matrices with the FREQ model

The translation of ramp counts to the set of OD matrices required by VISSIM was achieved with FREQ. As was mentioned in the previous section, FREQ was first used as a data verification tool. Specifically, it was used to check scale factors ($\alpha[k]$):

$$\alpha[k] = \frac{\sum_{\text{origins}} f_i^{\text{in}}[k]}{\sum_{\text{destination}} f_i^{\text{out}}[k]} \quad k = \text{all 15-minute time intervals} \quad (2.2)$$

The scale factors corresponding to the final selection of flows were shown in Figure 2.8.

FREQ's OD estimation capability was then used to convert the onramp and offramp demand data into a sequence of 20 OD matrices – one for each 15-minute time interval in the 5 hour period. Each of these matrices has dimensions $(22) \times (19) = (21 \text{ onramps} + 1 \text{ mainline origin}) \times (18 \text{ offramps} + 1 \text{ mainline destination})$. An intermediate step was performed here to incorporate the information of the percentage of HOV vehicles present in each of the source flows. As is explained in Section 2.9.3, each OD matrix in VISSIM applies to a specific *traffic composition*. Since the I-210 model includes two traffic compositions (MIX_TC and HOV_TC, defined in Section 2.9.3), each FREQ OD matrix spawned two VISSIM OD matrices, giving a total of 40 matrices. The following assumptions were made based on available data and on suggestions from Caltrans staff. They were sufficient to make the conversion from 20 to 40 OD matrices.

- The number of vehicles using the HOV lane at the upstream mainline boundary (Vernon St.) is a given time-varying fraction of the total (mixed-lanes plus HOV lane). This fraction, shown in Figure 2.9, was derived from PeMS data.
- In addition to the HOV vehicles in the HOV lane, 5% of the vehicles in the Vernon St. mixed-flow lanes are also HOV.
- 12% of the vehicles entering the freeway at onramps are HOV.
- Of the total number of HOV vehicles that reach the downstream mainline boundary, at Fair Oaks St., 20% are in mixed-flow lanes, and 80% are in the HOV lane.

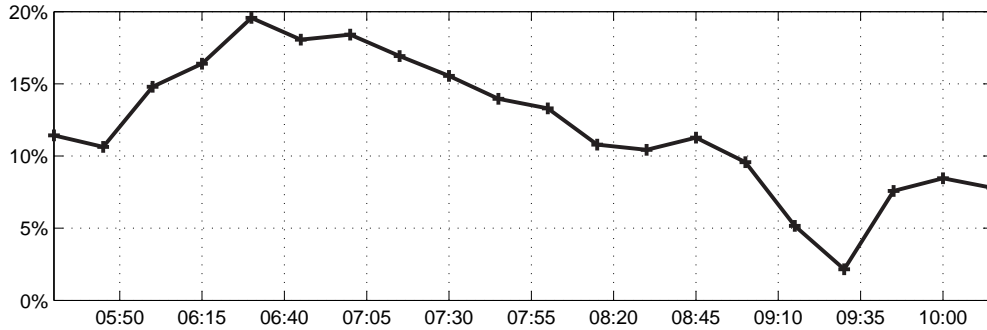


Figure 2.9: Percentage flow in the HOV lane at Vernon St.

2.8 Identification of recurring bottlenecks

The first step in the model calibration process was to identify the location and causes of the congestion on I-210. Appendix A contains three speed contour plots showing the congestion patterns for a heavy, a typical, and a light day of traffic. From these and other similar contour plots, three distinct problem areas, or bottlenecks, were identified. They are:

B1: Near Huntington St. (MP 33.049).

B2: Near the Rosemead and Michillinda St. ramps (MP 30.139).

B3: Near Hill St. (MP 26.8).

These three bottlenecks are illustrated in Figure 2.10. Mainline loop-detector stations are depicted in the figures with a \times , \circ , or \otimes symbol, depending on whether the station is characterized by heavy congestion (speed is often < 40 mph), by free flow (speed > 55 mph), or by decreased speeds not reaching full congestion (speed is between 40 mph and 55 mph). Distances between ramps are marked on the figure, along with the number of mixed-flow lanes in each section. The number accompanying each onramp and offramp is a representative (approximately average) level of flow on the ramp when congestion begins.

The following conclusions were reached on the probable causes of congestion at each bottleneck:

B1: This bottleneck is not easily explained with a simple comparison of nominal capacities and demands. The Myrtle ramps make no net contribution to the amount of traffic on the freeway ($600-600=0$). The Huntington ramps supply about 500 vph to the mainline, but this should be easily absorbed by the auxiliary lane between Huntington and Santa Anita. The observed deceleration of the traffic stream must therefore be caused by a reduction in capacity near the Huntington ramps, or somewhere between Huntington and Santa Anita. Localized reductions in capacity have a variety possible causes, including grades, curves, reduced visibility, street signs, and direct oncoming sunlight. In this case, the most probable cause is the series of reverse curves between Myrtle and Huntington (as suggested by Caltrans staff).

B2: Bottleneck B2 is less stable than B1, in the sense that its location and congestion pattern are less predictable. Congestion initiates somewhere near the Rosemead and Michillinda ramps (MPs 30.139 to 29.879), however, complete breakdown, with speeds in the 20's and 30's, only occurs upstream near the Baldwin onramp (MP 30.779). The Rosemead and

Michillinda detectors sometimes register speeds decreasing as low as 40 mph, but seldom less than that. Congestion in this region is probably caused by the two heavy onramps from Rosemead and Michillinda, which add approximately 1700 vph to the freeway. These on-ramp flows should be easily accommodated by the two additional auxiliary lanes. However, it appears that this increased capacity is not being fully utilized, probably due to increased weaving in that area.

B3: Mainline traffic near Hill St. (MP 26.8) is usually slow, and sometimes fully congested. Traffic near Altadena (MP 28.03) almost always becomes completely congested. As with the previous two, bottleneck B3 cannot be easily explained by comparing demands and nominal capacities, since the heavy flow from the Hill onramp is supported by an auxiliary lane. The observed congestion must therefore again be explained by a reduction in capacity. In this case, at least two probable causes exist: the S-shaped bend between Hill and Lake, and the heavy weaving that takes place in the 800-foot auxiliary lane before the Lake offramp.

2.9 The VISSIM model

2.9.1 Overview of the program

VISSIM is the microscopic/stochastic traffic simulator that was used to create the detailed model of I-210 West. In the past, it has been used mostly as a tool for the design of urban public transportation systems, but has been shown to be capable of reproducing freeway traffic behaviors as well. Its traffic model is based on the work of R. Wiedemann [3, 4], which combines a perceptual model of the driver with a vehicle model. The behavioral model for the driver involves a classification of reactions in response to the perceived relative speed and distance with respect to the preceding vehicle. Four driving modes are defined, as shown in Figure 2.11: Free driving, approaching, following, and braking. In each mode the driver behaves differently, reacting either to its following distance, or trying to match a prescribed target speed. These reactions result in a command acceleration given to the vehicle, which is processed according to its capabilities. Drivers can also make the decision to change lanes. This decision can either be forced by a routing requirement, for example when approaching an intersection, or made by the driver in order to access a faster-moving lane.

A useful feature in VISSIM is that it allows stochastic variations of several of its parameters, such as the desired speeds and accelerations. Stochastic sources of boundary flows (rates and compositions) are also supported. Randomness can further be introduced in the ability of the driver population to perceive changes in relative speeds and distances and to determine their mode of driving. More comprehensive descriptions of the VISSIM model and software can be found in [5, 6].

Traffic signals can be simulated, and are controlled in VISSIM by the Signal State Generator (SSG), which is a separate module from the traffic simulation module. One important feature of the SSG is that it is programmable – the user is allowed to specify signal control logics with a descriptive language called VAP (Vehicle Actuated Phasing). Through the VAP interface, the user can access loop-detector measurements, and use them to generate commands for the traffic signals. A trace file can be exported from the VAP process to record loop-detector and signal

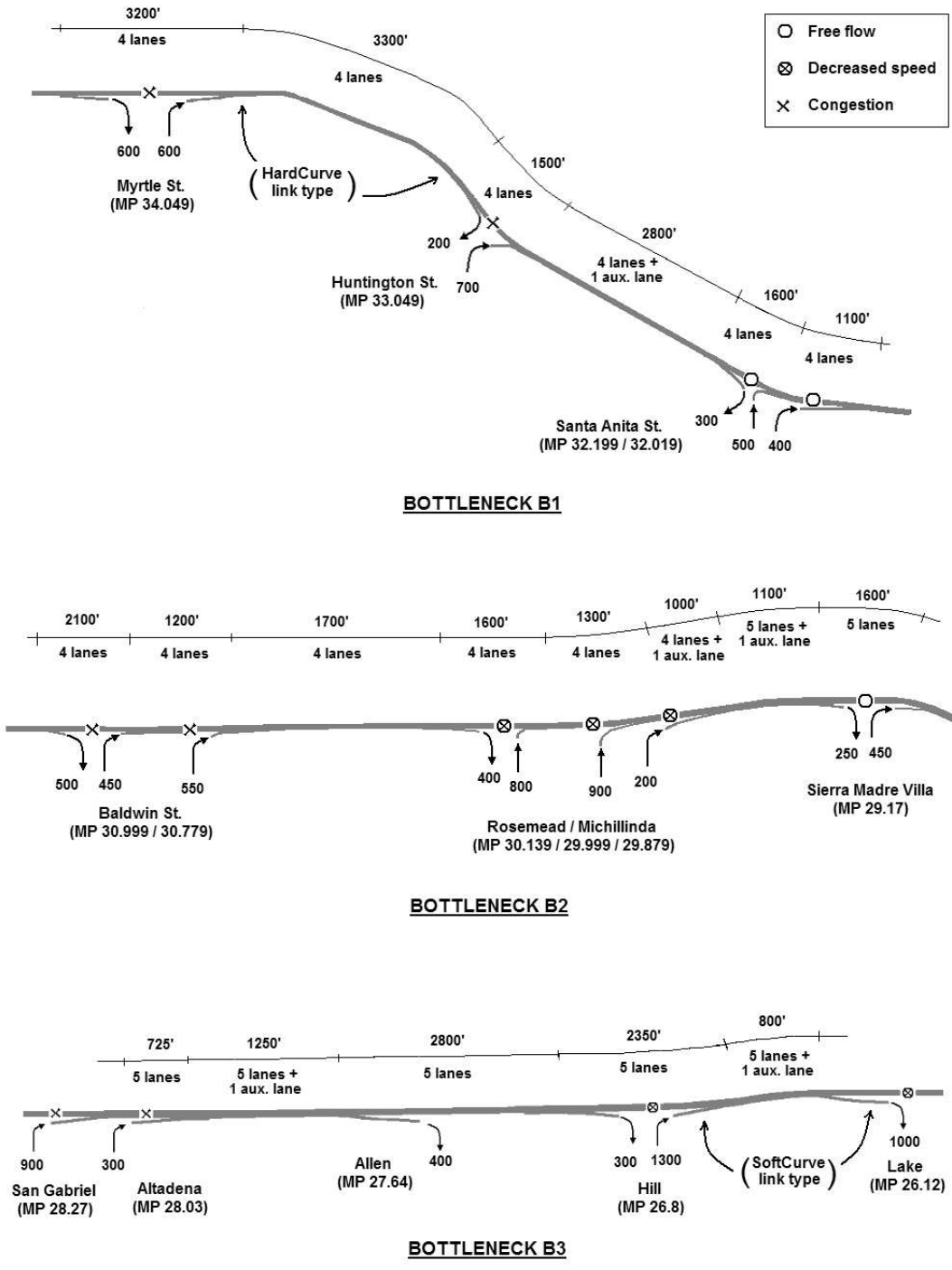


Figure 2.10: Three major bottlenecks

related variables. These traffic signaling features can be used, for example, on freeway onramps to simulate onramp metering control.

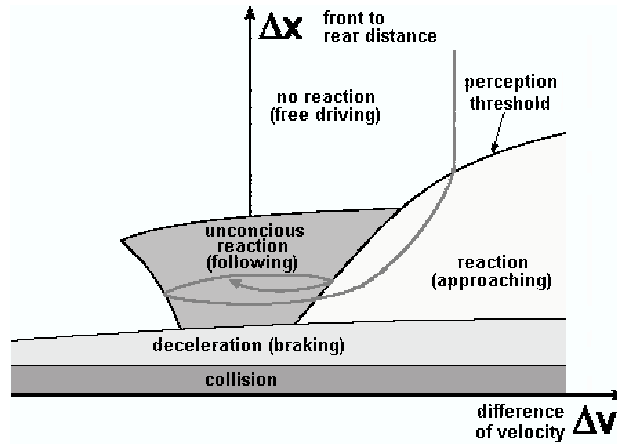


Figure 2.11: VISSIM's driver behavior model

2.9.2 Coding of the network geometry

As was described in Section 2.1, the relevant features of the I-210 test site were marked on a composite aerial photograph, which was downloaded from MapQuest (Figure 2.2). Scale was established on this image by matching landmarks with the scaled aerial photographs obtained from Caltrans HQ. Links and link connectors were then traced on this background image in VISSIM. A screenshot of VISSIM is shown in Figure 2.12.



Figure 2.12: Snapshot of VISSIM

Control Hardware

In addition to the freeway geometry, coding of the supply side of the model also entailed the placement of the control hardware elements: loop-detectors and signal heads. In VISSIM, each signal head is associated with a signal group. All signal heads in the same group display the same signal status at all times. For I-210, a separate signal group was created for each signal head, in order to allow every onramp, and even different signal heads on the same onramp, to act independently. Every signal group, in turn, is associated with a signal controlled junction (SCJ).

An SCJ can contain several signal groups. The control logic (i.e. VAP code) corresponding to a particular SCJ determines the signal status of all signal groups and signal heads within that SCJ. A single SCJ was used to control all of the signals in the I-210 model.

All signal heads were held on green for the calibration runs of this chapter. It should be mentioned that this is not the current situation on I-210. District 07 uses a combination of local traffic-responsive and fixed-time onramp metering for this freeway. However, as was shown in Figure 2.3, the survey counts used as input to the VISSIM model closely follow the measurements from the *entrance* loop recorded in PeMS. This loop-detector is placed at the gore of the onramp, beyond the metering light. It was therefore inferred that the survey counts represent the actual number of vehicles entering the freeway, not the demand entering the back of the onramp queue. It should also be pointed out that all freeway offramps, including the two bifurcating freeway connectors, were left uncontrolled, based on information received from Caltrans D07 that none of the offramps in the test site are affected by external queues (e.g. emanating from surface street traffic lights).

HOV lanes

Another important aspect of the network coding is the implementation of HOV lanes. VISSIM allows particular lanes of a link to be closed to certain vehicle types (vehicle types are defined in the next section). HOV-only restrictions were enforced by creating a separate vehicle type for the HOV vehicles, and by closing the HOV-only lanes to all non-HOV types. This method was used to create the HOV lanes on the mainline and HOV bypass lanes on the onramps.

Freeway connector

Almost all of the onramp merges were modeled following the method recommended in [6], where vehicles entering from the onramp join the mainline stream by changing lanes within a merge section. It was found however, that this approach only worked well for onramps with small or moderate flows. It failed for the heavy freeway connector from 605 NB (MP36), where it produced a large queue on the onramp. An alternative configuration was designed to shift some of the burden of the merge away from the onramp and onto the mainline, by forcing a percentage of the mainline vehicles to evacuate the right-most lane upstream of the ramp junction, thereby opening space for the flow from 605 NB. This was accomplished using VISSIM's *partial routing decisions* (see [6] for further details).

2.9.3 Coding of traffic demands

Vehicle Types and Traffic Compositions

The vehicle population in VISSIM is categorized into *vehicle types*. A single type gathers vehicles that share common vehicle performance attributes. These attributes include model, minimum and maximum acceleration, minimum and maximum deceleration, weight, power, and length. All of these, except for model and length, are defined in VISSIM with probabilistic distributions (as opposed to scalars). Four vehicle types were created to model I-210: LOV, HOV, HGV_MED, and HGV_LARGE. The LOV type represents passenger vehicles with a single occupant. HOV vehicles have 2 or more occupants and are allowed to use the HOV and bypass lanes. The vehicle specifications for these two types are identical to those of the default CAR type in VISSIM [6]. The HGV_MED and HGV_LARGE types represent, respectively, medium and large size trucks. Parameter values for each of the four vehicle types are provided in Appendix D. *Traffic compo-*

sitions are the proportions of each vehicle type present in each of the source flows. Two traffic compositions were defined: MIX_TC for mixed-flow lane sources (93% LOV, 3.5% HGV_MED, 3.5% HGV_LARGE) and HOV_TC for HOV lane sources (100% HOV type).

Dynamic Assignment

VISSIM supports two different forms of input for the traffic demands. We chose to use its *dynamic assignment* module, which automatically determines inlet flows and routing information based on a user-supplied set of OD matrices. Each OD matrix is related to a single traffic composition, and to a 15-minute period of the simulation. The demand specification for the I-210 model consists of 40 OD matrices - 2 traffic compositions (MIX_TC and HOV_TC) times 20 time intervals. Each OD matrix has entries in the ij^{th} position indicating the average flow of a given traffic composition entering the network at the i^{th} onramp, with destination at the j^{th} offramp, during a particular 15-minute period. Routes, or traffic assignments, are generated by the dynamic assignment module by assigning a cost to every route available to each OD pair, and then choosing the route with minimum cost. The cost function in VISSIM includes terms penalizing the total distance, total travel time, and a link cost. This last term serves to model factors not covered by the first two, such as tolls. The link cost was used here, as explained below, to encourage the use of the HOV lanes by HOV vehicles.

HOV lanes and link costs

The idea behind dynamic assignment is that repeated simulations using this method for generating routes, and updating the travel time cost between iterations, should eventually converge to an equilibrium solution, in the sense that traffic assignments and travel times will eventually stop changing between iterations. In the case of I-210, the only routing decision to be made is whether and where the HOV vehicles will access the HOV lane. The simulation runs presented in this chapter are based on a single iteration of dynamic assignment. Travel time was therefore not a consideration in the selection of routes for HOV vehicles (this is because travel time is only known after the first iteration). Instead, the HOV lane was given a favorable cost by using the link cost coefficient. A separate link cost coefficient can be assigned to each vehicle type. The LOV vehicle type's link cost coefficient was set to 0.0, whereas the HOV type was given a value of 1.0. In computing a cost for each route, the program multiplies this coefficient by a link cost associated with each link in a given route, and adds them up. HOV lanes were given a preferred status by attaching a lesser link cost to HOV lanes, as compared to mixed traffic lanes. Thus, the minimum-cost route available to HOV-type vehicles was always to enter the HOV lane at the gate nearest to its origin, and to exit it at the gate nearest to its destination. Non-HOV vehicles were declined the use of HOV lanes with type-specific lane closures (described in Section 2.9.2).

2.9.4 VISSIM output

Two output files were used to generate the contour and time-series plots included in this chapter. First, the VAP process (Section 2.9.1) produced a trace file that contains 5-minute averages of flow and occupancy measurements for all of the loop-detectors in the model. Second, VISSIM's *link evaluation* was used to export space-aggregated traffic variables, such as link flow, density, and speed, also at 5-minute intervals. A MATLAB-based interpreter was created to read these output files and to generate the Excel tables and Matlab plots used to evaluate the simulation outcome.

2.10 Changeable model parameters - default values

Section 2.9.3 listed the model parameters related to the physical attributes of the *vehicle*. These were assigned separately for each vehicle type. Fixing the vehicle population, we now look at the parameters of the *driver* model. We have assumed that driver behavior is not correlated with vehicle type, but instead with the position of the driver/vehicle unit in the freeway. For example, drivers might behave differently on curved sections, as compared to straight sections. Thus, the parameters described in this section apply equally to all vehicle types, but were adjusted for each *link type*. Link types are analogous to vehicle types. They gather links with similar driver behavior parameters. Six link types were created to model I-210. These are described in Section 2.11. The driver behavior parameters that were changed from their default values to define each link type are described below. This is a subset of the total number of adjustable driver behavior parameters available in VISSIM. A complete list can be found in [6].

Necessary lane change

The dynamic assignment module provides to each driver a sequence of links to follow that will take it from its origin to its destination. The parameters related to necessary lane changes dictate how far in advance each driver will be able to anticipate the next bifurcation (i.e. offramp) or lane drop on its list, and how aggressively that driver will change lanes to reach it. The first two items below – *look-back distance* and *emergency stop distance* – are the only driver behavior parameters that are not grouped into link types, but must be specified for each link connector separately (in VISSIM the *link connector* is the boundary between two links).

- Look-back distance: Distance in anticipation of a bifurcation that the driver will begin maneuvering towards the desired lane. Range=(0,∞). Default=200 m.
- Emergency stop distance: Distance before the bifurcation where the driver will stop if it has not reached its desired lane. Range=(0,∞). Default=5 m.
- Waiting time before diffusion: A driver/vehicle that has come to a halt at the emergency stop position will wait at most this amount of time for a gap to appear in the adjacent lane. After the waiting time has elapsed, it is removed from the simulation. Range=(0,∞). Default=60 seconds.

Vehicle following behavior

VISSIM includes two versions of the Wiedemann model: urban driver and freeway driver. Only the freeway driver type was used. The car-following mode of the freeway driver model involves 10 tunable parameters: CC0 through CC9. Below are described only those CC-parameters that were modified from their default values.

- CC0 and CC1: Coefficients used in the calculation of the safe bumper-to-bumper distance (in [m]): $dx_safe = CC0 + v \cdot CC1$, where v (in [m/s]) is the speed of the trailing vehicle. According to [6], CC1 is the parameter with the strongest influence on freeway capacity. In fact, it can be related almost directly to capacity by noting that $(dx_safe + \text{vehicle length}) \cdot \text{capacity} = \text{freeflow speed}$. With reasonable values of capacity, dx_safe , and freeflow speed, and default CC0, this calculation gives $CC1 = 1.5$ seconds. The range for both CC0 and CC1 is (0,∞). Default values are $CC0 = 1.5$ m and $CC1 = 0.90$ s.

- CC4 and CC5: These are dimensionless parameters influencing the coupling between leader and follower accelerations. Smaller absolute values result in driver behaviors that are more sensitive to changes in the speed of the preceding vehicle. It is recommended in [6] that these two parameters have opposite signs and equal absolute values. Default values are $CC4=-0.35$ and $CC5=0.35$. The absolute value of CC4 (or CC5) can be understood as the inverse of a stiffness coefficient between consecutive vehicles.

These three CC-parameters (CC0, CC1, and the CC4/CC5 pair) were used to model the curvature-induced capacity drops that are the supposed culprits of bottlenecks B1 and B3. We can infer from their definitions that increments in CC0, CC1, or in the absolute value of CC4/CC5 will lead to reductions in freeway capacity.

2.11 Variations of selected driver behavior parameters

With model inputs (network supply and traffic demand) fixed as described in Section 2.9, an initial simulation experiment was run using default driver behavior parameters. The resulting speed contour plot is shown in Figure 2.13. The immediate observation here is that there is a severe blockage near the downstream end of the freeway that produces a queue which quickly overruns the entire site. This problem was caused by the large number of vehicles attempting to exit through the last two offramps (the 210 and 710 freeway connectors), but were unable to complete the necessary lane changes before reaching and stopping at the emergency stop position. Several adjustments to the routing-imposed lane change parameters were made to correct this problem.

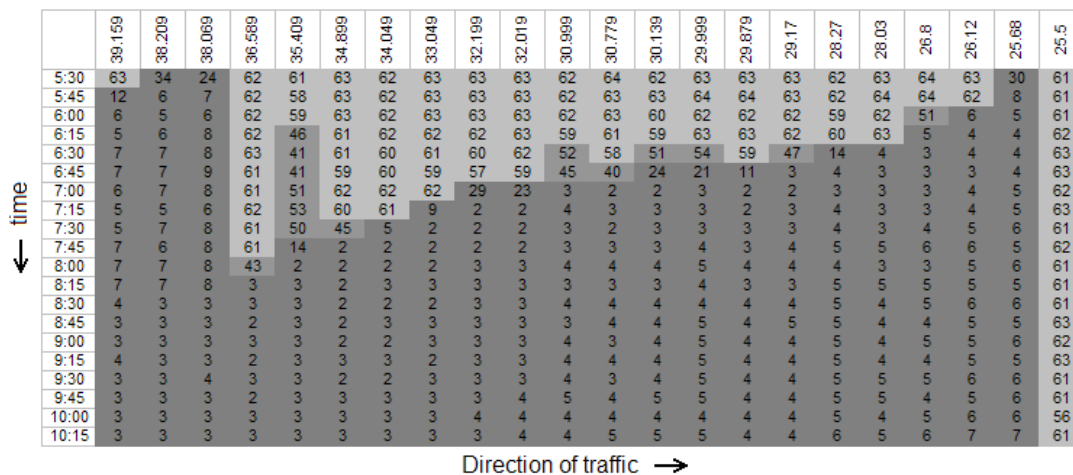


Figure 2.13: Speed contour plot with default driver behavior parameters (in [mph])

Adjustments to the look-back distance

It was determined that the default look-back distance of 200 m was too small for large numbers of vehicles crossing over several lanes of traffic to reach their exits. On the other hand, increasing this value too much had the unrealistic effect of bunching up all of the exiting vehicles in the right-most lane, far upstream of their intended offramp. These vehicles then obstructed other upstream

offramps and onramps. It was therefore necessary to tune the look-back distances individually for each offramp, in a way that allowed vehicles sufficient weaving space while ensuring that these lane-change regions did not overlap. The list of tuned look-back distances is given in Table 2.2. Figure E.1 in Appendix E shows the contour plot resulting from this adjustment. Note that the offramp blockage problem was corrected almost completely by tuning the look-back distances.

MP	Street Name	Mainline look-back	Offramp look-back
38.209	Irwindale	800'	800'
38	605-SB	1450'	1450'
37	Mount Olive	800'	800'
36	Buena Vista	400'	400'
35.409	Mountain	200'	400'
34.049	Myrtle	800'	800'
33.049	Huntington	800'	800'
32.019	Santa Anita	200'	800'
30.779	Baldwin	800'	800'
30.5	Rosemead	800'	800'
29.17	Sierra Madre Villa	800'	800'
28.27	San Gabriel	800'	800'
27.64	Allen	800'	800'
26.8	Hill	800'	800'
26.12	Lake	800'	800'
25.68	Marengo	600'	700'
25.6	210 connector	250'	700'
25.5	710 connector	200'	700'

Table 2.2: Adjusted look-back distances for mainline/offramp bifurcations

Adjustments to the Waiting time before diffusion

Another modification that was found useful for eliminating the offramp blockages was to decrease the *waiting time before diffusion* parameter, from its default 60 seconds to 1 second. With this setting, vehicles that stopped at the emergency stop position on the mainline (at the offramp bifurcation) were immediately removed from the simulation, thereby minimizing the obstruction to the freeway. Eliminating these vehicles has little impact on the total travel time, since they are few and very close to their exit anyway. However, this adjustment is only recommended after the number of affected vehicles has been minimized by tuning the look-back distances. Also, one should be careful not to affect other bifurcations and/or lane drops within the network where larger waiting times are desired. For example, in the case of I-210, vehicles attempting to enter the freeway also frequently reached the emergency stop position at the end of the onramp/mainline merge sections (which contain a lane drop). To avoid these vehicles from being evaporated, a set of *merge* link types was created. These match their non-merge counterparts in all features except for the waiting time, which was set to 60 seconds for the merge types (see Table 2.4). Merge link types were used on all onramps and onramp merge sections.

Link types - Variations of following behavior (CC-) parameters

The remainder of the calibration effort focused on finding a suitable set of values for the CC-parameters defined in Section 2.10. Three separate sets of CC-parameter values were defined: Freeway, HardCurve, and SoftCurve. Each was accompanied by a merge link type (with a 60 second diffusion time), giving a total of 6 link types. The Freeway and Freeway Merge types were used almost everywhere. The HardCurve and SoftCurve link types were applied only to the curved sections that affect bottlenecks B1 and B3 respectively (see Figure 2.10). As is described in the next section, one of the findings of this study is that only modest adjustments to the CC-parameters were required to produce the desired simulation response. Also, that capacity drops due to curvature can be reproduced with changes to the CC1 parameter alone.

2.12 Calibration goals - Final parameter selection

Having assembled the onramp and offramp flow inputs using data from several different days, it is not immediately obvious how the simulation results should be evaluated. The usual method of computing an error norm with respect to the measured data, and tuning the model parameters to minimize that norm is not applicable in this case due to the composite nature of the input data. The question arises, should a single typical day be used, or a composite day, as was done with the boundary flows? Added to this difficulty is the fact that none of the data sets considered as typical had a complete set of mainline measurements. Furthermore, there seems to be more variability in the mainline measurements than appears in the onramp flows, suggesting the influence of unseen factors, such as weather, day-to-day variations in driver behavior, traffic incidents, etc.

Instead, the goal for the calibration was to match more qualitative aspects of the freeway operation. These were:

1. location of the three identified bottlenecks,
2. initial and final times for each of the three mainline queues,
3. extent of the queues,
4. utilization of the HOV lane,
5. onramp performance.

The first three items on this list pertain to the simulated response of the mixed-flow lanes. Target values for these characteristics were extracted from contour plots similar to those in Appendix A, and are listed in Table 2.3. The goal for the HOV lane was to approximately match the flow values from PeMS. For the onramps, the only objective was to avoid large onramp queues that might obstruct the vehicle sources.

The parameter selection methodology consisted of iterated runs, visual evaluation of the results using speed contour plots (e.g. Figure 2.15), and manual adjustments of the parameters. These adjustments were limited to the CC-parameters described in Section 2.10, and were aided by the bottleneck analysis of Section 2.8 and by the physical interpretation of the parameters of Section 2.10. The iterative procedure was stopped when all of the qualitative calibration goals were met (see Sections 2.12.1, 2.12.2, and 2.12.3). This approach was favored over a more exhaustive

automated search method because of the potentially huge number of parameter variations, as well as the approximately 3 hour running time (PC/Windows XP, 2.6 GHz, 500 Mb RAM), and the advantage that it leads to a more sensible result.

The final selection of driver behavior parameters is shown in Table 2.4. This parameter set is the most parsimonious among those sets that also met the calibration goals. Notice that the CC4/CC5 parameter was increased (in absolute value), but was kept uniform throughout the freeway. It was found that this parameter, in addition to CC1, also has an important influence on capacity. Its default value of -0.35/0.35 produced almost no congestion. The CC0 parameter was also increased globally from 1.5 to 1.7. As expected from its definition, this parameter was more influential at low speeds (i.e. within the mainline queues), and was used to regulate the queue lengths. The CC1 parameter on the other hand, was changed only locally, at two locations. The HardCurve link type was used on the reverse curve near Huntington St. and the SoftCurve type was used on the curved section between Hill and Lake St. (see Figure 2.10). CC1 was adjusted in both cases to achieve the correct activation times for bottlenecks B1 and B3 respectively. Interestingly, bottleneck B2 did not require a separate CC1 value. This result supports the interpretations provided in Section 2.8 for the causes of the three bottlenecks; that B1 and B3 are probably caused by curvature, whereas B2 is probably due to weaving.

	Bottleneck	Location	Start time	End time	Queue length
Measured	B1	MP 33.049	6:00 - 6:30	10:00 - 10:30	To MP 39.159
	B2	MP 30.779 / 30.139	6:45 - 7:15	9:00 - 9:45	Into B1
	B3	MP 28.03 / 26.8	7:00 - 7:30	9:15 - 9:45	To MP 29.17
Simulated	B1	MP 33.049	6:00	10:15	To MP 39.159
	B2	MP 30.779	7:00	9:45	Into B1
	B3	MP 26.8	7:15	9:30	To MP 29.17

Table 2.3: Measured and Model predicted congestion pattern

Link type	CC0	CC1	CC4 / CC5	Waiting time
Freeway	1.7	0.9	-2.0 / 2.0	1
SoftCurve	1.7	1.1	-2.0 / 2.0	1
HardCurve	1.7	1.4	-2.0 / 2.0	1
Freeway Merge	1.7	0.9	-2.0 / 2.0	60
SoftCurve Merge	1.7	1.1	-2.0 / 2.0	60
HardCurve Merge	1.7	1.4	-2.0 / 2.0	60

Table 2.4: Calibrated CC values. (Defaults: CC0=1.5, CC1=0.9, CC4/CC5=-0.35/0.35, Waiting time=60)

2.12.1 Onramp response

One of the qualitative goals for the CC-parameter calibration was to avoid unrealistic queues on the onramps that might obstruct the vehicle sources. The only onramp queuing problem that arose was on the freeway connector from 605 NB (MP 36). As was mentioned in Section 2.11, this was corrected at an earlier stage with partial routing decisions and was not a factor in tuning CC-parameters. All other onramps were checked by comparing the supplied onramp flows with the simulated onramp flows. These were a close match in all cases (see Appendix F), indicating that none of the vehicles sources were obstructed by overflowing onramp queues.

2.12.2 HOV lane response

The goal of matching the utilization of the HOV lane was verified by checking the simulated HOV lane flows. Samples of simulated and field-measured HOV lane flows are shown in Figure 2.14. Recall that the upstream boundary flows (at Vernon) are an input to the model. The differences at other locations may reflect modeling errors, such as errors in the provided percentage of HOV vehicles at onramps, and/or errors in the modeling of route choice by HOV drivers (Section 2.7). In general, the result is considered a sufficiently good match for the control purposes of this model. However, this aspect of the model can be improved with a refinement of the HOV input percentages (Section 2.7), and/or more iterations of VISSIM's dynamic assignment routine.

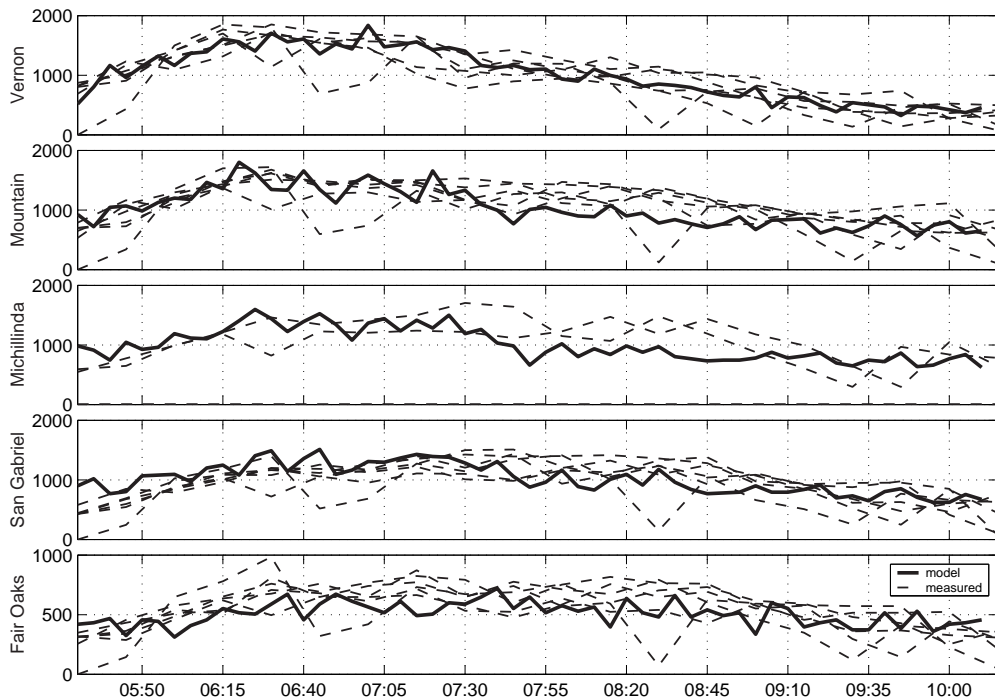


Figure 2.14: Measured and simulated HOV flows (in [vph])

2.12.3 Mixed-flow lane response

The bulk of the calibration effort was dedicated to matching the response of the mixed flow lanes, in terms of the start time, end time, and extent of the queue generated by each of the three major bottlenecks. The iterative procedure was stopped when all of the 9 indicators for the mixed-flow response fell within their target ranges. Target and simulated values for these 9 indicators are given in Table 2.3. The resulting speed contour plot, shown in Figure 2.15, is compared to the typical PeMS contour of Figure A.2. Notice that the model has approximately matched the period of activation and queue length for the three bottlenecks. This was accomplished with a few global changes to the default parameter values, and with a couple local changes that were based on the analysis of field data and freeway geometry.

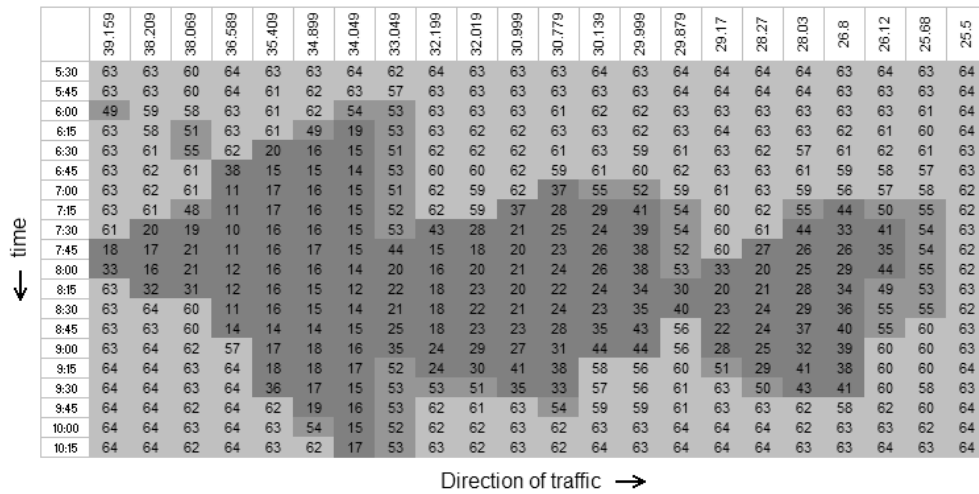


Figure 2.15: Contour plot with final parameters selection

2.12.4 Random seed variations

Finally, the calibrated parameter set was run with 10 different *random seeds*. The random seed affects the realization of the stochastic quantities in VISSIM, such as inlet flows and vehicle capabilities. Contour plots for three examples are shown in Appendix G. Average percent variations in several simulation inputs and outputs resulting from random seed variations are shown in Table 2.5.

Quantity	Average Value	% Variation
Onramp flow	e.g. Figure 2.16	12.20%
Offramp flow	e.g. Figure 2.16	14.04%
Average speed	Figure 2.16	2.26%
Average volume	Figure 2.16	1.05%
Total Passenger Hours	22,482 veh.hr	1.56%
Total Passenger Kilometers	1,539,700 veh.km	0.09%

Table 2.5: Variation in model output due to changes in the random seed

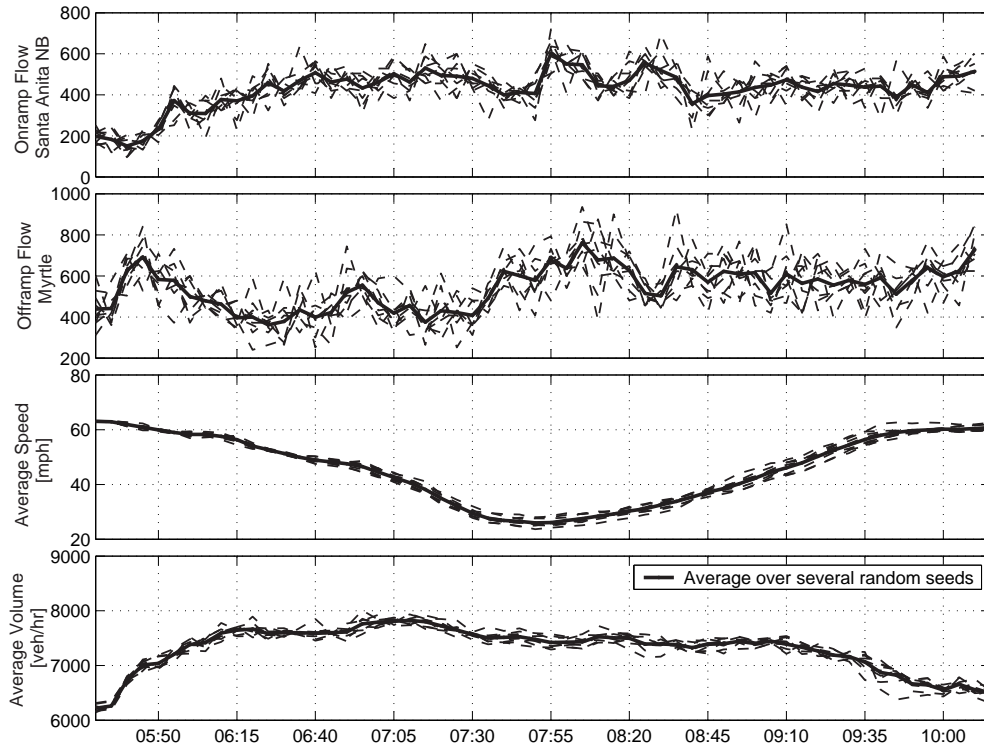


Figure 2.16: Mainline speed and flow measurements with several random seeds

2.13 Summary and Conclusions

This chapter has outlined a complete methodology for constructing and calibrating a simulation model of a unidirectional freeway with onramp control. The procedure included gathering and processing of field data from the PeMS database, estimation of OD matrices with *FREQ*, and microscopic simulation with *VISSIM*. Deficiencies in the field data were dealt with by assembling a composite typical day using data from several different days. The procedure was applied to I-210 West, a freeway that presents several challenging features: 20 metered onramps, with and without HOV bypass lanes, an HOV lane with an intermittent barrier, an uncontrolled freeway connector, and several interacting bottlenecks. All of these features were included in the model. Analysis of the supply and demand characteristics of the freeway lead to the conclusion that two of these bottlenecks were geometry-induced, while another was caused by weaving. A successful calibration of the *VISSIM* model was carried out based on this observation. As a conclusion, this study has shown that the *VISSIM* simulation environment is well-suited for such freeway studies involving complex interactions. With few and well reasoned modifications to its driver behavior parameters, the simulation model is capable of reproducing the field-measured response on the onramps, HOV lanes, and mixed-flow lanes.

Research will now continue using the calibrated *VISSIM* model to investigate a wide variety of ramp control strategies for the westbound I-210 freeway during the morning peak period. Ramp control strategies will include local and system-wide alternatives. Caltrans will consider implementing improved ramp control strategies based on their assessment of the predicted results.

Chapter 3

Experiments with Vissim

This chapter reports a series of simulation experiments conducted with the VISSIM model of I-210 described in Chapter 2. The objective is to compare several options of on-ramp metering, and to tune their parameters for this test site. The candidate metering strategies for I-210 are fixed-rate control, Alinea, and %-Occ. One of the issues pertaining to the potential use of Alinea is whether it can be employed when the feedback sensor is placed upstream of the on-ramp, and not downstream as envisioned by its creators. If Alinea can be used with upstream detectors, the next question is how then to tune Alinea when only upstream detectors are available?

An issue for any candidate controller on I-210 is that it may be overridden if the on-ramp queue threatens to spill onto the streets (queue override), or if the freeway is relatively empty (green ball override). These experiments also attempt to address the effect that these rules have on the controller performance and tuning.

3.1 Performance Measures

The performance measures used to evaluate the candidate metering strategies are defined here in terms of variables exported by VISSIM in its *link evaluation* output file and *DDE trace file*. The Total Travel Time and Total Travel Distance are referred to here as Total Vehicle Hours (TVH) and Total Vehicle Kilometers (TVK), to distinguish them from the the Total Passenger Hours and Total Passenger Kilometers. The latter are the total trip times and distances incurred by individual *passengers*, instead of *vehicles*. VISSIM's *link evaluation* file contains 5-minute average densities, flows, and speeds for every link in the model, including on-ramp, mainline, and offramp links. Separate variables are exported for each vehicle type (LOV, HOV, and trucks). LOV and truck type densities, flows, and speeds are aggregated and denoted with ρ_{ik}^l , f_{ik}^l , and v_{ik}^l respectively. Variables for the HOV type are denoted ρ_{ik}^h , f_{ik}^h , and v_{ik}^h . The sub-indices i and k in these variables indicate the link and 5-minute time interval respectively.

On-ramp, Freeway, and Total Passenger Hours (OPH, FPH, TPH, %TPH) :

The Total Passenger Hours (TPH in [pass.hr]) is the sum of the On-ramp Passenger Hours (OPH)

and the Freeway Passenger Hours (FPH). The formulas for these three quantities are:

$$\text{OPH} = \sum_i^{\text{on-ramps}} \sum_k^{\text{time}} (\alpha^h \rho_{ik}^h + \alpha^l \rho_{ik}^l) L_i \Delta t \quad (3.1)$$

$$\text{FPH} = \sum_i^{\text{!on-ramps}} \sum_k^{\text{time}} (\alpha^h \rho_{ik}^h + \alpha^l \rho_{ik}^l) L_i \Delta t \quad (3.2)$$

$$\text{TPH} = \text{OPH} + \text{FPH} \quad (3.3)$$

L_i is the length in kilometers of section i . Δt is the length of the data collection time interval in hours; $\Delta t = 5 \text{ min} = 1/12 \text{ hr}$. Coefficients α^h and α^l are the average number of passengers in HOV and LOV (including truck) type vehicles. They were assigned values of $\alpha^h = 2.5$ and $\alpha^l = 1.2$. %TPH is the percent improvement in passenger hours:

$$\% \text{TPH} = 100 \times \frac{\text{TPH}_g - \text{TPH}}{\text{TPH}_g} \quad (3.4)$$

where TPH_g is the passenger hours without on-ramp control with a particular random seed.

On-ramp, Freeway, and Total Passenger Kilometers (OPK, FPK, TPK) :

The Total Passenger Kilometers (TPK in [pass.km]) is the sum of the On-ramp Passenger Kilometers (OPK) and the Freeway Passenger Kilometers (FPK):

$$\text{OPK} = \sum_i^{\text{on-ramps}} \sum_k^{\text{time}} (\alpha^h f_{ik}^h + \alpha^l f_{ik}^l) L_i \Delta t \quad (3.5)$$

$$\text{FPK} = \sum_i^{\text{!on-ramps}} \sum_k^{\text{time}} (\alpha^h f_{ik}^h + \alpha^l f_{ik}^l) L_i \Delta t \quad (3.6)$$

$$\text{TPK} = \text{OPK} + \text{FPK} \quad (3.7)$$

Average Mainline Speed (AMS) :

The average mainline speed (AMS in [mile/hr]) is computed as the mean of the per link speeds over time and space:

$$\text{AMS} = \frac{1}{n_k} \sum_k^{\text{time}} \frac{\sum_i L_i v_{ik}}{\sum_i L_i} \quad (3.8)$$

The internal summations in Eq. (3.8) are over all mainline links. n_k is the number of 5-minute time intervals in the summation. As explained below, only measurements from the 5-hour period from 5:30 am to 10:30 am were used to compute AMS.

Average Throughput (ATh) :

The TPH, TPK, and AMS are computed with *link* data contained in the *link evaluations* file. Point-wise detector data printed in the *DDE trace file* is used to compute the throughput, or average mainline flow over the 5-hour period:

$$\text{ATh} = \frac{1}{n_k} \sum_k^{\text{time}} \frac{1}{n_{md}} \sum_i^{\text{mainline}} \frac{\text{vol}(i, k)}{\Delta t} \quad (3.9)$$

$n_{md} = 100$ is the number of mainline loop detectors in the test site. $vol(i, k)$ is the number of vehicles registered by detector i during time interval k . $\Delta t = 5$ min.

The simulation time for all of the runs reported in this chapter is 60,000 seconds. The first 900 seconds are *warmup time*, used to create a non-empty initial condition. The demands for the 5:30-5:45 am period were applied during the warmup time. The period of interest, from 5:30 am to 10:30 am, covers simulation seconds 900 to 18,900. All source flows were turned off after second 18,900 in order to allow the freeway to discharge. This period, from 18,900 to 60,000, is referred to as the *cool down* period. Output data from the entire simulation period was used to compute the travel time and travel distance performance measures: OPH, FPH, TPH, %TPH, OPK, FPK, and TPK. Only measurements collected during the period of interest, i.e. excluding warmup and cool-down periods, were used to find AMS and ATh.

Measures for the uncontrolled freeway with a number of different random seed values are provided in Table 3.1.

Random seed	OPH [pass.hr]	FPH [pass.hr]	TPH [pass.hr]	TVH [veh.hr]	TPK [pass.km]	TVK [veh.km]	AMS [mph]	ATh [vphpl]
11	5,300	24,779	30,079	22,731	2,161,429	1,597,989	49.6	1,662
15	5,313	24,199	29,512	22,254	2,165,870	1,598,657	50.4	1,659
22	5,236	24,253	29,489	22,232	2,170,573	1,600,880	50.2	1,662
28	5,265	25,001	30,266	22,883	2,164,348	1,600,268	49.0	1,666
35	5,516	25,061	30,577	23,120	2,167,644	1,602,424	49.0	1,666
41	5,305	24,064	29,369	22,167	2,163,746	1,599,573	50.4	1,663
42	5,412	25,282	30,693	23,227	2,161,107	1,598,105	48.8	1,660
52	5,215	23,779	28,994	21,873	2,158,866	1,595,752	50.9	1,656
66	5,729	26,175	31,904	24,184	2,162,793	1,600,595	47.8	1,659
73	5,531	25,723	31,254	23,648	2,165,615	1,600,901	48.0	1,665
mean	5,382	24,832	30,214	22,832	2,164,199	1,599,514	49.4	1,662
% dev.	2.45	2.48	2.40	2.54	0.12	0.09	2.35	1.02

Table 3.1: Performance measures with 9 different random seeds.

3.2 On-ramp configurations

Table 3.2 contains basic descriptions of each of the 20 controlled on-ramps in the test site. RH and LH in the second and third columns denote Right Hand and Left Hand on-ramps. Note that most of the on-ramps have one metered lane and an HOV bypass lane, 6 on-ramps have two metered lanes and no HOV bypass, and one on-ramp has a single metered lane and no HOV bypass. The storage capacities are given in total number of vehicles, not in vehicles per metered lane.

Each on-ramp is equipped with a set of loop detectors. A typical loop detector configuration for a single-metered lane on-ramp is shown in Figure 3.1. The *queue* detector is placed at the entrance to the on-ramp, and is used to trigger the queue override. The *presence* and *HOV bypass* detectors are placed side by side near the signal, in the metered and HOV bypass lanes respectively. The

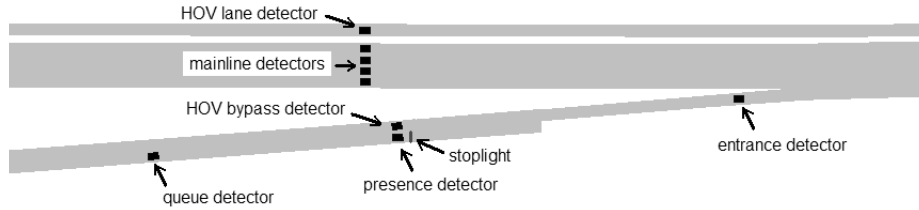


Figure 3.1: Loop detector layout on on-ramps.

Street Name	Number of metered lanes	HOV bypass	Number of lanes at gore	Storage capacity
Vernon	1 RH	Yes LH	1	28
Irwindale NB	1 RH	Yes LH	1	21
Irwindale SB	1 RH	Yes LH	1	27
Mount Olive	1 RH	Yes LH	1	33
Buena Vista	1 RH	Yes LH	1	19
Mountain	1 RH	Yes LH	1	25
Myrtle	1 RH	Yes RH	1	12
Huntington	1 RH	Yes RH	1	26
Santa Anita NB	2	No	1	45
Santa Anita SB	1 RH	Yes RH	1	21
Baldwin NB	1 RH	Yes LH	1	14
Baldwin-Foothill	2	No	1	30
Michillinda	2	No	1	19
Rosemead-Foothill	2	No	1	17
Rosemead	1 RH	Yes LH	1	10
Sierra Madre Villa	1	No	1	18
San Gabriel	1 RH	Yes LH	1	23
Altadena	1 RH	Yes LH	1	26
Hill	2	No	1	28
Lake	2	No	1	42

Table 3.2: On-ramp configurations.

entrance detector measures the total flow that enters the freeway. The mainline detector bank is located upstream of the on-ramp merge, at approximately the same distance from the junction as the stoplight.

3.3 The TMC and field controllers

The Traffic Management Center (TMC) is the “brain” of the freeway management system. It is in the TMC that freeway loop detector measurements are collected and processed, and the control commands for each of the on-ramps are calculated. These commands are updated and distributed to the on-ramp control boxes every 30 seconds. In the case of I-210, a chip inside each box

processes the TMC command and makes the decision to either implement or *override* it, depending on local conditions. This section describes the important features of the on-ramp control system currently installed on I-210 West. The control logic is schematically depicted in Figure 3.2. It was implemented in VISSIM using the software’s C-based scripting feature.

The task of the field controller chip is to adjust and enforce the control rate issued by the TMC. In Figure 3.2, the TMC commanded rate for period k is denoted $TMCrate[k]$. It is computed according to whatever control algorithm is being used – %-Occ, Alinea, etc. The control loop starts at point A at the top of the left side of the diagram, and ends at point A at the bottom right corner. Each on-ramp operates in one of three modes: *normal*, *queue override*, or *green ball*. In the normal mode, the TMC commanded rate is applied. The other two modes are described below.

The policy of the *queue override* is shown in the left-hand side of the diagram. The goal of this mode is to prevent the on-ramp queue from spilling onto the surface streets. It works by monitoring a *queue detector* placed near the entrance to the ramp (shown in Figure 3.1, page 40). The controller enters the queue override mode whenever the queue detector becomes “hot”, while the the speed on the mainline is above 35 mph. The queue detectors on I-210 are considered to be “hot” if they are continuously occupied for more than 3.2 seconds. In VISSIM a detector is “hot” if it reports a *smoothed occupancy rate* of 40% or higher ¹. However, if the average mainline speed is less than 35 mph, the on-ramp will remain in the normal mode, and the on-ramp queue will be allowed to invade the surface streets. This exception to the queue override is meant to prevent the on-ramp queue from being flushed into an already congested freeway. Once in the queue override mode, the TMC commanded rate is discarded. Instead, the metering rate from the previous interval is increased by 120 vphpl, without exceeding the maximum metering rate of 900 vphpl.

The second override, termed the *green ball override*, occurs when the local conditions on the mainline fall below an average flow of 1500 vphpl, at an occupancy of 14% or lower. In this situation, on-ramp metering is suspended and the signal status is set to green. The green ball condition has a minimum duration of 1 minute, or until either of the thresholds are exceeded. This override is intended to reduce the on-ramp waiting times when the freeway is relatively empty. However, it has the drawback that, because it is based only on local information, it may interfere with a system-wide metering strategy.

If neither of the two overrides are activated, then the per-lane metering rate is computed from the TMC command with:

$$rate[k] = \frac{TMCrate[k] - HOVflow[k-1]}{\# \text{ metered lanes}} \quad \text{in [vphpl]}$$

where $HOVflow[k-1]$ is the average flow measured by the *HOV bypass detector*, shown in Figure 3.1, during the previous time interval. In the queue override mode, $rate[k]$ is found with:

$$rate[k] = rate[k-1] + 120 \quad \text{in [vphpl]}$$

Both are subject to minimum and maximum bounds:

$$rate[k] = \max\{ \min\{ rate[k] ; 900 \} ; 180 \} \quad \text{in [vphpl]}$$

The duration of the red phase is then found with:

$$\text{red phase} = \frac{3600}{rate[k]} - \text{green phase} \quad \text{in [seconds]}$$

¹The smoothed occupancy rate is an output of VISSIM’s loop detector model.

where the green phase lasts a fixed 2 seconds. The metering lights on I-210 “rest on red”, meaning that they show a red light if there is no vehicle waiting at the stop line (i.e. detected by the *presence detector* in Figure 3.1). The red phase clock advances whether or not there is a vehicle waiting. Hence, a vehicle arriving to the stopline at second 8 of a 10 second red phase will have to wait for only 2 seconds.

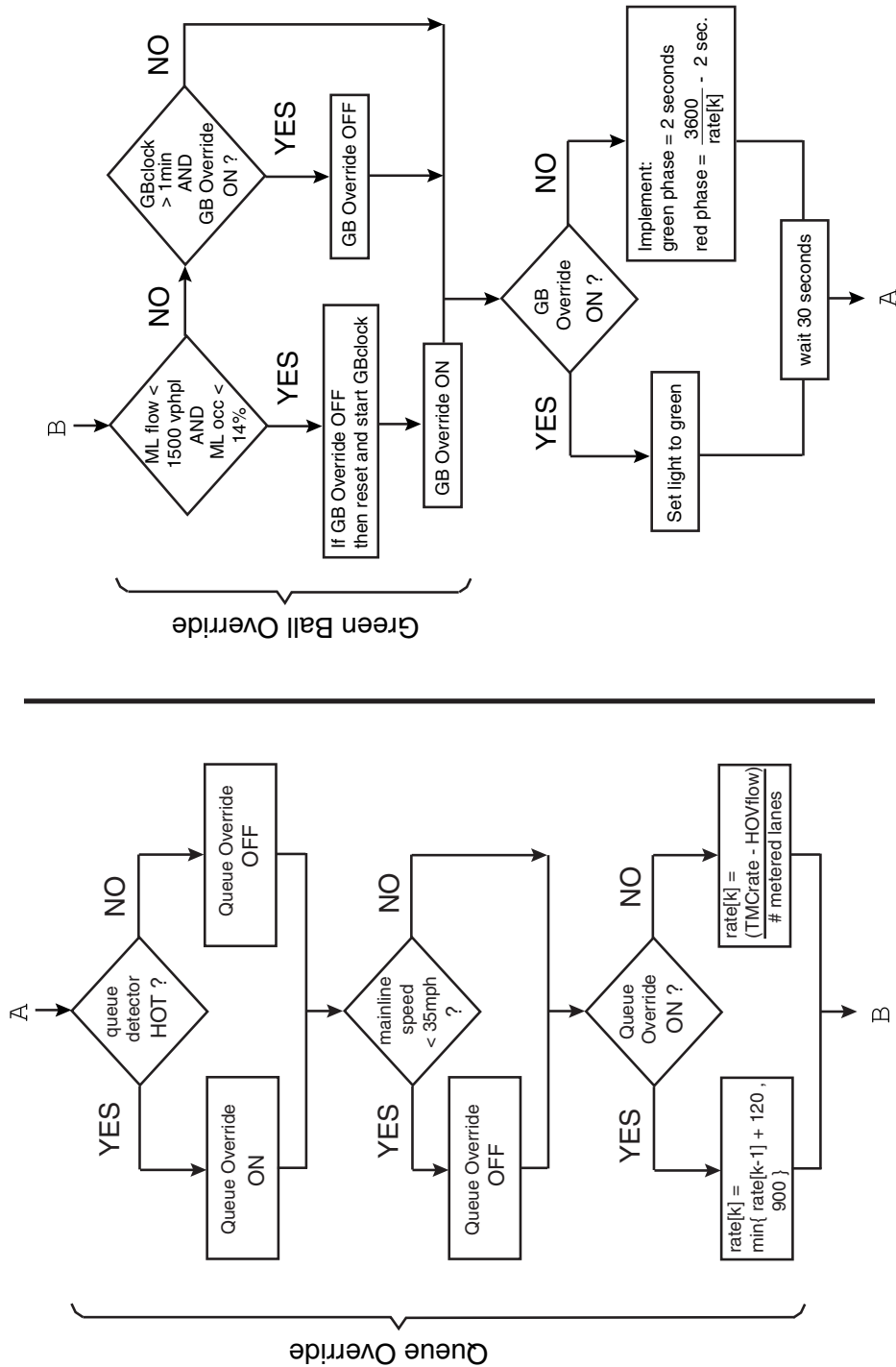


Figure 3.2: I-210 controller logic.

3.4 Fixed-rate metering

Fixed-rate metering, where the TMC commands to each of the on-ramps is a *constant*, is the simplest form of metering possible. This section investigates the use of fixed-rate metering using different constant rates, and activating or deactivating different portions of the controller logic described in the previous section. These experiments can be used to gain a better understanding of the effects of the two controller overrides and of the limited on-ramp storage space. For example, the longest possible queue lengths and on-ramp waiting times occur when the meters are held at 180 vphpl, and the queue override policy is deactivated. Maximum freeway delay occurs in the 900 vphpl experiment. These experiments also serve to identify ramps that trigger the queue override, even when metered at the maximum rate of 900 vphpl. These on-ramps are likely to be dominated by the queue override policy, regardless of the control strategy implemented by the TMC.

Four set of runs were conducted with fixed-rate metering. The experimental setup is given in Table 3.3. Each set contains five runs, with constant metering rates of 180, 300, 450, 600, and 900 vphpl. These rates correspond to integer-valued cycle durations of 20, 12, 8, 6, and 4 seconds respectively.

Batch	Number of trials	Fixed rate	Queue override	Green Ball override	Mainline speed exception
FR-1	5	180 - 900	-	-	-
FR-2	5	180 - 900	✓	-	-
FR-3	5	180 - 900	✓	✓	-
FR-4	5	180 - 900	✓	✓	✓

Table 3.3: Experiments with fixed-rate control.

In batch FR-1, no overrides were applied, and queues were allowed to grow without limit. Figure 3.3 shows flows from the Vernon St. on-ramp for the 180 vph and 900 vph experiments of FR-1. The solid gray line in both plots is the number of vehicles waiting in the on-ramp queue. In the 180 vph case the queue reaches a peak value of about 500 vehicles, or 3,461 meters in Table 3.4. Peak queue lengths for all of batch FR-1 are provided in Table 3.4. Peak queue lengths that exceed the on-ramp storage capacity (right-most column) have been highlighted in bold type. Notice in the table that four on-ramps (Myrtle, Huntington, San Gabriel, and Lake St.) develop excessive queues even when the metering rate is kept at its maximum value. This suggests that these on-ramps will be affected and possibly even driven by the queue override policy, regardless of the control strategy. Ramps other than these can withstand more restrictive metering rates.

Batches FR-2, FR-3, and FR-4 respectively incorporate the queue override, the green ball override, and the mainline speed exception to the queue override. The peak queue lengths for these three sets are shown in Tables 3.5, 3.6, and 3.7. Figures 3.4 through 3.6 show control related variables for the Rosemead NB on-ramp. These figures are intended to give some insight into the effect of each of the overrides. Each figure has 4 plots; the top plot shows the evolution of the on-ramp queue for each of the five fixed metering rates. The bottom three windows show a number between 0 and 1 indicating how often the queue override, green ball override, and mainline speed exception were active. This number was calculated every five minutes for each of the on-ramp

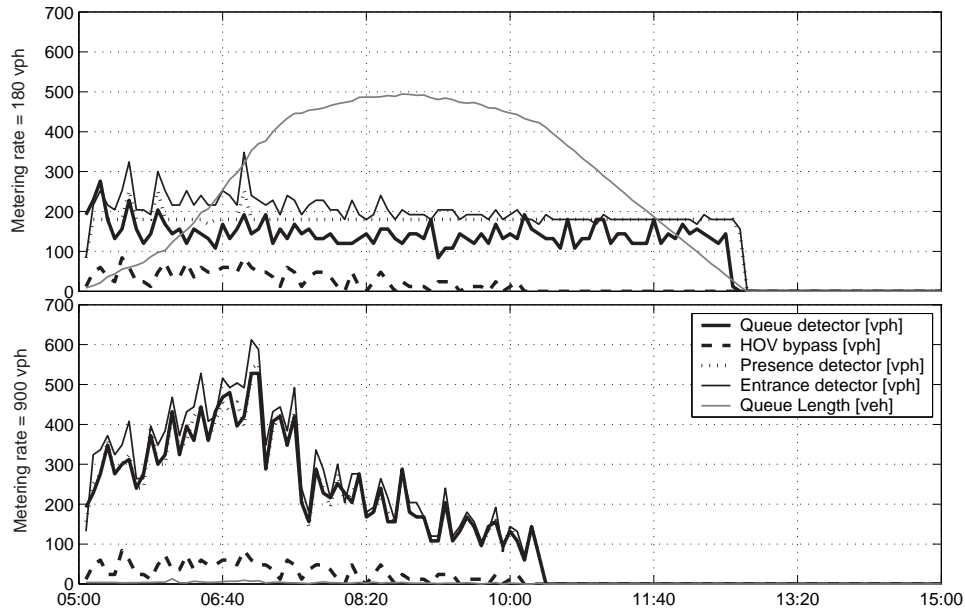


Figure 3.3: On-ramp detector measurements from the Vernon St. on-ramp.

Street Name	Ramp metering rate [vph]					Storage [veh]	Max. Queue Length [m]
	180	300	450	600	900		
Vernon	3,461	1,985	408	107	91	28	190
Irwindale NB	8,294	8,293	4,336	302	88	21	147
Irwindale SB	7,263	4,833	600	184	67	27	189
Mount Olive	480	102	48	30	27	33	231
Buena Vista	1,324	313	85	44	37	19	133
Mountain	2,394	1,014	145	56	52	25	175
Myrtle	7,755	7,753	5,241	1,663	203	12	84
Huntington	10,788	9,401	5,634	2,454	215	26	182
Santa Anita NB	3,974	82	39	35	22	45	155
Santa Anita SB	3,111	931	107	68	68	21	147
Baldwin NB	3,853	1,779	243	96	70	14	98
Baldwin SB	3,290	79	28	29	27	30	105
Michillinda	5,449	1,927	47	34	29	19	65
Rosemead NB	8,990	5,288	444	55	38	17	60
Rosemead SB	53	41	33	28	28	10	70
Sierra Madre	5,114	4,281	318	118	74	18	126
San Gabriel	10,375	9,024	5,791	2,669	207	23	161
Altadena	2,719	2,719	559	96	69	26	182
Hill	14,523	14,526	7,396	1,821	61	28	98
Lake	19,211	16,522	6,735	772	178	42	145

Table 3.4: Peak queue lengths for FR-1.

controllers as the number of 30 second cycles in which the override was active divided by the total number of cycles in the previous 5 minutes (i.e. 10). Figure 3.4 shows that the queue override was active at Rosemead NB in the 180 vphpl experiment during about 80% of the period between 7:00 am and 9:00 am.

Also evident in Figure 3.4 is the influence of the queue override on the maximum queue length: the peak queue length for the 180 vphpl experiment of 178 m is contrasted with the 8,990 m shown in Table 3.4 when the queue override was deactivated. Figure 3.5 shows the situation when both queue and green ball overrides were enforced, but without the mainline speed exception. It shows that the green ball override is only triggered before and after the peak period (6:30 am to 9:00 am). It therefore acts more or less like an automated on/off switch for the metering system. Figure 3.6 shows that the mainline speed exception, although sometimes active during the peak period (7:00 am to 9:00 am), does not have an important effect on the frequency of occurrence of the queue override at Rosemead NB. This is because these two rules respond to complementary situations: the queue override is more likely in the 180 vphpl experiment, whereas the mainline speed exception is more likely in the 900 vphpl experiment.

Street Name	Ramp metering rate [vph]					Storage [veh]	Max. Queue Length [m]
	180	300	450	600	900		
Vernon	266	267	96	95	91	28	190
Irwindale NB	345	314	259	161	88	21	147
Irwindale SB	280	325	209	158	69	27	189
Mount Olive	65	37	33	30	28	33	231
Buena Vista	85	59	37	38	34	19	133
Mountain	192	104	50	56	52	25	175
Myrtle	322	327	173	150	98	12	84
Huntington	690	450	360	431	134	26	182
Santa Anita NB	148	83	39	30	21	45	155
Santa Anita SB	205	188	88	68	68	21	147
Baldwin NB	174	174	124	83	70	14	98
Baldwin SB	156	79	28	29	27	30	105
Michillinda	200	166	47	34	29	19	65
Rosemead NB	178	123	91	55	38	17	60
Rosemead SB	53	41	33	28	28	10	70
Sierra Madre	295	281	150	91	74	18	126
San Gabriel	960	618	509	350	185	23	161
Altadena	302	297	242	91	69	26	182
Hill	523	484	239	231	56	28	98
Lake	788	460	329	314	179	42	145

Table 3.5: Peak queue lengths for FR-2.

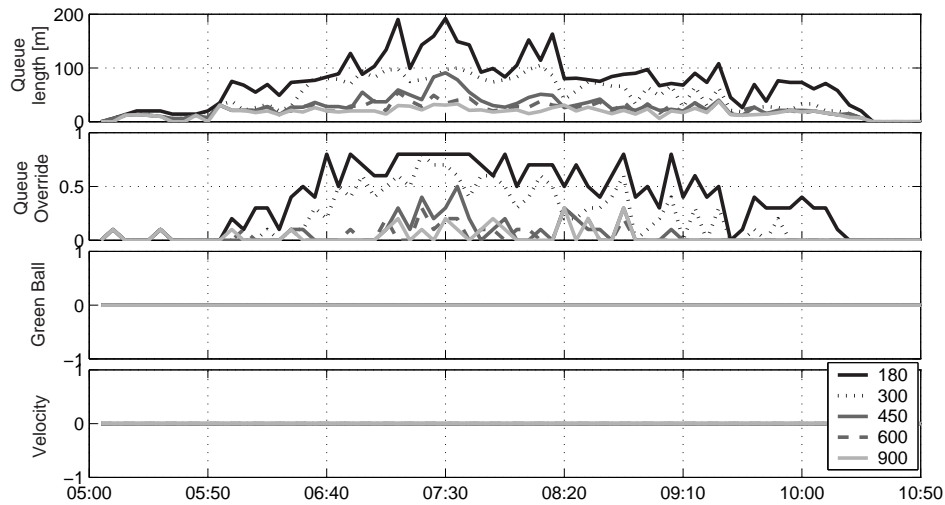


Figure 3.4: Queue length and overrides for FR-2 (Rosemead NB on-ramp).

Street Name	Ramp metering rate [vph]					Storage [veh]	Max. Queue Length [m]
	180	300	450	600	900		
Vernon	266	267	96	95	91	28	190
Irwindale NB	637	626	298	161	88	21	147
Irwindale SB	1,502	1,186	484	184	67	27	189
Mount Olive	54	63	33	30	28	33	231
Buena Vista	90	72	68	36	34	19	133
Mountain	327	256	56	56	52	25	175
Myrtle	1,691	1,155	395	204	81	12	84
Huntington	706	843	571	339	147	26	182
Santa Anita NB	453	82	38	35	22	45	155
Santa Anita SB	272	226	87	68	68	21	147
Baldwin NB	513	512	198	96	70	14	98
Baldwin SB	350	79	28	29	27	30	105
Michillinda	1,109	240	47	34	29	19	65
Rosemead NB	439	145	86	55	38	17	60
Rosemead SB	53	41	33	29	28	10	70
Sierra Madre	279	235	204	91	74	18	126
San Gabriel	2,889	4,508	1,758	609	178	23	161
Altadena	451	647	256	96	69	26	182
Hill	3,020	2,638	476	476	59	28	98
Lake	983	925	333	318	284	42	145

Table 3.6: Peak queue lengths for FR-3.

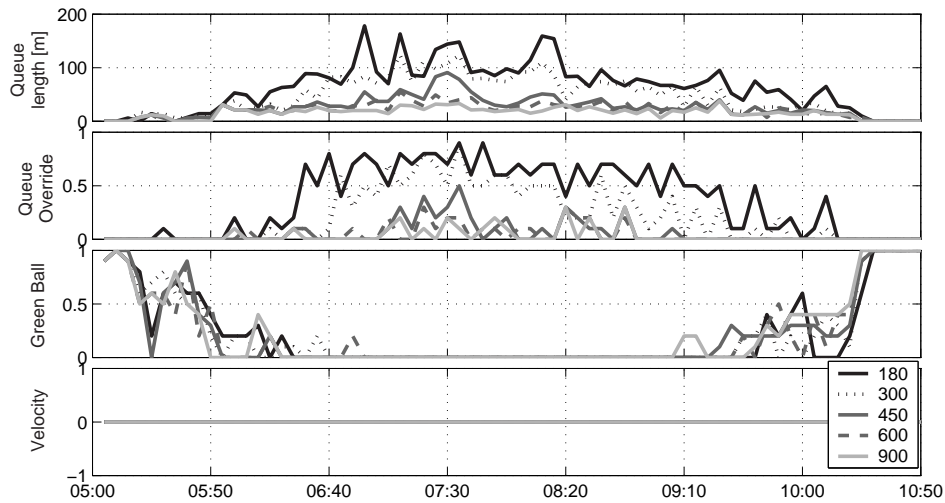


Figure 3.5: Queue length and overrides for FR-3 (Rosemead NB on-ramp).

Street Name	Ramp metering rate [vph]					Storage [veh]	Max. Queue Length [m]
	180	300	450	600	900		
Vernon	309	307	277	108	91	28	190
Irwindale NB	650	484	343	178	88	21	147
Irwindale SB	377	392	269	174	69	27	189
Mount Olive	243	102	48	30	27	33	231
Buena Vista	264	173	85	44	37	19	133
Mountain	241	216	147	56	52	25	175
Myrtle	617	393	338	281	203	12	84
Huntington	2,223	1,488	953	568	191	26	182
Santa Anita NB	218	82	39	35	22	45	155
Santa Anita SB	219	232	117	68	68	21	147
Baldwin NB	203	199	124	83	70	14	98
Baldwin SB	148	79	28	29	27	30	105
Michillinda	200	177	47	34	29	19	65
Rosemead NB	192	105	91	55	38	17	60
Rosemead SB	53	41	33	28	28	10	70
Sierra Madre	342	319	204	118	74	18	126
San Gabriel	2,092	1,378	1,161	470	198	23	161
Altadena	301	317	242	91	69	26	182
Hill	519	443	344	255	59	28	98
Lake	811	522	342	297	167	42	145

Table 3.7: Peak queue lengths for FR-4.

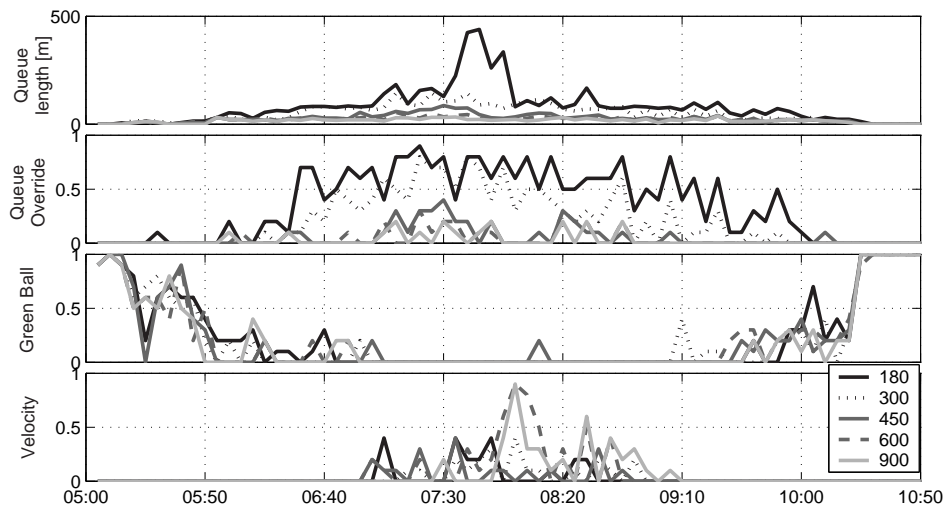


Figure 3.6: Queue length and overrides for FR-4 (Rosemead NB on-ramp).

Performance measures for all of the fixed-rate tests are provided in Table 3.8. The values are percent changes with respect to the uncontrolled freeway. Thus, improvements over no control are indicated by negative values in the %TPH and %TVH columns and positive values in %AMS and %TVH.

Batch FR-1 exhibits some expected tendencies: the %OPH and %AMS decreased and %ATH increased with increasing metering rate. The travel time measures (%TPH and %TVH) on the other hand, did not behave monotonically, but instead reached a minimum value in the 600 vphpl experiment. In fact, 600 vphpl was the only level of on-ramp flow that performed favorably as compared to no control. The reductions in travel time of -4.4% TPH and -4.3% TVH deteriorated quickly to 25.7% and 29.1% increases at 450 vphpl. This suggests that selecting a single fixed metering rate for a large and complex site such as I-210 is a delicate task, and probably not a wise approach.

Similar patterns in terms of %OPH and %AMS were observed when the queue override was added in batch FR-2. ATH remained more or less constant for all metering rates (also in batches FR-3 and FR-4) because the queue override ensured that relatively few vehicles remained in the on-ramp queues at 10:30 am. The %TPH and %TVH are less sensitive to the fixed metering rate in batches FR-2, FR-3, FR-4 than in FR-1. Thus, adding the queue override helped to avoid the huge travel time increases observed in batch FR-1 at low metering rates (e.g. 327% TPH in FR-1 became 4.1% in FR-4), but also reduced the potential benefits (-4.4% TPH became -1.5% at 600 vphpl).

Batch	metering rate [vph]	%OPH	%FPH	%TPH	%TVH	%TPK	%TVK	%AMS	%ATh
FR-1	180	2,019.9	-35.4	327.0	358.5	-2.7	-3.1	28.6	-15.9
	300	967.2	-30.5	145.4	160.1	-0.3	-0.5	24.4	-8.4
	450	256.4	-23.6	25.7	29.1	0.2	0.3	18.4	-2.8
	600	41.8	-14.2	-4.4	-4.3	0.1	0.0	10.2	-0.2
	900	3.2	4.4	4.2	4.3	0.4	0.3	-2.2	-0.2
FR-2	180	18.8	-2.9	0.9	0.9	0.2	0.1	2.1	0.0
	300	11.8	-0.8	1.5	1.5	0.1	0.1	0.4	0.1
	450	5.1	0.5	1.3	1.4	0.1	0.1	-0.3	0.1
	600	5.8	-2.6	-1.1	-1.3	0.3	0.2	1.8	0.2
	900	-1.6	-3.4	-3.0	-3.2	0.0	0.0	2.4	0.0
FR-3	180	40.0	-8.7	-0.1	-0.1	0.2	0.2	6.0	0.4
	300	33.2	-5.8	1.1	1.2	0.3	0.2	3.7	0.4
	450	10.4	-7.5	-4.4	-4.6	0.0	0.0	5.5	0.2
	600	4.4	0.4	1.1	1.0	0.3	0.2	0.3	0.0
	900	0.6	-0.2	-0.1	-0.1	0.3	0.3	0.0	0.4
FR-4	180	50.7	-5.8	4.1	4.4	0.2	0.2	3.9	0.2
	300	30.7	-5.6	0.8	1.0	0.1	0.1	3.6	0.4
	450	16.3	-1.6	1.6	1.6	0.3	0.3	1.1	0.5
	600	6.8	-3.3	-1.5	-1.7	0.2	0.2	2.2	0.3
	900	1.5	-1.9	-1.3	-1.4	0.2	0.2	1.3	0.3

Table 3.8: Performance measures with fixed-rate metering.

3.5 Alinea control

The Alinea control law was first introduced by Papageorgiou and others in [7]. It has since been tested in several European cities [8, 9], where it has performed favorably as compared to %-Occ, or a variant of %-Occ since a downstream measurement was used. It is interpreted as integral control of the *downstream* occupancy measurement. Its control law is expressed in the notation of this chapter as:

$$\text{TMCrate}[k] = \text{ENTflw}[k-1] + K_r (\hat{o} - \text{occ}[k]) \quad (3.10)$$

The two tunable parameters involved in this control law are the target occupancy (\hat{o}) and a positive gain (K_r). The desired metering rate for the upcoming time interval, $\text{TMCrate}[k]$, is computed as measured flow entering the freeway during the previous interval, $\text{ENTflw}[k-1]$, adjusted by an amount proportional to the difference between the measured mainline occupancy and the target mainline occupancy ($\hat{o} - \text{occ}[k]$). Thus, if the measured occupancy is less than the desired value, Alinea will increase the number of vehicles being released onto the freeway. The quickness with which Alinea reacts is determined by K_r .

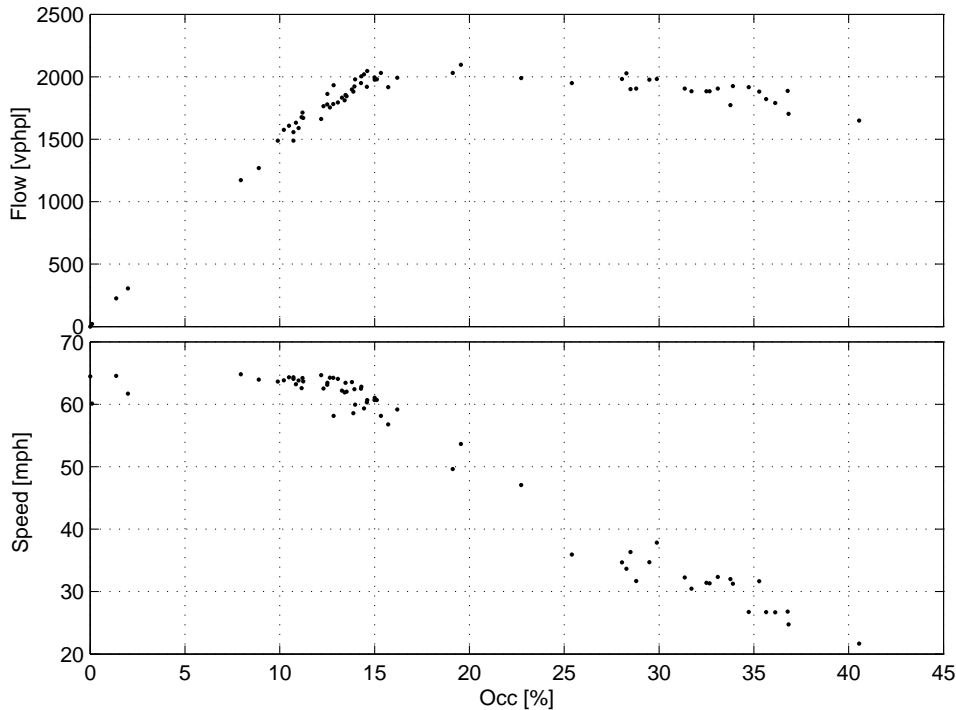


Figure 3.7: Simulated scatter plot for the Rosemead NB mainline detector station.

It is suggested in [8] that the target occupancy be set a little lower than the measured *critical occupancy* at which the freeway transitions from free-flow into congestion. Scatter plots from the VISSIM model such as the one shown in Figure 3.7 suggest that its critical occupancy is somewhere between 15% and 20%. The recommended value for the gain is 7000. Also, Alinea was conceived for freeways with mainline loop detectors placed *downstream* of the on-ramp.

The goals of the experiments with Alinea presented here are 1) to understand the influence of \hat{o} and K_r on performance, 2) to determine a best choice of controller parameters, 3) to see

whether Alinea can be successfully applied to a freeway such as I-210, equipped with upstream rather than downstream detectors, and 4) to study the effects of the controller overrides on Alinea’s performance.

Table 3.9 provides the experimental setup. The first three batches are a study of Alinea without overrides, using upstream detectors. AL-1 tests 13 different values of $\hat{\delta}$ between 8% and 40%, using the recommended values of $K_r = 7,000$. The gain is varied in AL - 2 and AL - 3 using a good and a not-so-good choice of $\hat{\delta}$ from AL-1. The study is repeated with detectors placed downstream of the on-ramps in AL - 4 through AL - 6. Finally, AL - 7, AL - 8, and AL - 9 investigate the effects of the overrides.

Batch	Number of trials	K_r	$\hat{\delta}$	Detector location	Queue override	Green Ball override	Speed exception
AL-1	13	7,000	8.0% - 40.0%	UP	-	-	-
AL-2	5	70 - 20,000	14.4%	UP	-	-	-
AL-3	5	70 - 20,000	27.2%	UP	-	-	-
AL-4	13	7,000	8.0% - 40.0%	DOWN	-	-	-
AL-5	5	70 - 20,000	14.4%	DOWN	-	-	-
AL-6	5	70 - 20,000	27.2%	DOWN	-	-	-
AL-7	13	7,000	8.0% - 40.0%	UP	✓	-	-
AL-8	13	7,000	8.0% - 40.0%	UP	✓	✓	-
AL-9	13	7,000	8.0% - 40.0%	UP	✓	✓	✓

Table 3.9: Experiments with Alinea.

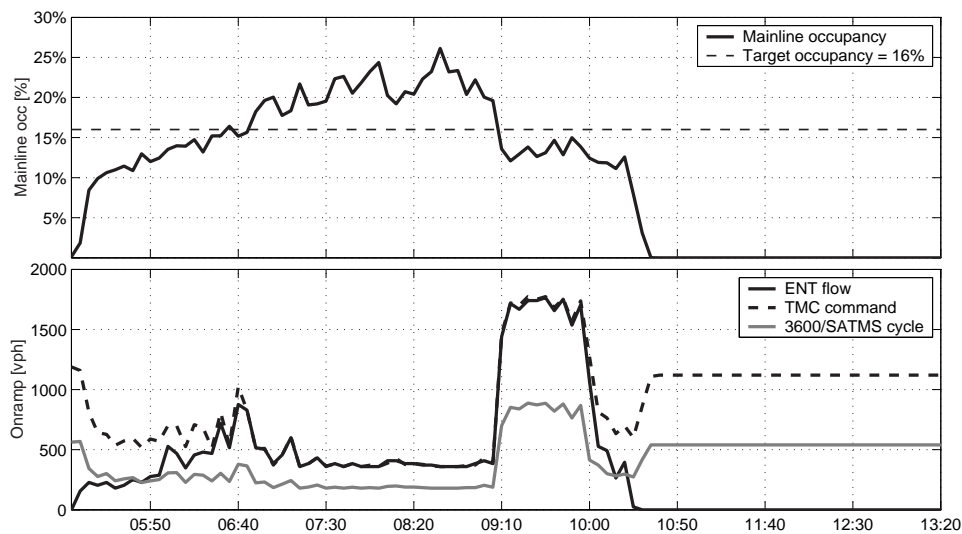


Figure 3.8: Control variables for Rosemead NB (AL-1).

First, however, Figure 3.8 illustrates how Alinea works. The top window shows the average mainline occupancy ($occ[k]$). Alinea reacts to “congestion”, i.e. $occ[k] > \hat{\delta}$, by reducing the metering rate. In the figure, congestion starts at around 6:40 am. At this point, Alinea starts to reduce its commanded rate, which quickly reaches its minimum value of 360 vph ($= 180 \text{ vphpl} \times$

2 metered lanes). The actual flow onto the freeway closely follows the commanded rate because there is a queue of vehicles waiting on the ramp. After congestion dissipates at around 9:00 am, mainline occupancy decreases below the threshold, and Alinea responds by increasing the on-ramp flow to its maximum value of 1,800 vph, until 10:30 am when simulated demand stops. After the freeway has emptied, the TMC commanded rate settles at 1,120 vph ($= K_r \hat{\rho}$), which is the value obtained by setting $\text{ENTflw}[k-1] = \text{occ}[k] = 0$ in Eq. (3.10).

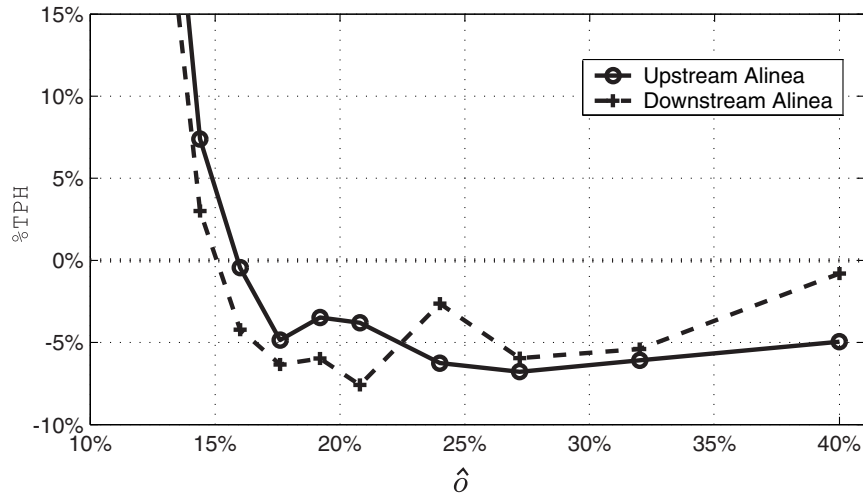


Figure 3.9: Upstream vs. Downstream Alinea (AL-1 vs. AL-3).

Tables 3.10 and 3.11 at the end of this section provide performance measures for all of the experiments with Alinea. Figure 3.9 compares the system performance when the mainline detectors are placed either immediately upstream or downstream of the on-ramp junction. Recall that the loop detectors on I-210 are located upstream of the on-ramps, and that the recommended placement according to [8] is downstream. The reasoning behind this recommendation is that, in the free-flow state, which is the state that Alinea attempts to preserve, changes in on-ramp flow are reflected in the downstream and not in the upstream measurement. Therefore, in the free-flow state, feedback control is only possible with a downstream measurement. However, one of the conclusions of Chapter 4 is that the opposite is true when the freeway is congested: observability is achieved with the upstream measurement. Figure 3.9 confirms this observation. Better performance was obtained with downstream detectors at low target occupancies, which lead to shorter congestion periods, whereas the upstream detectors performed better at high (i.e. super-critical) occupancies. Also, the best case performance was achieved with downstream detectors and a near critical target occupancy, as originally claimed by [8].

Figure 3.10 compares the performance of several variations of Alinea using upstream detectors. The four lines represent the four levels of override implementation (AL-1, AL-7, AL-8, AL-9), with target occupancy as the independent variable. Best case performance without overrides and using upstream detectors, is achieved at relatively high target occupancy values of 24% to 32%. This is also true when the queue override and later the green ball override are enforced in AL-7 and AL-8. As with fixed-rate control, the pattern becomes more irregular when all of the overrides are activated.

Batches AL-2 and AL-4 test the sensitivity of Alinea to changes in the value of K_r , for $\hat{\rho} =$

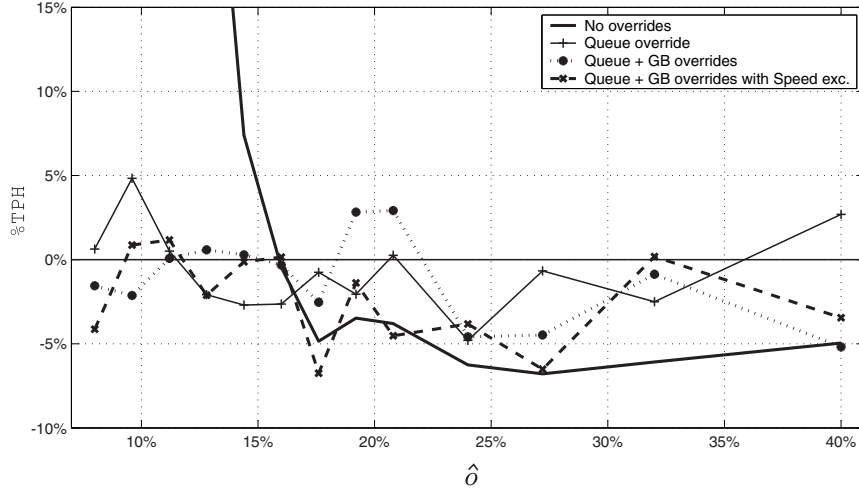


Figure 3.10: Performance with upstream Alinea (AL-1, AL-7, AL-8, AL-9).

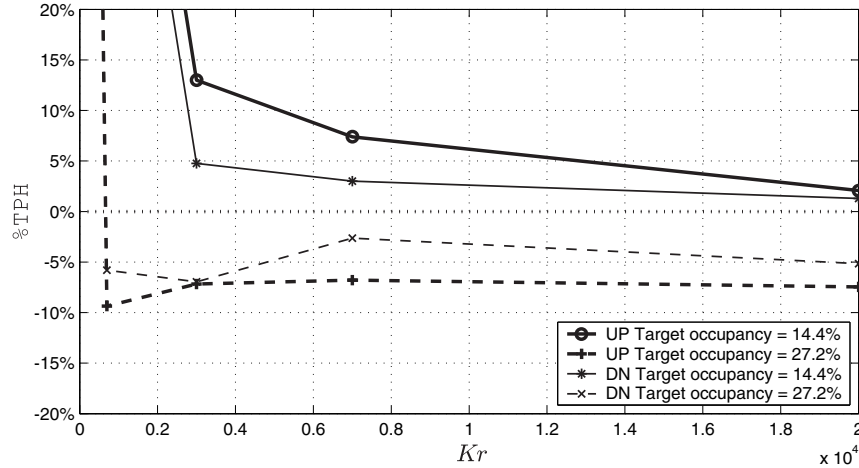


Figure 3.11: Alinea - Gain variations (AL-2, AL-4).

14.4% and 27.2%, and using either the upstream or downstream detectors. $\hat{\delta} = 27.2\%$ was the best choice in AL-1, when upstream detectors were used, and a near-best choice in AL-3 with downstream detectors. $\hat{\delta} = 14.4\%$ was a bad choice in both cases. The results are illustrated in Figure 3.11. With $\hat{\delta} = 14.4\%$, the controller never performs better than in the no control case, for any values of the gain, although the performance with the downstream detectors is consistently better than with the upstream detectors. For $\hat{\delta} = 27.2\%$, the best performance was recorded with relatively small values of the gain: $K_r = 3,000$ with downstream detectors and $K_r = 700$ with upstream detectors. The figure also reconfirms the observation from Figure 3.9, that upstream detectors perform better at high target occupancies (27.2%), and downstream perform better at low target occupancies (14.4%). Another interesting observation is that, for both super-critical and sub-critical target occupancies and for upstream and downstream detectors, $K_r = 20,000$ was a near-optimal choice. Although not tested, this suggests that a “bang-bang” controller, might be an effective strategy.

Batch	$\hat{\delta}$	K_r	%OPH	%FPH	%TPH	%TVH	%TPK	%TVK	%AMS	%ATH
AL-1	8.0		1170.0	-34.6	177.8	195.0	-1.8	-2.1	28.0	-13.3
	9.6		893.6	-33.5	130.0	143.0	-0.7	-0.8	27.0	-8.6
	11.2		569.7	-31.9	74.1	82.1	-0.3	-0.4	25.3	-4.0
	12.8		318.2	-28.4	32.7	36.7	0.1	0.1	21.8	-1.6
	14.4	↑	163.8	-26.1	7.4	8.9	0.3	0.3	19.6	0.1
	16.0		118.8	-26.0	-0.5	0.3	0.0	0.0	18.9	0.0
	17.6	7,000	94.8	-26.2	-4.9	-4.5	0.2	0.1	19.2	0.1
	19.2		90.7	-23.6	-3.5	-3.0	0.3	0.3	17.0	0.3
	20.8	↓	86.4	-23.1	-3.8	-3.4	0.2	0.2	16.3	0.2
	24.0		70.0	-22.6	-6.3	-6.0	0.1	0.1	15.8	0.0
	27.2		60.3	-21.2	-6.8	-6.7	0.4	0.3	14.5	0.4
	32.0		53.5	-18.8	-6.1	-5.9	0.3	0.2	12.7	0.3
40.0		32.7	-13.0	-5.0	-4.9	0.3	0.2	8.7	0.2	
AL-2	↑	70	1102.0	-30.1	169.5	185.7	-0.6	-0.7	24.2	-8.3
		700	521.7	-28.8	68.2	75.5	-0.5	-0.6	22.4	-2.7
	14.4	3,000	199.7	-27.0	13.0	15.1	0.0	0.0	20.2	-0.6
		7,000	163.8	-26.1	7.4	8.9	0.3	0.3	19.6	0.1
	↓	20,000	136.4	-26.7	2.1	3.1	0.2	0.2	19.9	0.3
AL-3	↑	70	1089.2	-29.7	167.6	183.6	-0.5	-0.7	23.9	-8.1
		700	60.8	-24.4	-9.4	-9.4	0.1	0.0	17.2	-0.2
	27.2	3,000	60.0	-21.5	-7.2	-7.0	0.1	0.1	14.7	0.1
		7,000	60.3	-21.2	-6.8	-6.7	0.4	0.3	14.5	0.4
	↓	20,000	55.1	-20.9	-7.5	-7.4	0.3	0.2	14.3	0.1
AL-4	8.0		1109.6	-34.7	167.1	183.7	-1.5	-1.8	28.2	-15.2
	9.6		789.9	-32.9	112.1	124.0	-0.2	-0.3	26.7	-10.3
	11.2		505.3	-31.4	63.2	70.3	0.4	0.3	25.0	-6.5
	12.8		276.6	-28.6	25.2	28.5	0.2	0.2	22.0	-3.2
	14.4	↑	141.5	-26.6	3.0	4.2	0.1	0.1	19.9	-2.4
	16.0		101.3	-26.8	-4.2	-3.7	0.3	0.3	19.9	-1.9
	17.6	7,000	82.6	-25.4	-6.3	-6.1	0.1	0.1	18.4	-2.1
	19.2		77.1	-23.8	-6.0	-5.8	0.4	0.3	17.1	-2.1
	20.8	↓	73.2	-24.9	-7.6	-7.4	0.3	0.3	17.8	-1.9
	24.0		75.0	-19.2	-2.6	-2.1	0.2	0.2	13.0	-2.0
	27.2		60.2	-20.1	-5.9	-5.7	0.2	0.2	13.7	-2.1
	32.0		46.5	-16.5	-5.4	-5.2	0.3	0.3	10.9	-1.9
40.0		12.2	-3.6	-0.8	-0.6	0.2	0.2	2.0	-1.6	
AL-5	↑	70	1091.4	-30.7	167.1	183.3	-0.7	-0.8	24.6	-11.0
		700	483.8	-30.3	60.3	66.9	-0.4	-0.5	23.7	-4.8
	14.4	3,000	160.8	-28.6	4.8	6.2	0.2	0.2	21.5	-2.3
		7,000	141.5	-26.6	3.0	4.2	0.1	0.1	19.9	-2.4
	↓	20,000	129.7	-26.2	1.3	2.3	0.3	0.2	19.5	-2.3
AL-6	↑	70	1091.4	-30.7	167.1	183.3	-0.7	-0.8	24.6	-11.0
		700	79.5	-24.1	-5.8	-5.5	0.1	0.1	17.0	-2.2
	27.2	3,000	65.7	-22.5	-7.0	-6.9	0.2	0.1	15.9	-2.2
		7,000	75.0	-19.2	-2.6	-2.1	0.2	0.2	13.0	-2.0
	↓	20,000	67.4	-20.7	-5.2	-4.9	0.4	0.4	14.3	-2.1

Table 3.10: Performance with Alinea.

Batch	$\hat{\sigma}$	K_r	%OPH	%FPH	%TPH	%TVH	%TPK	%TVK	%AMS	%ATh	
AL-7	8.0	7,000	36.5	-7.0	0.6	0.7	-0.1	-0.1	4.8	-0.1	
	9.6		34.2	-1.5	4.8	5.0	0.3	0.3	1.0	0.5	
	11.2		26.2	-5.0	0.5	0.5	0.1	0.0	3.6	0.0	
	12.8		22.5	-7.4	-2.1	-2.2	0.0	0.0	4.9	0.1	
	14.4		↑	19.2	-7.4	-2.7	-2.8	0.2	0.2	5.0	0.4
	16.0		14.3	-6.3	-2.6	-2.8	0.1	0.1	4.2	0.2	
	17.6		16.3	-4.4	-0.8	-0.8	0.1	0.1	2.8	0.2	
	19.2		15.5	-5.8	-2.1	-2.1	0.3	0.3	4.0	0.7	
	20.8		↓	16.7	-3.3	0.3	0.3	0.2	0.2	1.7	0.5
	24.0		10.9	-8.2	-4.8	-5.0	0.1	0.1	5.5	0.3	
	27.2		10.6	-3.1	-0.7	-0.7	0.3	0.2	2.0	0.3	
	32.0		6.2	-4.4	-2.5	-2.6	0.3	0.2	2.9	0.5	
40.0	7.2	1.7	2.7	2.8	0.3	0.3	-1.0	0.2			
AL-8	8.0	7,000	14.2	-4.9	-1.6	-1.7	0.2	0.1	3.2	0.3	
	9.6		15.7	-5.9	-2.1	-2.3	0.1	0.0	3.9	0.1	
	11.2		13.2	-2.7	0.1	0.0	0.0	0.0	2.2	0.0	
	12.8		13.1	-2.1	0.6	0.6	-0.1	-0.1	1.5	-0.1	
	14.4		↑	12.3	-2.3	0.3	0.2	0.1	0.1	1.9	0.1
	16.0		12.1	-3.0	-0.3	-0.4	0.2	0.2	2.0	0.5	
	17.6		6.3	-4.4	-2.5	-2.7	0.2	0.1	3.2	0.2	
	19.2		10.3	1.2	2.8	2.9	0.3	0.2	-0.2	0.0	
	20.8		↓	11.7	1.0	2.9	3.0	0.3	0.2	-0.1	0.0
	24.0		5.3	-6.7	-4.6	-4.9	0.1	0.0	4.6	0.1	
	27.2		2.6	-6.0	-4.5	-4.7	0.1	0.1	4.4	0.2	
	32.0		6.5	-2.4	-0.9	-1.0	0.1	0.1	1.7	0.1	
40.0	-2.0	-5.9	-5.2	-5.4	-0.1	-0.1	3.8	-0.1			
AL-9	8.0	7,000	33.8	-12.3	-4.1	-4.3	0.1	0.1	8.3	0.3	
	9.6		42.7	-8.1	0.9	1.0	0.4	0.3	5.6	0.6	
	11.2		45.7	-8.4	1.2	1.4	0.2	0.2	5.5	0.3	
	12.8		37.0	-10.5	-2.1	-2.1	0.1	0.1	7.0	0.4	
	14.4		↑	42.7	-9.3	-0.1	-0.1	0.1	0.1	6.3	0.1
	16.0		32.0	-6.7	0.1	0.2	0.3	0.2	4.5	0.5	
	17.6		21.0	-12.7	-6.8	-7.0	0.0	0.0	8.7	0.1	
	19.2		30.3	-8.2	-1.4	-1.5	0.2	0.1	5.8	0.3	
	20.8		↓	23.1	-10.4	-4.5	-4.7	0.2	0.2	7.3	0.3
	24.0		23.7	-9.7	-3.8	-4.0	0.3	0.3	6.7	0.6	
	27.2		14.3	-11.0	-6.5	-6.8	0.1	0.1	7.7	0.3	
	32.0		16.3	-3.3	0.2	0.2	0.1	0.1	1.8	0.2	
40.0	-1.6	-3.8	-3.4	-3.6	0.1	0.1	2.4	0.1			

Table 3.11: Performance with Alinea, continued.

3.6 Percent occupancy control

Percent-occupancy (%-Occ) control is one of the most widespread on-ramp metering schemes in the U.S. due to its simplicity of implementation and observed effectiveness. Along with Alinea, it falls under the category of local, traffic-responsive controllers, since the rate at every meter is computed independently of all others (i.e. no coordination). It is distinguished from Alinea by the fact that the feedback sensor is placed *upstream* of the on-ramp junction. %-Occ can be interpreted as a proportional control of the *occupancy* measurement. It is expressed in the notation of this chapter as,

$$\text{TMCrat}e[k] = 900 - \frac{900 - 180}{o^h - o^l} (\text{occ}[k] - o^l) \quad (3.11)$$

Under %-Occ control, the commanded rate is a decreasing linear function of the mainline occupancy, as plotted in Figure 3.12. The two parameters in the %-Occ control law are the low and high occupancy thresholds, o^l and o^h , at which the commanded rate is assigned the maximum and the minimum rate respectively. For values below o^l , the value computed by Eq. (3.11) exceeds 900 vphpl, but it is reduced to 900 vphpl by the control boxes. Similarly, the implemented rate is never less than 180 vphpl. The author knows of no published guidelines for tuning o^l and o^h .

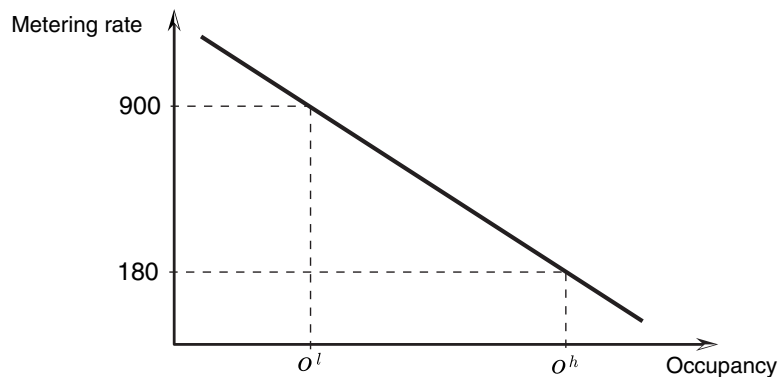


Figure 3.12: The %-Occ control function.

Three sets of simulation experiments were conducted, as shown in Table 3.12. Each set consists of 26 parameter selections with o^l ranging from 10% to 30%, and o^h from 18% to 30%. The resulting changes in TPH are shown in Table 3.12 and Figure 3.13.

Batch	Number of trials	occ_low	occ_high	Detector location	Queue override	Green Ball override	Speed exception
P0-1	26	10% - 30%	18% - 30%	UP	-	-	-
P0-2	26	10% - 30%	18% - 30%	UP	✓	-	-
P0-3	26	10% - 30%	18% - 30%	UP	✓	✓	✓

Table 3.12: Experiments with %-Occ.

The plots in Figure 3.13 are a bit erratic and difficult to interpret. Even in P0-1, when no overrides were enforced, there is no recognizable trend and no obvious best choice. All but one of the tests in this batch reduced travel time. A maximum reduction of -7.4% was recorded with $o^l = 14\%$ and $o^h = 30\%$. One consistent trend in P0-1 is in the performance of “bang-bang” controllers, whose performance worsened with increasing $o^l = o^h$. Enforcing the overrides in P0-2 and P0-3 has the general effect of diminishing travel time reductions.

$o^l \setminus o^h$	P0-1				P0-2				P0-3			
	18%	22%	26%	30%	18%	22%	26%	30%	18%	22%	26%	30%
10%	5.7	-4.0	-3.8	-5.4	-4.4	-3.2	-3.2	-2.4	-4.9	-5.8	-2.6	-4.4
12%	-	-	-5.5	-6.1	-	-	-2.6	0.2	-	-	-3.2	-2.4
13%	-	-	-7.1	-7.2	-	-	1.1	-2.1	-	-	-2.0	-3.3
14%	-3.5	-4.3	-4.5	-7.4	-7.6	-2.7	-2.5	-0.9	-3.0	-4.0	-2.4	-2.5
15%	-	-	-5.6	-3.0	-	-	-1.9	-2.5	-	-	-4.6	-0.3
17%	-	-	-5.3	-5.7	-	-	0.2	-4.9	-	-	0.8	-3.1
18%	-7.2	-4.8	-3.7	-6.9	-5.6	-2.4	-1.4	-4.4	-2.8	-1.7	-5.0	-3.2
22%	-	-6.5	-6.1	-2.8	-	-4.6	-2.3	-3.2	-	-3.3	-5.0	-3.6
26%	-	-	-6.4	-7.0	-	-	-2.4	-3.2	-	-	-3.5	1.5
30%	-	-	-	-2.9	-	-	-	0.2	-	-	-	-6.1

Table 3.13: Percent change in TPH with %-Occ.

3.7 Conclusions

This chapter has presented the results of a comparative simulation study involving several types of local ramp metering algorithms. Three candidate algorithms – fixed-rate metering, Alinea, and %-Occ – were implemented and tested on a Vissim simulation of the I-210W test segment. First, a number of performance measures, such as Total Vehicle Hours and Total Vehicle Kilometers, were defined in terms of aggregate traffic variables. Next, control-related elements of the I-210 infrastructure, e.g., possible on-ramp configurations, loop-detector layout, the TMC, and field-controller logic, were described. Two important features of the controller logic, the *queue override* and *green-ball override*, were reviewed. These overrides, respectively, act to prevent onramp

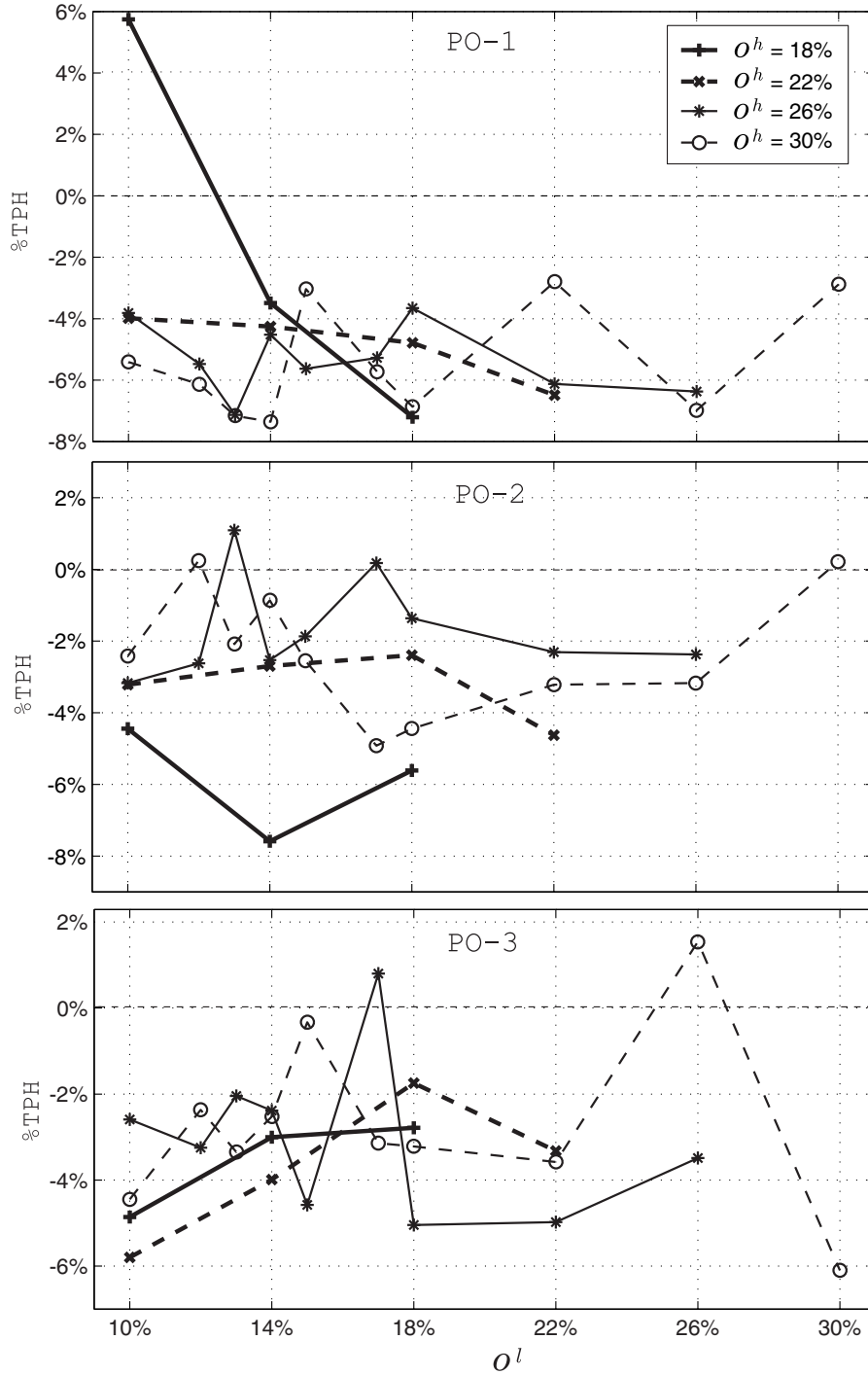


Figure 3.13: Performance with %-Occ.

queues from spilling back onto surface streets, and to suspend metering when mainline occupancies and flows are both low.

In the fixed-rate metering experiments, the metering rate on each of the 20 metered onramps was held at a constant value throughout the simulation period. The experiments were repeated

with different values of the constant (chosen between the minimum and maximum allowed metering rates) and different combinations of overrides engaged. It was discovered that performance improvements (e.g., in TVH) were possible, compared to the no-control case, for certain levels of fixed-rate metering, but that performance could deteriorate quickly when the constant metering value was varied. Queue override was shown to have the expected effect of limiting queue lengths, at the expense of possible reductions in improvements that were achieved in non-override cases. Tests with Alinea included two variations in mainline sensor placement: the downstream case (recommended by Papageorgiou), where occupancies are measured downstream of the on-ramp merge point, and the upstream case (as present on I-210 and other California freeways), where mainline occupancies are measured upstream of the merge point. It was shown that for target occupancies above 15%, a reduction in Total Passenger Hours could be achieved using either sensor arrangement, but that downstream placement worked better for relatively low target occupancies, whereas the upstream case worked better for high occupancies. This prediction is consistent with the observability results derived in Chapter 4. Experiments with %-Occ control included variations on the controller parameter values and engagement of the overrides. Although no obvious guidelines for adjusting the parameters were discovered, travel time reductions were achieved for some test runs. For cases where all overrides were engaged, Alinea appeared to yield a larger maximum TPH improvement, for the tested scenarios, than the other two algorithms.

Chapter 4

Macroscopic Traffic Simulation Models for Congested Freeways

In this chapter, the modified cell transmission and switching-mode models are described, and then applied to predict densities in a short subsegment of the I-210 testbed. The properties of observability and controllability, which are of fundamental importance for the design of data estimators and ramp-metering control systems, will be derived for the SMM in Section 4.3. In Sec. 4.4, simulation results for tests of the MCTM and SMM using data from a segment of I-210 are given.

4.1 Modified Cell Transmission Model

A modified CTM (MCTM) has been developed, which is similar to Daganzo's CTM of [10, 11], except that it uses cell densities as state variables instead of cell occupancies¹, and accepts nonuniform cell lengths. Using cell densities instead of cell occupancies permits the CTM to include uneven cell lengths, which leads to greater flexibility in partitioning the highway. Nonuniform cell lengths also enable the use of a smaller number of cells to describe a given highway segment, thus reducing the size of the state vector $[\rho_1 \dots \rho_N]^T$, where ρ_i is the density of the i^{th} cell. While it is expected that partitioning a segment finely, into a large number of cells, will improve numerical accuracy with respect to the LWR model, the interest here is to test methods using a smaller state vector, which will simplify the design of estimators and controllers. Note that rewriting the CTM in terms of density is not a new concept; for example, see [12], wherein Daganzo describes a density-based CTM that allows more general fundamental diagram shapes than a trapezoidal curve. However, the switching-mode model introduced later in this chapter is, to the authors' knowledge, an original traffic model.

In the modified CTM, a highway is partitioned into a series of cells. An example is shown in Fig. 4.1. The traffic density in any cell i evolves according to conservation of vehicles:

$$\rho_i(k+1) = \rho_i(k) + \frac{T_s}{l_i} (q_{i,in}(k) - q_{i,out}(k)) \quad (4.1)$$

where $q_{i,in}(k)$ and $q_{i,out}(k)$ are, respectively, the total flows, in vehicles per unit time, entering and leaving cell i during the k^{th} time interval, $T_s [k, k+1)$, including flows along the mainline and

¹Cell occupancy is defined as the number of vehicles in a cell; this is different from freeway loop-detector occupancy, which refers to the fraction of time a detector is occupied by vehicles.

the on- and off-ramps. k is the time index, T_s is the discrete time interval, l_i is the length of cell i , and $\rho_i(k)$ is the density, in vehicles per unit length of freeway, in cell i at time $k T_s$. The model parameters include v , w , Q_M , and ρ_J , which are depicted in the trapezoidal fundamental diagram of Fig. 4.2. The parameters can be uniform over all cells or allowed to vary from cell to cell. For

reference, the parameters are defined as:

- v ... free-flow speed (mph)
- w ... backward congestion wave speed (mph)
- Q_M ... maximum allowable flow (veh/hr, i.e., vph)
- ρ_J ... jam density (veh/mi, i.e., vpm)
- ρ_c ... critical density (vpm)

The free-flow speed v is the average speed at which vehicles travel down the highway under uncongested (low density) conditions. w is the speed at which congestion waves propagate upstream within congested (high density) regions of the highway. Q_M is the maximum flow rate, and ρ_J is the jam density (where traffic comes to a standstill).

Three different types of intercell connection are allowed: simple connection, merge, and diverge.

Simple Connection: If two cells are connected to one another without any intervening on-ramps or off-ramps (for example, cells 2 and 3 in Figure 4.1), then the cells are said to be simply connected. Let $i - 1$ be the upstream cell and i be the downstream cell in the pair. As described in [11], $q_i(k)$, the flow entering cell i from the mainline, is determined by taking the minimum of two quantities:

$$q_i(k) = \min\left(S_{i-1}(k), R_i(k)\right), \quad (4.2)$$

$$S_{i-1}(k) = \min\left(v_{i-1}\rho_{i-1}(k), Q_{M,i-1}\right), \quad (4.3)$$

$$R_i(k) = \min\left(Q_{M,i}, w_i(\rho_{J,i} - \rho_i(k))\right), \quad (4.4)$$

where $S_{i-1}(k)$ is the maximum flow that can be *supplied* by cell $i - 1$ under free-flow conditions, over the k^{th} time interval, and $R_i(k)$ is the maximum flow that can be *received* by cell i under congested conditions, over the same time interval.

The modified CTM also uses density-based versions of the merge and diverge laws of [11] to

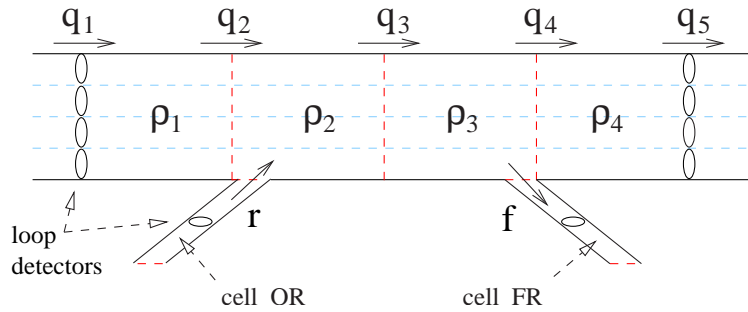


Figure 4.1: Highway segment partitioned into cells: 1–4 on mainline, cell OR on on-ramp, and cell FR on off-ramp.

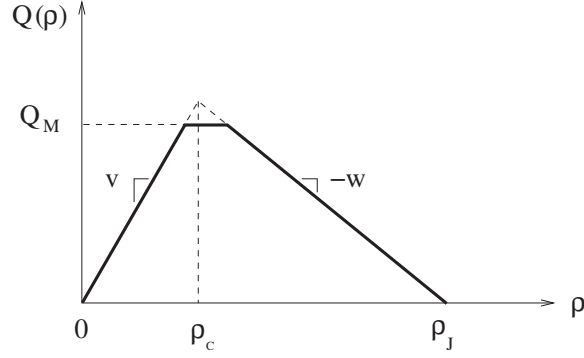


Figure 4.2: Trapezoidal fundamental diagram.

incorporate on-ramp and off-ramp flows. A merge and diverge are shown within the context of a freeway segment in Figure 4.1, where q_2 and r are the flows merging into cell 2 from cells 1 and OR, and q_4 and f are the flows diverging into cells 4 and FR from cell 3. For clarity, general cases of a merge and diverge are shown separately in Figure 4.3. Figure 4.3(a) depicts the case of a merge, where cell E receives flows from cells B and C , and Figure 4.3(b) depicts a diverge, where both cells E and C receive flow from cell B .

Merge Connection: The merge law is

$$q_{BE}(k) = \begin{cases} S_B(k) & \text{if } S_B(k) + S_C(k) \leq R_E(k) \\ \text{mid}\{S_B(k), R_E(k) - S_C(k), (1 - \gamma)R_E(k)\} & \text{otherwise.} \end{cases} \quad (4.5)$$

$$q_{CE}(k) = \begin{cases} S_C(k) & \text{if } S_B(k) + S_C(k) \leq R_E(k) \\ \text{mid}\{S_C(k), R_E(k) - S_B(k), \gamma R_E(k)\} & \text{otherwise.} \end{cases} \quad (4.6)$$

Here γ , the *merge coefficient*, is the proportion of vehicles that enter cell E from C in the case where both q_{BE} and q_{CE} are restricted below their supply flow values. The mid function returns the middle value in a set of three numbers, and can be implemented as follows: for any three real numbers, (1) sort the numbers in ascending order, and (2) return the second value in the sorted set.

Diverge Connection: The diverge law is

$$q_{B,out}(k) = \min \left(S_B(k), \frac{R_E(k)}{1 - \beta(k)}, \frac{R_C(k)}{\beta(k)} \right), \quad (4.7)$$

$$q_{BE}(k) = (1 - \beta(k))q_{B,out}(k), \quad (4.8)$$

$$q_{BC}(k) = \beta(k)q_{B,out}(k), \quad (4.9)$$

where $q_{B,out} = q_{BE} + q_{BC}$ is the total flow exiting cell B . $\beta(k)$ is the *split ratio* for the diverge junction, i.e., the fraction of vehicles leaving cell B which exits to cell C during the k^{th} time interval.

The MCTM is subject to the same intercell connectivity restrictions as those described in [11]. Specifically, the maximum number of separate flow streams allowed to enter any cell is 2, and the maximum number of flows allowed to exit any cell is 2. Furthermore, a flow between two cells may not be “doubly specified”, e.g., a merging flow entering one cell may not coincide with a diverging flow leaving another cell.

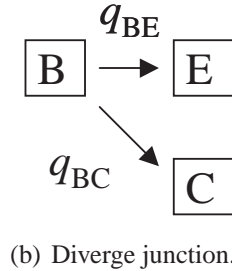
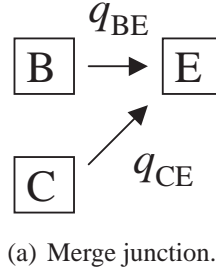


Figure 4.3: Merge and diverge connections for cells B , E , and C .

The modified CTM consists of flow conservation, Eq. (4.1), for each cell, along with the flow relations, Eqs. (4.2)–(4.9). The aforementioned equations are the density-based equivalents of those described in [11]. The state variable is $\boldsymbol{\rho} = [\rho_1 \dots \rho_N]^T$ for a freeway partitioned into N cells. One requirement of the MCTM is that the cell lengths must be longer than the free-flow travel distance, i.e.,

$$v_i T_s \leq l_i, \quad (4.10)$$

for cell i , where l_i is the cell length and T_s is the time step. For more information, see [12], where Daganzo extends the CTM to include more general fundamental diagram shapes, and explains that this condition is necessary for convergence of CTM solutions to LWR solutions.

As presented, the MCTM requires aggregate demand and boundary information, as opposed to O-D tables. For an O-D dependent version of the CTM that keeps track of disaggregated cell occupancies, which are indexed by destination and wait time, see [11]. In the case of a linear freeway segment, where there is only one route connecting each origin to each downstream destination, it is sufficient to specify either a set of time-varying split ratios (as in the MCTM formulation), or, alternatively, to specify a time-varying O-D table, and then keep track of the disaggregated occupancies, as demonstrated in [11]. In the latter case, the split ratios can be computed at run-time by counting the number of vehicles that ultimately enter each of the off-ramps at each time step. A point of complication is that the true O-D proportions in a freeway are typically not available, and in general cannot be determined uniquely from the aggregate link flows alone.

Before making use of an O-D or non-O-D model, an important consideration is whether either formulation is appropriate for the intended application. In the form presented in this report, an assumption of the MCTM is that the split ratios can be determined externally to the model as functions of time. For example, knowledge of the true O-D behavior appears not to be required for the calibration studies presented in Chapter 5, where the main interest is in reproducing the observed evolution of aggregate variables. However, if the split ratio assumption is determined not to be valid for a particular traffic scenario, a model with explicit O-D dependence becomes

necessary.

Congestion and Critical Density

An important feature of the MCTM is its ability to reproduce traffic congestion. *Congestion* refers to the traffic condition that occurs when a freeway is crowded; that is, if the vehicle density is sufficiently high, drivers will proceed at reduced speeds in order to avoid colliding with other vehicles. *Free-flow* is the opposite condition, where vehicle density is low, and drivers may attain (or exceed) the maximum posted freeway speed.

As explained by Lighthill and Whitham [13], for a density ρ , the space-mean speed of traffic (q/ρ) is the slope of the line connecting the origin of the fundamental diagram to the point $Q(\rho)$. Hence, for a concave-down curve like that of Figure 4.2, it can be seen that speed is a non-increasing function of density. Specifically, speed is a constant, v , on the left side of the fundamental diagram, and decreases with increasing density on the right side of the diagram. Solving the initial-value problem of the LWR equation, with the diagram in Figure 4.2, reveals that a profile of sufficiently low density will travel downstream at speed v ; however, a profile of sufficiently high density will travel upstream at speed w . This should not be confused with direction of travel of the vehicles, which is always downstream (unless the density is ρ_J , at which point travel halts); rather, the direction of travel of information, in the form of density waves, is opposite depending on whether the traffic is in a free-flow or congested condition.

In this research, two types of fundamental diagram have been considered; the simple triangular case of Figure 4.4(a) and the general trapezoidal case of Figure 4.4(b). In the case of a triangular fundamental diagram, it is natural to define the critical density as the density at which the free-flow ($Q(\rho) = v\rho$) and congestion ($Q(\rho) = w(\rho_J - \rho)$) curves intersect. For a trapezoidal fundamental diagram, three possible definitions are obvious:

- $\underline{\rho}_c := \frac{Q_M}{v}$, the density at the intersection of $Q(\rho) = v\rho$ and $Q(\rho) = Q_M$,
- $\rho_c := \frac{w\rho_J}{v+w}$, the density at the intersection of $Q(\rho) = v\rho$ and $Q(\rho) = w(\rho_J - \rho)$, and
- $\bar{\rho}_c := \rho_J - \frac{Q_M}{w}$, the density at the intersection of $Q(\rho) = Q_M$ and $Q(\rho) = w(\rho_J - \rho)$.

In the triangular case, $\underline{\rho}_c = \rho_c = \bar{\rho}_c$, whereas, in the trapezoidal case, $\underline{\rho}_c < \rho_c < \bar{\rho}_c$. Regarding the MCTM, two special cases of the intercellular flow are often considered:

1. the *pure free-flow* case where each supply flow $S_i(k)$ evaluates to $v_i\rho_i(k)$, and
2. the *pure congestion* case where each receiving flow $R_i(k)$ evaluates to $w_i(\rho_{J,i} - \rho_i(k))$.

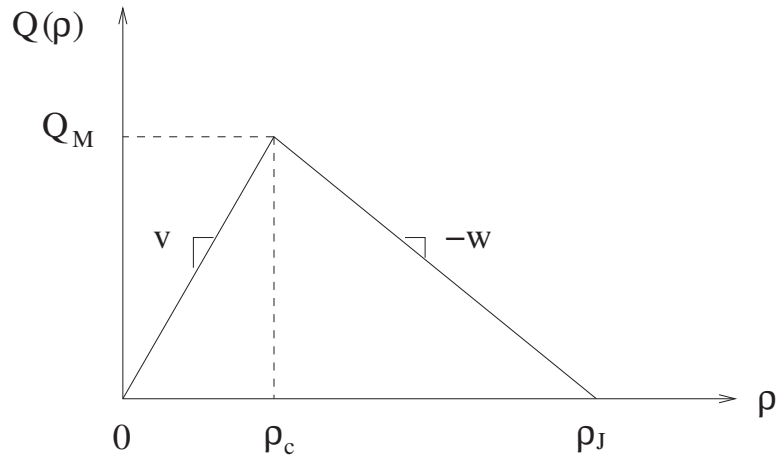
Since it is assumed that $v_i > 0$ for all i ,

- Pure free-flow, $S_i(k) = v_i\rho_i(k)$, is equivalent to $\rho_i(k) \leq \underline{\rho}_{c,i}$.

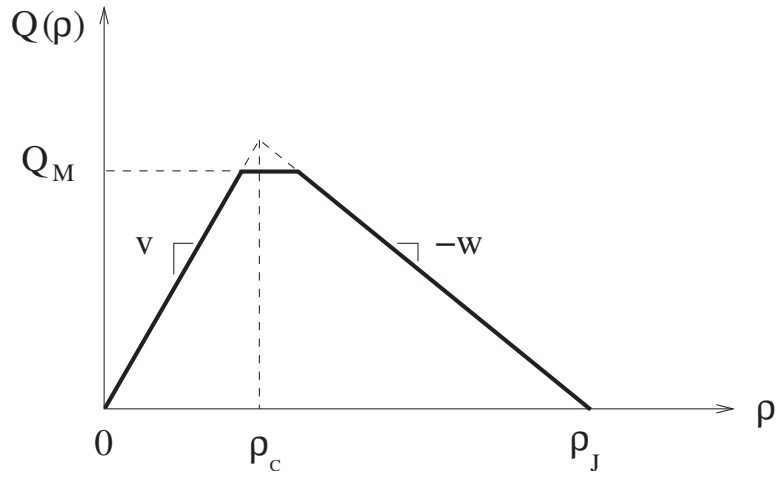
Similarly, since it is assumed that $w_i > 0$ for all i ,

- Pure congestion, $R_i(k) = w_i(\rho_{J,i} - \rho_i(k))$, is equivalent to $\rho_i(k) \geq \bar{\rho}_{c,i}$.

Then, the more general cases for the density are



(a) Triangular fundamental diagram.



(b) Trapezoidal fundamental diagram.

- Free-flow: $\rho_i(k) \leq \rho_{c,i}$
- Congestion: $\rho_i(k) \geq \rho_{c,i}$

Thus, the range of densities over which the pure free-flow or pure congested cases occur will vary depending on the shape of the fundamental diagram. In the short-segment study of the MCTM and SMM, described in Section 4.3, the fundamental diagrams are assumed to be triangular, hence checking whether $\rho_i \leq \rho_{c,i}$ or $\rho_i \geq \rho_{c,i}$ is sufficient to determine if the intercellular flows match the pure free-flow or pure congested cases. In the full I-210 study, described in Chapter 5, trapezoidal fundamental diagrams are allowed, which means the pure free-flow and congested cases of intercellular flow correspond to more restricted density ranges, $\rho_i \leq \underline{\rho}_{c,i}$ or $\rho_i \geq \bar{\rho}_{c,i}$, respectively. If cell parameters v_i , $Q_{M,i}$, and $\rho_{J,i}$ are known, we can calculate the critical density of a cell, $\rho_{c,i}$, from the triangular fundamental diagram of Figure 4.4(a). Then, the *congestion status* of cell i is determined by comparing the cell density with the critical density: if $\rho_i < \rho_{c,i}$, the cell has free-flow status, otherwise $\rho_i \geq \rho_{c,i}$ and the cell has congested status. In this writing, the term *critical density* will be used to refer to $\rho_c = \frac{w\rho_J}{v+w}$ unless otherwise stated.

Boundary Conditions

Regarding boundary conditions, the CTM simulation package NETCELL, described in [14], assumes that the downstream end of a highway segment can always discharge vehicles at either the maximum allowed speed or maximum allowed flow rate. However, in an actual highway segment, traffic at the downstream end may be either free-flowing or congested at different times of day. Thus, depending on the type of traffic behavior, allowing congested conditions at downstream boundaries may be necessary to enable the model to work with real highway data.

Consider the segment in Figure 4.4. The default boundary conditions for the MCTM are

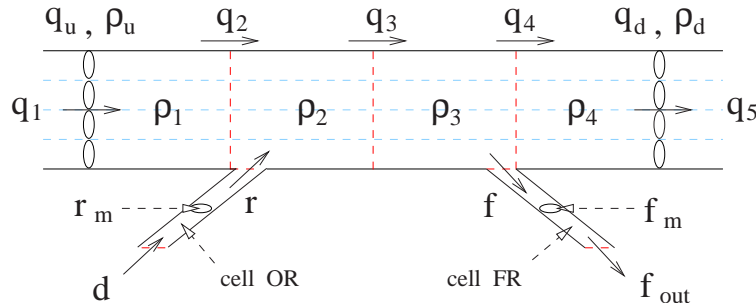


Figure 4.4: Highway segment partitioned into cells.

$$q_1(k) = q_u(k), \quad (4.11)$$

$$q_5(k) = \min(v\rho_4(k), Q_M), \quad (4.12)$$

$$d(k) = r_m(k), \quad (4.13)$$

$$f_{out}(k) = \min(v\rho_{FR}(k), Q_M). \quad (4.14)$$

Here, q_1 is the flow entering the upstream mainline boundary, q_5 is the flow exiting the downstream mainline boundary, d is the demand, i.e., the flow entering the upstream boundary of an on-ramp

cell, and f_{out} is the flow exiting the downstream boundary of an off-ramp cell. Measured flows are q_u , q_d , r_m , and f_m , and measured densities are ρ_u and ρ_d . In order to allow the MCTM to work with real traffic data, a set of modified boundary conditions were developed and used in the short-segment validation tests described in Section 4.4:

$$q_1(k) = \begin{cases} \min(q_u(k), Q_M), & \text{if } \rho_u \leq \rho_c \text{ and } q_u(k) \leq w(\rho_J - \rho_1(k)) \\ \min(Q_M, w(\rho_J - \rho_1(k))), & \text{otherwise} \end{cases} \quad (4.15)$$

$$q_5(k) = \begin{cases} \min(v\rho_4(k), Q_M), & \text{if } \rho_d \leq \rho_c \text{ or } q_d(k) \geq v\rho_4(k) \\ \min(q_d(k), Q_M), & \text{otherwise} \end{cases} \quad (4.16)$$

$$d(k) = \min(r_m(k), Q_M), \quad (4.17)$$

$$f_{out}(k) = \min(f_m(k), Q_M). \quad (4.18)$$

Eq. (4.15) prevents the flow entering the upstream mainline boundary from exceeding Q_M , and only uses the measured flow q_u when ρ_u is uncongested and q_u is not larger than the maximum amount of flow that the farthest upstream cell can receive. Eq. (4.16) prevents the flow exiting the downstream mainline boundary from exceeding Q_M , and only uses the measured flow q_d when ρ_d is congested and q_d is less than the maximum amount of flow that farthest downstream cell can expel under free-flow conditions. In general, these conditions are included to prevent unrealistic scenarios, such as a boundary flow that exceeds the maximum allowed flow rate (Q_M), for a cell, or a cell accepting vehicles at a flow rate beyond the density-limited capacity $w(\rho_J - \rho)$, or emitting vehicles above the free-flow rate $v\rho$.

4.2 Switching-Mode Model

In order to gain additional insight into freeway traffic behavior, and to simplify the control analysis, control design, and data-estimation design methods, a piecewise-linearized version of the MCTM, called the switching-mode model (SMM), has been designed. Since the SMM is composed of several linear models, straightforward linear techniques for model analysis and control design can be applied to the individual linear subsystems.

The SMM is a hybrid system that switches among five sets of linear difference equations, depending on the congestion status of the cells and the values of the mainline boundary data. Assuming the state variable is the cell densities, $\boldsymbol{\rho} = [\rho_1 \dots \rho_N]^T$, the key difference between the MCTM and the SMM is that, with respect to density, the former is nonlinear, whereas each mode of the latter is linear. The SMM can be extracted from the MCTM by writing each inter-cellular flow as either an explicit function of cell density, or as a constant. For example, in the case of a segment without merges or diverges, each q_i would be replaced with $v\rho_{i-1}(k)$, $w(\rho_J - \rho_i(k))$, or Q_M . This explicit density dependence is achieved by supplying a set of logical rules that determine the congestion status of each cell, at every time step, based on measurements at the segment boundaries.

For simplicity, the following assumptions are made:

1. The densities and flows at the upstream and downstream segment boundaries, as well as flows on all the on-ramps and off-ramps, are measured.
2. There is at most one status transition (or wave front) in the highway section. If both the upstream and downstream mainline boundaries are of the same status, i.e., both free-flow or both congested, it is assumed that all the mainline cells, 1 through N , have the same status; while if the two boundaries are of different status, there exists a single wave front in the segment, upstream of which all the cells have congested (free-flow) status, and downstream of which all cells have free-flow (congested) status.

The single-wave front assumption is an approximation that is expected to be acceptable for short highway segments with only one on-ramp and off-ramp, such as the example later in this section. To more accurately deal with longer sections with many on- and off-ramps, the switching logic can be modified to allow multiple wave fronts within a segment.

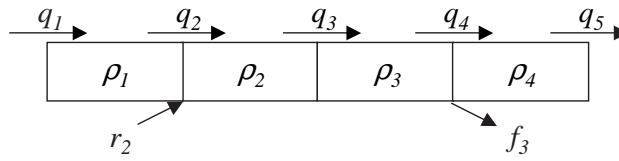
Since an SMM-modeled section contains at most one congestion wave front, the modes of the SMM can be distinguished by the congestion status of the cells upstream and downstream of the wave front. If there is no wave front in the section, a repeated label, e.g., “Free-flow–Free-flow”, can be used to indicate the absence of any status transition. The five modes are denoted: (1) “Free-flow–Free-flow” (FF), (2) “Congestion–Congestion” (CC), (3) “Congestion–Free-flow” (CF), (4) “Free-flow–Congestion 1” (FC1), and (5) “Free-flow–Congestion 2” (FC2), and are depicted in Figure 4.5. The two modes of “Free-flow–Congestion” are determined by the relative magnitudes of the *supplied* flow of the last uncongested cell upstream of the wave front and the *received* flow of the the first congested cell downstream of the wave front. If the former is smaller, the SMM is in FC1; while if the latter is smaller, it is in FC2. Respectively, these two cases are distinguished by whether the congestion wave is traveling forward or backward within the segment.

Consider the highway segment in Fig. 4.6, which is divided into 4 cells. The on- and off-ramps are not modeled as cells in this case. The measured aggregate flows and densities at the upstream and downstream mainline detectors are denoted by q_u, ρ_u , and q_d, ρ_d . All five modes of the SMM can be summarized as follows:

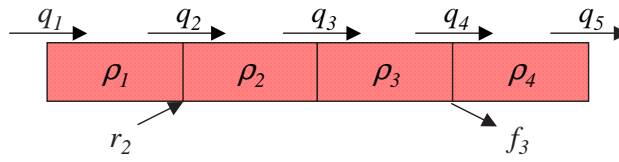
$$\boldsymbol{\rho}(k+1) = A_s \boldsymbol{\rho}(k) + B_s \mathbf{u}(k) + B_{J,s} \boldsymbol{\rho}_J + B_{Q,s} \mathbf{q}_M, \quad (4.19)$$

where $s = 1, 2, 3, 4, 5$ indicates the mode (1: FF, 2: CC, 3: CF, 4: FC1, 5: FC2), $\boldsymbol{\rho} = [\rho_1 \dots \rho_4]^T$ is the state, and $\mathbf{u} = [q_u \ r_2 \ f_3 \ \rho_d]^T$ are the flow and density inputs; specifically, r_2 and f_3 are the measured on-ramp and off-ramp flows entering and leaving the section, subscripted according to their cell of entry or exit. $\boldsymbol{\rho}_J = [\rho_{J1} \ \rho_{J2} \ \rho_{J3} \ \rho_{J4} \ \rho_{J5}]^T$ is the vector of jam densities, and $\mathbf{q}_M = [Q_{M1} \ Q_{M2} \ Q_{M3} \ Q_{M4}]^T$ is the vector of maximum flow rates. Eq. (4.19) can alternatively be written with the downstream flow, q_d , as an input instead of ρ_d , but the stated form has the advantage of eliminating the $B_{J,s} \boldsymbol{\rho}_J$ term for modes with downstream congestion, in the case where w_i and $\rho_{J,i}$ are the same for each cell.

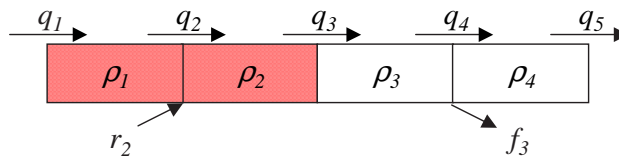
In FF mode, the flow across each cell boundary is dictated by *upstream* conditions; specifically, each cell releases traffic at the free-flow rate according to the first term in Eq. (4.3). That is, the total flow exiting cell i is given by $v_i \rho_i$. The flow across the upstream boundary of cell 1 is q_u . The



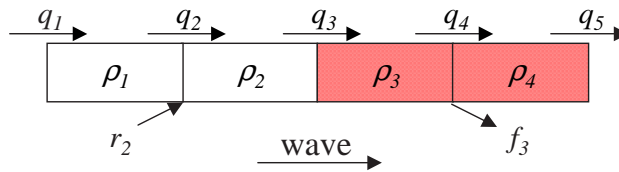
(a) Free-flow-Free-flow (FF) mode



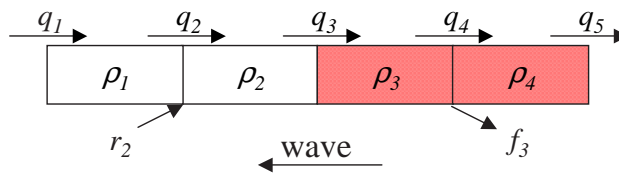
(b) Congestion-Congestion (CC) mode



(c) Congestion-Free-flow (CF) mode, with congestion wave front located in the middle of the segment



(d) Free-flow-Congestion 1 (FC1) mode, with congestion wave front located in the middle of the segment



(e) Free-flow-Congestion 2 (FC2) mode, with congestion wave front located in the middle of the segment

Figure 4.5: Sample congestion patterns for a 4-cell highway segment, corresponding to different modes of the SMM. Shading indicates a congested cell.

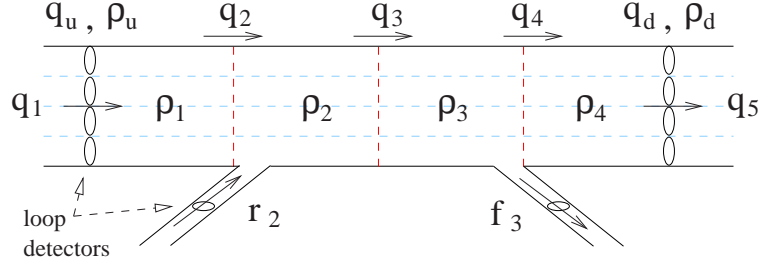


Figure 4.6: Highway segment divided into 4 cells.

state matrices are

$$A_1 = \begin{bmatrix} 1 - \frac{v_1 T_s}{l_1} & 0 & 0 & 0 \\ \frac{v_1 T_s}{l_2} & 1 - \frac{v_2 T_s}{l_2} & 0 & 0 \\ 0 & \frac{v_2 T_s}{l_3} & 1 - \frac{v_3 T_s}{l_3} & 0 \\ 0 & 0 & \frac{v_3 T_s}{l_4} & 1 - \frac{v_4 T_s}{l_4} \end{bmatrix}, \quad B_1 = \begin{bmatrix} \frac{T_s}{l_1} & 0 & 0 & 0 \\ 0 & \frac{T_s}{l_2} & 0 & 0 \\ 0 & 0 & 0 & 0 \\ 0 & 0 & -\frac{T_s}{l_4} & 0 \end{bmatrix},$$

$$B_{J,1} = 0_{4 \times 5}, \quad B_{Q,1} = 0_{4 \times 4}. \quad (4.20)$$

In CC mode, the flow across each cell boundary is dictated by *downstream* conditions; specifically, each cell absorbs flow according to the second term in Eq. (4.4). That is, the total flow entering cell i is given by $w_i(\rho_{J,i} - \rho_i)$. The flow released by cell 4 is determined by the downstream density ρ_d . The state matrices are

$$A_2 = \begin{bmatrix} 1 - \frac{w_1 T_s}{l_1} & \frac{w_2 T_s}{l_1} & 0 & 0 \\ 0 & 1 - \frac{w_2 T_s}{l_2} & \frac{w_3 T_s}{l_2} & 0 \\ 0 & 0 & 1 - \frac{w_3 T_s}{l_3} & \frac{w_4 T_s}{l_3} \\ 0 & 0 & 0 & 1 - \frac{w_4 T_s}{l_4} \end{bmatrix}, \quad B_2 = \begin{bmatrix} 0 & \frac{T_s}{l_1} & 0 & 0 \\ 0 & 0 & 0 & 0 \\ 0 & 0 & -\frac{T_s}{l_3} & 0 \\ 0 & 0 & 0 & \frac{w_5 T_s}{l_4} \end{bmatrix},$$

$$B_{J,2} = \begin{bmatrix} \frac{w_1 T_s}{l_1} & -\frac{w_2 T_s}{l_1} & 0 & 0 & 0 \\ 0 & \frac{w_2 T_s}{l_2} & -\frac{w_3 T_s}{l_2} & 0 & 0 \\ 0 & 0 & \frac{w_3 T_s}{l_3} & -\frac{w_4 T_s}{l_3} & 0 \\ 0 & 0 & 0 & \frac{w_4 T_s}{l_4} & -\frac{w_5 T_s}{l_4} \end{bmatrix},$$

$$B_{Q,2} = 0_{4 \times 4}. \quad (4.21)$$

In CF mode, there exists one congestion-to-free-flow transition inside the section. One assumption of the SMM is that the wave front will always lie on a cell boundary. Cells upstream of the wave front accept vehicles at the congested flow rate, while cells downstream of the wave front release vehicles at the free-flow rate. The wave front itself acts as a bottleneck, expelling vehicles at maximum allowed rate Q_M , and decoupling the region upstream of the wave front from the region downstream of the wave front. For the case where the wave front is located in between

cells 2 and 3, the state matrices are

$$\begin{aligned}
A_3 &= \begin{bmatrix} 1 - \frac{w_1 T_s}{l_1} & \frac{w_2 T_s}{l_1} & 0 & 0 \\ 0 & 1 - \frac{w_2 T_s}{l_2} & 0 & 0 \\ 0 & 0 & 1 - \frac{v_3 T_s}{l_3} & 0 \\ 0 & 0 & \frac{v_3 T_s}{l_4} & 1 - \frac{v_4 T_s}{l_4} \end{bmatrix}, \quad B_3 = \begin{bmatrix} 0 & \frac{T_s}{l_1} & 0 & 0 \\ 0 & 0 & 0 & 0 \\ 0 & 0 & 0 & 0 \\ 0 & 0 & -\frac{T_s}{l_4} & 0 \end{bmatrix}, \\
B_{J,3} &= \begin{bmatrix} \frac{w_1 T_s}{l_1} & -\frac{w_2 T_s}{l_1} & 0 & 0 & 0 \\ 0 & \frac{w_2 T_s}{l_2} & 0 & 0 & 0 \\ 0 & 0 & 0 & 0 & 0 \\ 0 & 0 & 0 & 0 & 0 \end{bmatrix}, \quad B_{Q,3} = \begin{bmatrix} 0 & 0 & 0 & 0 \\ 0 & 0 & -\frac{T_s}{l_2} & 0 \\ 0 & 0 & \frac{T_s}{l_3} & 0 \\ 0 & 0 & 0 & 0 \end{bmatrix}. \tag{4.22}
\end{aligned}$$

In both FC modes, one free-flow-to-congestion transition exists inside the section. Unlike the previous mode, the state matrices change depending on the direction of motion of the wave front. In FC1, the wave front moves downstream. Assuming, for example, that the wave front is between cells 2 and 3, the state matrices for this mode are

$$\begin{aligned}
A_4 &= \begin{bmatrix} 1 - \frac{v_1 T_s}{l_1} & 0 & 0 & 0 \\ \frac{v_1 T_s}{l_2} & 1 - \frac{v_2 T_s}{l_2} & 0 & 0 \\ 0 & \frac{v_2 T_s}{l_3} & 1 & \frac{w_4 T_s}{l_3} \\ 0 & 0 & 0 & 1 - \frac{w_4 T_s}{l_4} \end{bmatrix}, \quad B_4 = \begin{bmatrix} \frac{T_s}{l_1} & 0 & 0 & 0 \\ 0 & \frac{T_s}{l_2} & 0 & 0 \\ 0 & 0 & -\frac{T_s}{l_3} & 0 \\ 0 & 0 & 0 & \frac{w_5 T_s}{l_4} \end{bmatrix}, \\
B_{J,4} &= \begin{bmatrix} 0 & 0 & 0 & 0 & 0 \\ 0 & 0 & 0 & 0 & 0 \\ 0 & 0 & 0 & -\frac{w_4 T_s}{l_3} & 0 \\ 0 & 0 & 0 & \frac{w_4 T_s}{l_4} & -\frac{w_5 T_s}{l_4} \end{bmatrix}, \\
B_{Q,4} &= 0_{4 \times 4}. \tag{4.23}
\end{aligned}$$

For FC2, the wave moves upstream. Again assuming that the wave front is between cells 2 and 3, this mode differs from the previous case in that, due to the dominance of the congested flow rate at the wave front boundary, the tridiagonal row is now the second instead of the third row, and more terms appear in $B_{J,s}$:

$$\begin{aligned}
A_5 &= \begin{bmatrix} 1 - \frac{v_1 T_s}{l_1} & 0 & 0 & 0 \\ \frac{v_1 T_s}{l_2} & 1 & \frac{w_3 T_s}{l_2} & 0 \\ 0 & 0 & 1 - \frac{w_3 T_s}{l_3} & \frac{w_4 T_s}{l_3} \\ 0 & 0 & 0 & 1 - \frac{w_4 T_s}{l_4} \end{bmatrix}, \\
B_5 &= B_4, \\
B_{J,5} &= \begin{bmatrix} 0 & 0 & 0 & 0 & 0 \\ 0 & 0 & -\frac{w_3 T_s}{l_2} & 0 & 0 \\ 0 & 0 & \frac{w_3 T_s}{l_3} & -\frac{w_4 T_s}{l_3} & 0 \\ 0 & 0 & 0 & \frac{w_4 T_s}{l_4} & -\frac{w_5 T_s}{l_4} \end{bmatrix}, \\
B_{Q,5} &= 0_{4 \times 4}. \tag{4.24}
\end{aligned}$$

The switching rules, designed by Xiaotian Sun [15], used to determine the mode of the system are as follows:

if $\rho_u < \rho_c$ **and** $\rho_d < \rho_c$ **then**

```

mode = FF
else if  $\rho_u \geq \rho_c$  and  $\rho_d \geq \rho_c$  then
  mode = CC
else if  $\rho_u \geq \rho_c$  and  $\rho_d < \rho_c$  then
  Perform C/F boundary search (search from upstream to downstream until the first uncongested
  cell is found):
  if no congested cells then
    mode = FF
  else if all congested cells then
    mode = CC
  else
    mode = CF
  end if
else
  Perform F/C boundary search (search from upstream to downstream until the first congested
  cell is found):
  if no uncongested cells then
    mode = CC
  else if all uncongested cells then
    mode = FF
  else
    if boundary is moving downstream, i.e.,  $v\rho_{b,u} < w(\rho_J - \rho_{b,d})$  then
      mode = FC1
    else
      mode = FC2
    end if
  end if
end if

```

Here, $\rho_{b,u}$ and $\rho_{b,d}$ are the densities upstream and downstream of the boundary, respectively. The switching rules are summarized in Figure 4.7. At each time step, the SMM determines its mode based on the measured mainline boundary data and the congestion status of the cells in the section. If both ρ_u and ρ_d have free-flow status, the FF mode is selected, and if both of these densities are congested, the CC mode is selected. If ρ_u and ρ_d are of opposite status, then the SMM performs a search over the ρ_i to determine whether there is a status transition inside the section. This wave front search consists of searching through the cells, in order, looking for the first status transition between adjacent cells.

It is expected that some error will be induced in the wave front location predicted by the SMM, since the search for a status transition is performed on the states estimated by the SMM, and not the state of the traffic in the actual freeway segment (which is unmeasured due to a lack of sensors in the middle of the segment). A stochastic estimation method, based on the SMM, that uses output feedback to correct both estimated densities and predicted wave front locations, has been developed and is explained in [16, 17].

In Sections 4.3 and 4.4, the observability and controllability properties of the SMM will be derived, and the ability of both the MCTM and SMM to predict densities in a short freeway segment

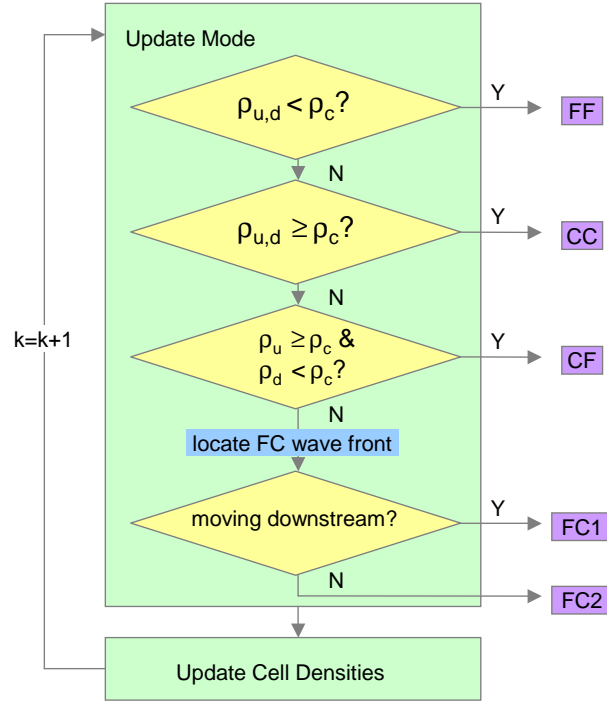


Figure 4.7: Transition rules for SMM.

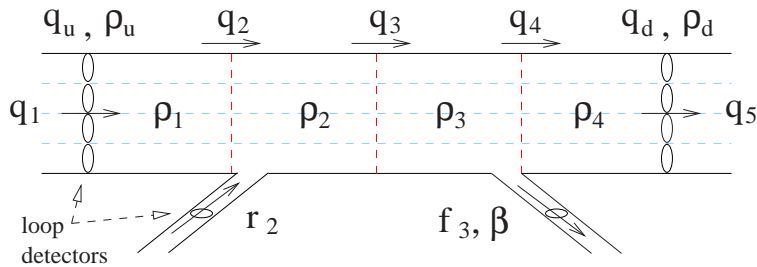


Figure 4.8: Highway segment divided into 4 cells.

will be tested. Chapter 5 presents a calibration methodology for the MCTM and shows the results of its application to the full 14-mile I-210 testbed.

4.3 Observability and Controllability

Observability and controllability properties will be derived for the split-ratio dependent version of the SMM. In the SMM, if the off-ramp flows (f_i) are known ahead of time, the state matrices can be written as in Eqs. (4.20)–(4.24). However, if only the split ratios, and not the f_i , are known, then the off-ramp flows are a function of the cell densities. In the case of time-varying split ratios, the FF-mode state matrices in Eq. (4.20) (for the segment of Figure 4.8) become

$$\begin{aligned}
A_1(k) &= \begin{bmatrix} 1 - \frac{v_1 T_s}{l_1} & 0 & 0 & 0 \\ \frac{v_1 T_s}{l_2} & 1 - \frac{v_2 T_s}{l_2} & 0 & 0 \\ 0 & \frac{v_2 T_s}{l_3} & 1 - \frac{v_3 T_s}{l_3} & 0 \\ 0 & 0 & (1 - \beta(k)) \frac{v_3 T_s}{l_4} & 1 - \frac{v_4 T_s}{l_4} \end{bmatrix} = \begin{bmatrix} a_{111} & 0 & 0 & 0 \\ a_{121} & a_{122} & 0 & 0 \\ 0 & a_{132} & a_{133} & 0 \\ 0 & 0 & a_{143}(k) & a_{144} \end{bmatrix}, \\
B_1 &= \begin{bmatrix} \frac{T_s}{l_1} & 0 & 0 & 0 \\ 0 & \frac{T_s}{l_2} & 0 & 0 \\ 0 & 0 & 0 & 0 \\ 0 & 0 & 0 & 0 \end{bmatrix}, \\
B_{J,1} &= 0_{4 \times 5}, \quad B_{Q,1} = 0_{4 \times 4}.
\end{aligned} \tag{4.25}$$

For the CC mode, the split-ratio-dependent matrices are

$$\begin{aligned}
A_2(k) &= \begin{bmatrix} 1 - \frac{w_1 T_s}{l_1} & \frac{w_2 T_s}{l_1} & 0 & 0 \\ 0 & 1 - \frac{w_2 T_s}{l_2} & \frac{w_3 T_s}{l_2} & 0 \\ 0 & 0 & 1 - \frac{w_3 T_s}{l_3} & \frac{1}{1 - \beta(k)} \frac{w_4 T_s}{l_3} \\ 0 & 0 & 0 & 1 - \frac{w_4 T_s}{l_4} \end{bmatrix} = \begin{bmatrix} a_{211} & a_{212} & 0 & 0 \\ 0 & a_{222} & a_{223} & 0 \\ 0 & 0 & a_{233} & a_{234}(k) \\ 0 & 0 & 0 & a_{244} \end{bmatrix}, \\
B_2 &= \begin{bmatrix} 0 & \frac{T_s}{l_1} & 0 & 0 \\ 0 & 0 & 0 & 0 \\ 0 & 0 & 0 & 0 \\ 0 & 0 & 0 & \frac{w_5 T_s}{l_4} \end{bmatrix}, \\
B_{J,2} &= \begin{bmatrix} \frac{w_1 T_s}{l_1} & -\frac{w_2 T_s}{l_1} & 0 & 0 & 0 \\ 0 & \frac{w_2 T_s}{l_2} & -\frac{w_3 T_s}{l_2} & 0 & 0 \\ 0 & 0 & \frac{w_3 T_s}{l_3} & -\frac{w_4 T_s}{l_3} & 0 \\ 0 & 0 & 0 & \frac{w_4 T_s}{l_4} & -\frac{w_5 T_s}{l_4} \end{bmatrix}, \\
B_{Q,2} &= 0_{4 \times 4}.
\end{aligned} \tag{4.26}$$

It can be seen that the B_Q and B_J matrices for the modes remain unchanged and will be omitted hereafter. The split-ratio-dependent CF mode is

$$\begin{aligned}
A_3(k) &= \begin{bmatrix} 1 - \frac{w_1 T_s}{l_1} & \frac{w_2 T_s}{l_1} & 0 & 0 \\ 0 & 1 - \frac{w_2 T_s}{l_2} & 0 & 0 \\ 0 & 0 & 1 - \frac{v_3 T_s}{l_3} & 0 \\ 0 & 0 & (1 - \beta(k)) \frac{v_3 T_s}{l_4} & 1 - \frac{v_4 T_s}{l_4} \end{bmatrix} = \begin{bmatrix} a_{311} & a_{312} & 0 & 0 \\ 0 & a_{322} & 0 & 0 \\ 0 & 0 & a_{333} & 0 \\ 0 & 0 & a_{343}(k) & a_{344} \end{bmatrix}, \\
B_3 &= \begin{bmatrix} 0 & \frac{T_s}{l_1} & 0 & 0 \\ 0 & 0 & 0 & 0 \\ 0 & 0 & 0 & 0 \\ 0 & 0 & 0 & 0 \end{bmatrix}.
\end{aligned} \tag{4.27}$$

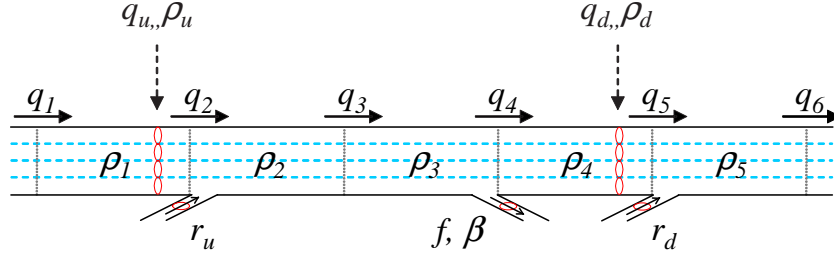


Figure 4.9: Highway segment used for observability and controllability analysis.

The split-ratio-dependent FC1 mode is

$$A_4 = \begin{bmatrix} 1 - \frac{v_1 T_s}{l_1} & 0 & 0 & 0 \\ \frac{v_1 T_s}{l_2} & 1 - \frac{v_2 T_s}{l_2} & 0 & 0 \\ 0 & \frac{v_2 T_s}{l_3} & 1 & \frac{1}{1-\beta(k)} \frac{w_4 T_s}{l_3} \\ 0 & 0 & 0 & 1 - \frac{w_4 T_s}{l_4} \end{bmatrix} = \begin{bmatrix} a_{411} & 0 & 0 & 0 \\ a_{421} & a_{422} & 0 & 0 \\ 0 & a_{432} & a_{433} & a_{434}(k) \\ 0 & 0 & 0 & a_{444} \end{bmatrix},$$

$$B_4 = \begin{bmatrix} \frac{T_s}{l_1} & 0 & 0 & 0 \\ 0 & \frac{T_s}{l_2} & 0 & 0 \\ 0 & 0 & 0 & 0 \\ 0 & 0 & 0 & \frac{w_5 T_s}{l_4} \end{bmatrix}.$$

(4.28)

The split-ratio-dependent FC2 mode is

$$A_5 = \begin{bmatrix} 1 - \frac{v_1 T_s}{l_1} & 0 & 0 & 0 \\ \frac{v_1 T_s}{l_2} & 1 & \frac{w_3 T_s}{l_2} & 0 \\ 0 & 0 & 1 - \frac{w_3 T_s}{l_3} & \frac{1}{1-\beta(k)} \frac{w_4 T_s}{l_3} \\ 0 & 0 & 0 & 1 - \frac{w_4 T_s}{l_4} \end{bmatrix} = \begin{bmatrix} a_{511} & 0 & 0 & 0 \\ a_{521} & a_{522} & a_{523} & 0 \\ 0 & 0 & a_{533} & a_{534}(k) \\ 0 & 0 & 0 & a_{544} \end{bmatrix},$$

$$B_5 = B_4.$$

(4.29)

Observability and controllability analysis will be performed on the $A_s(k)$ considering several scenarios for the sensors and control inputs. The possible sensor and on-ramp locations are shown in the freeway segment in Figure 4.9. If the downstream on-ramp is active, this induces changes in the B -matrices of the SMM for modes where the downstream end of the segment is congested. These will be discussed in the section on controllability.

For reference, from [18],

1. A discrete-time, time-varying system $x(k+1) = A(k)x(k) + B(k)u(k)$, $y(k) = C(k)x(k)$ is *observable* at $k=0$ iff there exists a finite $k_1 > 0$ such that the observability Gramian

$$V(0, k_1) = \sum_{k=0}^{k_1} \Phi_1^T(k, 0) C^T(k) C(k) \Phi_1(k, 0)$$

has nonzero determinant.

2. A discrete-time, time-varying system $x(k+1) = A(k)x(k) + B(k)u(k)$ is *controllable* at $k=0$ iff there exists a finite $k_1 > 0$ such that the controllability Grammian

$$W(0, k_1) = \sum_{k=0}^{k_1} \Phi_1(k_1, k) B(k) B^T(k) \Phi_1^T(k_1, k)$$

has nonzero determinant.

Here, $\Phi_1(k, k_0) = A(k-1)A(k-2) \cdots A(k_0) = \prod_{j=0}^{k-1} A(j)$ is the transition matrix.

4.3.1 General Results on Observability

Table 4.1 summarizes the observability for each SMM mode. The observability results can be derived using standard linear systems techniques, as shown later in this section. On the left side, “upstream cells” and “downstream cells” give the status of cells both upstream and downstream of the congestion wave front. If there is no such wave front, both sets of cells have the same status. The right side indicates which of the two mainline boundary measurements, if either, can be used to make the SMM observable. To relate the measurements to the model variables, in Figure 4.9, it is assumed that ρ_u is a measurement of ρ_1 and ρ_d is a measurement of ρ_4 . These results can be obtained by computing the observability matrices for the $A_s(k)$ with the output matrices $C_u = [1 \ 0 \ 0 \ 0]$ and $C_d = [0 \ 0 \ 0 \ 1]$. For example, for the FF mode, it can be shown that $(A_1(k), C_u)$ is not observable, whereas $(A_1(k), C_d)$ is.

Observability Analysis of FF mode: To evaluate $V(0, k_1)$ for $(A_1(k), C_u)$, we must compute $C_u \Phi_1(k, 0)$ for $k \in \{0 \dots k_1\}$. It can be shown that $C_u \Phi_1(k, 0) = [a_{111}^k \ 0 \ 0 \ 0]$ for all $k \geq 0$ as follows:

- For $k=0$, $C_u \Phi_1(0, 0) = C_u I_4 = [a_{111}^0 \ 0 \ 0 \ 0]$.
- Assume $C_u \Phi_1(j, 0) = [a_{111}^j \ 0 \ 0 \ 0]$ for $j \in \{1 \dots k-1\}$.
- Then

$$\begin{aligned} C_u \Phi_1(k, 0) &= C_u A_1(k-1) A_1(k-2) \cdots A_1(0) \\ &= C_u A_1(k-1) \Phi_1(k-1, 0) \\ &= C_u \begin{bmatrix} a_{111} & 0 & 0 & 0 \\ \dots & \dots & \dots & \dots \\ \dots & \dots & \dots & \dots \\ \dots & \dots & \dots & \dots \end{bmatrix} \begin{bmatrix} a_{111}^{k-1} & 0 & 0 & 0 \\ \dots & \dots & \dots & \dots \\ \dots & \dots & \dots & \dots \\ \dots & \dots & \dots & \dots \end{bmatrix} \\ &= C_u \begin{bmatrix} a_{111}^k & 0 & 0 & 0 \\ \dots & \dots & \dots & \dots \\ \dots & \dots & \dots & \dots \\ \dots & \dots & \dots & \dots \end{bmatrix} \\ &= [a_{111}^k \ 0 \ 0 \ 0], \end{aligned} \tag{4.30}$$

Hence,

$$\begin{aligned}
V(0, k_1) &= \sum_{k=0}^{k_1} \Phi_1^T(k, 0) C_u^T C_u \Phi_1(k, 0) \\
&= \sum_{k=0}^{k_1} \begin{bmatrix} a_{111}^k \\ 0 \\ 0 \\ 0 \end{bmatrix} [a_{111}^k \quad 0 \quad 0 \quad 0] \\
&= \begin{bmatrix} \sum_{k=0}^{k_1} a_{111}^{2k} & 0 & 0 & 0 \\ 0 & 0 & 0 & 0 \\ 0 & 0 & 0 & 0 \\ 0 & 0 & 0 & 0 \end{bmatrix}, \tag{4.31}
\end{aligned}$$

which has rank ≤ 1 for all $k_1 \geq 0$. Thus $(A_1(k), C_u)$ is not observable at $k = 0$ for any $k_1 \geq 0$, i.e., the FF mode is not observable from an upstream measurement.

For the downstream measurement, the observability of $(A_1(k), C_d)$, is assessed by computing $V(0, 3)$. Note that

$$\begin{aligned}
V(0, 3) &= C_d^T C_d + \Phi_1^T(1, 0) C_d^T C_d \Phi_1(1, 0) \cdots + \Phi_1^T(3, 0) C_d^T C_d \Phi_1(3, 0) \\
&= P_o^T(0, 3) P_o(0, 3),
\end{aligned}$$

where

$$P_o(0, 3) = \begin{bmatrix} C_d \\ C_d \Phi_1(1, 0) \\ C_d \Phi_1(2, 0) \\ C_d \Phi_1(3, 0) \end{bmatrix} = \begin{bmatrix} 0 & 0 & 0 & 1 \\ 0 & 0 & a_{143}(0) & \cdots \\ 0 & a_{143}(1) a_{132} & \cdots & \cdots \\ a_{143}(2) a_{132} a_{121} & \cdots & \cdots & \cdots \end{bmatrix}.$$

Note that $\det(V(0, 3)) = \det(P_o^T(0, 3) P_o(0, 3)) = \det(P_o(0, 3))^2$, thus $\det(P_o(0, 3)) \neq 0 \Leftrightarrow \det(V(0, 3)) \neq 0$. Furthermore,

$$\det(P_o(0, 3)) = (-1)^2 a_{143}(0) a_{143}(1) a_{143}(2) a_{132}^2 a_{121}$$

Since it is assumed, in general, that $T_s > 0$ and $l_i > 0$, sufficient conditions for observability of $(A_1(k), C_d)$ are $v_i \neq 0$ for $i \in \{1, 2, 3\}$ and $\beta(k) \neq 1$ for $k \in \{0, 1, 2\}$.

Observability Analysis of CC mode: For the upstream measurement, the observability of $(A_1(k), C_u)$, is assessed by computing $V(0, 3)$. Note that

$$\begin{aligned}
V(0, 3) &= C_u^T C_u + \Phi_2^T(1, 0) C_u^T C_u \Phi_2(1, 0) \cdots + \Phi_2^T(3, 0) C_u^T C_u \Phi_2(3, 0) \\
&= P_o^T(0, 3) P_o(0, 3),
\end{aligned}$$

where

$$P_o(0, 3) = \begin{bmatrix} C_u \\ C_u \Phi_2(1, 0) \\ C_u \Phi_2(2, 0) \\ C_u \Phi_2(3, 0) \end{bmatrix} = \begin{bmatrix} 1 & 0 & 0 & 0 \\ \cdot & a_{212} & 0 & 0 \\ \cdots & \cdots & a_{212} a_{223} & 0 \\ \cdots & \cdots & \cdots & a_{212} a_{223} a_{234}(0) \end{bmatrix}.$$

Since P_o is upper triangular,

$$\det(P_o(0, 3)) = a_{212}^3 a_{223}^2 a_{234}(0)$$

Since $T_s > 0$ and $l_i > 0$, sufficient conditions for observability of $(A_2(k), C_u)$ are $w_i \neq 0$ for $i \in \{2, 3, 4\}$.

To evaluate $V(0, k_1)$ for $(A_2(k), C_d)$, we must compute $C_d \Phi_2(k, 0)$ for $k \in \{0 \dots k_1\}$. It can be shown that $C_d \Phi_2(k, 0) = [0 \ 0 \ 0 \ a_{244}^k]$ for all $k \geq 0$ as follows:

- For $k = 0$, $C_d \Phi_2(0, 0) = C_d I_4 = [0 \ 0 \ 0 \ a_{244}^0]$.
- Assume $C_d \Phi_2(j, 0) = [0 \ 0 \ 0 \ a_{244}^j]$ for $j \in \{1 \dots k - 1\}$.
- Then

$$\begin{aligned} C_d \Phi_2(k, 0) &= C_d A_2(k-1) A_2(k-2) \cdots A_2(0) \\ &= C_d A_2(k-1) \Phi_2(k-1, 0) \\ &= C_d \begin{bmatrix} \cdots \\ \cdots \\ \cdots \\ 0 \ 0 \ 0 \ a_{244} \end{bmatrix} \begin{bmatrix} \cdots \\ \cdots \\ \cdots \\ 0 \ 0 \ 0 \ a_{244}^{k-1} \end{bmatrix} \\ &= C_d \begin{bmatrix} \cdots \\ \cdots \\ \cdots \\ 0 \ 0 \ 0 \ a_{244}^k \end{bmatrix} \\ &= [0 \ 0 \ 0 \ a_{244}^k]. \end{aligned} \tag{4.32}$$

Hence,

$$\begin{aligned} V(0, k_1) &= \sum_{k=0}^{k_1} \Phi_2^T(k, 0) C_d^T C_d \Phi_2(k, 0) \\ &= \sum_{k=0}^{k_1} \begin{bmatrix} 0 \\ 0 \\ 0 \\ a_{244}^k \end{bmatrix} [0 \ 0 \ 0 \ a_{244}^k] \\ &= \begin{bmatrix} 0 & 0 & 0 & 0 \\ 0 & 0 & 0 & 0 \\ 0 & 0 & 0 & 0 \\ 0 & 0 & 0 & \sum_{k=0}^{k_1} a_{244}^{2k} \end{bmatrix}, \end{aligned} \tag{4.33}$$

which has rank ≤ 1 for all $k_1 \geq 0$. Thus $(A_2(k), C_d)$ is not observable at $k = 0$ for any $k_1 \geq 0$, i.e., the CC mode is not observable from a downstream measurement.

Observability Analysis of CF mode: According to the foregoing results, cells in FF mode are observable from a downstream measurement, whereas cells in CC mode are observable from an upstream measurement. Consequently, if the segment in Figure 4.9 is in CF mode, with cells 1 and

2 congested and cells 3 and 4 uncongested, it is expected that the densities in the two upstream cells could be reconstructed using the upstream density measurement, while the downstream densities could be reconstructed from the downstream measurement. In fact, it can be shown that the CF mode is observable if both the upstream and downstream measurement are available.

$V(0, 3)$ will be computed for $(A_3(k), C)$, where $C = [C_u^T \ C_d^T]^T$:

$$\begin{aligned} V(0, 3) &= C^T C + \Phi_3^T(1, 0) C^T C \Phi_3(1, 0) \cdots + \Phi_3^T(3, 0) C^T C \Phi_3(3, 0) \\ &= P_o^T(0, 3) P_o(0, 3), \end{aligned}$$

where

$$P_o(0, 3) = \begin{bmatrix} C \\ C\Phi_1(1, 0) \\ C\Phi_1(2, 0) \\ C\Phi_1(3, 0) \end{bmatrix} = \begin{bmatrix} 1 & 0 & 0 & 0 \\ 0 & 0 & 0 & 1 \\ a_{311} & a_{312} & 0 & 0 \\ 0 & 0 & a_{343}(0) & a_{344} \\ a_{311}^2 & a_{312}(a_{311} + a_{322}) & 0 & 0 \\ 0 & 0 & a_{343}(1)a_{333} + a_{344}a_{343}(0) & a_{344}^2 \\ a_{311}^3 & a_{312}(a_{311}^2 + a_{322}(a_{311} + a_{322})) & 0 & 0 \\ 0 & 0 & (a_{343}(2)a_{333} + a_{344}a_{343}(1))a_{333} & a_{344}^3 \\ & & + a_{344}^2 a_{343}(0) & \end{bmatrix}.$$

Sufficient conditions for $P_o(0, 3)$ to have rank 4 are $a_{312} \neq 0$ and $a_{343}(0) \neq 0$, i.e., $w_2 \neq 0$, $v_3 \neq 0$, and $\beta(0) \neq 1$. Under these conditions, $\text{nullity}(P_o(0, 3)) = \dim(\mathbb{R}^4) - \text{rank}(P_o(0, 3)) = 4 - 4 = 0 \Rightarrow \|P_o(0, 3)x\|_2^2 = x^T P_o^T(0, 3) P_o(0, 3)x \neq 0 \Leftrightarrow x \in \mathbb{R}^4 \neq 0 \Rightarrow V(0, 3) = P_o^T(0, 3) P_o(0, 3) > 0 \Rightarrow V(0, 3)$ is nonsingular, hence $(A_3(k), C)$ is observable.

Observability Analysis of FC modes: It can be shown that the FC1 and FC2 modes are not observable from either the upstream or the downstream measurement. Since the first row of $A_s(k)$ is $[a_{s11} \ 0 \ 0 \ 0]$ for all $k \geq 0$ and $s \in \{4, 5\}$, it follows from the result of (4.30) that $C_u \Phi_s(k, 0) = [a_{s11}^k \ 0 \ 0 \ 0]$ for $s \in \{4, 5\}$. By (4.31), the FC1 and FC2 modes are not observable from an upstream measurement. Similarly, from (4.32), since the last row of $A_s(k)$ is $[0 \ 0 \ 0 \ a_{s44}]$ for all $k \geq 0$ and $s \in \{4, 5\}$, it can be seen that $C_d \Phi_s(k, 0) = [0 \ 0 \ 0 \ a_{s44}^k]$ for $s \in \{4, 5\}$. Hence, by (4.33), the FC1 and FC2 modes are not observable a downstream measurement.

Summary: From the table, it can be seen, as a general result, that if all cells have free-flow status, the densities are observable using a downstream measurement, while in congested mode, they are observable using an upstream measurement. If there is no downstream measurement available when cells are in free-flow mode, or there is no upstream measurement when cells are congested, as in the last two cases listed in Table 4.1, the system is unobservable. This is related to the wave (information) propagation directions on a highway in different congestion modes. When a highway section is in free-flow mode, the information propagates downstream at speed v , which is the vehicle traveling speed. Therefore, in order to be able to estimate the cell densities, the downstream density measurement is needed. When the highway is in congestion, the information propagates upstream at speed w , which is the backward congestion wave traveling speed, and an upstream measurement is needed to estimate densities.

Upstream Cells	Downstream Cells	Observable with
Free-flow	Free-flow	Downstream Measurement
Congested	Congested	Upstream Measurement
Congested	Free-flow	Upstream and Downstream Measurement
Free-flow	Congested 1	Unobservable
Free-flow	Congested 2	Unobservable

Table 4.1: Observability for different SMM modes.

4.3.2 General Results on Controllability

Two scenarios will be considered, as shown in Figure 4.9. In the first, the on-ramp located at the upstream end of the segment is the control input (r_u); in the second, the on-ramp located at the downstream end of the segment is the control input (r_d). Unlike the output (C) matrices, the input (B) matrices are dependent upon the mode of the SMM, as discussed subsequently.

Controllability Analysis of FF mode: For the FF mode, the on-ramp dependent column of the B_1 matrix becomes $B_{1,r,u} = [\frac{T_s}{l_1} \ 0 \ 0 \ 0]^T$ if the on-ramp enters cell 1 and $B_{1,r,d} = [0 \ 0 \ 0 \ 0]^T$ if the on-ramp enters cell 5. To check the controllability from the upstream on-ramp, $W(0, 3)$ is evaluated for $(A_1(k), B_{1,r,u})$. Note that

$$\begin{aligned} W(0, 3) &= \Phi_1(3, 0)B_{1,r,u}B_{1,r,u}^T\Phi_1^T(3, 0) + \Phi_1(3, 1)B_{1,r,u}B_{1,r,u}^T\Phi_1^T(3, 1) \cdots + B_{1,r,u}B_{1,r,u}^T \\ &= P_c(0, 3)P_c^T(0, 3), \end{aligned}$$

where

$$\begin{aligned} P_c(0, 3) &= [B_{1,r,u} \quad \Phi_1(3, 2)B_{1,r,u} \quad \Phi_1(3, 1)B_{1,r,u} \quad \Phi_1(3, 0)B_{1,r,u}] \\ &= \frac{T_s}{l_1} \begin{bmatrix} 1 & \dots & \dots & \dots \\ 0 & a_{121} & \dots & \dots \\ 0 & 0 & a_{132}a_{121} & \dots \\ 0 & 0 & 0 & a_{143}(2)a_{132}a_{121} \end{bmatrix}. \end{aligned}$$

Note that $\det(W(0, 3)) = \det(P_c(0, 3)P_c^T(0, 3)) = \det(P_c(0, 3))^2$, thus $\det(P_c(0, 3)) \neq 0 \Leftrightarrow \det(W(0, 3)) \neq 0$. Furthermore,

$$\det(P_c(0, 3)) = a_{143}(2)a_{132}^2a_{121}^3.$$

Since $T_s > 0$ and $l_i > 0$, sufficient conditions for controllability of $(A_1(k), B_{1,r,u})$ are $v_i \neq 0$ for $i \in \{1, 2, 3\}$ and $\beta(2) \neq 1$.

It can be seen from the structure of $B_{1,r,d}$ that a downstream on-ramp does not affect the cells upstream of the merge point while the segment is in FF mode. Specifically, $B_{1,r,d} = [0 \ 0 \ 0 \ 0]^T$ means that $W(0, k_1) = \mathbf{0}_{4 \times 4}$ has rank 0 for any $k_1 \geq 0$, hence the segment is not controllable from the downstream on-ramp.

Controllability Analysis of CC mode: For the CC mode, the on-ramp dependent column of the B_2 matrix becomes $B_{2,r,u} = [0 \ 0 \ 0 \ 0]^T$ if the on-ramp enters cell 1 and $B_{2,r,d} = [0 \ 0 \ 0 \ \frac{T_s}{l_4}]^T$ if the on-ramp enters cell 5.

It can be seen from the structure of $B_{2,r,u}$ that an upstream on-ramp does not affect the cells downstream of the merge point while the segment is in CC mode. Specifically, $B_{2,r,u} = [0 \ 0 \ 0 \ 0]^T$

means that $W(0, k_1) = \mathbf{0}_{4 \times 4}$ has rank 0 for any $k_1 \geq 0$, hence the segment is not controllable from the upstream on-ramp.

To check the controllability from the downstream on-ramp, $W(0, 3)$ is evaluated for $(A_2(k), B_{2,r,d})$. Note that

$$\begin{aligned} W(0, 3) &= \Phi_2(3, 0)B_{2,r,d}B_{2,r,d}^T\Phi_2^T(3, 0) + \Phi_2(3, 1)B_{2,r,d}B_{2,r,d}^T\Phi_2^T(3, 1) \cdots + B_{2,r,d}B_{2,r,d}^T \\ &= P_c(0, 3)P_c^T(0, 3), \end{aligned}$$

where

$$\begin{aligned} P_c(0, 3) &= [B_{2,r,d} \quad \Phi_2(3, 2)B_{2,r,d} \quad \Phi_2(3, 1)B_{2,r,d} \quad \Phi_2(3, 0)B_{2,r,d}] \\ &= \frac{T_s}{l_4} \begin{bmatrix} 0 & 0 & 0 & a_{212}a_{223}a_{234}(0) \\ 0 & 0 & a_{223}a_{234}(1) & \dots \\ 0 & a_{234}(2) & \dots & \dots \\ 1 & \dots & \dots & \dots \end{bmatrix}. \end{aligned}$$

Hence,

$$\det(P_c(0, 3)) = (-1)^2 a_{234}(2) a_{234}(1) a_{234}(0) a_{223}^2 a_{212}.$$

Since $T_s > 0$ and $l_i > 0$, sufficient conditions for controllability of $(A_2(k), B_{2,r,d})$ are $w_i \neq 0$ for $i \in \{2, 3, 4\}$.

Controllability Analysis of CF mode: For the CF mode, the on-ramp dependent column of the B_3 matrix becomes $B_{3,r,u} = [0 \ 0 \ 0 \ 0]^T$ if the on-ramp enters cell 1 and $B_{3,r,d} = [0 \ 0 \ 0 \ 0]^T$ if the on-ramp enters cell 5. Thus, for either $B_{3,r,u}$ or $B_{3,r,d}$, $W(0, k_1) = \mathbf{0}_{4 \times 4}$ has rank 0 for any $k_1 \geq 0$, hence the segment is not controllable from either an upstream or a downstream on-ramp.

Controllability Analysis of FC modes: The FC1 and FC2 modes can be shown to be controllable if both an upstream and downstream on-ramp are present, as shown in Figure 4.9. For this configuration,

$$B_{s,r} = \begin{bmatrix} \frac{T_s}{l_1} & 0 \\ 0 & 0 \\ 0 & 0 \\ 0 & \frac{T_s}{l_4} \end{bmatrix}$$

for $s \in \{4, 5\}$. $A_4(k)$ and $A_5(k)$ can collectively be written as

$$A_s(k) = \begin{bmatrix} a_{s11} & 0 & 0 & 0 \\ a_{s21} & a_{s22} & a_{s23} & 0 \\ 0 & a_{s32} & a_{s33} & a_{s34}(k) \\ 0 & 0 & 0 & a_{s44} \end{bmatrix}.$$

The values for a_{s22} , a_{s23} , a_{s32} , and a_{s33} differ depending on the value of $s \in \{4, 5\}$.

To check the controllability from the upstream and downstream on-ramps, $W(0, 3)$ is evaluated for $(A_s(k), B_{s,r})$. Note that

$$\begin{aligned} W(0, 3) &= \Phi_s(3, 0)B_{s,r}B_{s,r}^T\Phi_s^T(3, 0) + \Phi_s(3, 1)B_{s,r}B_{s,r}^T\Phi_s^T(3, 1) \cdots + B_{s,r}B_{s,r}^T \\ &= P_c(0, 3)P_c^T(0, 3), \end{aligned}$$

Upstream Cells	Downstream Cells	Controllable from
Free-flow	Free-flow	Upstream On-Ramp
Congested	Congested	Downstream On-Ramp
Congested	Free-flow	Not Controllable
Free-flow	Congested 1	Upstream and Downstream On-Ramp
Free-flow	Congested 2	Upstream and Downstream On-Ramp

Table 4.2: Controllability for different SMM modes.

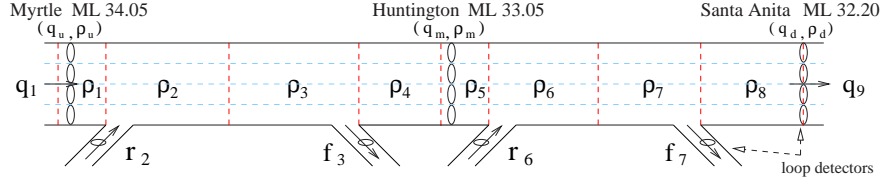


Figure 4.10: A segment of I-210W divided into cells.

where

$$P_c(0, 3) = [B_{s,r} \quad \Phi_s(3, 2)B_{s,r} \quad \Phi_s(3, 1)B_{s,r} \quad \Phi_s(3, 0)B_{s,r}]$$

$$= \begin{bmatrix} \frac{T_s}{l_1} & 0 & 0 & 0 & 0 \\ 0 & 0 & 0 & 0 & \frac{T_s}{l_4} \\ a_{s11} \frac{T_s}{l_1} & a_{s21} \frac{T_s}{l_1} & 0 & 0 & 0 \\ 0 & 0 & 0 & a_{s34} (2) \frac{T_s}{l_4} & a_{s44} \frac{T_s}{l_4} \\ a_{s11}^2 \frac{T_s}{l_1} & a_{s21} (a_{s11} + a_{s22}) \frac{T_s}{l_1} & 0 & a_{s32} a_{s21} \frac{T_s}{l_1} & 0 \\ 0 & a_{s23} a_{s34} (1) \frac{T_s}{l_4} & 0 & (a_{s33} a_{s34} (1) + a_{s34} (2) a_{s44}) \frac{T_s}{l_4} & a_{s44}^2 \frac{T_s}{l_4} \\ a_{s11}^3 \frac{T_s}{l_1} & a_{s21} (a_{s11}^2 + a_{s22}) & 0 & a_{s32} a_{s21} (a_{s11} + a_{s22} + a_{s33}) \frac{T_s}{l_1} & 0 \\ 0 & (a_{s11} + a_{s22}) + a_{s23} a_{s32}) \frac{T_s}{l_1} & 0 & + a_{s22} + a_{s33}) \frac{T_s}{l_1} & 0 \\ 0 & a_{s23} (a_{s22} a_{s34} (0) + a_{s33} (a_{s33} a_{s34} (0) + a_{s34} (1) a_{s44})) \frac{T_s}{l_4} & (a_{s32} a_{s23} a_{s34} (0) + a_{s33} (a_{s33} a_{s34} (0) + a_{s34} (1) a_{s44})) \frac{T_s}{l_4} & a_{s34} (1) a_{s44} + a_{s34} (2) a_{s44}^2 \frac{T_s}{l_4} & a_{s44}^3 \frac{T_s}{l_4} \end{bmatrix}^T$$

Sufficient conditions for $P_c(0, 3)$ to have rank 4 are $a_{s21} \neq 0$ and $a_{s34} (2) \neq 0$, i.e., $v_1 \neq 0$ and $w_4 \neq 0$. Under these conditions, $\text{nullity}(P_c^T(0, 3)) = \dim(\mathbb{R}^4) - \text{rank}(P_c^T(0, 3)) = 4 - 4 = 0 \Rightarrow \|P_c^T(0, 3)x\|_2^2 = x^T P_c(0, 3) P_c^T(0, 3)x \neq 0 \Leftrightarrow x \in \mathbb{R}^4 \neq 0 \Rightarrow W(0, 3) = P_c(0, 3) P_c^T(0, 3) > 0 \Rightarrow W(0, 3)$ is nonsingular, hence $(A_s(k), B_{s,r})$ is controllable.

Summary: Controllability results are summarized in Table 4.2. Generally, a section in free-flow mode is controllable from an on-ramp at its upstream end, whereas a congested section can be controlled from an on-ramp at its downstream end. If a section is in CF mode, it cannot be controlled by an on-ramp at either end of the section, while the FC modes are controllable from an upstream/downstream on-ramp pair.

4.4 Density Estimation Results

Figure 4.10 is a schematic diagram of the freeway section used to test both the modified cell transmission model and switching-mode model. It is a subsection of I-210 West, approximately 2 miles (3 km) in length, with four mainline lanes, three mainline loop detector stations labeled Myrtle (ML 34.05), Huntington (ML 33.05), Santa Anita (ML 32.20), and additional detector

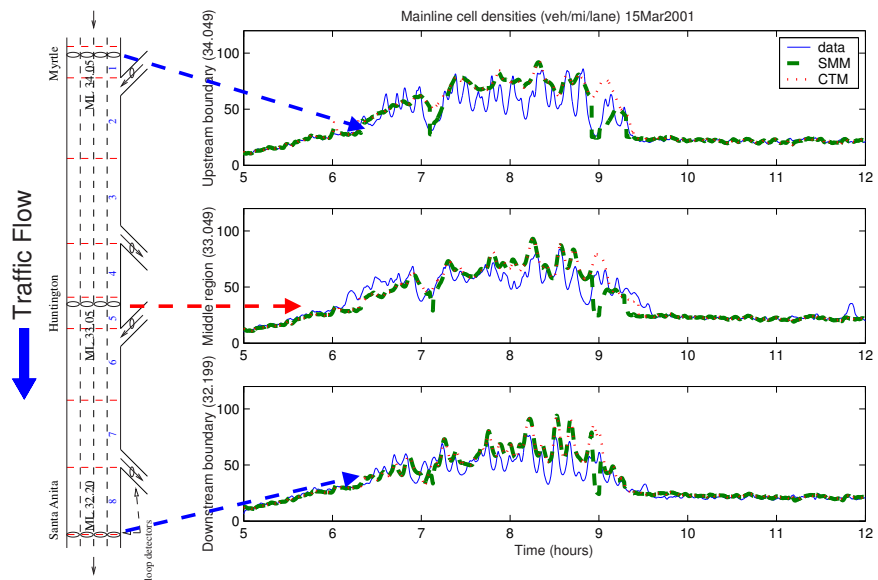


Figure 4.11: Measured and simulated mainline densities for a segment of I-210W on March 15, 2001

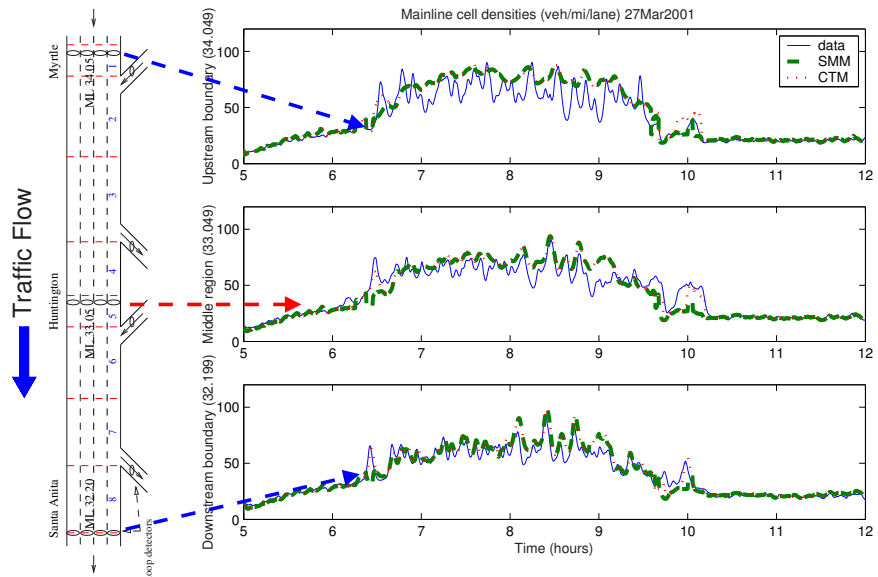


Figure 4.12: Measured and simulated mainline densities for a segment of I-210W on March 27, 2001.

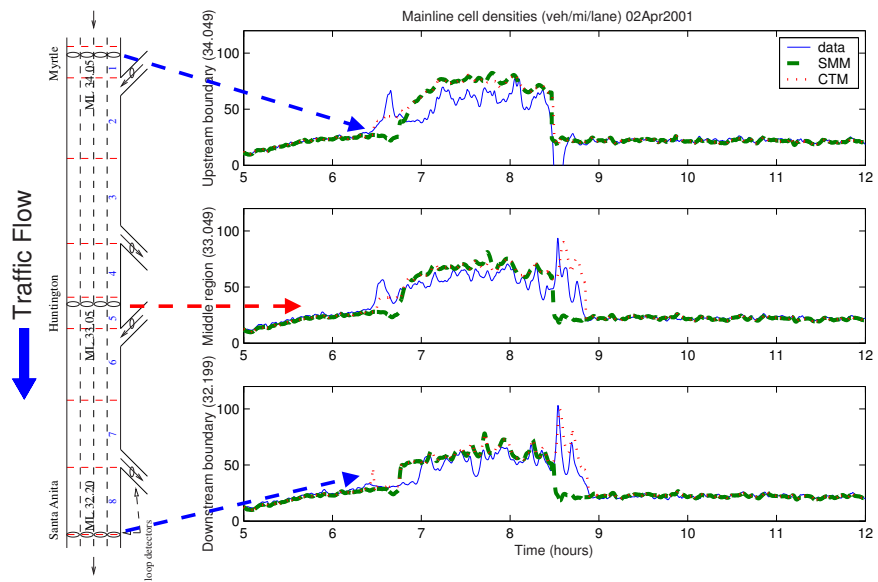


Figure 4.13: Measured and simulated mainline densities for a segment of I-210W on April 02, 2001.

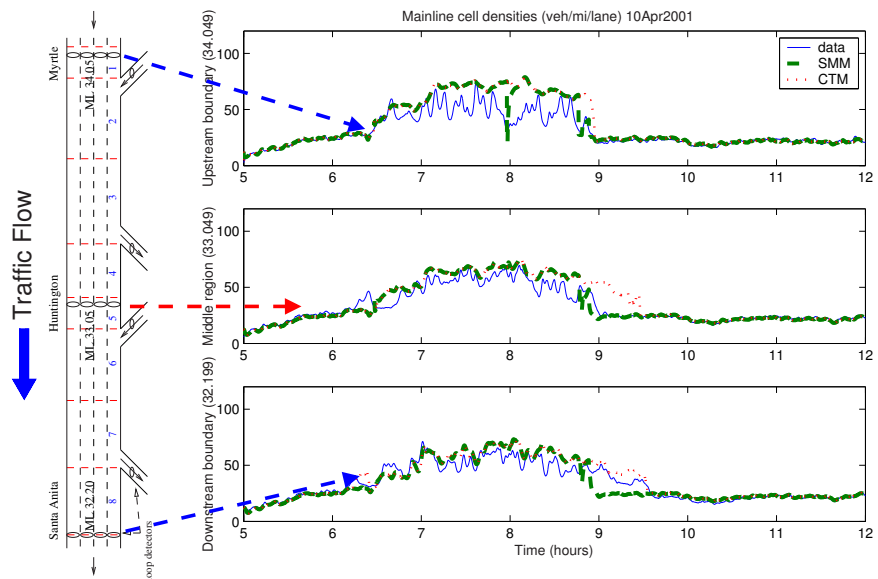


Figure 4.14: Measured and simulated mainline densities for a segment of I-210W on April 10, 2001.

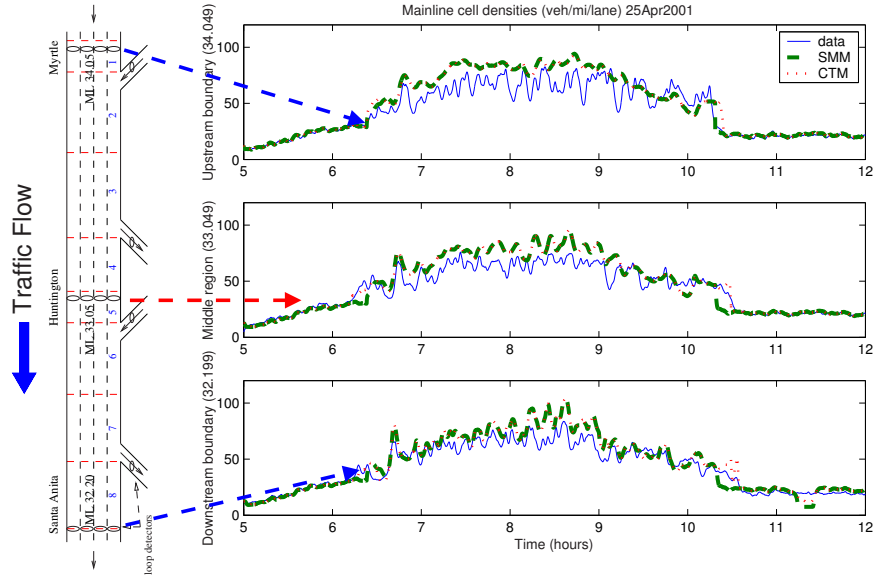


Figure 4.15: Measured and simulated mainline densities for a segment of I-210W on April 25, 2001.

stations on each ramp. ML stands for “mainline”, and the numbers, e.g. 34.05, are the absolute postmile indices of the detector stations (postmiles are a measurement of distance, in miles, along the highway). Figure 4.10 shows the mainline segment partitioned into eight cells. The on-ramp flow into cell i is r_i , and f_j is the off-ramp flow exiting cell j . The mainline cell lengths chosen for the segment were $[0.088 \ 0.375 \ 0.375 \ 0.192 \ 0.088 \ 0.276 \ 0.276 \ 0.246]$ mi.

Several assumptions are made in order to relate the measured quantities ($q_u, \rho_u, q_m, \rho_m, q_d, \rho_d$, and flows measured at each on- and off-ramp) to flows and densities used by the model: (1) ρ_u is a measurement of the density in the first cell, ρ_1 ; (2) similarly, ρ_d is a measurement of the density in the last cell, ρ_8 ; (3) the middle density ρ_m is a measurement of ρ_5 , since the middle ML station (Huntington) lies within cell 5; (4) r_i (or f_j) is equal to the measured on-ramp (or off-ramp) flow at the corresponding on-ramp (or off-ramp) station.

The loop detector data used in this study was obtained from the Performance Measurement System (PeMS) [19]. Each loop detector provides measurements of volume (veh/timestep) and percent occupancy every 30 sec. In the case of the ML detectors, densities (veh/mi) can be computed for each lane using $density = \frac{occupancy}{g\text{-factor}}$, where the g -factor is the effective vehicle length, in miles, for that detector. For single loop-detector freeways such as I-210, PeMS provides g -factors calculated according to the PeMS algorithm, described in [20].

As explained in [12], for a general fundamental diagram shape, a necessary condition for convergence of the CTM solution to the LWR solution is that vehicles traveling at the maximum speed may not cross multiple cells in one time step, that is, $vT_s \leq l_i, i = 1, 2, \dots, N$. This, combined with the aforementioned cell lengths prohibits a simulation time step as large as 30 seconds, thus a zeroth-order interpolation was applied to the PeMS data to yield data with $T_s = 5$ sec. To counteract noise in the PeMS 30-sec data, a 1st-order Butterworth lowpass filter with cutoff frequency $.01T_s^{-1}$ Hz was applied to the data using a zero-phase forward-and-reverse filtering technique. One difficulty in selecting a test section is that it is rare for all the loop detectors in a section to

be functioning properly at the same time. In the cases where detectors were not functional, the data was corrected using information from neighboring sensors. The ML detector bank at Myrtle was known to have a bad loop in Lane 2, and only 1 out of 2 of the loops on the Santa Anita off-ramp was functional. Scaling corrections were applied to the data from these detector banks as a means of compensating for the lost measurements. Thus, the aggregate flow and density at Myrtle were multiplied by 4/3 to account for the missing loop 2 data, and the Santa Anita off-ramp flow was multiplied by a factor of 2. The interpolated, filtered, and corrected data sets were used as simulation inputs.

Several of the cell parameters used in these simulations ($v = 63$ mph, $Q_M = 8000$ veh/hr, $\rho_J = 688$ veh/mi) were estimated through a hand-tuning procedure, wherein Eq. (4.2) was evaluated over the 5AM–12PM time range using measured mainline densities in place of cell densities, with nominal values for v , w , and ρ_J . v , Q_M and ρ_J were subsequently adjusted to improve the agreement between the empirical evaluation of Eq. (4.2) and the measured mainline flows. $w = 14.26$ mph and $\rho_c = 127$ veh/mi were then computed as functions of the estimated v , Q_M , and ρ_J , assuming that all the parameters must satisfy the triangular fundamental diagram shape of Figure 4.4(a). Since a flow-density hysteresis loop was often observed in the empirical flow vs. density plots, an approximate flow hysteresis was induced in the models by reducing w from 14.26 mph to 12.5 mph at 9AM. Spatially uniform parameters are a reasonable assumption for this freeway segment, which contains no abrupt variations in geometry.

Both the switching model and modified CTM were simulated, in Matlab, for the section of Figure 4.10 using data collected from I-210 West for several weekdays, over the interval 5AM–12PM, during which the morning rush-hour congestion normally occurs. It was assumed that the upstream and downstream mainline data (q_u, ρ_u, q_d, ρ_d), as well as the ramp flow data, were known, whereas the middle density, ρ_m , was considered to be “missing”, hence in need of estimation. The purpose of the test was to determine whether the models could accurately reproduce ρ_m .

Figures 4.11–4.15 show each of the three measured densities compared with its corresponding simulated density, for the cells nearest the ML stations, for several mornings (3/15, 3/27, 4/02, 4/10, and 4/25/01, 5AM–12PM). In the top graph of each of the figures, the measured upstream density, ρ_u , is plotted along with the simulated cell 1 density, ρ_1 , for both the switching and modified cell transmission models. The cell 8 density, ρ_8 , is compared with ρ_d in the bottom plot. Note that the simulated ρ_1 and ρ_8 are not identical to the nearby measured densities; this discrepancy between the model outputs and the “known” measurements ρ_u and ρ_d can be eliminated using an appropriate closed-loop estimation scheme. In the middle graph, ρ_m is plotted against the cell 5 density $\rho_5 = \hat{\rho}_m$. All the densities displayed in Figures 4.11–4.15 were divided by the number of ML lanes.

Table 4.3 shows the mean-percentage error, defined as

$$E_{MPE} = \frac{1}{M} \sum_{k=1}^M \left| \frac{\rho_m(k) - \hat{\rho}_m(k)}{\rho_m(k)} \right|,$$

of each of the estimates for five different days in 2001. The mean error over the five days is approximately 13%. The results indicate that both the SMM and modified CTM provide a good estimate of ρ_m . As seen in Figures 4.11–4.15 and Table 4.3, the performance of the two models is quite similar.

Date	MCTM	SMM
Mar. 15, 2001	0.117	0.129
Mar. 27, 2001	0.108	0.129
Apr. 02, 2001	0.109	0.125
Apr. 10, 2001	0.165	0.111
Apr. 25, 2001	0.126	0.142
mean	0.125	0.127
std. dev.	0.023	0.011

Table 4.3: Mean percentage errors of ρ_5 estimates for several different days.

4.5 Conclusions

In this chapter, the SMM equations were re-stated for the case where the split ratio for each off-ramp in the freeway is known as a function of time and off-ramp index. The observability and controllability properties of the individual modes of the SMM were then determined using standard linear systems techniques. It was discovered that

- The free-flow mode is observable from a downstream measurement and controllable from an upstream on-ramp,
- The congested mode is observable from an upstream measurement and controllable from a downstream on-ramp,
- The mixed “Congestion–Free-flow” mode is observable if both an upstream and downstream measurement are available, and is not controllable from either an upstream or downstream on-ramp,
- The mixed “Free-flow–Congestion” modes are not observable from either an upstream or downstream measurement, and are controllable from an upstream/downstream on-ramp pair.

These results can be understood intuitively by noting that under free-flow conditions, information, in the form of density waves, will travel downstream along the freeway, whereas density waves travel upstream under congested conditions. Hence, whether the density in a region can be re-constructed from the measurements at a particular detector station or controlled from a particular on-ramp depends on the congestion status of the freeway segment. The aforementioned properties should be taken into account when designing estimators and controllers for traffic density.

Both the SMM and MCTM were simulated over a section of I-210 West, roughly 2 miles in length, in Southern California, using several days of loop detector data collected during the morning rush-hour period. The simulation results show that the SMM and MCTM produce density estimates that are both similar to one another and in good agreement with measured densities on I-210. The mean percentage error averaged over all the test days was approximately 13% for both models. Thus, the MCTM-derived switching-mode model can be used as a freeway traffic density estimator. It has been shown to be useful for analyzing the controllability and observability properties of freeway traffic, which are of fundamental importance in the design of data estimators and ramp-metering control systems.

A number of research efforts relying on the SMM or CT-derived models have been completed or are underway. For instance, a closed-loop, mixture-Kalman-filtering based congestion mode and density estimator has been designed by Xiaotian Sun and is documented in [16, 17]. It incorporates a piecewise-linear traffic model similar to the SMM. Additionally, a hybrid system model closely related to the SMM has been used by Gomes et al. to analyze the stability of local traffic responsive ramp metering controllers [21]. Ongoing related work includes the the development of a locally responsive ramp-metering regulator that is based upon the CTM.

Chapter 5

Calibration Methodology for the Cell Transmission Model

In this chapter, a methodology for tuning the MCTM parameters to reproduce observed freeway traffic behavior is described. The calibration method has been tested on a 14-mile stretch of Interstate 210 Westbound (I-210W) in Pasadena, California, which typically endures heavy congestion during the weekday morning commute period.

5.1 Simplified Merge and Diverge Laws

In this calibration study, simplified versions of the merge and diverge laws of (4.5)– (4.7) were used. In general, the actual on-ramp demands (flows entering the rear of the on-ramp queues) are not measured, but the flows at the "ON" detectors, which are located on the on-ramps just downstream of the meter heads, are recorded. That is, measurements of the metered flows that actually enter the freeway are available, but the demand flows are not. If it is desired to test metering control strategies on the MCTM, an on-ramp storage or queueing model must be included, and the on-ramp demands must be approximated from existing data. However, for calibration purposes, it is desired to test the response of the model to the measured inflows; thus, it is sensible to feed the measured metered flows directly into the freeway mainline, without passing the metered flow through an on-ramp queue, since the actual demands at the back of the queue are not measurable. In the MCTM, this can be accomplished by setting $S_c = r$ in Eqs. (4.5) and (4.6) and setting the merge coefficient $\gamma = 1$.

Additionally, in the I-210 testbed, from the available data there does not appear to be congestion on the off-ramps. In particular, none of the recurring bottlenecks appears to be caused by a backed-up off-ramp. Hence, another simplification is to model the off-ramps as having infinite capacity, which can be achieved by assuming R_c is infinite in Eq. (4.7).

The simplified merge and diverge laws are as follows:

Simplified Merge: A merge connection corresponds to the case where an on-ramp intervenes between two cells (e.g. between cells 1 and 2 in Fig. 5.1). Assume that $r_{m,i+1}(k)$ is the measured demand at on-ramp $i + 1$, and that $r_{i+1}(k)$ is the flow that actually enters the mainline from the on-ramp. We consider two cases, one where the downstream cell can accept both the supply flow from the upstream cell and the demand from the on-ramp, and one where the combined supply

flow and on-ramp demand exceed the maximum receiving flow.

$$q_{i+1} = \begin{cases} S_i, & \text{if } S_i + r_{m,i+1} \leq R_{i+1}, \\ \max(0, R_{i+1} - r_{m,i+1}), & \text{otherwise.} \end{cases} \quad (5.1)$$

In the latter case, i.e., when $S_i(k) + r_{m,i+1}(k) > R_{i+1}(k)$, we assume that the total flow entering the downstream cell is equal to $R_{i+1}(k)$, thus, in the event that $r_{m,i+1}(k)$ exceeds $R_{i+1}(k)$, a flow of $R_{i+1}(k)$ will be supplied by the on-ramp. In all other cases the on-ramp demand is given by $r_{i+1}(k) = r_{m,i+1}(k)$. That is,

$$r_{i+1} = \begin{cases} r_{m,i+1}, & \text{if } S_i + r_{m,i+1} \leq R_{i+1}, \\ R_{i+1} - q_{i+1}, & \text{otherwise.} \end{cases} \quad (5.2)$$

For clarity, the time index k has been suppressed in Eqs. (5.1) and (5.2).

Simplified Diverge: If the outflow from a cell is split between the downstream mainline region and an off-ramp, a diverge connection is warranted; an example is shown between cells 3 and 4 in Fig. 5.1. We assume that each off-ramp has unlimited capacity. Then the diverge law of Eq. (4.7) simplifies to

$$q_{i,out}(k) = \min \left(S_i(k), \frac{R_{i+1}(k)}{1-\beta_i(k)} \right), \quad (5.3)$$

where $q_{i,out}(k) = q_{i+1}(k) + f_i(k)$ is the total flow exiting cell i , and $f_i(k)$ is the off-ramp flow. The flow entering the downstream cell is then given by

$$q_{i+1}(k) = (1 - \beta_i(k))q_{i,out}(k), \quad (5.4)$$

and the flow exiting through the off-ramp is

$$f_i(k) = \beta_i(k)q_{i,out}(k), \quad (5.5)$$

where $\beta_i(k)$ is the *split ratio* for off-ramp i , i.e., the fraction of vehicles leaving cell i which exits through the off ramp during the k^{th} time interval.

5.2 Freeway Representation

The 14-mile I-210W test segment has been divided into 41 cells, as shown in Fig. 5.2. This partition was adapted from a 40-cell partition that was designed by Gabriel Gomes for use in

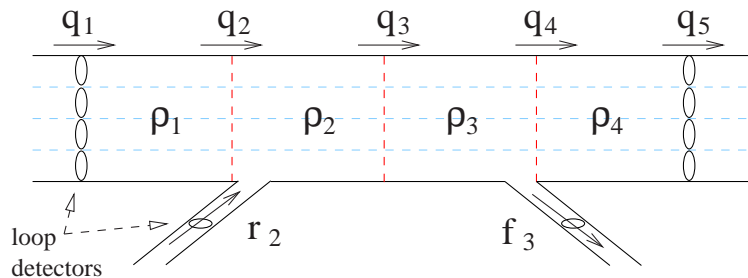


Figure 5.1: Highway segment partitioned into 4 cells.

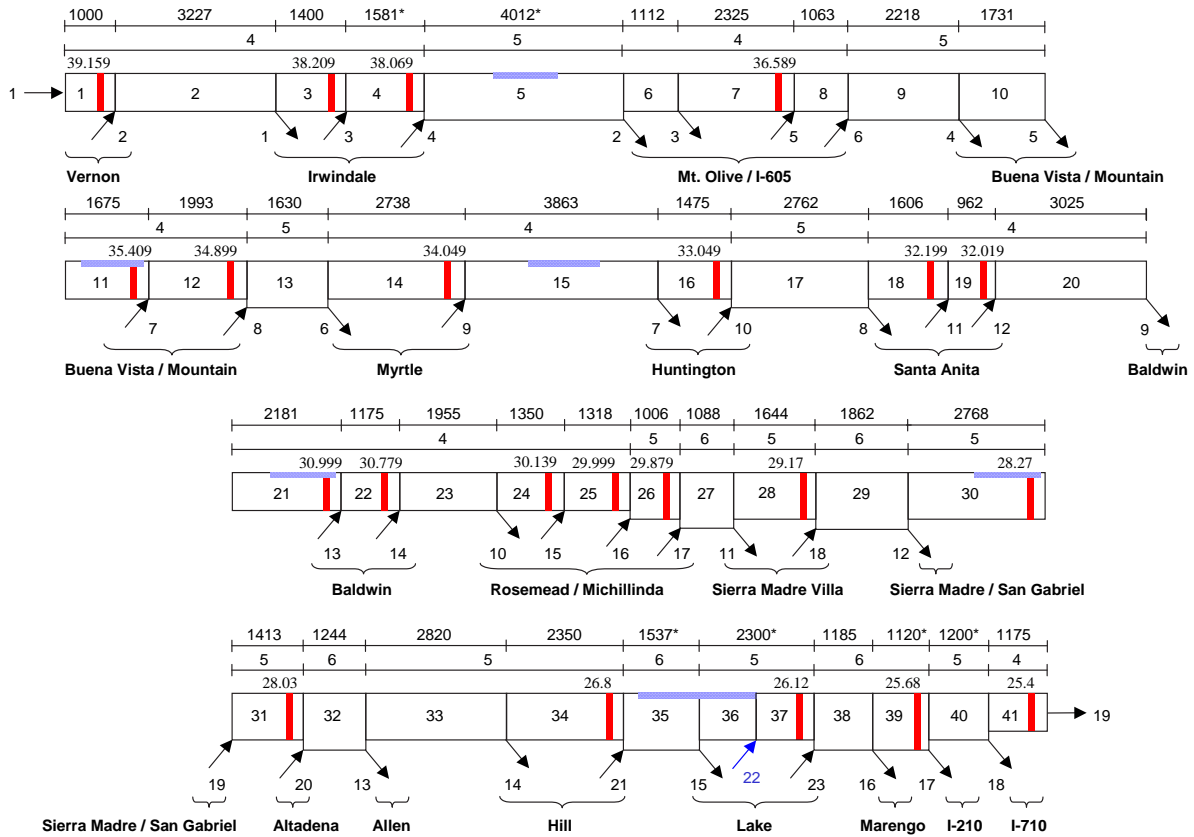


Figure 5.2: 41-cell partition of I-210W testbed. Adapted from a 40-cell partition developed by Gabriel Gomes for use in optimization studies related to [22, 23].

the optimization work of [22, 23]. The 41-cell partition was derived from the 40-cell version by dividing the original cell 36 in half, in order to accommodate an additional on-ramp (number 22), described in Section 5.5. The divided cell is shown as cells 36 and 37 in Figure 5.2.

The traffic flow direction is in order of increasing cell index, i.e., left to right, starting at the top of the figure. The cell index is located in the center of each cell. The uppermost row of numbers above the cells is the cell length (in feet). The second row of numbers gives the number of mixed-flow lanes (4 to 6) in each cell. Vertical red (gray in a gray-scale printout) bars mark the locations of the mainline loop detectors, and the postmile of the detector (e.g. 39.159) is listed above the detector marker. On- and off-ramps are depicted as numbered arrows. Associated street names are given for each set of ramps. A single high-occupancy vehicle (HOV) lane runs parallel to the leftmost mainline lane on this segment of I-210W. Each of the six HOV-lane gates is indicated by a horizontal blue (gray) bar. In the real freeway, vehicles are only allowed to enter and leave the HOV lane through these gates. In this study, HOV/mixed-flow lane interaction is only partially modeled, as explained in Sec. 5.5.

In the default partitioning method, cell boundaries are placed on the mainline immediately upstream of on-ramps and immediately downstream of off-ramps; however, for the chosen time step of 10 sec., and a typical free flow speed of 63 mph, three of the cells were found to be shorter than the minimum allowed cell length of 924 ft. The minimum allowed cell length is determined

from requirement (4.10), in which cell lengths must be longer than the free-flow travel distance. In this partition, the length of these cells was increased by borrowing length from their respective downstream cells, and these adjusted cell lengths are shown with asterisks in Fig. 5.2.

5.3 Demand Reconstruction

One obstacle encountered is that the PeMS and Caltrans data sources, collectively, do not provide a complete data set, which would include flows and densities for each mainline and HOV-lane detector, along with flows measured at each of the ramps, over the entire morning period, for any single day of data collection. Missing measurements are mainly caused by malfunctioning detectors, or problems affecting the transmission of loop data, in the case of the PeMS data sets. For the manually-counted data, on any given day there are some ramps for which no volumes have been recorded.

When constructing a set of demands for the MCTM, the goal is, whenever possible, to use measurements corresponding to the same time period on the same day. For the MCTM representation of the full I-210 test site, a complete demand data set consists of:

1. The measured flow at the upstream mainline (Vernon) boundary, interpolated to 10-second intervals, covering the period 5AM–12PM for a selected day.
2. The measured flow at each on-ramp, interpolated to 10-second intervals, covering the period 5AM–12PM for the same selected day.

If PeMS data is faulty or absent at a particular on-ramp, the first preference is to substitute manual counts, if they are available for that day. If there is no hand-counted data for the chosen day, a historical average of the manually-counted flows for that on-ramp is substituted. Specifically, the demand reconstruction procedure is as follows. For a given on-ramp,

1. Check if PeMS flow data is available for the selected day over 5AM–12PM.
2. If the PeMS data is faulty or absent, check if hand-counted flow data is available for the selected day over 5AM–12PM.
3. If there is no hand-counted data for the selected day and time range, use a historical average of hand-counted flows for the on-ramp.

An additional reconstructive procedure is applied to the flow measured at the upstream mainline detector station, near Vernon St., during the early-morning period (5–6AM). During this period, the flow measured at Vernon is unusually high, and is replaced with a flow-balance estimate using the Mt. Olive flow along with the intervening on-ramps and off-ramps: $\hat{q}_{\text{Vernon}} = q_{\text{Mt. Olive}} - \text{off-ramp flows} + \text{on-ramp flows}$. Although the mainline stations at Irwindale are closer to Vernon, the Mt. Olive mainline measurements were used instead, since the Irwindale stations have faulty or incomplete measurements.

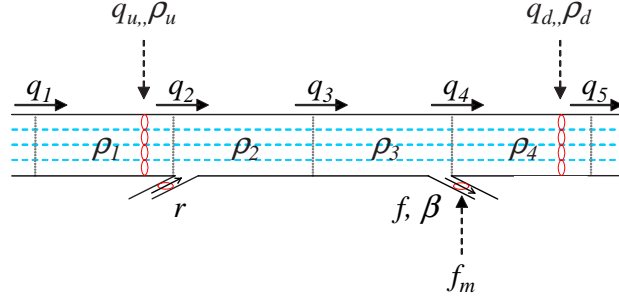


Figure 5.3: Single off-ramp.

5.4 Split Ratio Estimation

The procedure for estimating the MCTM split ratios is to compute, for each off-ramp, the ratio of the measured off-ramp flow to the total measured flow (mainline plus off-ramp) exiting the diverge junction. Since only a limited amount of accurate off-ramp data is accessible, historically averaged split ratios have been used in the MCTM simulations.

For the purpose of computing split ratios, two types of off-ramp configurations are considered.

Case 1 (One off-ramp): A typical single off-ramp configuration is shown in Figure 5.3. f_m is the measured off-ramp flow, which is interpreted as a measurement of f , the off-ramp flow predicted by the MCTM. By Eq. 5.5, the split ratio is

$$\beta(k) = \frac{f(k)}{q_{3,out}(k)},$$

assuming $q_{3,out}(k)$ is not zero. However, a direct measurement of q_4 , and hence $q_{3,out} = q_4(k) + f(k)$, is not available. The selected remedy involves assuming an approximate instantaneous flow balance between the entrance of cell 4 and the downstream mainline detector in Figure 5.3, in which case $q_4(k) \approx q_d(k)$. Then,

$$\begin{aligned} q_{out,3}(k) &= q_4(k) + f(k) \\ &\approx q_d(k) + f_m(k), \end{aligned}$$

and

$$\hat{\beta}(k) = \frac{f_m(k)}{q_d(k) + f_m(k)} \quad (5.6)$$

is the estimate of $\beta(k)$ used in the MCTM.

Case 2 (Two off-ramps): There are four pairs of double off-ramps in the I-210 test site: I-605 SB and I-605 NB/Mt. Olive, Buena Vista and Mountain, Allen and Hill, and the I-210 and I-710 off-ramps. A typical paired off-ramp configuration is shown in Figure 5.4. Note there is no mainline detector station in between the two off-ramps. $f_{m,u}$ and $f_{m,d}$, the measured flows exiting through the two off-ramps, are taken as measurements of the MCTM quantities f_u and f_d . By

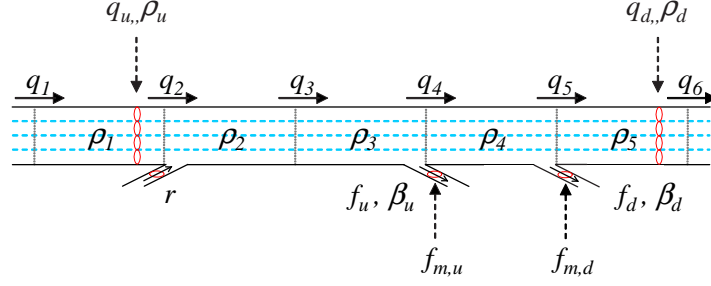


Figure 5.4: Two off-ramps.

Eq. 5.5, the split ratios are

$$\beta_d(k) = \frac{f_d(k)}{q_{4,out}(k)},$$

$$\beta_u(k) = \frac{f_u(k)}{q_{3,out}(k)},$$

assuming $q_{3,out}(k)$ and $q_{4,out}(k)$ are not zero. However, direct measurements of q_4 and q_5 , and hence $q_{3,out} = q_4(k) + f_u(k)$ and $q_{4,out} = q_5(k) + f_d(k)$, are not available. To make up for the unavailable measurements, an approximate flow balance is assumed in the region between the entrance of cell 4 and the downstream mainline detector station, which yields $q_5(k) \approx q_d(k)$. Specifically, the following substitutions are made:

$$\begin{aligned} q_{out,4}(k) &= q_5(k) + f_d(k) \\ &\approx q_d(k) + f_{m,d}(k), \end{aligned} \tag{5.7}$$

$$\begin{aligned} q_{out,3}(k) &= q_4(k) + f_u(k) \\ &\approx q_{out,4}(k) + f_u(k) && \dots \text{flow balance} \Rightarrow q_4(k) \approx q_{out,4}(k) \\ &= (q_5(k) + f_d(k)) + f_u(k) && \dots \text{by (5.7)} \\ &\approx q_d(k) + f_{m,d}(k) + f_{m,u}(k). \end{aligned}$$

Then,

$$\hat{\beta}_d(k) = \frac{f_{m,d}(k)}{q_d(k) + f_{m,d}(k)}, \tag{5.8a}$$

$$\hat{\beta}_u(k) = \frac{f_{m,u}(k)}{q_d(k) + f_{m,d}(k) + f_{m,u}(k)}, \tag{5.8b}$$

are the estimates of $\beta_u(k)$ and $\beta_d(k)$ used in the MCTM.

Computing the split ratios requires matching data from two separate sources; most of the off-ramp flows are obtained from Caltrans hand-counted data, whereas the mainline flows are derived from the PeMS database. For each off-ramp (or off-ramp pair), the following data processing procedure was applied:

1. Make a list of all days for which the flows required for evaluating (5.6) or (5.8) are available. Exclude all days where either the mainline or off-ramp flow data is incomplete or faulty.

2. If acceptable hand-counted off-ramp data is found within the range of days covered by the PeMS data set, but no matching fault-free days of mainline data can be found, create a mainline/off-ramp data set using flows from different days. If possible, match mainline and off-ramp flows from the same day of the week. This type of substitution was used at two locations: the Rosemead/Michillinda and Sierra Madre Villa off-ramps.
3. If no hand-counted data is available for the off-ramp, use off-ramp and mainline flows derived from a specific composite set of flow measurements and estimates. This composite data set was prepared by Gabriel Gomes as part of the Vissim I-210 calibration project [24]. This method was applied for the Marengo, I-210 and I-710 off-ramps.
4. Compute split ratio(s) according to (5.6) or (5.8) above, for each day of data compiled in the preceding steps. All flows used in the calculations are 15-minute averages, covering the period 5AM–12PM.
5. Compute the mean

$$\bar{\beta}(k) = \frac{1}{P} \sum_{p=1}^P \hat{\beta}(k, p)$$

of the split ratios determined in the previous step, where P is the number of days of data selected for the off-ramp (or off-ramp pair) in the foregoing steps. In the case of an off-ramp pair, there should be a separate average for each ramp. These are the historical averages used in the MCTM simulations described later in Chapter 5. The list of days used to calculate the historically averaged split ratios, along with time-series plots of the split-ratio estimates, are given in Appendix H.

5.5 HOV Gate Flow Reconstruction

To estimate the extent to which the HOV lane affects the mixed-flow lanes in the I-210 testbed, the measured flow difference (upstream minus downstream flow) in the HOV lane across each of the HOV gates was computed. Historical averages of gate flow estimates are shown (bold circled line) in Figure 5.5. Positive values indicate vehicles are flowing into the mixed-flow lanes from the HOV lane, while negative values indicate flow in the opposite direction. The three largest flow estimates were observed at the Mt. Olive, Buena Vista, and Lake Ave. gates. However, the flow estimates at the consecutive Mt. Olive and Buena Vista gates approximately cancel, whereas the Lake Ave. flow remains large (over 1000 vph) and positive throughout the morning. Given that there are three major off-ramps (Lake, 210, 710) near the Lake HOV gate, it seems likely that many vehicles exit the HOV lane at this location in order to take one of these off-ramps.

To approximate the effect of vehicles entering the mixed-flow lanes from the Lake Ave. HOV gate, an additional on-ramp (no. 22) was created, the time-dependent net flow rate across the Lake HOV gate was computed, and this flow was inserted into the mixed-flow lanes through the new ramp. The remaining HOV gates are currently not modeled. At present, the flow data used to compute net flow rates across HOV gates is taken, when available, from the same day as the target day for calibration.

It is noted that Daganzo has already extended the kinematic wave (LWR) model to cover traffic behavior on a freeway with special lanes [25]. This extended model keeps track of two types of vehicles. One type of vehicle (e.g., high passenger occupancy) is able to access all lanes in the freeway and the other type (e.g., low passenger occupancy) is restricted to use only certain lanes. A discretized version of the special-lanes model has been presented in [26]. Since the special-lanes model is sufficiently general to handle the case of a freeway with an HOV lane, applying the methods of [25, 26] would allow a more complete representation of the interaction between regular and HOV traffic in the I-210 testbed.

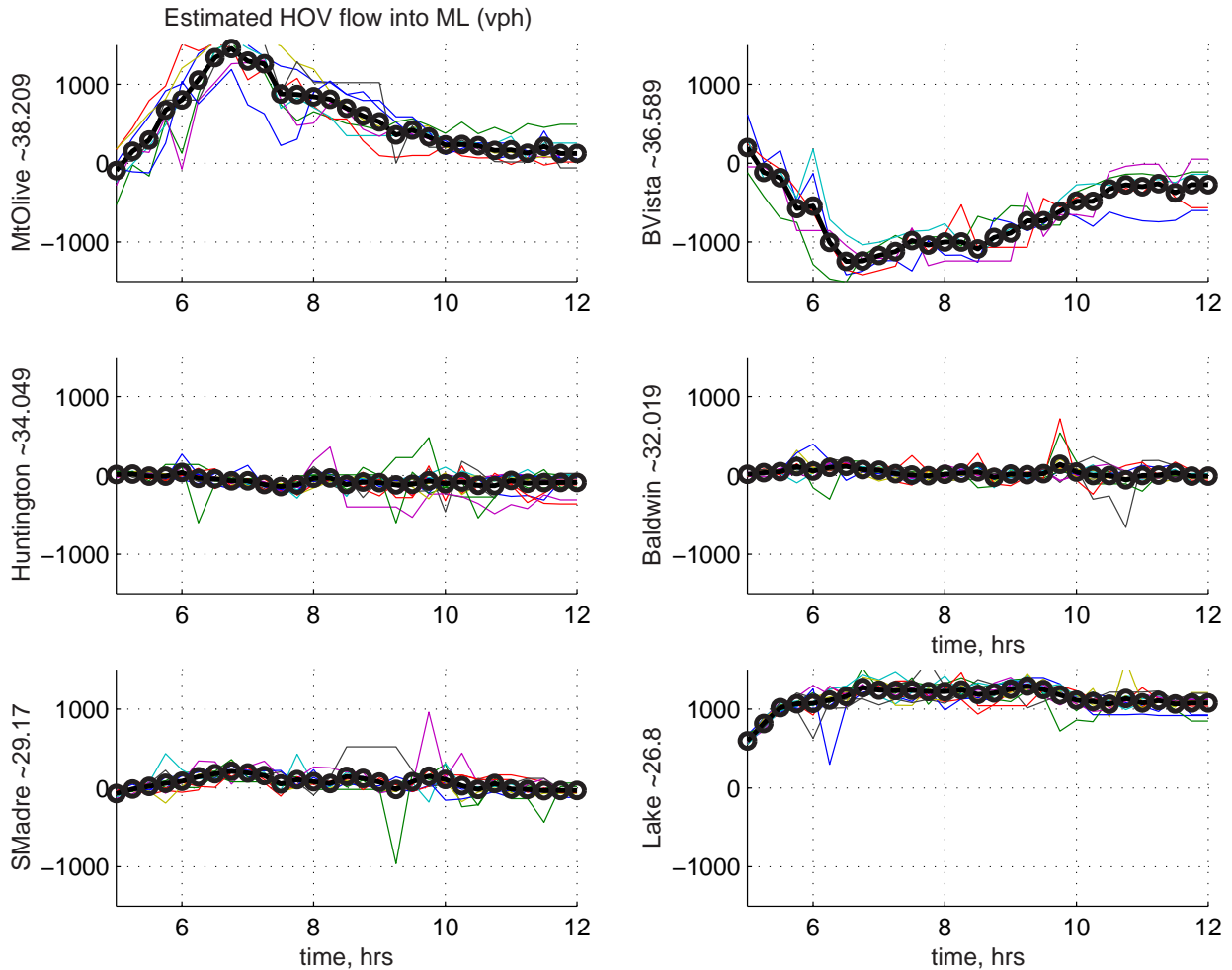


Figure 5.5: Estimated flows from HOV gates into mainline. Historical averages are bold circled lines.

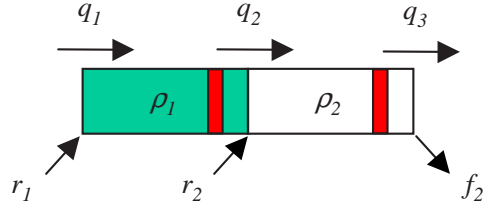


Figure 5.6: An active bottleneck: the upstream cell (1) is congested, while the downstream cell (2) is in free-flow mode. Vertical red bars indicate detectors.

5.6 Calibration Methodology

The main steps of the calibration procedure are as follows:

1. **Free-flow Parameter Calibration:** The free-flow traffic velocities, v_i , are determined by performing a least-squares fit on the flow versus density data over the period 5:00–6:00AM. For the I-210 section, traffic typically flows freely during this period. For the j^{th} detector, v_j is the solution, in the least-squares sense, to the equation

$$\Phi_j v_j = Y_j,$$

where

$$\Phi_j^T = [\rho_{d_j}(k_{5:00}) \dots \rho_{d_j}(k_{6:00})],$$

and

$$Y_j^T = [q_{d_j}(k_{5:00}) \dots q_{d_j}(k_{6:00})],$$

are the measured densities and flows over the specified time interval. If no data is available, or the data is of poor quality, a default value of 60 mph is used. The free-flow speed v_j is assigned to the cell containing detector j , and free-flow speeds are computed for non-detector cells by linear interpolation. The resulting v_i are typically in the range of 60–65 mph.

2. **Bottleneck Identification:** Bottleneck locations are identified by examining contour plots of the measured traffic densities and/or speeds, and determining the locations of fixed spatial boundaries which divide the freeway into an upstream congested region and a downstream free-flow region. For example, in the top plot of Fig. 5.7, a bottleneck was observed to form between the detectors at 33.049 and 32.199 during the 6:00 time slice.
3. **Non-Bottleneck Capacity Selection:** Currently, a set of nominal $Q_{M,i}$ are assigned to the cells that are not located at bottlenecks. It is expected that $Q_{M,i}$, which represents the maximum flow that can possibly enter or exit cell i , will typically not be achieved (and hence not observed) in the real system. Thus, it is not advisable to set $Q_{M,j}$ equal to the maximum observed flow at each detector-equipped cell, since this will most likely result in underestimating the true capacity of the freeway. In general, the nominal $Q_{M,i}$ must be chosen to be larger than the maximum observed flows (usually ≥ 2000 veh/hr per lane (vphpl)) in each region of the highway, in order to avoid inducing unwanted bottlenecks in the simulation.

4. **Bottleneck Capacity Determination:** Consider the scenario suggested by Fig. 5.6: an active bottleneck exists between cell 1 and cell 2, hence the upstream cell is congested, while the downstream cell remains in free-flow status. We assume that the inflow into cell 1 is $w_1(\rho_{J,1} - \rho_1(k))$, the total inflow to cell 2 is $Q_{M,2}$, the total outflow from cell 2 is $v_2\rho_2(k)$, and that the second case in the maximum of Eq. (5.1) holds, that is, the measured demand $r_{m,2}$ is not larger than the amount of flow that cell 2 can accommodate. In this situation, the MCTM equations for these two cells reduce to a linear system. The density dynamics are given by:

$$\rho_1(k+1) = \rho_1(k) + \frac{T_s}{l_1} \left(w_1(\rho_{J,1} - \rho_1(k)) - Q_{M,2} + r_2(k) \right), \quad (5.9)$$

$$\rho_2(k+1) = \rho_2(k) + \frac{T_s}{l_2} (Q_{M,2} - v_2\rho_2(k)). \quad (5.10)$$

The total flow entering cell 2 is $Q_{M,2} = q_2 + r_2$, where q_2 is the flow entering from the mainline. Since both q_2 and r_2 are measurable, these quantities are used to estimate the bottleneck flow rate, specifically, $\hat{Q}_{M,2} = \text{mean}_{k \in K_M} (q_2(k) + r_2(k))$. K_M corresponds to the half-hour time interval ending at $\arg \max (q_2(k) + r_2(k))$. If, for a selected day, the q_2 or r_2 data are considered faulty, $Q_{M,2}$ is estimated using historically averaged q_2 or r_2 data sets.

5. **Congestion Parameter Calibration:** w_i and $\rho_{J,i}$ are estimated by performing a constrained least-squares fit on the flow versus density measurements. First, the critical density is estimated for each detector; $\hat{\rho}_{c,j} = \max_k (q_{d_j}(k)) / v_j$. The $(\rho_{d_j}(k), q_{d_j}(k))$ data is sorted so that only congested pairs are used in the estimation. Let $\kappa = \{k_1 \dots k_{N_c}\}$ denote the set of all k for which $\rho_{d_j}(k) > \hat{\rho}_{c,j}$. $[w_j \ w_j \rho_{J,j}]^T$ is the solution, in the least-squares sense, to

$$\Phi_j \begin{bmatrix} w_j \\ w_j \rho_{J,j} \end{bmatrix} = Y_j, \quad (5.11)$$

where

$$\Phi_j^T = \begin{bmatrix} -\rho_{d_j}(k_1) & \dots & -\rho_{d_j}(k_{N_c}) \\ 1 & \dots & 1 \end{bmatrix},$$

and

$$Y_j = \begin{bmatrix} q_{d_j}(k_1) + \frac{l_j}{T_s} \Delta \rho_{d_j}(k_1) \\ \vdots \\ q_{d_j}(k_{N_c}) + \frac{l_j}{T_s} \Delta \rho_{d_j}(k_{N_c}) \end{bmatrix},$$

where $\Delta \rho_{d_j}(k) = \rho_{d_j}(k+1) - \rho_{d_j}(k)$. Note that Eq. (5.11), which is linear in the unknown parameters $[w_j \ w_j \rho_{J,j}]^T$, is a rewriting of the congested case of the MCTM, where q_{d_j} is taken as a measurement of the flow exiting the cell containing detector j . In the congested case, inter-cellular flow is determined by the downstream density in each pair of cells; for example, the congested-mode equation for cell 1 in Fig. 5.6 is

$$\rho_1(k+1) = \rho_1(k) + \frac{T_s}{l_1} \left(w_1(\rho_{J,1} - \rho_1(k)) - w_2(\rho_{J,2} - \rho_2(k)) + r_2(k) \right). \quad (5.12)$$

The least-squares solution is subject to the constraint

$$Q_{M,j} \leq \frac{v_j w_j \rho_{J,j}}{v_j + w_j}. \quad (5.13)$$

The constraint, which can be written as linear in $[w_j \ w_j \rho_{J,j}]^T$, is included to prevent the solution $[w_j \ w_j \rho_{J,j}]^T$ from limiting the maximum possible flow in cell j below $Q_{M,j}$, which is either the $\hat{Q}_{M,j}$ identified in step 4, or the nominal value for that location. As an example, referring to Fig. 4.4(b), suppose that the flow associated with a density ρ is given by $Q(\rho)$. It can be shown that for a given set of $(v, Q_M, w, \rho_J) > 0$, the maximum possible flow rate is $\min(Q_M, \frac{vw\rho_J}{v+w})$. Thus, the constraint prevents the lines $Q(\rho) = v\rho$ and $Q(\rho) = w(\rho_J - \rho)$ from intersecting below the $Q(\rho) = Q_M$ line. Since Q_M is intended to represent the maximum permissible flow in a cell, this constraint ensures that the maximum flow rate is achievable by the model. Currently, only values of w_j that fall within a range that is considered physically reasonable, $10 \leq w_j \leq 20$ mph, are retained. If Eqs. (5.11) and (5.13) fail to produce a solution in the acceptable range for a particular detector cell n , this cell is assigned the w_j of the nearest downstream neighbor with a w inside the range. The corresponding $\rho_{J,n}$ is found by solving the equality case of constraint (5.13). w_i and $\rho_{J,i}$ are then determined for non-detector cells through linear interpolation.

6. **Time-Varying Parameter Adjustments:** If necessary, temporary parameter changes (e.g. reduction of $Q_{M,i}$ in a region) can be applied to reproduce the effect of an incident. Also, by reducing w_i in the mid-morning time range, when the traffic is still congested but beginning its recovery back to the free-flow mode, the effect of flow-density hysteresis can be approximated.

5.7 Results

Figures 5.7–5.9 show contour plots for the measured (top) and simulated (bottom) densities for three days (Thursday, Jan. 10, 2002, Wednesday, Nov. 28, 2001, and Tuesday, Nov. 13, 2001) in the I-210 testbed. The numbers inside the shaded cells are traffic densities, in vehicles per mile per lane (vpmpl). Free-flow densities (0–33 vpmpl) are shown as green (or white in a gray-scale printout). Mid-range congestion (33–43 vpmpl) is shaded yellow (medium gray). Red (dark gray) indicates heavy congestion (43 vpmpl or greater). Traffic is flowing from left to right in these plots, and the time, in 15-minute intervals, is given in the leftmost column. The time range is 5:30–10:30AM. Loop detector outages are indicated by crossed-out boxes in the measured-data contour plot. Loop detectors which were suspected to be faulty for the whole day have their postmile labels surrounded by a dashed box at the top of the measured-data plot.

The MCTM parameters used in these simulations are plotted in Fig. 5.10. The nominal $Q_{M,i}$ was chosen as 2300 vphpl for the 5 cells farthest upstream, and 2100 vphpl for the remaining cells. “V”-shapes in the Q_M profile indicate the locations, determined from visual assessment of the density contour plots, of suspected bottlenecks: postmiles 33.049, 30.779, 29.879, 28.03, and 26.12. Recalling from the previous section that bottlenecks are modeled by adjusting Q_M in the cell immediately downstream of the congestion–free-flow boundary, the corresponding cells are: 17, 23, 27, 32, and 36. On all three days, a historically averaged bottleneck capacity was used at postmile 28.03, due to a lack of complete data in this region. For the Jan. 10, 2002 parameters, it

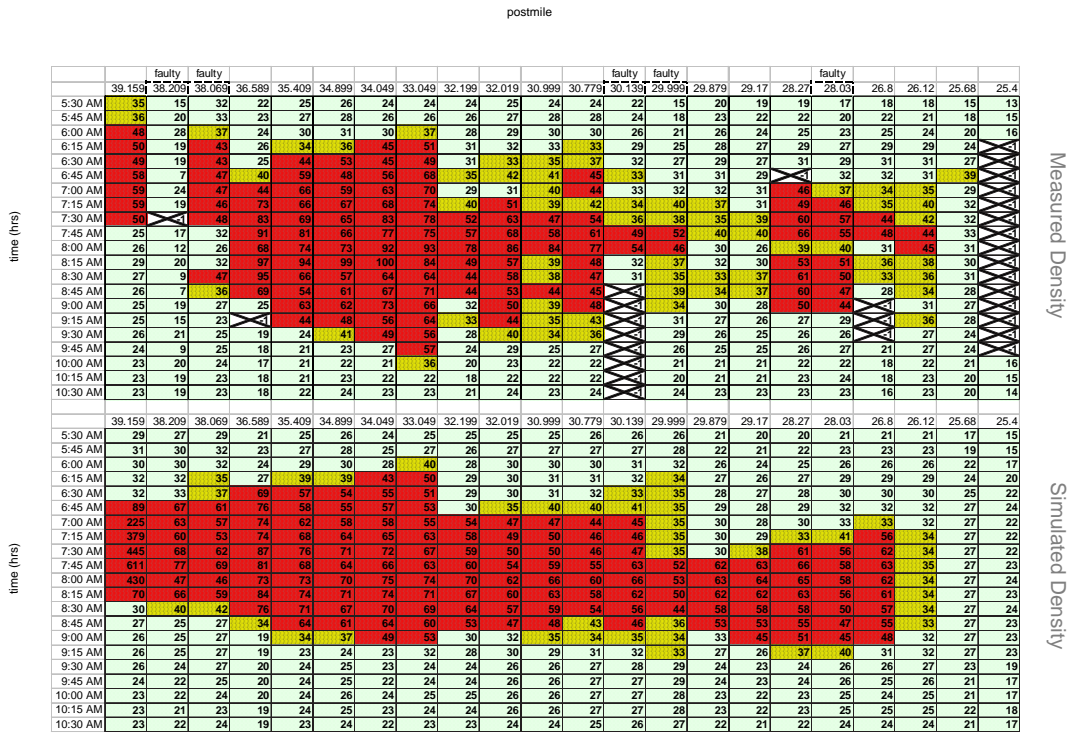


Figure 5.7: Contour plots of 15-minute average measured (top) and simulated (bottom) densities (vpmpl) on Jan. 10, 2002.

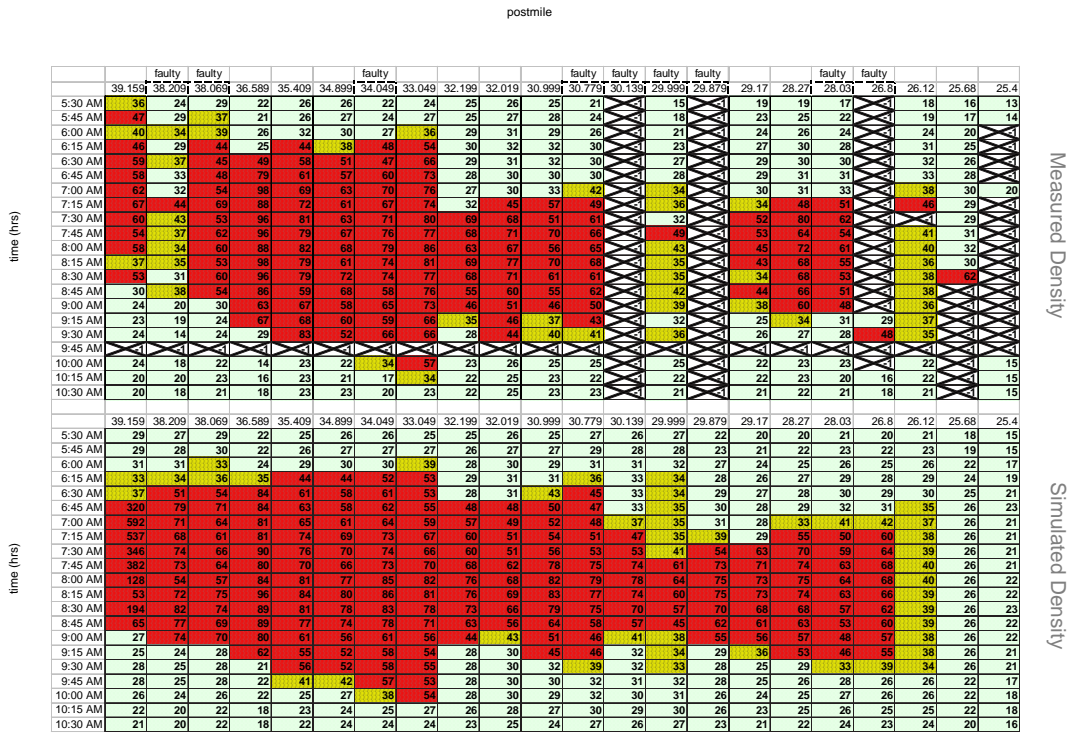


Figure 5.8: Contour plots of 15-minute average measured (top) and simulated (bottom) densities (vpmpl) on Nov. 28, 2001.

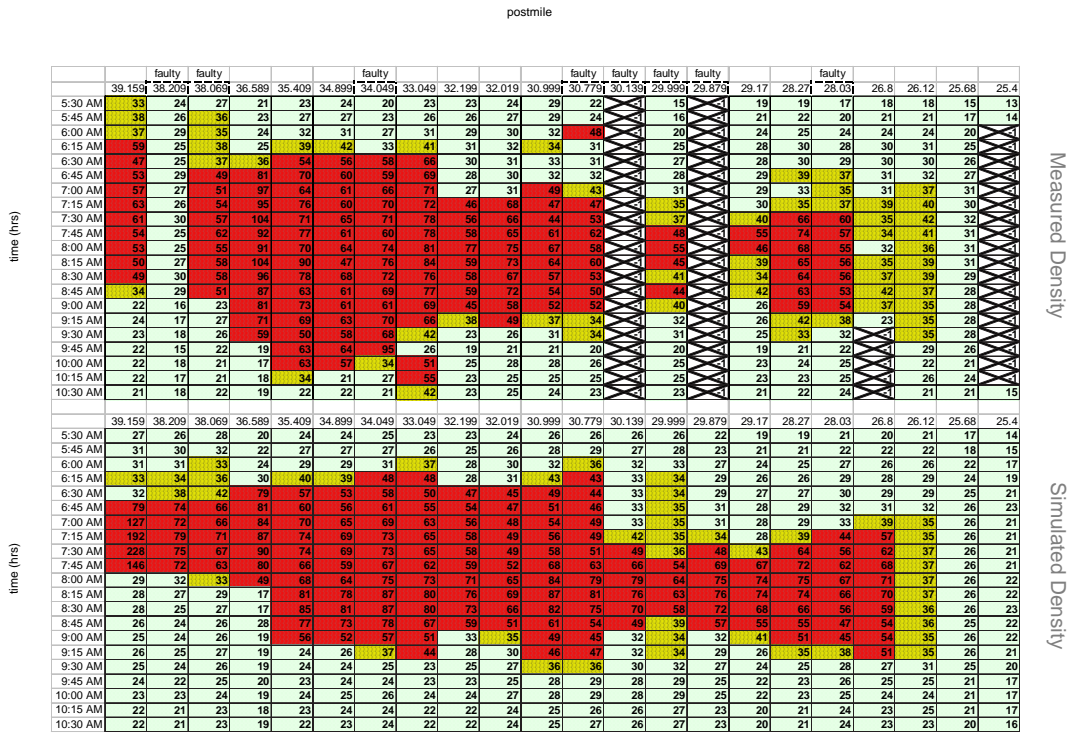


Figure 5.9: Contour plots of 15-minute average measured (top) and simulated (bottom) densities (vpmpl) on Nov. 13, 2001.

Date	Meas.	Sim.	% TTT Err.	MMPE
Jan. 10, 2002	3778	3766	-0.32	14.2
Nov. 28, 2001	4273	4289	0.37	14.3
Nov. 13, 2001	4163	3895	-6.44	15.2
mean	4071	3983	-2.13	14.6
std. dev.	260	272	3.75	0.6

Table 5.1: Total Travel Time (veh-hr) error and mean MPE for three different days.

can be seen that w_i and $\rho_{J,i}$ differ from those of the other two days, in the region between cells 20 and 30. This difference was caused by the lack of good data in this region, including bottlenecks at postmiles 30.779 and 28.879, on Nov. 11 and 28, 2001. For these two days, historically averaged data were used to estimate the $Q_{M,i}$, and the w_i and $\rho_{J,i}$ were determined from the interpolation methods described in Sec. 5.6, in the region of faulty data. A larger amount of good data was available in this region on Jan. 10, 2002, which produced different parameter estimates for this day.

To evaluate the performance of the simulation, we define the Total Travel Time (TTT):

$$TTT = T_s \sum_{k=k_{5:00}}^{k_{11:45}} \sum_{i \in C_d} l_i \rho_i(k).$$

Here, C_d is the set of cells which had problem-free mainline detectors over each of the examined days. C_d excludes detectors at postmiles 38.209, 38.069, 34.049, 30.779, 30.139, 29.999, 29.879, 28.030, 26.800, and 25.400. Although it functions properly, the detector at 39.159 is also excluded, since the MCTM boundary condition prevents the model from accurately reproducing congestion that (in the real system) spills upstream outside of the simulated region. Results for TTT are summarized in Table 5.1, along with the spatial mean of the MPE at the non-excluded detectors, defined as

$$E_{MMPE} = 100 \times \frac{1}{N_{C_d}} \sum_{i \in C_d} \frac{1}{M} \sum_{k=1}^M \left| \frac{\rho_i(k) - \hat{\rho}_i(k)}{\rho_i(k)} \right|,$$

where N_{C_d} is the number of non-excluded detectors (11 out of 22 in this case). The resulting values of MMPE are not surprising, since they are similar to the MPEs in the short-segment tests of Chapter 4. From Figures 5.7–5.9 and Table 5.1, it can be seen that the MCTM reproduces the observed bottlenecks and the approximate duration and spatial extent of the congestion upstream of each bottleneck, and predicts the total travel time with approximately 2% mean error over three days.

An example of the curve fit resulting from the calibration method is shown in Figure 5.11, for a particular mainline station. PeMS 5-minute lane aggregate (flow, density) points are shown as “x”s, and the data points that were classified as congested are displayed as circled “x”s. The solid lines are the $v\rho$ and $w(\rho_J - \rho)$ curves implied by the estimated parameters, and the dashed horizontal line is the Q_M line. Note that the default value of $Q_M = 2100 \text{ vphpl} \times 4 \text{ lanes} = 8400 \text{ vph}$ is larger than the maximum observed flow rate at this location.

Table 5.2 gives the mean standard deviations (MSD) of the parameters; these are computed by taking the standard deviation across days for each cell, then averaging over all the cells. For a

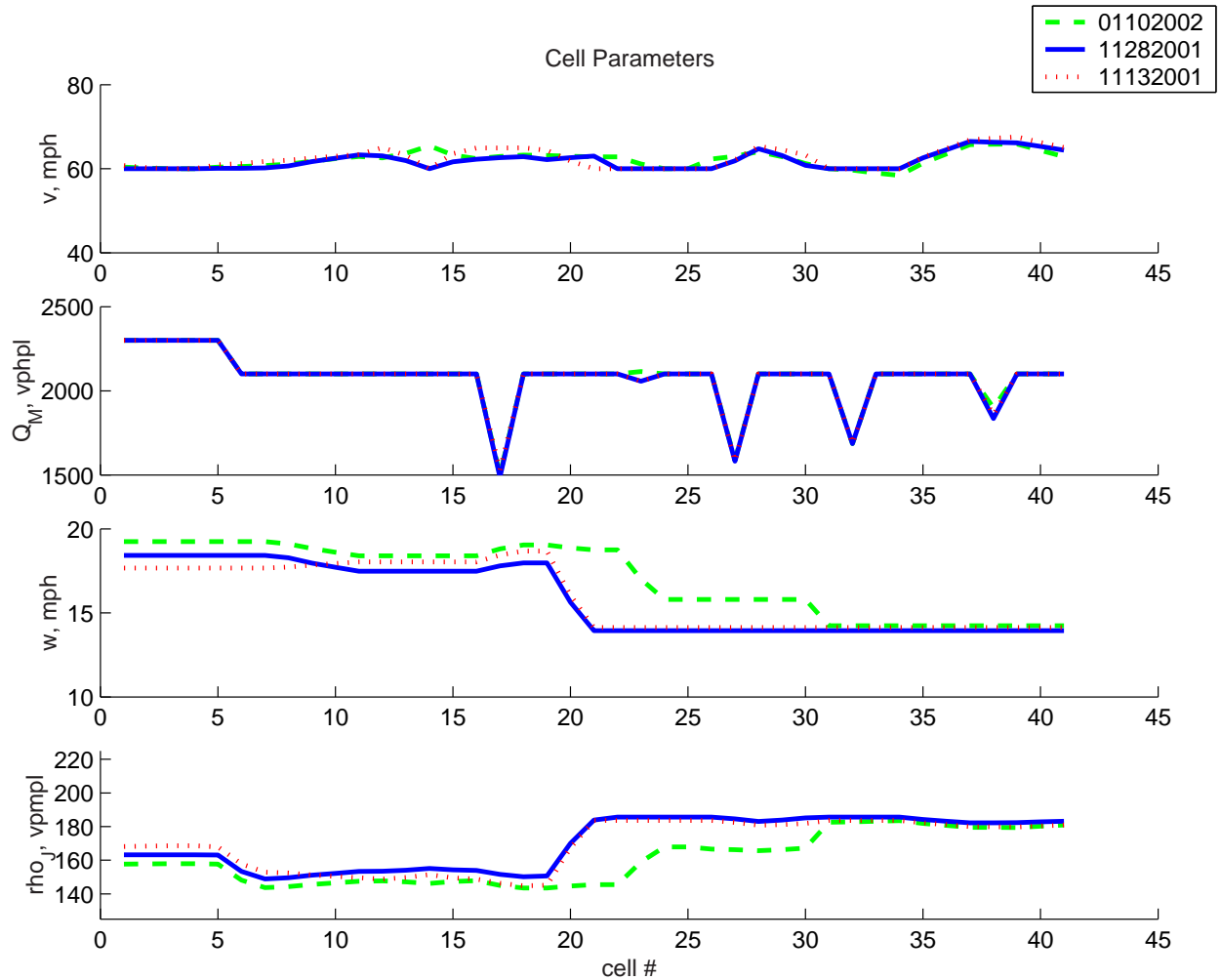


Figure 5.10: MCTM parameters used for Nov. 13, 2001, Nov. 28, 2001 and Jan. 10, 2002 simulations.

Parameter	MSD
Q_M	2.22 vphpl
ρ_J	5.72 vpmpl
v	0.78 mph
w	0.71 mph

Table 5.2: Mean standard deviations of parameter estimates for 11/13/01, 11/28/01, and 01/10/02.

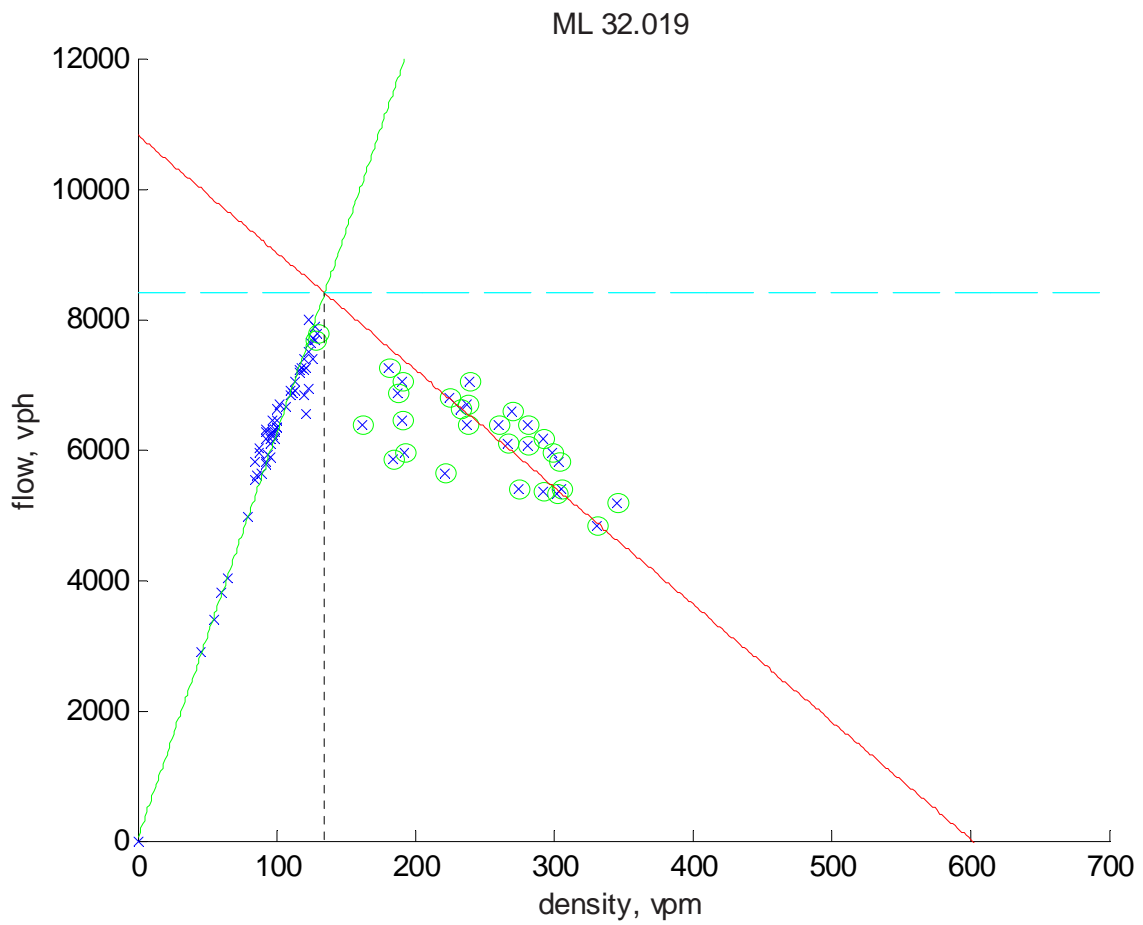


Figure 5.11: Estimated free-flow, congestion, and maximum flow curves compared with a scatter plot of 5-minute PeMS data used in the estimation; lane-aggregate flow vs. lane-aggregate density, mainline station 32.019, on Nov. 28, 2001.

parameter θ , it is defined as

$$MSD = \frac{1}{N} \sum_{i=1}^N \sigma(i),$$

where $N = 41$ (the total number of cells) and the standard deviation is

$$\sigma(i) = \sqrt{\frac{1}{P-1} \sum_{p=1}^P (\hat{\theta}(i,p) - \bar{\theta}(i))^2},$$

and the mean is

$$\bar{\theta}(i) = \frac{1}{P} \sum_{p=1}^P \hat{\theta}(i,p).$$

Here, P is the number of days of data for which parameters were estimated (3 in this case), and $\hat{\theta}(i,p)$ is the estimate for the i^{th} cell on the p^{th} day. It can be seen that the resulting mean standard deviations were small compared to the estimated parameter values.

5.8 Conclusions

Simplified versions of the MCTM merge and diverge laws were given in this chapter. The selected 41-cell freeway partition was described, along with the methods used to estimate demands, split ratios, and flows across HOV gates. A procedure for calibrating the modified CTM was then presented. The calibrated model was tested on a section of I-210W, about 14 miles long, in southern CA, and was shown to reproduce the main features of the observed traffic congestion on the freeway, such as approximate location of bottlenecks and duration and spatial extent of congestion. In addition, the model accurately predicted the total travel time in the freeway. An area of ongoing work is to determine a consistent method for estimating bottleneck capacities from incomplete mainline data.

Chapter 6

Simulation Software for Macroscopic Traffic Models

The research group has created a number of software tools, including programs in C/C++, and scripts in Matlab, SQL, and Vissim's VAP language, in support of the studies described throughout this report. Software developed for the macroscopic modeling tests in Chapters 4 and 5 is complete, hence it will be reviewed in this chapter; however, programs associated with the Chapters 2, 3, and 7 will be documented in upcoming reports for the continuation project, T.O. 5503. A CD containing the tools listed herein will be provided by the authors upon request.

6.1 Data Processing and Simulation Software (Short Freeway Segments)

To carry out the short-segment validation tests of Chapter 4, several programs were prepared in Matlab for both the MCTM and SMM. A more efficient MCTM simulator was later developed in C/C++, and was then applied to the full 14-mile I-210W segment to perform the calibration tests described in Chapter 5.

6.1.1 Processing Software for PeMS Data

A Matlab M-file (**dataproc_gab_old.m**) was prepared to process PeMS data to produce quantities necessary for the SMM/MCTM simulation tests described in Chapter 4.

Inputs:

- Station definition file (**defstation210.m**)
- 30-second and 5-minute PeMS data files (gooddaysX_o30.mat and gooddaysX_o5.mat)

Processing Notes:

- Aggregate and average quantities computed
- Scaling corrections: aggregate flow and density at Myrtle were multiplied by 4/3 to account for missing loop 2 data, and the Santa Anita off-ramp flow was multiplied by a factor of 2

Outputs:

- Time vectors and calendar date
- Mainline (ML): 30-sec lane-aggregate flow and density
- Off-ramp (FR): 30-sec aggregate flow, 30-sec split ratios (FR flow / total section outflow)
- On-ramp (OR): 30-sec Loop 1 flow, 30-sec merge ratios (OR flow / total section inflow)
- All of the above quantities are also available in interpolated form (5-sec nearest-neighbor), and interpolated then filtered form (1st-order Butterworth filter with coefficients [bf, af] = butter(1,0.02), implemented with filtfilt forward-and-reverse filtering to eliminate phase distortion)

All split and merge ratios are Zero-Order-Hold (ZOH) -corrected to remove NaNs and negative entries. The number of blank entries in each split ratio (prior to correction) is stored.

6.1.2 MCTM and SMM Simulators in Matlab

Matlab simulation software was developed for the short-segment validation tests described in Chapter 4.

- MCTM: **netcell_matlab_vX.m** series. The MCTM structure described in Chapter 4 is implemented in these files.
- SMM: **observer.m** and supporting files. The switching-mode model structure described in Chapter 4 is implemented in these files. There is an option of running the SMM by itself (in which case it can be considered an open-loop density estimator), or as a closed-loop Luenberger observer for densities.
- Plotting outputs: **plotdens_rho5.m** generates a plot comparing measured density at the middle detector with densities predicted by the MCTM and SMM at this location. It also computes density estimation errors and error statistics for both models.

6.2 MCTM Simulator in C++

The modified CTM described in Sections 4.1 and 5.5, with simplified merge and diverge laws, has been implemented in C++ by Dengfeng Sun [27]. The simulator is very efficient; for a 10-sec model time step, it has been determined that the simulation-to-real-time ratio for a coarse partition of the I-210 testbed (40 cells) was approximately 2500:1 on a 1.0 GHz, 256 MB PIII PC running Win2K. The C++ simulator is independent of O-D types. Its inputs are a series of text files describing the mainline and on-ramp demands, initial condition, starting and ending times, and time-varying MCTM parameters (i.e., free-flow speed, backward speed of congestion propagation, maximum flow rate, and jam density for each cell, along with split ratios). Time-varying quantities are assumed to be coded in the form of 15-minute averages; these are later zero-order interpolated down to the model time step during run time. Other quantities, such as the number of cells, cell

lengths, ramp locations, and simulation time step can be adjusted by editing the appropriate C++ files.

Variations on the MCTM simulator have also been prepared, including a "control-ready" version that incorporates a queueing model for metered on-ramps. If desired, it is a simple matter to restore the full merge and diverge laws of Section 4.1. In the following list, the main steps for setting up and running a freeway simulation are reviewed.

1. *Define simulation timing parameters.* To alter the model time step, the file **datadef.h** must be changed. This can be accomplished by editing the file in Microsoft Visual C++ or another text editor. The following variables are important:

<code>ControlDt</code>	metering update time interval (sec)
<code>ModelRatio</code>	number of modeling intervals per <code>ControlDt</code>

Since control-update intervals for on-ramp meter heads are often on the order of minutes, and the model equations may be updated every few seconds, the metering interval is assumed to be an integer number of model time steps. The model time step is then `ControlDt/ModelRatio` seconds. When choosing the cell lengths and model time step, the constraint (4.10) should be observed.

2. *Define highway geometry.* It is assumed that the user decides on a freeway partition in advance, based on his or her knowledge of the chosen freeway segment. Allowed configurations are restricted to linear freeways, where the freeway mainline is divided into `numCells` cells. The freeway partition must obey the connectivity constraints described in [11]. Typically, the mainline cells are designed such that there exist mainline cell boundaries slightly upstream of merge junctions and slightly downstream of diverge junctions, as in the example of Chapter 5. In **datadef.h**, several variables can be adjusted:

<code>numCells</code>	total number of cells in freeway segment
<code>numOR</code>	total number of on-ramps in freeway segment
<code>numFR</code>	total number of off-ramps in freeway segment
<code>numDet</code>	total number of mainline detectors in freeway segment

The simulator is currently configured for the geometry of a 14-mile segment of I-210W, which contains 22 on-ramps and 18 off-ramps. For any freeway, the mainline entrance and exit are treated, respectively, as an additional on-ramp and additional off-ramp, so for this case, `numOR=23` and `numFR=19`. To encode a particular freeway geometry, the user must specify the contents of several arrays in **datadef.cpp**:

- **Cell2Detector**: this array of length `numCells` describes which cells contain loop detectors. Each entry can be set to either `-1`, representing no detector, or to a whole number representing the index of the detector in that cell. It is assumed that detectors are numbered in increasing order from upstream to downstream, starting at 0 and ending at `numDet-1`. The default for I-210W is

```
int Cell2Detector[numCells] = { 0,-1, 1, 2,-1,-1, 3,-1,-1,-1,
                               4, 5,-1, 6,-1, 7,-1, 8, 9,-1,
                               10,11,-1,12,13,14,-1,15,-1,16,
                               17,-1,-1,18,-1,-1,19,-1,20,-1,21};
```

- **Detector2Cell**: this array of length `numDet` gives the cell index, between 0 and `numCells-1`, associated with each detector location. The default for I-210W is

```
int Detector2Cell[numDet] = { 0, 2, 3, 6,10,11,13,15,17,18,
                             20,21,23,24,25,27,29,30,33,36,
                             38,40};
```

- **Cell2OnRamp**: this array of length `numCells` describes which cells are connected to on-ramps. `Cell2OnRamp[i] = -1` indicates that no on-ramp enters cell i , while `Cell2OnRamp[i] = j` indicates that on-ramp j enters cell i , where j is an integer between 0 and `numOR-1`. It is assumed that on-ramps are numbered in increasing order from upstream to downstream. The mainline entrance is on-ramp number 0.
 - **OnRamp2Cell**: this array of length `numOR` gives the index, between 0 and `numCells-1`, of the cell connected to each on-ramp.
 - **Cell2OffRamp**: similar to `Cell2OnRamp` above, `Cell2OffRamp[i] = -1` indicates that no off-ramp exits cell i , while `Cell2OffRamp[i] = j` indicates that off-ramp j exits cell i , where j is an integer between 0 and `numFR-1`. It is assumed that off-ramps are numbered in increasing order from upstream to downstream. The mainline exit is off-ramp number `numFR-1`.
 - **OffRamp2Cell**: this array of length `numFR` gives the index, between 0 and `numCells-1`, of the cell connected to each off-ramp.
 - **Length**: each entry gives the length, in feet, of the corresponding cell.
 - **Lanes**: each entry gives the total number of mixed-flow lanes, plus 1, for the corresponding cell. The additional lane was originally included to account for a high-occupancy vehicle (HOV) lane that may run the length of the freeway segment. In the current versions the HOV lane is not modeled explicitly; if `Lanes[i] = N`, then all computations for cell i are performed assuming $N - 1$ lanes.
3. *Build executable file.* After editing any of the `*.h` or `*.cpp` files, the project should be re-compiled. For MS Visual C++, the user can open the project file (CTM.dsw) and select "Build CTM.exe", the default name for the executable.
 4. *Prepare files for time range, initial condition, demands, and model parameters.* These quantities are specified in a series of text files that are read by the simulator at run-time. There are 8 input files, which contain the simulation time range, initial condition, on-ramp demands, and 5 parameters for the MCTM. Any input file representing a time-varying quantity, with the exception of the time-range file itself, must have its number of rows equal to number of 15-minute time intervals listed in the time-range input file. The number of columns in each file will vary according to the nature of the represented quantity, i.e., whether the quantity is associated with each cell, each on-ramp, etc. Time-varying quantities are interpolated automatically by the simulator down to the simulation time step, using a zero-order-hold method. It is assumed that the simulation time step (computed as `ControlDt/ModelRatio` seconds) is less than 15 minutes. All the input data files are kept in the directory `CTM_HOME/inputdata/`.

The calibration procedure of Chapter 5 is implemented in the Matlab M-files **LSconges-tion_params*.m** (yields v, w, ρ_j), **findBNcaps*.m** (Q_M), and **betacompute*.m** (β), which compute MCTM parameters using data from PeMS and in some cases the manual ramp survey. The input file formats are described next.

- **Simulation Time Range:** The simulation time range is stored in the input file **Gtime.txt**. **Gtime.txt** is a one-line tab-delimited text file. The numerical values stand for the time intervals at which the time-varying parameters are specified. Each time is represented by a floating point number¹. For example, 8:00am is represented by 8.0000, 8:15am is 8.2500 (.25 is used for quarter hour), etc. Here is an example of **Gtime.txt**:

```
5.75 6 6.25 6.5 6.75 7 7.25 7.5 7.75 8 8.25 8.5 8.75 9 9.25 9.5 9.75 10 10.25 10.5 10.75 11 11.25 11.5 11.75 12
```

For this time range, the simulation starts at 5:45am and ends at 12:15pm. The time-varying parameters are updated every 15 minutes.

- **Initial Condition:** The initial cell occupancies (in number of vehicles [veh]) are read in from the file **Gni.txt**. **Gni.txt** is a one-line tab-delimited text file. In the file there are N floating point numbers, corresponding to the initial occupancies of the N cells in the selected freeway partition. Here is an example of the **Gni.txt** file for $N = 40$:

```
14 38 15 20 54 11 22 10 27 21 17 20 26 37 14 32 15 9 28 20 11 18 12 10 10 13 16 22 27 13 13 23 17 14 20 11 10 8 6
```

For the results in Chapter 5, initial conditions were computed from PeMS data using the Matlab script **inputfiles.m**.

- **Demands:** The on-ramp demands (in vehicles per hour [vph]) are specified in the file **Gdemand.txt**. **Gdemand.txt** is a multiple-line tab-delimited text file. In each line, there are 22 floating point numbers, corresponding to the on-ramp demands of the 22 on-ramps in the CTM (the first “on-ramp” demand is actually the mainline input). The number of lines of the file is set to 29 by default, which covers the simulation time range from 5:00am to 12:15pm. Each row denotes the average demands at the on-ramps over the 15-min time interval corresponding to the row number. If the simulation time range specified by **Gtime.txt** is not from 5:00am to 12:15pm, then the CTM simulator only extracts the lines corresponding to the specified time range. For example, if the simulation time range is from 6:00am to 11:45am, only the lines 5 through 27 will be fed into the simulator. Here is an example of the **Gdemand.txt** file:

```
4692.0 128.0 217.3 285.3 60.0 718.7 56.0 108.0 156.0 136.0 120.0 91.4 76.0 88.0 43.0 112.0 12.0 44.8 100.0 90.4 153.3 136.0
7063.1 244.1 348.0 325.3 152.0 1068.0 88.0 140.0 216.0 140.0 128.0 125.1 120.0 73.0 75.0 244.0 24.0 81.6 116.0 122.4 248.0 228.0
8404.0 328.0 473.3 446.7 208.0 1590.7 144.0 216.0 296.0 184.0 192.0 145.1 80.0 117.0 120.0 200.0 84.0 96.0 176.0 102.4 330.7 340.0
8652.0 296.0 556.0 389.3 172.0 1788.0 172.0 240.0 284.0 232.0 196.0 173.1 88.0 150.0 140.0 284.0 60.0 114.4 232.0 81.6 365.3 340.0
8508.0 348.0 544.0 453.3 280.0 1945.3 232.0 228.0 328.0 288.0 372.0 236.0 128.0 266.0 211.0 284.0 72.0 124.0 268.0 104.8 529.3 444.0
7772.0 460.0 637.3 377.3 392.0 2392.0 168.0 296.0 380.0 316.0 356.0 309.1 212.0 308.0 263.0 408.0 80.0 172.8 420.0 132.0 633.3 528.0
7780.0 472.0 668.0 462.7 352.0 2530.7 264.0 356.0 632.0 408.0 428.0 415.4 196.0 396.0 371.0 520.0 88.0 220.0 460.0 129.6 732.0 644.0
7664.9 463.4 621.3 484.0 208.0 2542.7 272.0 276.0 600.0 536.0 648.0 414.3 280.0 505.0 457.0 764.0 148.0 244.0 580.0 178.4 850.7 792.0
7532.0 480.0 516.0 396.0 216.0 2289.3 308.0 368.0 600.0 696.0 600.0 442.3 312.0 577.0 619.0 820.0 136.0 321.6 628.0 224.0 193.3 832.0
8152.0 444.0 532.0 441.3 232.0 2306.7 336.0 428.0 748.0 724.0 668.0 501.1 284.0 629.0 705.0 900.0 200.0 372.0 708.0 259.2 169.3 128.0
7364.0 424.0 581.3 436.0 192.0 2288.0 412.0 436.0 704.0 816.0 728.0 465.1 356.0 599.0 753.0 920.0 204.0 385.6 936.0 348.0 154.7 108.0
7044.0 276.0 562.7 418.7 220.0 2324.0 264.0 484.0 588.0 704.0 492.0 432.6 372.0 598.0 754.0 102.0 208.0 424.0 888.0 371.2 126.7 104.0
7024.0 232.0 540.0 478.7 220.0 2149.3 312.0 448.0 648.0 576.0 552.0 458.3 396.0 524.0 775.0 920.0 168.0 424.0 824.0 351.2 163.3 100.0
7468.0 260.0 538.7 432.0 164.0 2205.3 204.0 448.0 520.0 540.0 508.0 444.6 324.0 488.0 735.0 784.0 165.5 376.8 724.0 386.4 140.7 124.0
6968.0 220.0 469.3 434.7 104.0 2048.0 224.0 312.0 608.0 492.0 474.3 320.0 538.0 717.0 680.0 140.0 432.0 752.0 368.0 144.0 136.0
6450.7 215.2 458.7 433.3 168.0 1986.7 188.0 312.0 460.0 556.0 496.0 434.3 312.0 450.0 599.0 640.0 164.0 455.2 700.0 380.8 133.3 976.0
6292.0 176.0 445.3 474.7 136.0 1974.7 240.0 348.0 512.0 484.0 420.0 406.9 296.0 363.0 416.0 636.0 104.0 415.2 556.0 332.0 198.7 836.0
6284.0 168.0 474.7 440.0 164.0 2024.0 240.0 352.0 468.0 496.0 480.0 436.0 344.0 416.0 298.0 590.0 144.0 397.6 520.0 369.6 113.3 892.0
6277.3 165.5 566.7 382.7 145.7 1960.0 248.3 314.5 397.2 380.7 492.4 473.7 281.4 327.0 280.0 471.7 128.3 394.4 509.0 340.0 120.0 831.7
5872.0 172.0 637.3 432.0 208.0 1992.0 372.0 292.0 492.0 376.0 476.0 433.7 268.0 342.0 386.0 556.0 168.0 426.4 504.0 326.4 958.7 776.0
5652.0 164.0 412.0 441.3 216.0 2092.0 360.0 408.0 432.0 428.0 472.0 428.0 280.0 267.0 222.0 452.0 112.0 360.8 424.0 487.2 957.3 828.0
5493.3 155.6 473.3 417.3 204.4 1992.0 360.0 328.9 533.3 462.2 497.8 432.6 257.8 265.0 213.0 511.1 102.2 386.4 435.6 478.4 893.3 897.8
5528.0 188.0 457.3 498.7 156.0 1729.3 376.0 352.0 448.0 400.0 392.0 434.3 296.0 295.0 189.0 468.0 88.0 415.2 432.0 481.6 916.0 912.0
5114.2 206.9 549.3 470.7 196.0 2118.7 440.0 424.0 420.0 424.0 432.0 407.4 392.0 266.0 171.0 396.0 68.0 437.6 392.0 464.8 909.3 860.0
```

¹Note that each time stamp actually denotes a 15-min interval, e.g. 7.25 indicates the interval from 7:15-7:30AM.

- **Split Ratios:** The split ratios (β 's) are encoded in the file **Gbeta.txt**. **Gbeta.txt** is a multiple-line tab-delimited text file. Each row contains 19 β 's (floating point numbers), corresponding to the average split ratios of the 19 off-ramps in the CTM over a particular 15-min interval. The number of rows of the file is set to be 29 by default, one row for each 15-min interval in the simulation time range from 5:00am to 12:15pm. Each row denotes the split ratios of the off-ramps for the corresponding 15-min time interval. Here is an example of the **Gbeta.txt** file:

```

0.0695 0.2875 0.0148 0.0295 0.0434 0.0500 0.0170 0.0416 0.0269 0.0421 0.0140 0.0286 0.0208 0.0234 0.0624 0.0275 0.2352 0.3075 1
0.0642 0.3009 0.0189 0.0380 0.0432 0.0533 0.0214 0.0416 0.0269 0.0454 0.0279 0.0256 0.0208 0.0234 0.0576 0.0395 0.2397 0.3153 1
0.0871 0.3069 0.0189 0.0303 0.0457 0.0674 0.0205 0.0416 0.0269 0.0385 0.0285 0.0302 0.0208 0.0234 0.0727 0.0483 0.2291 0.2972 1
0.0806 0.3286 0.0174 0.0393 0.0580 0.0899 0.0280 0.0416 0.0269 0.0674 0.0410 0.0410 0.0208 0.0234 0.0706 0.0583 0.2403 0.3164 1
0.0566 0.3002 0.0199 0.0378 0.0537 0.0809 0.0847 0.0353 0.0259 0.0421 0.0370 0.0331 0.0180 0.0132 0.0727 0.0365 0.2495 0.3324 1
0.0495 0.2924 0.0397 0.0286 0.0609 0.1073 0.0700 0.0319 0.0303 0.0495 0.0221 0.0364 0.0201 0.0180 0.0686 0.0451 0.2406 0.3168 1
0.0446 0.3448 0.0778 0.0475 0.0991 0.0826 0.0297 0.0346 0.0342 0.0472 0.0297 0.0373 0.0252 0.0192 0.0974 0.0436 0.2254 0.2911 1
0.0572 0.3616 0.0801 0.0560 0.1393 0.0715 0.0338 0.0442 0.0435 0.0488 0.0280 0.0350 0.0245 0.0302 0.1017 0.0599 0.2077 0.2622 1
0.0793 0.3673 0.0840 0.0544 0.1387 0.0806 0.0329 0.0390 0.0545 0.0496 0.0255 0.0302 0.0330 0.0348 0.0965 0.0568 0.2355 0.3080 1
0.0576 0.3781 0.0982 0.0832 0.1767 0.0748 0.0323 0.0445 0.0707 0.0466 0.0274 0.0299 0.0358 0.0329 0.0993 0.0504 0.2434 0.3216 1
0.0712 0.4016 0.0941 0.0656 0.1526 0.0988 0.0406 0.0505 0.0821 0.0553 0.0316 0.0454 0.0381 0.0253 0.0898 0.0560 0.2383 0.3129 1
0.1183 0.3778 0.0941 0.0650 0.2062 0.1286 0.0513 0.0721 0.0925 0.0745 0.0251 0.0661 0.0444 0.0324 0.0954 0.0647 0.2341 0.3057 1
0.1057 0.3778 0.1057 0.0987 0.1794 0.1400 0.0582 0.0612 0.0969 0.0669 0.0337 0.0515 0.0422 0.0358 0.0965 0.0675 0.2213 0.2841 1
0.0973 0.3907 0.1280 0.0794 0.1700 0.1274 0.0471 0.0694 0.1010 0.0548 0.0272 0.0469 0.0368 0.0416 0.1067 0.0668 0.2257 0.2915 1
0.1433 0.3481 0.1409 0.0895 0.1699 0.1126 0.0564 0.0544 0.0790 0.0454 0.0253 0.0484 0.0394 0.0458 0.1214 0.0576 0.2198 0.2818 1
0.1167 0.3383 0.1187 0.0599 0.1250 0.1171 0.0568 0.0486 0.0781 0.0674 0.0316 0.0519 0.0465 0.0468 0.1241 0.0734 0.2268 0.2934 1
0.0838 0.3217 0.1039 0.0543 0.0778 0.1040 0.0553 0.0550 0.0710 0.0682 0.0333 0.0445 0.0486 0.0569 0.1330 0.0633 0.2283 0.2958 1
0.0864 0.2989 0.0803 0.0575 0.0878 0.0911 0.0519 0.0493 0.0587 0.0571 0.0297 0.0451 0.0439 0.0552 0.1359 0.0655 0.2325 0.3029 1
0.0995 0.2879 0.0631 0.0530 0.0693 0.0863 0.0550 0.0560 0.0562 0.0695 0.0438 0.0478 0.0442 0.0509 0.1310 0.0593 0.2371 0.3107 1
0.1137 0.2680 0.0471 0.0729 0.0869 0.1099 0.0559 0.0549 0.0595 0.0738 0.0490 0.0534 0.0515 0.0603 0.1469 0.0744 0.2439 0.3226 1
0.0779 0.2618 0.0393 0.0528 0.0845 0.1042 0.0683 0.0612 0.0589 0.0873 0.0383 0.0535 0.0564 0.0597 0.1407 0.0591 0.2402 0.3161 1
0.0914 0.2760 0.0340 0.0497 0.0749 0.1030 0.0720 0.0682 0.0592 0.0783 0.0472 0.0518 0.0515 0.0593 0.1274 0.0634 0.2359 0.3087 1
0.0874 0.2677 0.0276 0.0570 0.0801 0.1072 0.0690 0.0733 0.0616 0.0595 0.0464 0.0557 0.0501 0.0578 0.1498 0.0701 0.2395 0.3150 1
0.0834 0.2629 0.0232 0.0517 0.0701 0.1026 0.0862 0.0833 0.0712 0.0671 0.0372 0.0555 0.0561 0.0645 0.1412 0.0639 0.2497 0.3329 1
0.1089 0.2499 0.0277 0.0544 0.0898 0.1112 0.0840 0.0791 0.0719 0.0666 0.0394 0.0543 0.0576 0.0587 0.1390 0.0667 0.2572 0.2462 1
0.1029 0.2508 0.0212 0.0481 0.0927 0.1061 0.0981 0.0872 0.0782 0.0622 0.0385 0.0587 0.0667 0.0877 0.1441 0.0647 0.2496 0.3326 1
0.0841 0.2727 0.0217 0.0559 0.1005 0.0983 0.1040 0.0817 0.0749 0.0591 0.0385 0.0551 0.0630 0.0817 0.1500 0.0785 0.2408 0.3172 1
0.0916 0.2799 0.0251 0.0465 0.1028 0.1110 0.1077 0.0860 0.0772 0.0762 0.0464 0.0571 0.0641 0.0736 0.1398 0.0703 0.2454 0.3252 1
0.0916 0.2799 0.0251 0.0465 0.1028 0.1110 0.1077 0.0860 0.0772 0.0762 0.0464 0.0571 0.0641 0.0736 0.1398 0.0703 0.2454 0.3252 1

```

The 19th off-ramp actually corresponds to the downstream mainline outlet at Fair Oaks, hence its split ratio is set to 1 by default.

5. *Run simulation.* Two Matlab M-files, which are stored in the directory **\$CTM_HOME\$/matlab/**, can be used to set up and run simulations. The user can edit the list of input file names in **loadtip*.m**, and can then run **simscript*.m** to invoke the MCTM simulator from the Matlab command prompt.
6. *Process outputs and display results.* The output data are generated by the C++ simulator in the form of Matlab M-files. All the output data files are written to the directory **\$CTM_HOME\$/Output0/**. The Matlab command “*load*” can be used to extract the data from the M-files. There are 7 output data files created by the MCTM simulator.
 - **paraout.m** This file stores the geometry information of the highway, such as the number of lanes in each cell, lengths of the cells, and additionally stores the split ratios, demands, and initial condition. It also contains information relating to the simulation time step and control interval.
 - **time.m** This file records the simulation time step indices. The default step size is 10 sec. Here is an example of the **time.m** file (showing the first 20 lines here; the actual file has more than 2, 600 lines):

```

1
2
3
4
5
6
7
8
9
10
11
12

```



```

273.3088 1290.8706 50.9051 118.6129 177.2455 204.5195 53.7306 159.2116 84.0611 126.8682 55.2102 110.9079 73.7315 62.6227 194.7838
293.0300 1286.7256 47.9485 116.7659 173.0330 185.8474 54.4687 151.6920 85.3010 132.7470 48.0442 102.2351 67.8939 68.7171 175.1453
305.2011 1269.3483 47.3223 115.9974 169.6614 178.3976 55.9904 146.3045 85.7322 134.8632 38.9115 103.1816 69.1126 70.7076 169.8037
313.7426 1252.6591 46.6868 116.7267 167.5038 179.7942 57.2975 142.9482 89.0027 135.4961 40.1992 101.9604 72.1253 72.4857 172.9364
319.8274 1246.0581 46.0707 117.1559 167.0538 184.1255 58.1967 141.5673 91.8738 135.8667 41.6890 95.4710 74.0119 74.7687 178.6048
324.1690 1250.3254 45.7654 117.1393 167.1712 188.0205 58.8540 141.6258 93.5329 136.2541 43.0696 90.3525 75.1085 76.9846 184.6415
327.2675 1262.7117 45.8438 116.7539 167.2132 190.4547 59.4494 142.4832 94.1684 137.3899 44.1680 87.8012 75.6133 78.8702 190.7459
329.4787 1279.8818 46.2346 116.1005 166.9391 191.6875 60.0670 143.6908 94.2312 139.3895 44.8717 87.3034 75.0843 80.3203 196.7877
331.0568 1299.0662 46.8239 115.3482 166.3132 192.2361 60.7094 145.0325 94.1138 141.8337 45.2768 88.0145 73.6437 81.1042 202.5471
332.1830 1318.3225 47.5083 114.6933 165.4482 192.4521 61.3446 146.4377 94.0536 144.2004 45.5213 89.1894 71.8122 81.1113 207.7693
332.9867 1336.4492 48.2108 114.2923 164.5457 192.4769 61.9392 147.8881 94.1507 146.1438 45.7822 90.3665 70.1060 80.4550 212.1098
333.5603 1352.8038 48.8821 114.2282 163.8194 192.3252 62.4709 149.3659 94.4226 147.5572 46.1917 91.3531 68.8351 79.3979 215.2152
333.9697 1367.1254 49.4940 114.5101 163.4319 191.9779 62.9288 150.8406 94.8511 148.5094 46.7715 92.1691 68.0854 78.2284 216.8837
334.2618 1379.3937 50.0339 115.0940 163.4661 191.4449 63.3084 152.2735 95.4082 149.1503 47.4499 92.9499 67.7912 77.1715 217.1593
334.4703 1389.7283 50.4991 115.9068 163.9271 190.7892 63.6089 153.6266 96.0661 149.6378 48.1233 93.8309 67.8274 76.3548 218.3127
334.6191 1398.3208 50.8927 116.8670 164.7614 190.1167 63.8314 154.8676 96.7988 150.0985 48.7094 94.8695 68.0577 75.8172 214.7441
334.7253 1405.3903 51.2212 117.8991 165.8822 189.5506 63.9796 155.9722 97.5810 150.6176 49.1707 96.0314 68.4114 75.5404 212.8687
334.8011 1411.1573 51.4921 118.9404 167.1914 189.2019 64.0607 156.9236 98.3881 151.2421 49.5105 97.2258 68.8481 75.4819 211.0314
334.8552 1415.8285 51.7137 119.9441 168.5953 189.1483 64.0867 157.7121 99.1963 151.9904 49.7579 98.3533 69.3618 75.6003 209.4673
334.8938 1419.5898 51.8935 120.8783 170.0148 189.4250 64.0738 158.3358 99.9837 152.8602 49.9505 99.3425 69.9536 75.8653 208.3030
...

```

- **n.m** This file records the occupancies of the cells during the simulation (in number of vehicles) at every step. Here is an example of the **n.m** file (showing the first 20 rows and first 16 columns; the actual file has more than 2,600 rows and 40 columns):

```

14.1290 40.9027 15.2560 18.6683 53.9802 10.8304 22.5567 10.1525 26.3925 20.7473 18.3389 20.0481 18.2138 28.1692 37.2090 13.8495
14.1071 42.6016 16.0849 18.4305 53.2512 10.6889 22.4584 10.4587 26.2188 20.3430 18.8166 21.0254 17.4837 28.4715 38.2486 13.9224
14.1055 43.7939 16.8194 18.8787 52.5511 10.5454 22.2833 10.4597 26.3837 20.0843 18.8243 21.8131 17.6205 28.2786 39.1415 14.1941
14.1054 44.6432 17.3868 19.5497 52.2741 10.4062 22.0604 10.3902 26.4807 20.0304 18.6957 22.2399 18.0450 28.2245 39.7557 14.5055
14.1053 45.2492 17.8060 20.2030 52.4532 10.3373 21.8121 10.2925 26.4769 20.0445 18.6105 22.3978 18.4267 28.4172 40.2048 14.7663
14.1053 45.6817 18.1100 20.7512 52.9728 10.3550 21.6060 10.1811 26.3898 20.0495 18.5794 22.4356 18.6653 28.7505 40.6115 14.9693
14.1053 45.9904 18.3285 21.1796 53.6931 10.4432 21.4963 10.0846 26.2421 20.0166 18.5681 22.4387 18.7861 29.0998 41.0333 15.1407
14.1053 46.2107 18.4851 21.5019 54.4979 10.5764 21.5025 10.0284 26.0721 19.9416 18.5462 22.4341 18.8399 29.3962 41.4722 15.3040
14.1053 46.3679 18.5970 21.7392 55.3057 10.7309 21.6152 10.0235 25.9241 19.8379 18.4981 22.4196 18.8610 29.6216 41.9061 15.4681
14.1053 46.4800 18.6770 21.9117 56.0662 10.8896 21.8096 10.0677 25.8334 19.7296 18.4236 22.3852 18.8635 29.7823 42.3123 15.6315
14.1053 46.5601 18.7340 22.0361 56.7523 11.0412 22.0567 10.1507 25.8189 19.6426 18.3349 22.3257 18.8486 29.8901 42.6756 15.7880
14.1053 46.6173 18.7748 22.1255 57.3531 11.1795 22.3297 10.2598 25.8827 19.5961 18.2507 22.2448 18.8146 29.9535 42.9883 15.9319
14.1053 46.6580 18.8038 22.1895 57.8678 11.3014 22.6074 10.3825 26.0146 19.6002 18.1892 22.1550 18.7623 29.9772 43.2477 16.0592
14.1053 46.6871 18.8246 22.2353 58.3013 11.4065 22.8745 10.5089 26.1983 19.6555 18.1637 22.0729 18.6981 29.9647 43.4530 16.1677
14.1053 46.7079 18.8394 22.2680 58.6618 11.4954 23.1215 10.6316 26.4154 19.7555 18.1805 22.0148 18.6322 29.9219 43.6050 16.2565
14.1053 46.7227 18.8500 22.2914 58.9584 11.5696 23.3432 10.7458 26.6487 19.8899 18.2391 21.9929 18.5767 29.8580 43.7061 16.3254
14.1053 46.7333 18.8575 22.3081 59.2003 11.6308 23.5374 10.8488 26.8940 20.0469 18.3340 22.0135 18.5425 29.7858 43.7616 16.3750
14.1053 46.7409 18.8629 22.3200 59.3963 11.6808 23.7046 10.9395 27.1109 20.2152 18.4567 22.0769 18.5373 29.7196 43.7794 16.4065
14.1053 46.7463 18.8667 22.3285 59.5541 11.7215 23.8463 11.0178 27.3221 20.3854 18.5977 22.1786 18.5644 29.6729 43.7706 16.4225
14.1053 46.7501 18.8695 22.3346 59.6805 11.7542 23.9650 11.0844 27.5133 20.5501 18.7478 22.3109 18.6233 29.6565 43.7481 16.4264
...

```

The command script, **simscript*.m**, calls another file, **plotctm*.m**, which processes the aforementioned output files to produce a variety of assessment aids, such as the simulated Total Travel Time, and error measures that compare simulated quantities to their PeMS-derived counterparts. Contour tables for density, flow and speed are produced, which can be loaded into Excel for further analysis.

6.2.1 Data Processing Software for MCTM C++ Simulator

Matlab M-files were prepared to process elements of PeMS data to produce quantities necessary for the MCTM simulation tests described in Chapter 5.

gabdata_15minavgNaN5.m

Inputs:

- Station definition file (**defstation210p.m**)
- 30-second and 5-minute PeMS data files (dataweekX_o30.mat and dataweekX_o5.mat, where X is the week index, 1 through 10)

Processing Notes:

- Aggregate and average quantities computed

- Scaling corrections: automatic scaling corrections for missing lanes of ML data, encoded in the `goodMLloops` array, which is created by **`makegoodMLloops.m`**.
- All output quantities are first ZOH-corrected to remove NaNs and negative entries (and zeros in some cases). The number of missing entries initially in each data vector is recorded. Missing PeMS data is represented by zeros for the following quantities: 5-min ML flows, occupancies and speeds (`TMLflow5`, `TMLocc5`, `TMLvel5` matrices). Missing PeMS data is represented by negative values for the following quantities: 5-min ML g -factors, and 30-sec occupancies and speeds (`TMLg5`, `T**flow30`, `T**occ30` matrices). All negatives and NaNs (and zeros in some cases) are excluded from averages.

Outputs:

- HOV: flow, speed, and density – 5-min lanewise, 15-min averages of 5-min values
- ML: flow and density – 5-min lanewise and lane-aggregate, 15-min averages of 5-min lane-aggregate values
- FR: 15-min averages of 30-sec flows; cumulative and lanewise
- OR: 15-min averages of 30-sec Loop 1 flow

`gabdata_15minavgZOH5.m`: Applies ZOH to `gabdata_15minavgNaN5.m` ML data sets.

Hand-counted data preparation:

Data plotting and adjustments to manual-count data ordering. The following are the main steps added to Gabriel Gomes's [24] `readdata2.m` file:

1. Generate Matlab plot showing available days of hand-counted data for each ramp (days vs. ramp indices).
2. Create `ORindices` and `FRindices` vectors that map the natural OR/FR indices (1:22 and 1:14) to the mixed hand-count indices (1:36).
3. Create `rampdayid` array, which maps PeMS-set-2 week and day indices to a matrix containing the hand-count ramp indices (1:36) along the rows and Excel sheet indices along the columns. The day-to-sheet correspondence varies from ramp to ramp.
4. Use `rampdayid` to rearrange hand-count data into a similar format as PeMS set 2 data, to allow easier comparisons.
5. Create `CdataDayOrder`, `CdataOR`, and `CdataFR` arrays that contain ramp volumes that can be accessed using PeMS-set-2 week and day indices, in addition to hand-count ramp indices.
6. Plot sorted data and create 5-sec interpolated and filtered data sets.
7. Store sorted ramp data in `Caltrans210Data_DayOrder.mat`.

Adjustments to composite boundary flow data set of [24]. The following are the main steps added to the readdata3.m file:

1. Extend time range to 5a-11.75p.
2. Remove HOV flows from mainline flows in composite data set. This was later used as a basis for creating demand sets for individual days.
3. Store original and non-HOV boundary flows for full segment (to Fair Oaks ML) in BoundaryFlowsFO_5_12.mat.

Chapter 7

Globally Optimal Solutions to the Onramp Metering Problem

This chapter considers the problem of regulating access flows to freeways as a means of reducing the effects of recurrent congestion. The many possible approaches to this problem can be classified in several ways: traffic-responsive versus open-loop, local versus system-wide, static versus dynamic, network versus freeway models, considering versus ignoring the effects of diversion. The approach presented here falls, in all cases, in the latter category.

One of the first applications of mathematical programming to the problem of onramp control was by Wattleworth in 1965 [28]. This early formulation was based on a static model of traffic behavior, whereby the flows at any cross-section in the system could be expressed as the sum of the flows entering the freeway upstream of that location, scaled by a known proportion of vehicles that did not exit at any upstream offramp. This density-less model allowed the formulation of a linear program, since it avoided the important non-linearity in freeway traffic behavior - the relationship between flow and density also known as the *fundamental diagram*.

Many later contributions have built upon the original formulation by Wattleworth. Yuan and Kreer [29] proposed a quadratic cost to replace Wattleworth's linear maximization of onramp flows, in order to achieve a more equitable distribution of the control effort. Chen et al. [30] suggested the use of Total Travel Distance as the objective. Wang and May [31] discussed several more enhancements, and extended the model to consider the effects of voluntary diversion to surface streets. Later authors further extended the model to capture the entire *corridor*, which comprises both the freeway and an alternative parallel route that allows drivers some flexibility in their choice of freeway access points. Payne and Thompson [32] considered "Wardrop's first principle" as dictating the selection of routes by drivers, coupled with an onramp control formulation similar to Wattleworth's, and solved it with a suboptimal dynamic programming algorithm. Iida et al. [33] posed a similar problem, and employed a heuristic numerical method consisting of iterated solutions of two linear programs (control and assignment).

Another more recent enhancement has been the consideration of dynamic models. Most problem formulations using dynamic models have reverted to the simpler situation, where the effect of onramp control on access point selection is not considered. Examples include Lei [34], Kotsialos [35], and Hegyi [36]. In these three cases, the numerical method used to solve the resulting nonlinear optimization problem was gradient-based, and therefore provided only local solutions.

The approach presented here is based on an observation stemming from two facts. The first fact,

shown in [37], is that minimizing the Total Travel Time is equivalent to maximizing a weighted sum of flows. The second fact is the specification by the LWR theory [13] of a *concave* fundamental diagram. Relaxing the equality constraint imposed by the fundamental diagram to a “ \leq ” constraint therefore results in a convex problem. Because travel time is favored by higher flows, it is not unreasonable to expect the solution to “naturally” seek the upper boundary.

This idea of relaxing the flow constraint has been suggested previously by Papageorgiou in [38] and Ziliaskopoulos in [39]. However [38] wrongly asserted that the solution to the relaxed problem would always fall on the upper boundary as long as positive and sufficiently large cost weights were assigned to the mainline and onramp flows. To see why this is not so, consider a flow $f_i^{[k]}$ from a section i into a *congested* section $i + 1$ during time interval k (see Figure 7.1). An increase in $f_i^{[k]}$ produces an increase in the density of $i + 1$ at time $k + 1$, which in turn causes $f_i^{[k+1]}$ to fall, because $i + 1$ is congested. Thus, the initial increase to $f_i^{[k]}$ will be favored by the objective (weighted maximization of flows) only if its positive effect outweighs the negative effect of decreasing $f_i^{[k+1]}$. One of the findings of this work is that, in addition to positivity, the cost weights must also decrease in time.

In this chapter we first introduce a model for a freeway with onramp control. The model is similar to the Modified Cell Transmission Model (MCTM) reviewed in Chapter 4, in that inter-cellular flows are computed as the minimum of what can be sent by the upstream cell and what can be received by the downstream cell. The important distinction is in the treatment of merging flows: to make the model more amenable to mathematical optimization, we have replaced the rule-based procedure of the MCTM with extra terms in the $\min()$ functions, weighted by *influence parameters* ($\alpha_i, \xi_i, \gamma_i$). It is shown that an appropriate selection of the parameters and boundary conditions guarantees an evolution of the model that remains within certain implicit constraints (Eq. (7.8)). This result is used to ensure the physical realizability of the results. Two optimization problems, one nonlinear and one linear, are then formulated. The solutions to these two problems are generally not the same. However, it is found that cost weights can be found that render them equivalent. A numerical method for generating such cost weights is designed and tested.

7.1 Notation

The freeway is partitioned into I sections, or links, each containing at most one onramp and/or one offramp. The sections are identified with indices beginning with zero at the upstream end, and increasing sequentially downstream. Time is divided into K discrete intervals of duration Δt . Figure 7.1 illustrates the model variables.

Sets

- \mathcal{I} : set of all freeway sections. $\mathcal{I} = \{0 \dots I - 1\}$
- \mathcal{K} : set of time intervals. $\mathcal{K} = \{0 \dots K - 1\}$
- \mathcal{E}_n : set of sections with onramps. $\mathcal{E}_n \subseteq \mathcal{I}$
- \mathcal{E}_n^+ : set of sections with metered onramps. $\mathcal{E}_n^+ \subseteq \mathcal{E}_n$

Variables (All normalized to vehicle units)

- $\rho_i^{[k]}$: vehicles in section i at time $k\Delta t$.
- $l_i^{[k]}$: vehicles queuing in onramp i at time $k\Delta t$.

$f_i[k]$: vehicles going from i to $i+1$ during interval k .
 $r_i[k]$: vehicles entering i from an onramp during k .
 $r_i^c[k]$: metering rate for onramp i .
 $d_i[k]$: demand for onramp i .
 $s_i[k]$: vehicles using offramp i during interval k .
 $\beta_i[k]$: dimensionless split ratio for offramp i .

$\beta_i[k]$ is defined $\forall i \in \mathcal{I}$, and is set to 0 whenever i does not contain an offramp. We also define an onramp indicator δ_i :

$$\delta_i \triangleq \begin{cases} 1 & \text{if } i \in \mathcal{E}n \\ 0 & \text{else} \end{cases}$$

Model parameters

v_i	: normalized freeflow speed	$\in [0, 1]$
w_i	: congestion wave speed	$\in [0, 1]$
$\bar{\rho}_i$: jam density	[veh]
\bar{f}_i	: mainline capacity	[veh]
\bar{s}_i	: offramp capacity	[veh]
$\alpha_i, \gamma_i, \xi_i$: influence parameters	$\in [0, 1]$

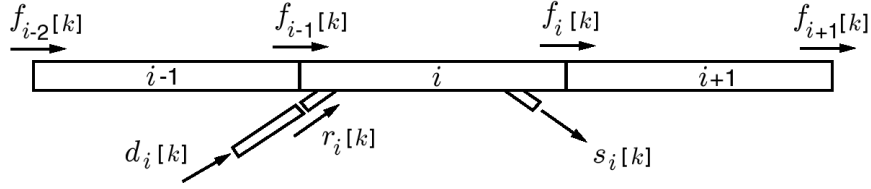


Figure 7.1: Interpretation of model variables

7.2 Traffic Model

The five components of the freeway model are given in Eqs. (7.1) through (7.5). Similarly to [38] and in contrast to [39], it is assumed that the offramp split ratios are known and control independent.

Offramp flows $\forall i \in \mathcal{I}, k \in \mathcal{K}$:

$$s_i[k] = \beta_i[k] f_i[k] \quad (7.1)$$

Mainline conservation $\forall i \in \mathcal{I}, k \in \mathcal{K}$:

$$\rho_i[k+1] = \rho_i[k] + f_{i-1}[k] + \delta_i r_i[k] - f_i[k] - s_i[k] \quad (7.2)$$

with initial condition $\rho_i[0]$. The upstream mainline boundary is modeled as an additional onramp, and $f_{-1}[k]$ is set to 0, in order to avoid the numerical problems related to mainline congestion obstructing vehicle sources.

Onramp conservation $\forall i \in \mathcal{E}n, k \in \mathcal{K} :$

$$l_i[k+1] = l_i[k] + d_i[k] - r_i[k] \quad (7.3)$$

with initial and boundary conditions $l_i[0]$ and $d_i[k]$.

Mainline flows $\forall i \in \mathcal{I}, k \in \mathcal{K} :$

$$f_i[k] = \min \left\{ \begin{array}{l} v_i(\rho_i[k] + \delta_i \gamma_i r_i[k]) - s_i[k] ; \\ w_{i+1}(\bar{\rho}_{i+1} - \rho_{i+1}[k]) - \delta_{i+1} \alpha_{i+1} r_{i+1}[k] ; \\ \bar{f}_i - s_i[k] ; \frac{\bar{s}_i}{\beta_i[k]} \end{array} \right\} \quad (7.4)$$

Onramp flows $\forall i \in \mathcal{E}n, k \in \mathcal{K} :$

$$r_i[k] = \begin{cases} \min \{ l_i[k] + d_i[k] ; \xi_i(\bar{\rho}_i - \rho_i[k]) ; r_i^c[k] \} & i \in \mathcal{E}n^+ \\ \min \{ l_i[k] + d_i[k] ; \xi_i(\bar{\rho}_i - \rho_i[k]) \} & i \in \mathcal{E}n \setminus \mathcal{E}n^+ \end{cases} \quad (7.5)$$

For compactness of notation, define $\bar{\beta}_i[k] = 1 + \beta_i[k]$. Then, using (7.1) to eliminate $s_i[k]$ in (7.2) and (7.4) we get:

$$\rho_i[k+1] = \rho_i[k] + f_{i-1}[k] + \delta_i r_i[k] - \bar{\beta}_i[k] f_i[k] \quad (7.6)$$

$$f_i[k] = \min \left\{ \begin{array}{l} \frac{v_i}{\bar{\beta}_i[k]}(\rho_i[k] + \delta_i \gamma_i r_i[k]) ; \\ w_{i+1}(\bar{\rho}_{i+1} - \rho_{i+1}[k]) - \delta_{i+1} \alpha_{i+1} r_{i+1}[k] ; \\ \frac{\bar{f}_i}{\bar{\beta}_i[k]} ; \frac{\bar{s}_i}{\beta_i[k]} \end{array} \right\} \quad (7.7)$$

The complete traffic model consists of equations (7.3), (7.5), (7.6), and (7.7). α_i , γ_i , and ξ_i respectively dictate the influence of downstream and upstream onramp flows on mainline flow, and the influence of mainline density on onramp flow.

7.2.1 Theorem

The following theorem provides conditions on the model parameters and boundary conditions that ensure a physically reasonable evolution of the model.

$$\left\{ \begin{array}{l} \rho_i[0] \in [0, \bar{\rho}_i] ; v_i, w_i, \alpha_i, \gamma_i \in [0, 1] \\ l_i[0], \bar{f}_i, \bar{s}_i, \beta_i[k], d_i[k], f_{-1}[k], r_i^c[k] \geq 0 \\ \xi_i \in [0, \min(\frac{w_i}{\alpha_i}, \frac{1-w_i}{1-\alpha_i})] \end{array} \right\} \begin{array}{l} \forall k \in \mathcal{K} \\ \forall i \in \mathcal{I} \end{array} \quad (7.8)$$

↓

$$\left\{ \begin{array}{l} \rho_i[k] \in [0, \bar{\rho}_i] \\ l_i[k], f_i[k], r_i[k] \geq 0 \end{array} \right\} \begin{array}{l} \forall k \in \mathcal{K} \\ \forall i \in \mathcal{I} \end{array}$$

Proof

The proof is by induction. Assuming that $\rho_i[k] \in [0, \bar{\rho}_i]$ and $l_i[k] \geq 0$ for some k , we show that it holds for $k+1$. First, from (7.5), with $l_i[k] \geq 0$, $d_i[k] \geq 0$, $\xi_i \geq 0$, $\rho_i[k] \leq \bar{\rho}_i$, $r_i^c[k] \geq 0$, it follows that $r_i[k] \geq 0$. To show $f_i[k] \geq 0$, we need to check that each of the four terms in (7.7) is positive. The only non-obvious one is the second. But,

$$\begin{aligned} \xi_{i+1} &\leq \frac{w_{i+1}}{\alpha_{i+1}} \\ &\Downarrow \\ \xi_{i+1}(\bar{\rho}_{i+1} - \rho_{i+1}[k]) &\leq \frac{w_{i+1}}{\alpha_{i+1}}(\bar{\rho}_{i+1} - \rho_{i+1}[k]) \\ &\Downarrow \\ \delta_{i+1}r_{i+1}[k] &\leq \frac{w_{i+1}}{\alpha_{i+1}}(\bar{\rho}_{i+1} - \rho_{i+1}[k]) \\ &\Downarrow \\ w_{i+1}(\bar{\rho}_{i+1} - \rho_{i+1}[k]) - \delta_{i+1}\alpha_{i+1}r_{i+1}[k] &\geq 0 \end{aligned}$$

Therefore, $f_i[k] \geq 0$. Using the above, we can deduce $l_i[k+1] \geq 0$ and $\rho_i[k+1] \in [0, \bar{\rho}_i]$:

$$\begin{aligned} l_i[k+1] &= l_i[k] + d_i[k] - r_i[k] \\ &\geq l_i[k] + d_i[k] - (l_i[k] + d_i[k]) \\ &= 0 \end{aligned}$$

$$\begin{aligned} \rho_i[k+1] &= \rho_i[k] + f_{i-1}[k] - \bar{\beta}_i[k]f_i[k] + \delta_i r_i[k] \\ &\geq \rho_i[k] - \bar{\beta}_i[k]f_i[k] + \delta_i r_i[k] \\ &\geq \rho_i[k] - \bar{\beta}_i[k] \frac{v_i}{\bar{\beta}_i[k]} (\rho_i[k] + \delta_i \gamma_i r_i[k]) + \delta_i r_i[k] \\ &= (1 - v_i)\rho_i[k] + \delta_i(1 - v_i \gamma_i)r_i[k] \\ &\geq 0 \end{aligned}$$

$$\begin{aligned} \rho_i[k+1] &= \rho_i[k] + f_{i-1}[k] - \bar{\beta}_i[k]f_i[k] + \delta_i r_i[k] \\ &\leq \rho_i[k] + f_{i-1}[k] + \delta_i r_i[k] \\ &\leq \rho_i[k] + w_i(\bar{\rho}_i - \rho_i[k]) - \delta_i \alpha_i r_i[k] + \delta_i r_i[k] \\ &= (1 - w_i)\rho_i[k] + \delta_i r_i[k](1 - \alpha_i) + w_i \bar{\rho}_i \\ &\leq (1 - w_i)\rho_i[k] + \delta_i \xi_i (\bar{\rho}_i - \rho_i[k])(1 - \alpha_i) + w_i \bar{\rho}_i \\ &= \begin{cases} (1 - w_i)\rho_i[k] + w_i \bar{\rho}_i & \text{if } i \notin \mathcal{E}n \\ (1 - \bar{w}_i)\rho_i[k] + \bar{w}_i \bar{\rho}_i & \text{if } i \in \mathcal{E}n \end{cases} \\ &\leq \bar{\rho}_i \end{aligned}$$

where $\bar{w}_i \triangleq w_i + \xi_i(1 - \alpha_i)$. The last line holds since by assumption both w_i and $\bar{w}_i \in [0, 1]$. \blacksquare

7.3 Problem Formulation

Papageorgiou shows in [40] that *Total Travel Time* (TTT) can be expressed as a weighted sum of offramp flows and other control independent terms, with weights decreasing linearly in time so as

to favor earlier exiting flows. Similarly, the *Total Travel Distance* is also a linear combination of mainline and onramp flows. These two popular objective functions are captured by the *Generalized Total Travel Time* (gTTT):

$$g^{TTT} \triangleq - \sum_{k \in \mathcal{K}} \left[\sum_{i \in \mathcal{I}} a_i[k] f_i[k] + \sum_{i \in \mathcal{E}n} b_i[k] r_i[k] \right] \quad (7.9)$$

$a_i[k]$ and $b_i[k]$ in (7.9) are positive *cost weights* that can be selected to obtain a desired objective function. For example, TTT is minimized by setting:

$$\begin{aligned} a_i[k] &= (\mathbf{K} - k) \beta_i[k] \\ b_i[k] &= 0 \end{aligned} \quad (7.10)$$

Bounds on the control and state are often required. Explicit bounds on flows and densities are not necessary due to Eq. (7.8). Eq. (7.11) places upper and lower limits on the ramp metering rates.

$$\underline{r}_i^c \leq r_i^c[k] \leq \bar{r}_i^c \quad (7.11)$$

An upper limit on the length of the onramp queue is not enforced here for reasons explained in Section 7.4.1. The nonlinear optimization problem \mathcal{P}_A is now stated as follows:

Problem \mathcal{P}_A : Given initial and boundary conditions satisfying (7.8), find

$$\psi_A^* = \arg \min_{\psi \in \Omega_A} g^{TTT}(\psi) \quad (7.12)$$

$$\Omega_A = \left\{ \begin{aligned} &\psi = \{\rho_i[k], l_i[k], f_i[k], r_i[k], r_i^c[k]\} : \\ &\text{Dynamic equations : (7.3), (7.6),} \\ &\text{Concave constitutive relations : (7.5), (7.7)} \\ &\text{Control Bounds : (7.11) } \end{aligned} \right\}$$

Problem \mathcal{P}_B is a linear program formed by relaxing equality constraints (7.5) and (7.7).

Problem \mathcal{P}_B : Given initial and boundary conditions satisfying (7.8), find

$$\psi_B^* = \arg \min_{\psi \in \Omega_B} g^{TTT}(\psi) \quad (7.13)$$

$$\Omega_B = \left\{ \begin{aligned} &\psi = \{\rho_i[k], l_i[k], f_i[k], r_i[k], r_i^c[k]\} : \\ &\text{Dynamic equations : (7.3), (7.6),} \\ &\text{Linear inequality constraints : (7.14) – (7.19)} \\ &\text{Control Bounds : (7.11) } \end{aligned} \right\}$$

$\forall k \in \mathcal{K}, i \in \mathcal{I}$:

$$f_i[k] \leq \frac{v_i}{\beta_i[k]} (\rho_i[k] + \delta_i \gamma_i r_i[k]) \quad (7.14)$$

$$f_i[k] \leq w_{i+1} (\bar{\rho}_{i+1} - \rho_{i+1}[k]) - \delta_{i+1} \alpha_{i+1} r_{i+1}[k] \quad (7.15)$$

$$f_i[k] \leq \min \left\{ \frac{\bar{f}_i}{\beta_i[k]} ; \frac{\bar{s}_i}{\beta_i[k]} \right\} \quad (7.16)$$

$$\forall k \in \mathcal{K}, i \in \mathcal{E}n : \quad r_i[k] \leq l_i[k] + d_i[k] \quad (7.17)$$

$$r_i[k] \leq \xi_i (\bar{\rho}_i - \rho_i[k]) \quad (7.18)$$

$$\forall k \in \mathcal{K}, i \in \mathcal{E}n^+ : \quad r_i[k] \leq r_i^c[k] \quad (7.19)$$

7.4 The Cost Weights Synthesis Problem

The goal of the cost weights synthesis (CWS) problem is to construct weights $a_i[k]$ and $b_i[k]$ that render problems \mathcal{P}_A and \mathcal{P}_B *equivalent* ($\mathcal{P}_A \equiv \mathcal{P}_B$), in the sense that their solution sets are identical:

$$\{\psi^* \text{ solves } \mathcal{P}_A\} \Leftrightarrow \{\psi^* \text{ solves } \mathcal{P}_B\} \quad (7.20)$$

For $\mathcal{P}_A \equiv \mathcal{P}_B$, all of the solutions to both \mathcal{P}_A and \mathcal{P}_B must lie in $\Omega_A \cap \Omega_B$, which in this case equals Ω_A . Furthermore, the solutions to \mathcal{P}_B must also solve \mathcal{P}_A . Given the first requirement, the second is trivially satisfied since \mathcal{P}_B is a relaxation of \mathcal{P}_A . The CWS problem can therefore be stated as: Find weights $a_i[k]$ and $b_i[k]$ such that all solutions to \mathcal{P}_B are in Ω_A . For this to happen, the weights must be such that any feasible solution *not* in Ω_A ($\psi \in \Omega_B \setminus \Omega_A$) is not a minimizer of gTTT. This requirement can be expressed in terms of feasible perturbations about ψ : $\mathcal{P}_A \equiv \mathcal{P}_B$ if for every $\psi \in \Omega_B \setminus \Omega_A$ there exists a *feasible* perturbation Δ that improves the cost. Due to the linearity of the objective, improving perturbations are characterized by $\text{gTTT}(\Delta) < 0$. The formulation of the CWS problem now becomes: Find weights $a_i[k]$ and $b_i[k]$ such that for all $\psi \in \Omega_B \setminus \Omega_A$ there exists a feasible perturbation Δ with $\text{gTTT}(\Delta) < 0$.

7.4.1 The MWCC perturbation

Points $\psi \in \Omega_B \setminus \Omega_A$ can be categorized according to which nonlinear equality constraint they violate. We define member sets $\mathbf{I}_{l\kappa}$ and $\mathbf{II}_{l\kappa}$ as:

$$\mathbf{I}_{l\kappa} = \left\{ \psi \in \Omega_B \setminus \Omega_A : \text{Eq. (7.7) not satisfied with} \right. \\ \left. i=l, k=\kappa \right\}$$

$$\mathbf{II}_{l\kappa} = \left\{ \psi \in \Omega_B \setminus \Omega_A : \text{Eq. (7.5) not satisfied with} \right. \\ \left. i=l, k=\kappa \right\}$$

There are $I \times K$ member sets of the $I_{\ell\kappa}$ type and $|\mathcal{E}n| \times K$ member sets of the $II_{\ell\kappa}$ type. A member of $I_{\ell\kappa}$ is a point $\psi \in \Omega_B \setminus \Omega_A$ for which Eq. (7.7) is violated with $i = \ell$ and $k = \kappa$, or equivalently Eqs. (7.14), (7.15), and (7.16) with $i = \ell$ and $k = \kappa$ apply as strict inequalities.

To each of the $(I + |\mathcal{E}n|) \times K$ member sets corresponds a Maximal Worst-Case Causal (MWCC) perturbation; $\bar{\Delta}_{\ell\kappa}^I$ for $I_{\ell\kappa}$ and $\bar{\Delta}_{\ell\kappa}^{II}$ for $II_{\ell\kappa}$. The definition of the MWCC perturbations is given below. The MWCC is a feasible perturbation for all points in its corresponding member set because it is feasible for the *worst-case* point, where all inequality constraints, aside from the one that defines it, are active. It is *maximal* because it selects the largest (least negative) feasible value for each of the Δf 's and Δr 's. This is done in order to maximize its beneficial effect on the cost.

$\bar{\Delta}_{\ell\kappa}^I$ is defined for $\kappa \in \mathcal{K}$, $\ell \in \mathcal{I}$ as: (7.21)

$$\begin{aligned} \Delta \rho_{i[k+1]} &= \Delta \rho_{i[k]} + \Delta f_{i-1[k]} - \bar{\beta}_{i[k]} \Delta f_{i[k]} + \delta_i \Delta r_{i[k]} \\ \Delta l_{i[k+1]} &= \Delta l_{i[k]} - \Delta r_{i[k]} \\ \Delta f_{i[k]} &= \begin{cases} 1 & i = \ell, k = \kappa \\ \min \left\{ \begin{array}{l} \frac{v_i}{\bar{\beta}_{i[k]}} (\Delta \rho_{i[k]} + \delta_i \gamma_i \Delta r_{i[k]}) ; \\ -w_{i+1} \Delta \rho_{i+1[k]} - \delta_{i+1} \alpha_{i+1} \Delta r_{i+1[k]} ; \\ 0 \end{array} \right\} & k > \kappa \\ 0 & k < \kappa \end{cases} \\ \Delta r_{i[k]} &= \min \{ \Delta l_{i[k]} ; -\xi_i \Delta \rho_{i[k]} ; 0 \} \\ \Delta r_i^c[k] &= 0 \end{aligned}$$

$\bar{\Delta}_{\ell\kappa}^{II}$ is defined for $\kappa \in \mathcal{K}$, $\ell \in \mathcal{E}n$ as: (7.22)

$$\begin{aligned} \Delta \rho_{i[k+1]} &= \Delta \rho_{i[k]} + \Delta f_{i-1[k]} - \bar{\beta}_{i[k]} \Delta f_{i[k]} + \delta_i \Delta r_{i[k]} \\ \Delta l_{i[k+1]} &= \Delta l_{i[k]} - \Delta r_{i[k]} \\ \Delta f_{i[k]} &= \min \left\{ \begin{array}{l} \frac{v_i}{\bar{\beta}_{i[k]}} (\Delta \rho_{i[k]} + \delta_i \gamma_i \Delta r_{i[k]}) ; \\ -w_{i+1} \Delta \rho_{i+1[k]} - \delta_{i+1} \alpha_{i+1} \Delta r_{i+1[k]} ; \\ 0 \end{array} \right\} \\ \Delta r_{i[k]} &= \begin{cases} 1 & i = \ell, k = \kappa \\ \min \{ \Delta l_{i[k]} ; -\xi_i \Delta \rho_{i[k]} ; 0 \} & k > \kappa \\ 0 & k < \kappa \end{cases} \\ \Delta r_i^c[k] &= 0 \end{aligned}$$

A fact not shown here is that a general perturbation such as the MWCC perturbation cannot be defined if any of the following constraints are included in \mathcal{P}_A and \mathcal{P}_B : $f_i[k] \geq 0$, $r_i[k] \geq 0$, $0 \leq l_i[k] \leq \bar{l}_i$, $0 \leq \rho_i[k] \leq \bar{\rho}_i$. This observation underscores the importance of the theorem, which guarantees all except $l_i[k] \leq \bar{l}_i$. It is also the reason why queue length constraints have been omitted.

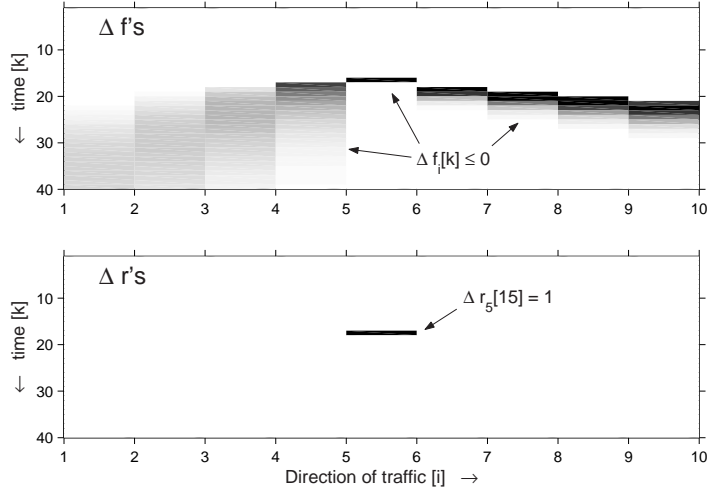


Figure 7.2: $\bar{\Delta}_{5,15}^{\text{II}}$ with parameters of Section 7.5

Each of the $(I + |\mathcal{E}n|) \times K$ MWCC perturbations can be computed offline given the layout of the freeway, the model parameters, and the offramp split ratios. Figure 7.2 shows a sample MWCC perturbation ($\bar{\Delta}_{5,15}^{\text{II}}$) with the parameters of Section 7.5. Here, a unit increase in $r_{5[15]}$ produces negative waves that propagate forward in time, and upstream and downstream on the mainline.

With all of the MWCC perturbations computed, the CWS problem can be restated as: Find $a_i[k]$ and $b_i[k]$ such that:

$$g_{\text{TTT}}(\bar{\Delta}_{\iota\kappa}^{\text{I}}) < 0 \quad \forall \kappa \in \mathcal{K}, \iota \in \mathcal{I} \quad (7.23)$$

$$g_{\text{TTT}}(\bar{\Delta}_{\iota\kappa}^{\text{II}}) < 0 \quad \forall \kappa \in \mathcal{K}, \iota \in \mathcal{E}n \quad (7.24)$$

Because each MWCC perturbation is feasible for every point in its member set, conditions (7.23) and (7.24) are sufficient to guarantee non-optimality for all $\psi \in \Omega_B \setminus \Omega_A$, and thus $\mathcal{P}_A \equiv \mathcal{P}_B$.

7.4.2 Backstepping Numerical Method

Using Eq. (7.9), Eqs. (7.23) and (7.24) are expressed as $(I + |\mathcal{E}n|) \times K$ linear equations of the form:

$$-\sum_{k \in \mathcal{K}} \left[\sum_{i \in \mathcal{I}} a_i[k] \Delta f_i[k] + \sum_{i \in \mathcal{E}n} b_i[k] \Delta r_i[k] \right] = -\epsilon \quad (7.25)$$

where Δf 's and Δr 's are components of $\bar{\Delta}_{\iota\kappa}^{\text{I}}$ or $\bar{\Delta}_{\iota\kappa}^{\text{II}}$, and ϵ is a positive number. Because the MWCC perturbation is *causal*, the summations in Eq. (7.25) only contain non-zero Δf 's and Δr 's for $k \geq \kappa$. They therefore have the following recursive formula:

$$a_{\iota[\kappa]} = - \sum_{k=\kappa+1}^{K-1} \left(\sum_{i \in \mathcal{I}} a_i[k] \Delta f_i[k] + \sum_{i \in \mathcal{E}n} b_i[k] \Delta r_i[k] \right) + \epsilon \quad (7.26)$$

$$b_{\iota[\kappa]} = - \sum_{k=\kappa+1}^{K-1} \left(\sum_{i \in \mathcal{I}} a_i[k] \Delta f_i[k] + \sum_{i \in \mathcal{E}n} b_i[k] \Delta r_i[k] \right) - a_{\iota[\kappa]} \Delta f_{\iota[\kappa]} + \epsilon \quad (7.27)$$

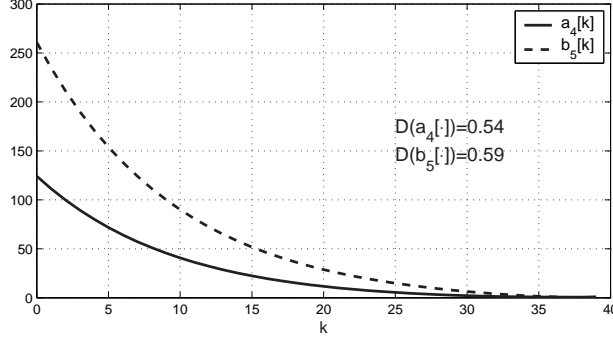


Figure 7.3: Cost weights with $\alpha_5 = \gamma_5 = 0.2$ and $\xi_5 = 0.06$

Δf 's and Δr 's in (7.26) are components of $\bar{\Delta}_{\iota\kappa}^I$, and Δf 's and Δr 's in (7.27) are components of $\bar{\Delta}_{\iota\kappa}^II$. These equations can be easily solved by setting $a_i[k-1]$ and $b_i[k-1]$ to some positive value, and computing the rest sequentially backwards.

7.5 A Simple Example

The CWS problem was solved for a simple test freeway consisting of 10 sections and 40 time intervals. A single onramp was placed at $i = 5$. Offramps were placed at $i = 4, 5$, and 9 with $\beta_i[k] = 0.1$ for all three. $v_i = 0.7$ and $w_i = 0.2$ was used for all sections.

Figure 7.3 shows cost weights found with $\alpha_5 = \gamma_5 = 0.2$, and $\xi_5 = 0.06$. A *time decay index* (D) was computed for each sequence $a_i[\cdot]$ and $b_i[\cdot]$ as the number of entries in the sequence that exceeded 10% of the first value, divided by the length of the sequence; for example, $D(a_4[\cdot]) = \text{size} \{a_4[\cdot] \geq 0.1 \times a_4[0]\} / 40$. The decay index for a constant sequence is 1.0, and the decay index for a linearly decreasing sequence, such as the TTT weights of Eq. (7.10), is 0.9. We inspect the decay indices because they give some measure of the similarity of gTTT with TTT. A minimum of 0.9 or higher among the decay indices for all $a_i[\cdot]$'s would suggest that the resulting objective function is “close” to total travel time. The decay indices for the sequences of Figure 7.3 are $D(a_4[\cdot]) = 0.54$ and $D(b_5[\cdot]) = 0.59$.

Figure 7.4 shows $\min_i \{D(a_i[\cdot])\}$ (i.e. the index of the fastest decaying mainline weight) in the top window, and $\min_i \{D(b_i[\cdot])\}$ (i.e. the index of the fastest decaying onramp weight) in the bottom window, as functions of ξ_5 , and for several values of α_5 . The decay index was found to be insensitive to γ_5 . The figure shows that the cost weights degrade less quickly, and are therefore more similar to TTT, for smaller values of α_i and ξ_i .

7.6 Modifications to the original formulation

7.6.1 Additional Assumptions

The example presented in Section 7.5 exposed two basic deficiencies in the proposed solution to the CWS problem. Ideally we would like the computed cost weights to equal the TTT costs of Eq. (7.10). Short of that, we would at least want the cost weights to be similar to Eq. (7.10) in

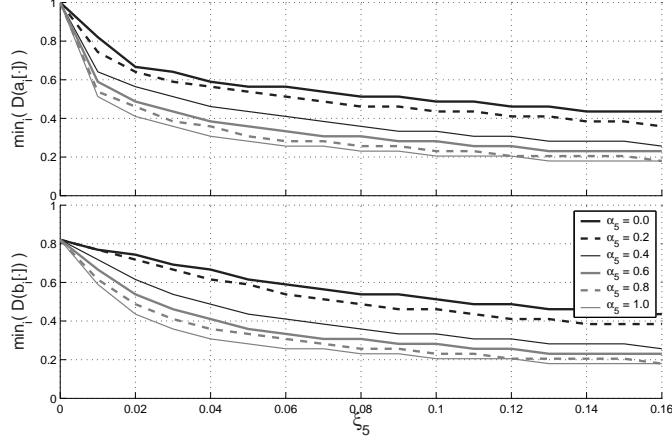


Figure 7.4: Fastest decay index vs. ξ_5 and α_5 . ($\gamma_5 = 0.2$)

some quantifiable way. The cost weights of the Figure 7.3 differed from Eq. (7.10) in two ways: 1) the $a_i[k]$'s decayed faster than a straight line, and 2) the $b_i[k]$'s were not identically zero.

A third deficiency, this one in the formulation of the optimization problem itself, was the omission of upper bounds on the lengths of the onramp queues.

$$l_i[k] \leq \bar{l}_i \quad , \quad \forall i \in \mathcal{I} \quad , \quad k \in \mathcal{K} \quad (7.28)$$

The reason for excluding the queue length constraints was that they made impossible the definition of a generalized feasible perturbation, such as the MWCC perturbation. To illustrate, consider ψ^c a feasible candidate solution to problem \mathcal{P}_B for which none of Eqs. (7.14) through (7.16) are active for a particular $i = \iota$ and $k = \kappa$ (i.e. $f_{\iota}[\kappa]$ is strictly less than the right-hand side of Eq. (7.7)). Such a candidate solution is classified as a member of $\mathbf{I}_{\iota\kappa}$. Assume also that ψ^c has:

$$\begin{aligned} f_{\iota+1}[\kappa] &= \bar{f}_{\iota+1} \\ r_{\iota+1}[\kappa+1] &= \xi_{\iota+1}(\bar{\rho}_{\iota+1} - \rho_{\iota+1}[\kappa+1]) \\ l_{\iota+1}[\kappa+2] &= \bar{l}_{\iota+1} \end{aligned}$$

In this situation, any positive perturbation to $f_{\iota}[\kappa]$ produces an increase in $\rho_{\iota+1}[\kappa+1]$, which in turn forces $r_{\iota+1}[\kappa+1]$ to decrease, and $l_{\iota+1}[\kappa+2]$ to grow beyond $\bar{l}_{\iota+1}$. We have demonstrated that no positive causal perturbation exists that is feasible for *all* members of $\mathbf{I}_{\iota\kappa}$, whenever queue length constraints are included.

Two additional assumptions are sufficient to remedy the three above-noted shortcomings:

Assumption #1: Eq. (7.18) is not active in the optimal solution for any i or k .

In other words, we assume that congestion on the mainline never obstructs vehicles entering from the onramps. This assumption permits the removal of Eq. (7.18) from the problem statement, and the “ $-\xi_i \Delta \rho_i[k]$ ” terms from the definitions of $\bar{\Delta}_{\iota\kappa}^{\text{I}}$ and $\bar{\Delta}_{\iota\kappa}^{\text{II}}$. Notice that then $\Delta r_i[k] = \Delta l_i[k] = 0$ in $\bar{\Delta}_{\iota\kappa}^{\text{I}}$, and $\Delta l_i[k] \leq 0$ in $\bar{\Delta}_{\iota\kappa}^{\text{II}}$. There is no longer a conflict between the MWCC perturbation and the queue length constraint, which requires only $\Delta l_i[k] \leq 0$. As we shall see in Section 7.7, this assumption also eliminates the problem of rapidly decaying $a_i[k]$'s. Section 7.7 also shows that the assumption is not overly restrictive, and in fact holds true for the I-210 test freeway.

Assumption #2: $\underline{r}_i^c = 0$.

This is almost never true in practice: the actual minimum metering rate on I-210 is 180 vph, which corresponds to 1 vehicle every 20 seconds. The assumption is adopted nevertheless because it reduces the number of variables and constraints, but more importantly because it leads to $b_i[k] = 0$. Recall that this is one of the qualitative features of TTT-like objective functions. Under Assumption #2, in addition to Assumption #1, the following linear program is equivalent to Problem \mathcal{P}_B :

Problem \mathcal{P}_C :

$$\psi_C^* = \arg \min_{\psi \in \Omega_C} \text{gTTT}(\psi) \quad (7.29)$$

$$\Omega_C = \left\{ \psi = \{\rho_i[k], l_i[k], f_i[k], r_i[k]\} : \right. \\ \left. \begin{array}{l} \text{Dynamic equations : (7.6), (7.3),} \\ \text{Relaxed constitutive relations : (7.14) – (7.16)} \\ \text{Onramp flow constraints : (7.30) – (7.32) } \end{array} \right\}$$

$$\forall k \in \mathcal{K}, i \in \mathcal{E}n \setminus \mathcal{E}n^+ : \quad r_i[k] = d_i[k] \quad (7.30)$$

$$\forall k \in \mathcal{K}, i \in \mathcal{E}n^+ : \quad r_i[k] \leq l_i[k] + d_i[k] \quad (7.31)$$

$$\forall k \in \mathcal{K}, i \in \mathcal{E}n^+ : \quad 0 \leq r_i[k] \leq \bar{r}_i^c \quad (7.32)$$

Problem \mathcal{P}_C is equivalent to Problem \mathcal{P}_B whenever Assumptions #1 and #2 are used. Notice that the constraint $0 \leq r_i[k]$ in Eq. 7.32 need not be explicitly enforced since it is guaranteed by the theorem of Section 7.2.1 (assuming that the solution to \mathcal{P}_C falls on the “upper boundary”). Thus, $r_i[k]$ ’s for controlled onramps in Problem \mathcal{P}_C is only explicitly constrained from above. This leads to an important simplification in the definition of the MWCC perturbation of Eqs. 7.21 and 7.22. Furthermore, having eliminated the $r_i^c[k]$ variable in Problem \mathcal{P}_C , the optimal $r_i[k]$ ’s for controlled onramps are no longer required to fall on the “upper boundary”, since that boundary can be adjusted by a-posteriori selection of $\bar{r}_i^c[k]$. A valid metering plan can be derived once the solution to \mathcal{P}_C is found, with:

$$r_i^c[k] = \max\{ r_i[k] ; 180 \text{ vph} \} \quad (7.33)$$

The main advantage of \mathcal{P}_C over \mathcal{P}_B is that neither metered nor uncontrolled $r_i[k]$ ’s in \mathcal{P}_C are required to fall on their “upper boundary”. Perturbations to $r_i[k]$ ’s and the resulting non-zero $b_i[k]$ ’s are therefore not needed.

The CWS problem is solved for Problem \mathcal{P}_C by setting all $b_i[k]$ ’s to zero, and computing $a_i[k]$ ’s with the procedure developed in Section 7.4.2, with $\bar{\Delta}_{i\kappa}^I$ ’s adjusted as per Assumption #1.

7.6.2 Dual Time Scales

A modification to the original model that was found useful for reducing the size of the LP problem, was to consider different discrete time intervals for the mainline and onramp variables. Consistency of the mainline conservation and flow equations (Eqs. (7.6) and (7.7)) requires:

$$v_i \Delta t_{mnl} \leq L_i \quad \forall i \in \mathcal{I}$$

where Δt_{mnl} is the duration of the discrete time interval, and L_i is the length of the i th section. Consistency of the onramp model (Eqs. (7.3) and (7.5)) on the other hand, is not constrained by the duration of the time interval. The example of Section 7.7 uses a freeway partition with a shortest section of 1000 ft. At a freeflow speed of 65 mph, this corresponds to a maximum Δt_{mnl} of 10.5 seconds. Most onramp control systems only update the control rate at regular intervals of 1 to 5 minutes, making it unnecessary to model the onramps at the faster rate.

The modified dual-scale model assumes that the onramp interval, Δt_{orp} , is an integer multiple of Δt_{mnl} , with $m \triangleq \Delta t_{orp}/\Delta t_{mnl}$. The modified model equations are obtained by replacing the $r_{i[k]}$ terms in Eqs. (7.6), (7.3), and (7.7) with $r_{i[k]}/m$. To retain the important properties given by the theorem, Eq. (7.5) must be modified by including all m $\xi_i(\bar{\rho}_i - \rho_{i[k]})$ -like terms of the *upcoming* Δt_{orp} interval. That is, $r_{i[k]}$ at time $t = k \cdot \Delta t_{orp} = k \cdot m \Delta t_{mnl}$ is computed as the minimum of $l_{i[k]} + d_{i[k]}$ and the m terms $\xi_i m (\bar{\rho}_i - \rho_{i[x]})$, with $x = k \cdot m \dots (k+1)m - 1$. This, unfortunately, destroys the causality of the model (and MWCC perturbations), as $r_{i[k]}$ ($\Delta r_{i[k]}$) now depends on future values of $\rho_{i[k]}$ ($\Delta \rho_{i[k]}$). A specialized iterative algorithm was created to integrate the model equations. Although the problem of non-causality also complicates the backstepping method for computing $a_{i[k]}$ and $b_{i[k]}$, this issue was not addressed here since, under Assumption #1, the $\xi_i(\bar{\rho}_i - \rho_{i[k]})$ constraints were removed anyway.

7.7 Experiments and results

In this section we report on simulation tests using the suggested procedure for solving the CWS problem and resulting LP problem, with the modifications outlined in this chapter. Model parameters and traffic data were taken from a 14-mile stretch of Interstate 210 WB in Pasadena, California. This site contains 20 metered on-ramps and a single uncontrolled freeway connector from I-605 NB. A speed contour plot constructed from loop detector data is shown in Figure 7.5. The darker shaded areas indicate average speeds below 40 mph. A study of the traffic characteristics of this site [41] identified three recurring bottlenecks. The severest of the three can be seen in the contour plot to affect the first third of the test section over a time period of about 4 hours (6:30 to 10:30 am).

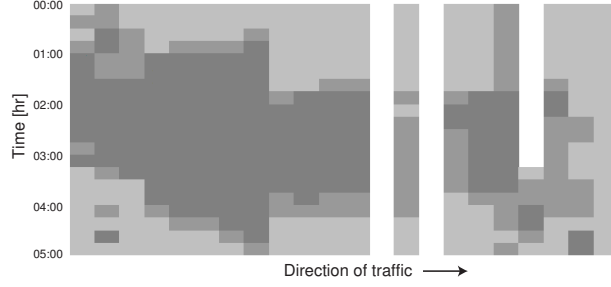


Figure 7.5: Measured speed contour plot [mph]

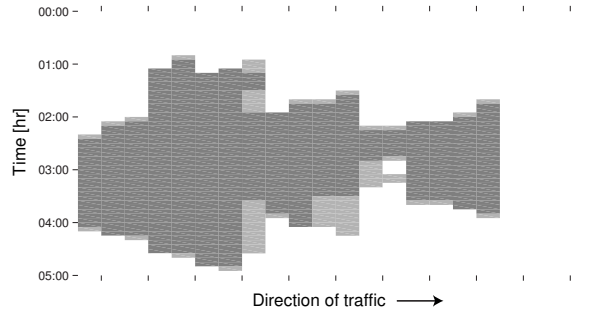


Figure 7.6: Simulated uncontrolled contour

A manual calibration of the model parameters (v_i , w_i , \bar{f}_i , \bar{s}_i , $\bar{\rho}_i$, α_i , γ_i , ξ_i) was performed, with resulting speed contour plot shown in Figure 7.6. The speed variable used in Figure 7.6 was calculated with:

$$\text{vel}_i[k] \triangleq \frac{f_i[k]/\bar{\beta}_i[k]}{\rho_i[k] + \gamma_i r_i[k]/p} \left(\frac{L_i}{\Delta t_{mnl}} \right) \quad (7.34)$$

This equation ensures $\text{vel}_i[k] = v_i$ when the freeway section is free flowing.

The CWS and LP problems were solved for 1, 2 and 5-hour time horizons. In all cases, an additional half-hour “cool-down” period was appended to the end of the simulation period. The optimizations were performed over the entire 1.5, 2.5, and 5.5 hour time windows. During the cool-down period, all traffic demands were set to zero, and the freeway was allowed to empty completely.

The cost weights generated by the CWS problem, with Assumptions #1 and #2, are shown in Figure 7.7. As opposed to the result of Part I, these cost weights have the desired TTT-like properties of linear decay and $b_i[k] \equiv 0$. The optimal solution to Problem \mathcal{P}_C posed with these weights is also a global solution to \mathcal{P}_A (with the same objective), and probably a near-optimal controller in terms of TTT.

Problem \mathcal{P}_C was solved using the commercial LP solver MOSEK 3.0. Each of the three time horizons was solved with and without on-ramp queue length restrictions (Eq. (7.28)). The size of the problem ranged from 92,310 constraints and 41,480 variables for the 1-hour problem without queue constraints, to 352,950 constraints and 158,600 variables for the 5-hour problem with queue constraints. Percent improvements in TTT are reported in Table 7.1. TTT was calculated from the

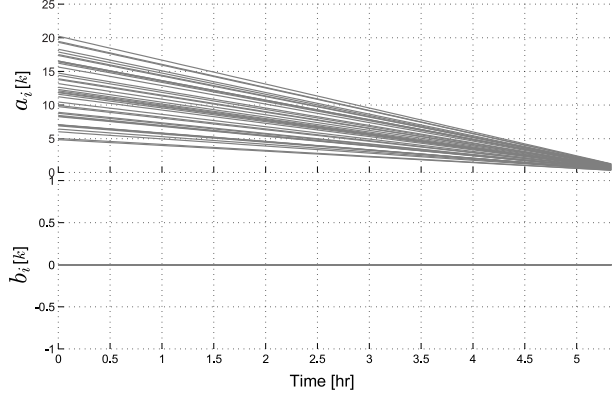


Figure 7.7: Computed cost weights

optimal solution with the following formula:

$$TTT = \sum_k \sum_{i \in \mathcal{I}} \rho_i[k] \Delta t_{mnl} + \sum_k \sum_{i \in \mathcal{E}n} l_i[k] \Delta t_{orp} \quad (7.35)$$

This computation included the cool-down period. It was confirmed in every case that the solution to the LP problem satisfied the equations of the model to a high degree of precision - i.e. $\psi^* \in \Omega_A$.

The validity of the two assumptions was also confirmed. For Assumption #1, it was verified that the optimal $r_i[k]$'s never exceeded $\xi_i p(\bar{\rho}_i - \rho_i[x])$. Assumption #2 was found to have little effect on the solution. This was confirmed by generating an *implementable* metering plan from the optimal solution using Eq. (7.33). The TTT for the implementable plan was found by running it through the model. TTT values for the optimal and implementable controllers are shown in Table 7.1. These results show that increasing the minimum metering rate from 0 (optimal) to 180 (implementable) induces only a small loss in travel time savings (0.04% without queue constraints and 1.12% with queue constraints). It should be noted that applying Eq. (7.33) can never cause the queue constraint to be violated, since increasing the metering rate will only make the queues shorter.

Table 7.1: Travel time savings and run times

Period [hr:min]	TTT no control	TTT optimal	% saved	TTT implem.	% saved
Without queue constraints					
1:00	1,716	1,715	0.06%	1,716	0.00%
2:00	4,080	4,035	1.10%	4,036	1.08%
5:00	13,075	11,535	11.78%	11,540	11.74%
With queue constraints					
1:00	1,716	1,715	0.06%	1,716	0.00%
2:00	4,080	4,053	0.66%	4,060	0.49%
5:00	13,075	11,824	9.56%	11,971	8.44%

It is also interesting to note that the 1-hour and 2-hour time horizons yielded almost no improvement over no control. This is because, as can be seen in Figure 7.6, congestion only begins after the first hour, and starts to dissipate in the fourth hour. These two experiments tend to corroborate Zhang’s observations in [42]. The 1-hour experiment demonstrates that an uncongested freeway should not be metered. In the 2-hour case there is no post-peak period. Hence, vehicles retained in the on-ramps cannot be released without increasing congestion. Not much can be gained by metering in these two situations. In the 5-hour experiment, however, the optimizer is able to shift the surplus demand to the post-peak period by holding vehicles on the on-ramps. Only the 5-hour time horizon produced a substantial improvement over no control: 11.78% travel time savings without queue constraints, and 9.56% with queue constraints. This result also emphasizes the importance of using a numerical technique that is efficient enough to produce optimal plans for sufficiently long time horizons, within a relatively short computation time.

Optimized speed contour plots and queue lengths for the 5-hour experiments are shown in Figures 7.8 and 7.9. Figure 7.8 shows that the optimal strategy, when on-ramp queue lengths are left unrestricted, is to keep the freeway almost completely uncongested by storing large numbers of vehicles in the on-ramps. In this situation, one of the on-ramp queues accumulates over 500 vehicles. Figure 7.9 shows that congestion cannot be avoided when the on-ramp queues are limited to at most 50 vehicles. The implementable metering plan nevertheless achieves a reduction of 8.44% in TTT in this case.

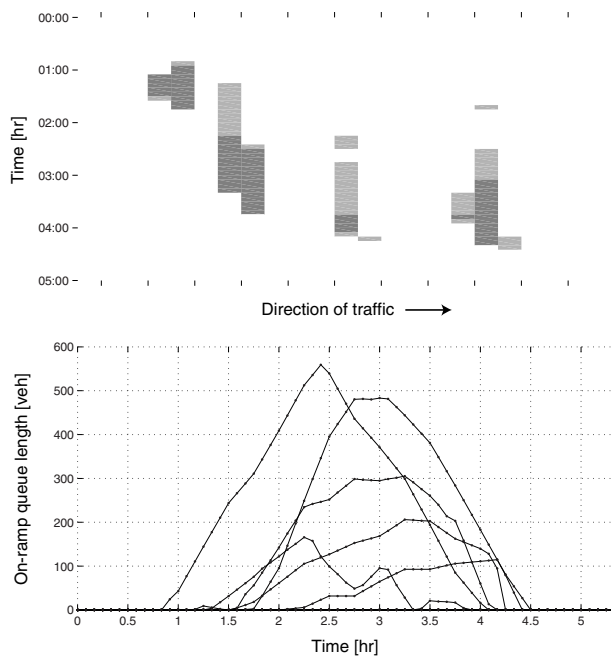


Figure 7.8: Congestion and queue lengths without queue constraints.

7.8 Conclusions

This chapter has outlined a complete methodology for solving the feedforward optimal metering problem efficiently and with near-global optimality. The unadulterated result was described in the

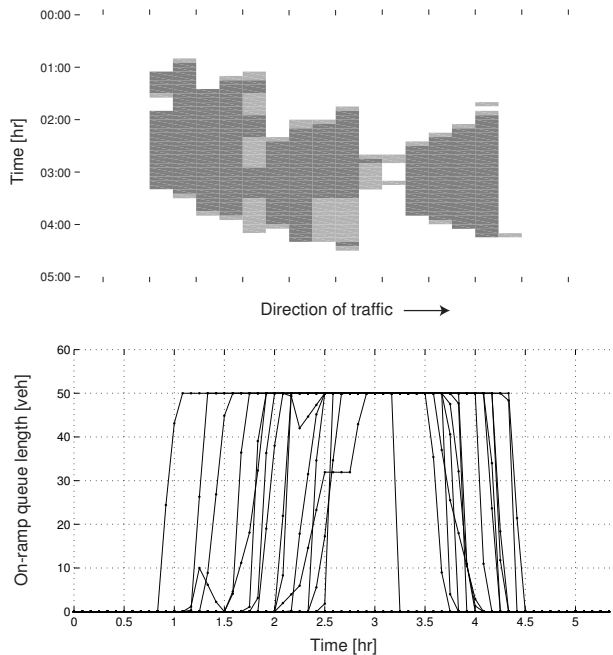


Figure 7.9: Congestion and queue lengths with queue constraints.

Sections 7.4 and 7.4.2, and was found to have a few drawbacks. Section 7.6 focused on solving those problems. The approach was tested in Section 7.7 on realistic freeway setup. The repairs required the use of two additional assumptions. The first, that congestion does not propagate from the mainline onto the onramps, can be easily verified in the optimal solution. Future work will consider the question of what to do if this assumption is temporarily violated. The second assumption was that the onramp flows could be reduced to zero by the onramp meters. This is never true, but it was found to induce only a small sacrifice of global optimality. It was found that, under these two assumptions, the cost weights generated by the CWS problem were qualitatively similar to the values that minimize total travel time, in that 1) the weights on the mainline flows decayed linearly in time, and 2) the onramp flow weights were all zero. Also, these assumptions enabled the inclusion of queue length constraints, and allowed the formulation of a simplified but equivalent problem (Problem \mathcal{P}_C).

This technique has several advantages over many other predictive onramp metering designs. First, it requires only to solve a single linear program, which can be done with extreme efficiency using any modern LP solver. Second, it takes onramp storage constraints explicitly into account. Finally, the optimal solution is a global optimum, or near global if slowly varying onramp flows are imposed, with respect to a cost function that is qualitatively similar to Total Travel Time. This technique is envisioned as part of a larger and more robust traffic-responsive control structure. The complete freeway control system will include the optimizer within a “rolling-horizon” framework, and will update the model parameter values using on-line parameter estimation [27, 16].

Chapter 8

Conclusions and Future Work

The main goals of Task Order 4136, and its continuation, T.O. 5503, are to (1) develop new traffic-responsive on-ramp metering control algorithms for freeways that will improve upon previous methods and reduce traffic congestion, (2) validate these methods in simulation, and (3) implement recommended strategies on California freeways. A 14-mile segment of Interstate 210 Westbound, in southern California, was selected as the intended test site. This report has documented the accomplishments carried out under T.O. 4136, in particular, the coding of I-210W in a microsimulation model (Vissim) and its calibration to observed conditions, tests of local ramp metering controllers in the resulting Vissim I-210 model, development, analysis, and calibration of macroscopic models of the I-210 testbed, and the development of an efficient method for determining globally optimal metering control plans for a congested freeway.

In Chapter 2, a complete methodology was presented for constructing and calibrating a simulation model of a unidirectional freeway with onramp control. Main steps in the method, such as gathering and processing of field data from the PeMS database, estimation of OD matrices with *FREQ*, and microscopic simulation with *VISSIM*, were described, then applied to I-210 West, a freeway that presents several challenging features: 20 metered onramps, with and without HOV bypass lanes, an HOV lane with an intermittent barrier, an uncontrolled freeway connector, and several interacting bottlenecks. All of these features were included in the model. It was concluded that two of the bottlenecks were geometry-induced, while another was caused by weaving. The I-210 *VISSIM* model was successfully calibrated, and it was shown that the *VISSIM* simulation environment is well-suited for freeway studies involving complex interactions. The simulation model was demonstrated to be capable of reproducing the field-measured response on the onramps, HOV lanes, and mixed-flow lanes, with few and well reasoned modifications to its driver behavior parameters.

Chapter 3 documented the results of a comparative simulation study, in which several types of local ramp metering algorithms – fixed-rate metering, *Alinea*, and %-Occ – were implemented in the *Vissim* I-210 model. In the fixed-rate metering experiments, it was discovered that performance improvements (e.g., in TVH) were possible, compared to the no-control case, for certain levels of fixed-rate metering, but that performance could deteriorate quickly when the constant metering value was varied. Queue override was shown to have the expected effect of limiting queue lengths, at the expense of possible reductions in improvements that were achieved in non-override cases. Two varieties of *Alinea* were tested: the downstream case (recommended by Papageorgiou), where mainline occupancies are measured downstream of the on-ramp merge point, and the upstream

case (present on I-210 and other California freeways), where mainline occupancies are measured upstream of the merge point. For target occupancies above 15%, a reduction in Total Passenger Hours could be achieved using either sensor arrangement, but the downstream placement worked better for relatively low target occupancies, whereas the upstream case worked better for high occupancies. This prediction is consistent with the observability results derived in Chapter 4. Tests using %-Occ control included variations on the controller parameter values and engagement of the overrides. No obvious guidelines for adjusting the parameters were discovered, although travel time reductions were achieved for some test runs. For cases where all overrides were engaged, Alinea appeared to yield a larger maximum TPH improvement, over the tested scenarios, than the other two algorithms.

The MCTM was introduced in Chapter 4. The dynamic equations were described for the three allowed types of intercellular connection: simple connection, merge, and diverge. Default boundary conditions were specified for the model. The characteristics of freely flowing and congested freeway traffic were discussed. In addition, the switching-mode model (SMM), a piecewise linearized version of the MCTM, was described in this chapter, for the case where each of the off-ramp flows is known as a function of time. The SMM equations were then re-stated, for the case where the split ratio for each off-ramp in the freeway is known as a function of time and off-ramp index. The observability and controllability properties of the individual modes of the SMM were then determined using standard linear systems techniques. It was discovered that these properties depend on the congestion statuses of the cells: the free-flow mode is observable from a downstream measurement and controllable from an upstream on-ramp, the congested mode is observable from an upstream measurement and controllable from a downstream on-ramp, the mixed “Congestion–Free-flow” mode is observable from an upstream/downstream measurement pair, and is not controllable from either an upstream or downstream on-ramp, and the mixed “Free-flow–Congestion” modes are not observable from either an upstream or downstream measurement, and are controllable from an upstream/downstream on-ramp pair. Matlab simulation results for the SMM and MCTM were shown for a section of I-210W, about 2 miles in length, using several days of loop detector data collected during the morning rush-hour period. The simulation results revealed that the SMM and MCTM produce density estimates that are both similar to one another and in good agreement with measured densities on I-210. The mean percentage error averaged over all the test days was approximately 13% for both models. It was concluded that the SMM can be used as a freeway traffic density estimator, and that it is useful for analyzing the controllability and observability properties of freeway traffic, which are of fundamental importance in the design of data estimators and ramp-metering control systems.

A procedure for calibrating the modified CTM was presented in Chapter 5. The calibrated model was tested on the full 14-mile test section of I-210W, and has been shown to reproduce the main features of the observed traffic congestion on the freeway, such as approximate location of bottlenecks and duration and spatial extent of congestion. In addition, the model accurately predicts the total travel time (TTT) in the freeway. A main benefit of the overall calibration method is that it provides a well-defined, automatable procedure for estimating free-flow speeds, congestion parameters, and bottleneck capacities for the MCTM from loop-detector data.

In Chapter 6, the Matlab and C++ software developed for the macroscopic simulation studies of Chapters 4 and 5 was described. An efficient, C++-based MCTM simulator was introduced, which is capable of representing a linear freeway segment with a user-specified geometry. Guidelines were given for specifying cell layouts, configuring and running simulations, and processing

simulation outputs, using the I-210W site as an example.

A complete methodology for solving the feedforward optimal metering control problem efficiently, and with near-global optimality, was outlined in Chapter 7. The first part of the chapter described the unadulterated result, which was found to have a few drawbacks. In the second part of the chapter, methods for solving those problems were presented, and the approach was tested with a realistic numerical example. These fixes to the original method required adoption of two additional assumptions. The first assumption, that congestion does not propagate from the mainline to the onramps, can be easily verified in the optimal solution. Future work will consider the question of what to do if this assumption is temporarily violated. The second assumption was that the on-ramp flows could be reduced to zero by the onramp meters. This is never true, but it was found to induce only a small sacrifice on global optimality. These assumptions enabled the inclusion of queue length constraints, and allowed the formulation of a simplified but equivalent problem. This technique has several advantages over many other predictive onramp metering designs. First, it requires only to solve a single linear program, which can be done with extreme efficiency using any modern LP solver. Second, it takes onramp storage constraints explicitly into account. Finally, the optimal solution is a global optimum, or near global if slowly varying onramp flows are imposed, with respect to a cost function that is qualitatively similar to Total Travel Time.

The global optimization technique is envisioned as part of a larger and more robust traffic-responsive control structure. The complete freeway control system will include the optimizer within a “rolling-horizon” framework, and will update the model parameter values using on-line parameter estimation, which will combine the approach of Chapter 5 with the mixture-Kalman-filtering (MKF) based estimator of [16, 17]. The MKF estimator, part of the ongoing work under T.O. 5503, uses feedback from loop detectors to determine traffic densities, along with the congestion status of each portion of the freeway. For the on-line parameter estimator, the quantities which still remain to be determined automatically include the bottleneck locations, the cell capacities away from the bottleneck locations, and the locations of faulty loop detectors. Since the MKF estimator determines the congestion status of each portion of the freeway, it can be used to automatically locate bottlenecks, i.e., the boundaries separating upstream congested regions from downstream free-flow regions. Regarding faulty detectors, Chao Chen has developed an algorithm to detect data errors and impute missing data values [43, 44]. This algorithm is employed by the current version of PeMS to reconstruct bad or missing data. Combining the automatic bottleneck detection and data imputation approaches with the existing calibration methodology will lead to a fully-automated algorithm, which will be used to provide parameter values for the global on-ramp metering optimizer.

A preliminary assessment has been performed concerning the feasibility of executing the on-ramp optimization scheme of Chapter 7 with automatic model calibration in real time. In the envisioned scenario, the MKF-based estimator will be run first. This estimator has been shown to be able to successfully identify active bottleneck locations even if its model parameters are only roughly tuned. Next, the parameter calibration method described in Chapter 5 will be executed, using the bottleneck locations provided by the MKF-based estimator. The resulting calibrated parameters will be sent to the optimizer, which will compute optimal metering rates for the current traffic condition. If the bottleneck identification, calibration, and optimization components are run sequentially, it is estimated that less than 5 minutes would be required to produce a new set of

optimal metering rates¹. This would be sufficiently fast to incorporate real-time freeway detector data, which is typically available in 5-minute intervals, if PeMS is used as the data source.

Further ongoing work involves using the calibrated VISSIM I-210 model to perform more comprehensive studies of ramp control strategies, for example, testing the global on-ramp metering optimizer and comparing it with existing coordinated methods, such as SWARM. In addition, a CTM-based, locally-responsive ramp-metering regulator has been designed and successfully applied to the VISSIM and macroscopic models of I-210W. These developments will be further documented in the T.O. 5503 final report.

¹These predictions were derived from experiments with computers commonly available at the time of writing. For the full 14-mile I-210 test segment, the estimates were: less than one second for determining congestion parameter values for all detector locations on a 1.0 GHz, 256 MB Pentium III computer, less than one second for identifying bottleneck locations on a 1.4 GHz Pentium M computer, and 2.5 minutes for solving the optimization problem over a 2-hour window on a 2.6 GHz, 512 MB Pentium 4 computer.

Bibliography

- [1] Office of Freeway Operations. SWARM Study Final Report, on W/B Foothill Freeway (W/B LA-210). Technical report, Caltrans District 07, 2002.
- [2] F. Hall, L. Bloomberg, N.M. Roupail, B. Eads, and A.D. May. Validation results for four models of oversaturated freeway facilities. *Transportation Research Record No.1710, National Research Council*, 2000.
- [3] R. Wiedemann. Simulation des straßenverkehrsflusses. *Schriftenreihe des Instituts für Verkehrswesen der Universität Karlsruhe, Heft 8*, 1974.
- [4] R. Wiedemann. Modelling of rti-elements on multi-lane roads. *Advanced Telematics in Road Transport*, 1991.
- [5] M. Fellendorf and P. Vortisch. Validation of the microscopic traffic flow model vissim in different real-world situations. *National Research Council. 80th Meeting of the Transportation Research Board*, Washington, D.C., January, 2001.
- [6] PTV AG. Vissim user manual - v.3.70. 2003.
- [7] M. Papegeorgiou, H. Hadj-Salem, and H.M. Blosseville. Alinea: A local feedback control law for onramp metering. *Transportation Research Record*, 1320, 1991.
- [8] M. Papegeorgiou, H. Hadj-Salem, and F. Middelham. Alinea local ramp metering. summary of field results. *Transportation Research Record*, 1603.
- [9] H. Hadj-Salem and J.M. Blosseville. Alinea: A local feedback law for on-ramp metering; a real-life study.
- [10] Carlos F. Daganzo. The Cell Transmission Model: A Dynamic Representation of Highway Traffic Consistent with the Hydrodynamic Theory. *Transportation Research - B*, 28(4):269–287, 1994.
- [11] Carlos F. Daganzo. The Cell Transmission Model, Part II: Network Traffic. *Transportation Research - B*, 29(2):79–93, 1995.
- [12] Carlos F. Daganzo. A Finite Difference Approximation of the Kinematic Model of Traffic Flow. *Transportation Research - B*, 29(4):261–276, 1995.
- [13] M.J. Lighthill and G.B. Whitham. On kinematic waves II, a theory of traffic flow on long crowded roads. *Proceedings Royal Society of London*, 229(1178):317–345, 1955.

- [14] Randall Cayford, Wei-Hua Lin, and Carlos F. Daganzo. The NETCELL Simulation Package: Technical Description. PATH Research Report UCB-ITS-PRR-97-23, Institute of Transportation Studies, University of California at Berkeley, 1997.
- [15] Laura Muñoz, Xiaotian Sun, Roberto Horowitz, and Luis Alvarez. Traffic Density Estimation with the Cell Transmission Model. In *2003 American Control Conference Proceedings*, pages 3750–3755, Denver, CO, June 4–6 2003.
- [16] Xiaotian Sun, Laura Muñoz, and Roberto Horowitz. Highway Traffic State Estimation Using Improved Mixture Kalman Filters for Effective Ramp Metering Control. In *Proceedings of the 42nd IEEE Conference on Decision and Control*, pages 6333–6338, Maui, Hawaii, December 9–12 2003.
- [17] Xiaotian Sun, Laura Muñoz, and Roberto Horowitz. Mixture Kalman Filter Based Highway Congestion Mode and Vehicle Density Estimator and its Application. In *2004 American Control Conference Proceedings*, pages 2098–2103, Boston, Massachusetts, June 30–July 2 2004.
- [18] William L. Brogan. *Modern Control Theory*. Prentice Hall, 3rd edition, 1991.
- [19] Freeway Performance Measurement Project. <http://pems.eecs.berkeley.edu/>.
- [20] Zhanfeng Jia, Chao Chen, Ben Coifman, and Pravin Varaiya. The PeMS Algorithms for Accurate, Real-Time Estimates of g-factors and Speeds from Single-Loop Detectors. In *2001 IEEE Intelligent Transportation Systems Conference Proceedings*, pages 536–41, Oakland, CA, August 2001.
- [21] Gabriel Gomes and Roberto Horowitz. A Study of Two Onramp Metering Schemes for Congested Freeways. In *2003 American Control Conference Proceedings*, Denver, CO, June 4–6 2003. To appear.
- [22] Gabriel Gomes and Roberto Horowitz. Globally Optimal Solutions to the Onramp Metering Problem - Part I. In *2004 IEEE Conference on Intelligent Transportation Systems*, Washington, D.C., October 3–6 2004. To appear.
- [23] Gabriel Gomes and Roberto Horowitz. Globally Optimal Solutions to the Onramp Metering Problem - Part II. In *2004 IEEE Conference on Intelligent Transportation Systems*, Washington, D.C., October 3–6 2004. To appear.
- [24] Gabriel Gomes, Adolf May, and Roberto Horowitz. Calibration of Vissim for a Congested Freeway. PATH Research Report UCB-ITS-PRR-2004-4, Institute of Transportation Studies, University of California at Berkeley, 2004.
- [25] Carlos F. Daganzo. A Continuum Theory of Traffic Dynamics for Freeways with Special Lanes. *Transportation Research - B*, 31(2):83–102, 1997.
- [26] Carlos F. Daganzo, Wei-Hua Lin, and Jose M. Del Castillo. A Simple Physical Principle for the Simulation of Freeways with Special Lanes and Priority Vehicles. *Transportation Research - B*, 31(2):103–125, 1997.

- [27] Laura Muñoz, Xiaotian Sun, Dengfeng Sun, Gabriel Gomes, and Roberto Horowitz. Methodological calibration of the cell transmission model. In *2004 American Control Conference Proceedings*, pages 798–803, Boston, Massachusetts, June 30–July 2 2004.
- [28] J. Wattleworth. Peak period analysis and control of a freeway system. *Highway Research Record*, 157, 1965.
- [29] L. Yuan and J. Kreer. Adjustment of freeway ramp metering rates to balance entrance ramp queues. *Transportation Research*, 5, 1971.
- [30] C. Chen, J. Cruz, and J. Paquet. Entrance ramp control for travel-rate maximization in expressways. *Transportation Research*, 8:503–508, 1974.
- [31] J. Wang and A. May. Computer model for optimal freeway on-ramp control. *Highway Research Record*, 469, 1973.
- [32] H. Payne and W. Thompson. Allocation of freeway ramp metering volumes to optimize corridor performance. *IEEE Transactions on Automatic Control*, 19(3), 1974.
- [33] Y. Iida, T. Hasegawa, Y. Asakura, and C. Shao. A formulation of on-ramp traffic control system with route guidance for urban expressway. *Communications in Transportation*, 1989.
- [34] Y. Lei. Model and technology of the on-ramp control over freeway traffic flow. *Transportation systems : theory and application of advanced technology*, 2:859–864, 1995.
- [35] A. Kotsialos, M. Papageorgiou, M. Mageas, and H. Hadj-Salem. Coordinated and integrated control of motorway networks via nonlinear optimal control. *Transportation Research Part C*, 10:65–84, 2002.
- [36] A. Hegyi, B. De Schutter, H. Hellendoorn, and T. Van den Boom. Optimal coordination of ramp metering and variable speed control - an mpc approach. *Proceedings of the American Control Conference*, 2002.
- [37] M. Papageorgiou and A. Kotsialos. Freeway ramp metering: An overview. *IEEE Transactions on Intelligent Transportation Systems*, 3(4), 2002.
- [38] M. Papageorgiou. An integrated control approach for traffic corridors. *Transportation Research C*, 3(1):19–30, 1995.
- [39] A. Ziliaskopoulos. A linear programming model for the single destination system optimum dynamic traffic assignment problem. *Transportation Science*, 34(1), 2000.
- [40] M. Papageorgiou and A. Kotsialos. Freeway ramp metering: An overview. In *IEEE Intelligent Transportation Systems*, 2000.
- [41] Gabriel Gomes, Adolf D. May, and Roberto Horowitz. Calibration of VISSIM for a congested highway. In *The 83rd Annual Meeting of the Transportation Research Board*, Washington, D.C., January 2004.

- [42] M. Zhang, S. Ritchie, and W. Recker. Some general results on the optimal ramp control problem. *Transportation Research Part C*, 4(2), 1996.
- [43] Chao Chen, Jaimyoung Kwon, Alexander Skabardonis, and Pravin Varaiya. Detecting Errors and Imputing Missing Data for Single Loop Surveillance Systems. In *Transportation Research Board 82nd Annual Meeting*, Washington, D.C., August 2002.
- [44] Chao Chen. *Freeway Performance Measurement System (PeMS)*. PhD thesis, University of California, Berkeley, 2002.

Appendix A

PeMS speed contours

	39,159	38,209	38,069	36,569	35,409	34,899	34,049	33,049	32,199	32,019	30,999	30,779	30,139	29,999	29,879	29,17	28,27	28,03	26,8	26,12	25,68	25,5	
5:30																							
5:45	55	53	49	58	60	58	55	52	58	58	57	59		65		78	60	61	57	59	58	60	
6:00	49	49	45	57	58	57	60	51	59	58	57	58		62		73	58	57	56	58	59	59	
6:15	37	54	51	59	52	52	52	44	53	44	53	56		61		74	56	56	55	55	57	33	
6:30	30	63	59	54	34	31	26	27	56	56	48	49		56		89	36	47	47	40	25	7	
6:45	39	59	53	21	25	30	24	20	53	34	50	53		63		64	36	46	21	26	22	22	
7:00	34	44	38	13	20	25	26	18	47	21	27	24		44		33	20	28	44	45	54	58	
7:15	30	40	35	13	18	20	14	15	23	17	30	27		41		35	25	30	33	46	54	60	
7:30	23	38	29	10	10	16	14	13	23	20	25	21		36		31	22	28	36	46	55	60	
7:45	24	34	21	9	12	19	14	14	18	11	15	20		35		32	24	33	38	48	57	60	
8:00	27	40	27	10	11	14	10	14	24	20	28	25		37		33	24	31	47	47	55	59	
8:15	35	36	26	9	14	17	17	15	16	12	17	24		48		50	29	35	44	47	54	58	
8:30	24	26	17	8	14	15	20	13	20	9	30	28		34		25	24	30	53	51	7	61	
8:45	29	21	23	11	20	21	19	14	30	28	25	29		40		45	27	32	41	48	42	59	
9:00	49	22	38	10	16	21	20	20	49	44	32	31		39		39	23	29	47	44	52	58	
9:15	61	20	40	16	25	27	18	20	35	28	34	35		40		35	21	26	55	49	34	57	
9:30	62	21	56	15	26	28	19	21	31	28	38	35	52	50		39	22	28	55	45	53	55	
9:45	59	19	53	12	22	26	32	23	60	57	45	44	51	49		61	33	39	55	45	54	58	
10:00	59	18	53	28	31	34	29	23	58	54	51	51	55	52		64	54	56	58	44	54	58	
10:15	62	17	56	51	41	30	28	20	59	56	57	54	64	55		65	53	59	59	44	53	58	

Figure A.1: A heavy day (11/8/2001)

	39,159	38,209	38,069	36,569	35,409	34,899	34,049	33,049	32,199	32,019	30,999	30,779	30,139	29,999	29,879	29,17	28,27	28,03	26,8	26,12	25,68	25,5
5:30	58	42	65	61	64	63	66	64	63	63	62	63		79		66	64	48		67	66	65
5:45	47	42	58	61	63	63	68	62	64	62	62	63		78		65	64	51		68	68	67
6:00	56	38	54	60	57	60	61	48	60	60	61	60		70		63	60	50		63	63	63
6:15	47	35	49	63	44	52	40	35	61	61	60	61		72		65	61	46		60	63	66
6:30	35	43	48	39	30	36	38	27	60	61	60	61		70		62	61	46		60	62	65
6:45	32	44	45	19	25	32	28	23	59	61	61	61		68		65	62	41		61	63	66
7:00	30	26	37	12	20	27	21	20	58	59	53	45		57		60	60	45		54	60	67
7:15	27	32	30	12	16	24	21	20	53	39	36	39		54		54	35	31		35	57	64
7:30	27	30	31	13	16	25	21	18	28	27	31	31		56		38	22	26		25	57	64
7:45	35	28	29	12	17	22	18	18	26	24	24	25		42		37	28	31		47	55	66
8:00	34	35	30	14	15	24	16	14	24	25	30	28		45		40	23	23		51	55	63
8:15	53	37	34	11	16	27	22	16	21	20	21	25		52		41	26	26		55	58	64
8:30	34	38	28	12	15	20	18	16	22	23	28	29		53		52	25	28		51	56	64
8:45	61	43	32	14	22	20	24	18	30	27	29	28		46		40	25	28	61	50	56	64
9:00	68	56	57	22	21	28	22	19	39	36	38	36		44		43	28	32	54	51	54	62
9:15	66	74	59	20	20	27	25	23	46	37	49	41		53		63	51	45	55	47	53	59
9:30	67	51	60	48	33	32	26	26	51	43	49	47		52		61	57	41	28	51	54	60
9:45	63	59	58	66	46	43	29	26	64	63	69	67		63		66	63	50	18	58	56	63
10:00	67	37	58	66	67	67	50	27	65	64	72	67		59		66	63	59	48	67	11	64
10:15	66	69	56	65	69	70	75	52	69	67	72	70		62		67	65	53	65	68	36	64

Figure A.2: A typical day (11/28/2001)

	39,159	36,209	38,069	36,589	35,409	34,889	34,049	33,049	32,189	32,019	30,999	30,779	30,139	29,999	29,679	29,17	28,27	28,03	26,8	26,12	25,88	25,5
5:30	61	58	66	61	62	64	65	64	64	63	76			79		65	63	41	44	66	64	66
5:45	58	25	59	60	61	64	64	62	63	61	61	74		77		64	62	49	26	66	67	66
6:00	57	40	54	59	57	61	63	60	59	60	59	68		72		62	61	46	28	61	62	65
6:15	55	44	47	61	52	53	47	39	60	61	60	69		71		63	60	48	50	61	62	66
6:30	45	45	47	47	36	35	34	33	58	60	58	68		67		63	61	43	19	61	62	66
6:45	49	50	47	22	32	36	31	24	58	60	60	68		67		63	61	46	20	60	62	67
7:00	50	40	43	17	23	29	29	22	57	59	60	65		65		63	60	43	19	60	61	67
7:15	67	41	44	17	23	32	30	25	59	60	53	46		59		61	54	37	20	56	59	64
7:30	66	32	61	15	29	36	25	24	42	37	55	49		62		61	54	33	43	50	57	65
7:45	65	67	61	19	22	23	15	14	32	33	52	51		61		63	62	45	59	59	61	67
8:00	65	47	60	15	20	27	30	22	36	32	21	42		60		62	58	41	56	58	58	65
8:15	66	38	59	39	26	26	22	18	25	27	33	38		57		59	57	46	56	54	59	65
8:30	63	66	62	64	24	29	33	23	50	43	40	40		58		57	43	35	46	47	55	63
8:45	59	33	57	64	59	61	40	26	47	34	52	40		54		58	31	21	43	46	56	63
9:00	54	37	58	63	69	70	65	25	61	58	62	53		49		51	40	34	34	41	53	61
9:15	59	61	54	61	66	68	69	44	65	64	69	63		62		62	48	33	42	42	51	60
9:30	62	54	57	61	67	67	67	30	63	63	66	61		59		62	65	44	29	44	54	63
9:45	62	31	56	62	66	66	65	29	62	62	67	62		59		62	66	36	25	48	55	62
10:00	62	61	59	63	71	69	68	59	66	65	66	59		58		61	64	58	64	53	56	66
10:15	62	14	62	61	69	65	66	30	65	63	62	65		61		67	69	48	66	57	60	69

Figure A.3: A light day (11/21/2001)

Appendix B

Counts from the District 7 ramp survey

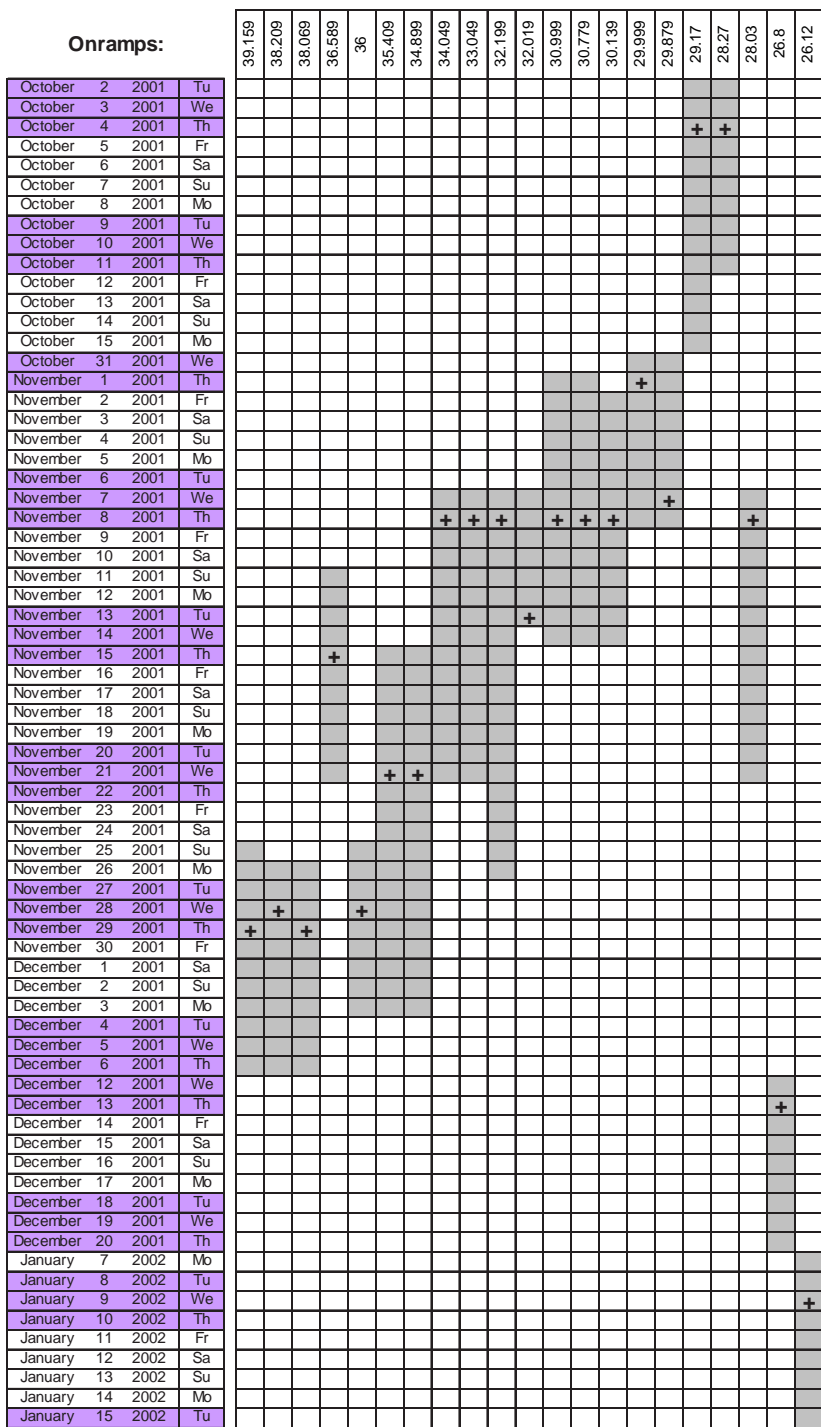


Figure B.1: Onramp days

Offramps:				38.209	38	37	36	35.409	34.049	33.049	32.019	30.779	30.5	29.17	28.27	27.64	26.8	26.12
October 2 2001	Tu																	
October 3 2001	We																	
October 4 2001	Th																	
October 5 2001	Fr																	
October 6 2001	Sa																	
October 7 2001	Su																	
October 8 2001	Mo																	
October 9 2001	Tu																	
October 10 2001	We																	
October 11 2001	Th																	
October 12 2001	Fr																	
October 13 2001	Sa																	
October 14 2001	Su																	
October 15 2001	Mo																	
October 31 2001	We																	
November 1 2001	Th																	
November 2 2001	Fr																	
November 3 2001	Sa																	
November 4 2001	Su																	
November 5 2001	Mo																	
November 6 2001	Tu																	
November 7 2001	We																	
November 8 2001	Th																	
November 9 2001	Fr																	
November 10 2001	Sa																	
November 11 2001	Su																	
November 12 2001	Mo																	
November 13 2001	Tu																	
November 14 2001	We																	
November 15 2001	Th																	
November 16 2001	Fr																	
November 17 2001	Sa																	
November 18 2001	Su																	
November 19 2001	Mo																	
November 20 2001	Tu																	
November 21 2001	We																	
November 22 2001	Th																	
November 23 2001	Fr																	
November 24 2001	Sa																	
November 25 2001	Su																	
November 26 2001	Mo																	
November 27 2001	Tu																	
November 28 2001	We																	
November 29 2001	Th																	
November 30 2001	Fr																	
December 1 2001	Sa																	
December 2 2001	Su																	
December 3 2001	Mo																	
December 4 2001	Tu																	
December 12 2001	We																	
December 13 2001	Th																	
December 14 2001	Fr																	
December 15 2001	Sa																	
December 16 2001	Su																	
December 17 2001	Mo																	
December 18 2001	Tu																	
December 19 2001	We																	
December 20 2001	Th																	
January 7 2002	Mo																	
January 8 2002	Tu																	
January 9 2002	We																	
January 10 2002	Th																	
January 11 2002	Fr																	
January 12 2002	Sa																	
January 13 2002	Su																	
January 14 2002	Mo																	
January 15 2002	Tu																	

Figure B.2: Offramp days

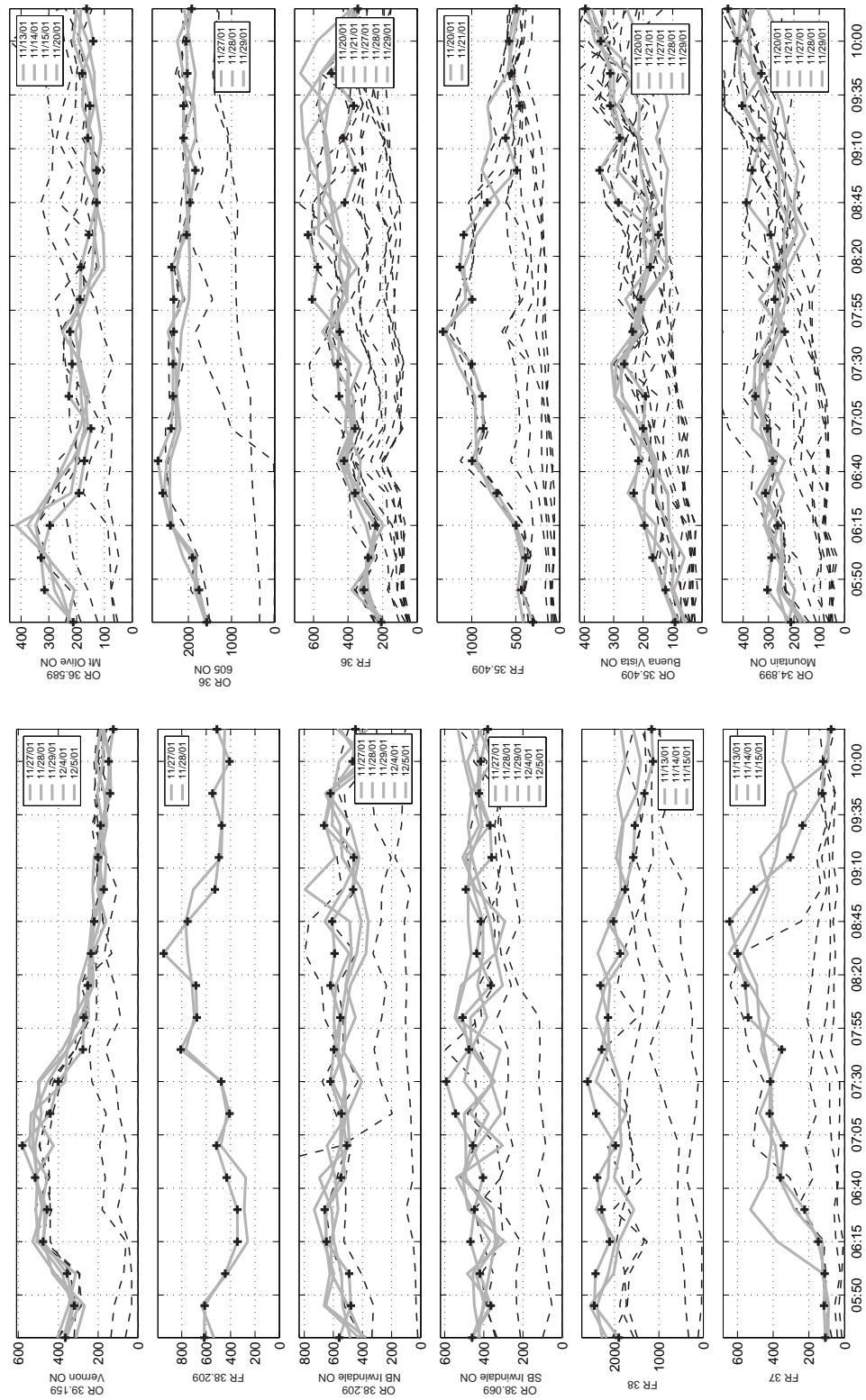


Figure B.3: District 07 ramp survey (OR=onramp, FR=offramp)

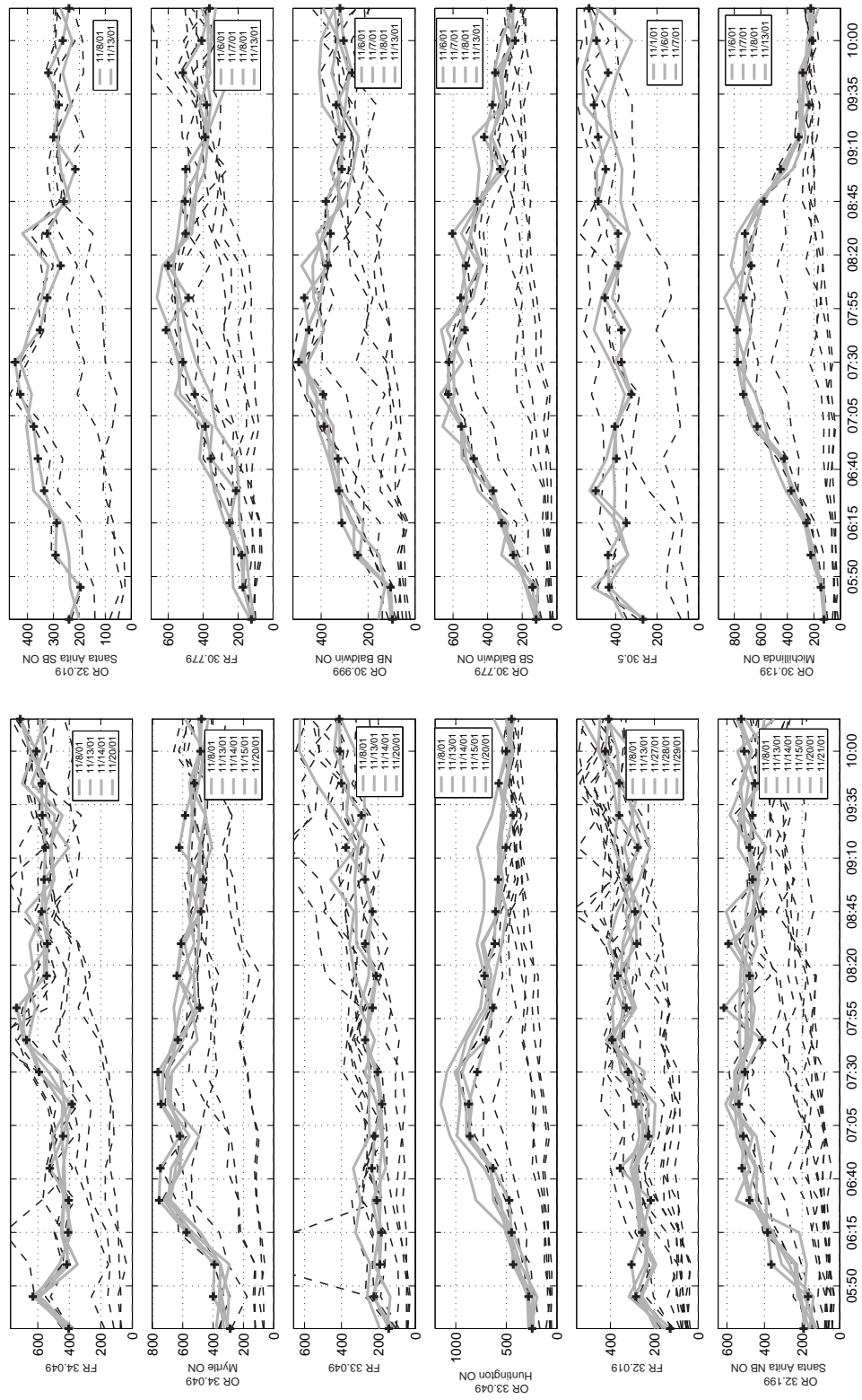


Figure B.4: District 07 ramp survey (OR=onramp, FR=offramp)

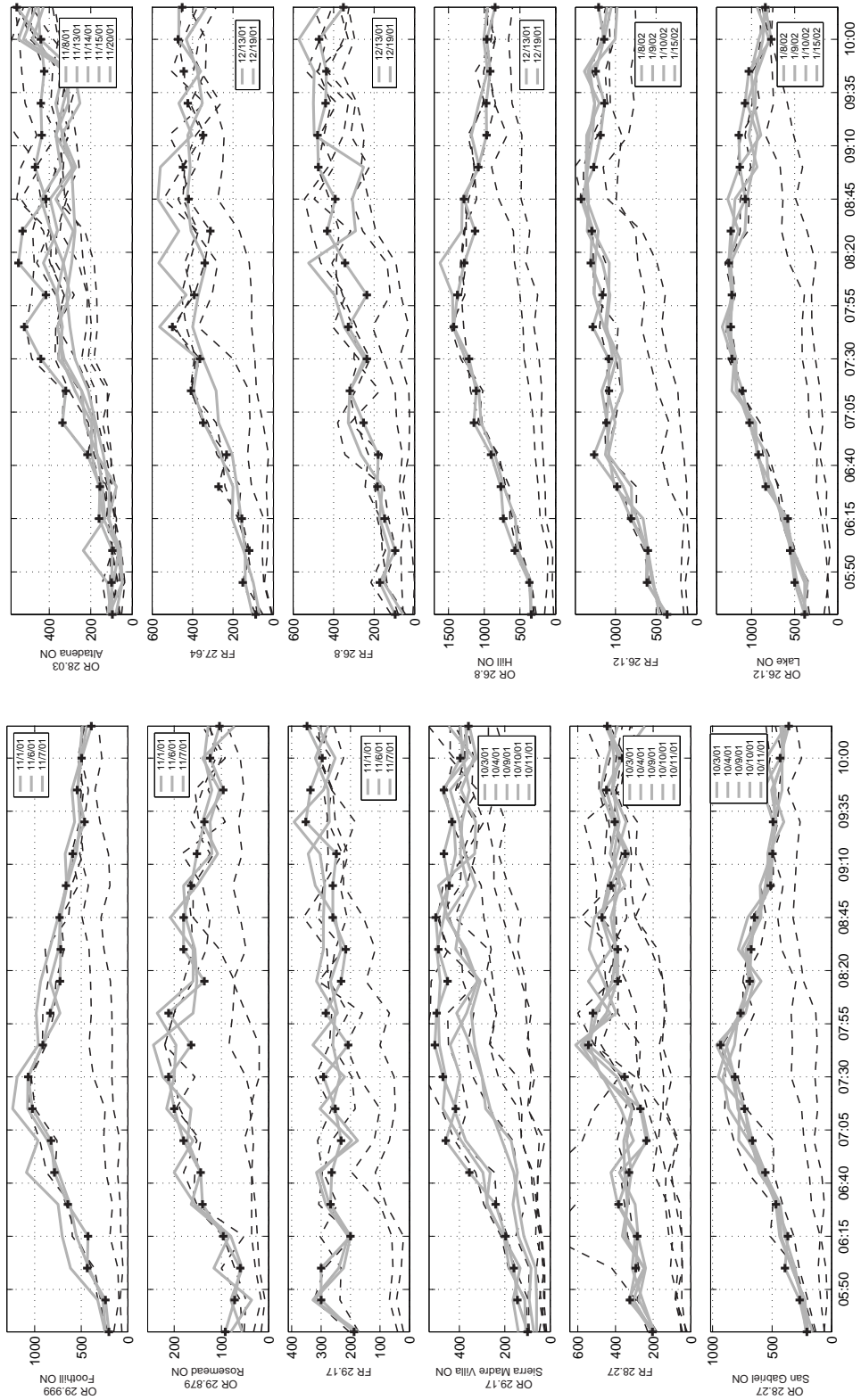


Figure B.5: District 07 ramp survey (OR=onramp, FR=offramp)

Appendix C

Final selection of boundary flows

		39.159	39.159	38.209	38.069	36.589	36	35.409	34.899	34.049	33.049	32.199	32.019	30.999	30.779	30.139	29.999	29.879	29.17	28.27	28.03	26.8	26.12
Onramps(vph)	5:30	7632	364	560	460	212	1576	92	212	288	244	192	240	96	120	124	204	92	100	208	96	340	384
	5:45	9521	320	480	364	316	1752	124	304	400	280	168	196	104	140	148	240	72	144	268	100	368	500
	6:00	8948	356	492	420	328	1908	168	288	392	432	364	292	244	252	224	436	60	160	392	96	572	552
	6:15	9152	476	648	468	296	2416	196	264	576	448	384	288	312	320	256	428	96	196	368	160	732	580
	6:30	8608	456	660	448	192	2596	232	312	756	472	480	336	324	368	372	644	140	240	468	156	768	836
	6:45	8552	516	548	404	172	2704	216	284	748	632	520	360	328	480	424	788	144	356	556	216	904	920
	7:00	8820	580	508	456	148	2400	200	304	620	860	512	376	388	552	628	824	180	460	664	336	1144	1024
	7:15	9028	440	544	544	228	2356	192	352	744	872	536	428	392	628	732	1024	200	416	732	320	1112	1104
	7:30	8744	400	620	592	216	2356	264	304	764	788	504	448	496	624	776	1068	212	472	812	440	1212	1228
	7:45	7936	276	596	476	224	2340	236	236	632	704	412	352	452	532	780	912	164	508	932	520	1428	1240
	8:00	7252	272	552	508	188	2340	208	276	488	632	616	324	472	556	732	832	212	500	764	416	1376	1228
	8:15	7968	252	620	364	184	2388	176	268	640	716	480	272	372	524	672	728	136	452	688	548	1280	1264
	8:30	7100	236	592	436	156	2040	148	292	612	616	592	324	360	604	720	720	180	492	676	528	1128	1240
	8:45	6672	220	608	416	128	1964	284	388	480	608	408	260	380	460	576	732	180	504	648	416	1284	1072
	9:00	6648	172	464	492	128	1836	348	364	464	580	464	216	312	328	452	664	164	444	512	468	1084	1136
	9:15	6432	200	460	360	160	2112	280	328	624	504	480	300	312	420	316	592	152	468	496	436	968	1148
	9:30	6298	188	664	368	152	2112	312	404	584	432	464	280	336	372	236	464	136	432	492	440	972	1076
9:45	6072	140	620	424	180	2024	312	328	524	576	452	320	268	356	284	544	96	468	576	424	916	1032	
10:00	6192	148	468	416	140	2052	344	424	484	500	508	264	304	240	212	496	124	396	432	440	964	772	
10:30	6368	124	448	380	164	1924	396	460	476	448	524	240	320	264	224	392	104	360	360	556	848	840	

Figure C.1: Onramp flows (first column is upstream mainline)

		38.209	38	37	36	35.409	34.049	33.049	32.019	30.779	30.5	29.17	28.27	27.64	26.8	26.12	25.68	25.6	25.5	25.4
Offramps (vph)	5:30	616	2200	108	208	304	404	144	128	124	268	188	204	88	96	364	304	1372	1372	3568
	5:45	612	2456	116	308	436	632	224	284	172	432	300	324	152	172	612	436	1692	1692	4088
	6:00	444	2428	112	284	388	416	192	304	180	436	300	292	120	96	600	300	1974	1974	4456
	6:15	344	2108	148	240	496	408	184	256	248	348	200	284	156	148	808	432	2202	2202	5376
	6:30	344	2288	224	360	716	404	208	216	212	496	268	384	272	184	980	440	2176	2176	6044
	6:45	432	2392	360	424	996	524	236	356	356	396	264	328	232	180	1264	592	1930	1930	6176
	7:00	516	1976	340	360	868	440	220	228	388	404	232	236	348	252	1112	648	2534	2534	6472
	7:15	408	2416	420	452	880	384	180	284	448	324	252	268	408	320	1080	600	2752	2752	6560
	7:30	476	2608	416	460	1000	592	204	320	516	372	292	352	364	236	1084	656	2636	2636	6556
	7:45	808	2288	352	448	1328	672	272	392	612	372	208	544	500	328	1280	764	2584	2584	6648
	8:00	676	2148	540	608	996	736	232	328	484	452	284	520	392	236	1160	776	2372	2372	6720
	8:15	684	2320	556	576	1136	544	212	368	600	388	232	388	340	344	1304	748	2358	2358	6420
	8:30	948	1872	600	632	1092	540	272	280	500	388	216	388	312	432	1292	640	2304	2304	6540
	8:45	752	2024	644	420	824	576	232	288	504	484	260	472	420	392	1424	776	2222	2222	6052
	9:00	528	1764	508	360	488	560	272	316	500	448	260	424	448	476	1268	628	2120	2120	5536
	9:15	496	1576	304	428	616	552	376	276	388	484	248	348	348	480	1184	640	2122	2122	5280
	9:30	472	1544	236	368	456	572	292	360	380	504	352	404	424	440	1136	512	1926	1926	4732
9:45	548	1328	124	496	548	576	400	360	516	436	336	448	444	436	1244	672	2040	2040	4664	
10:00	408	1132	120	380	576	608	408	424	408	492	296	364	472	472	1140	472	1806	1806	4216	
10:30	512	1164	76	344	492	712	412	408	364	528	348	444	452	352	1208	456	1588	1588	3808	

Figure C.2: Offramp flows (last column is downstream mainline)

Appendix D

Vehicle types

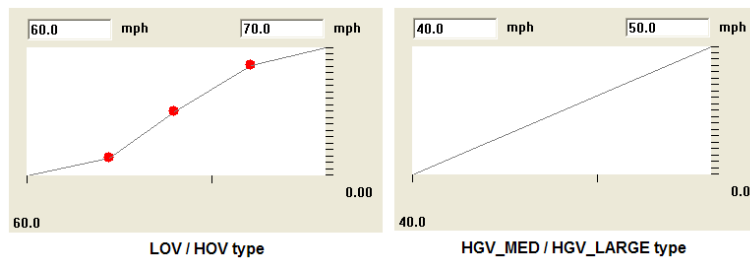


Figure D.1: Desired velocity

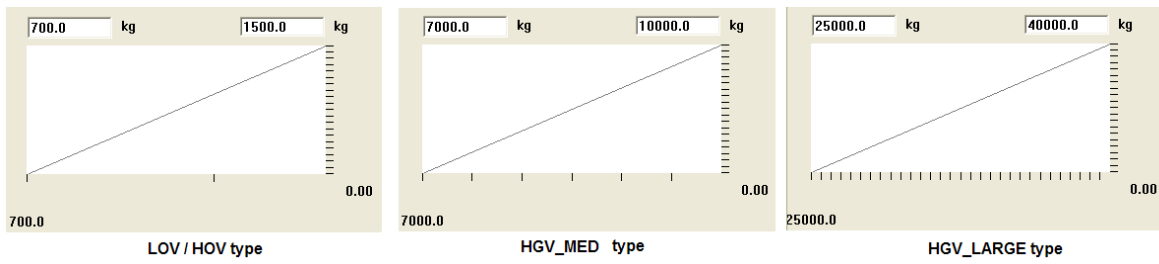


Figure D.2: Weight

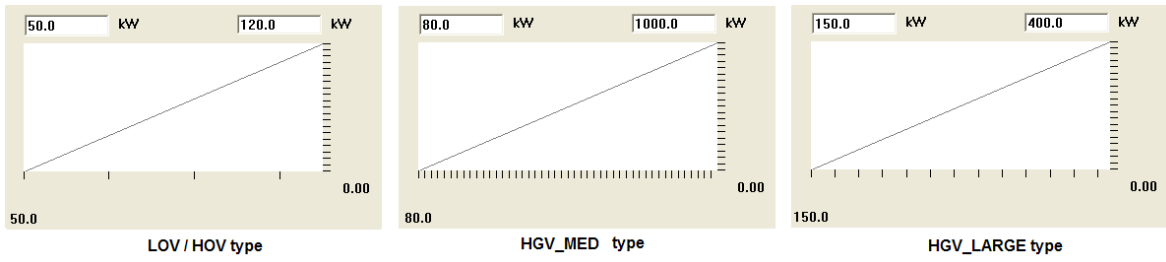


Figure D.3: Power

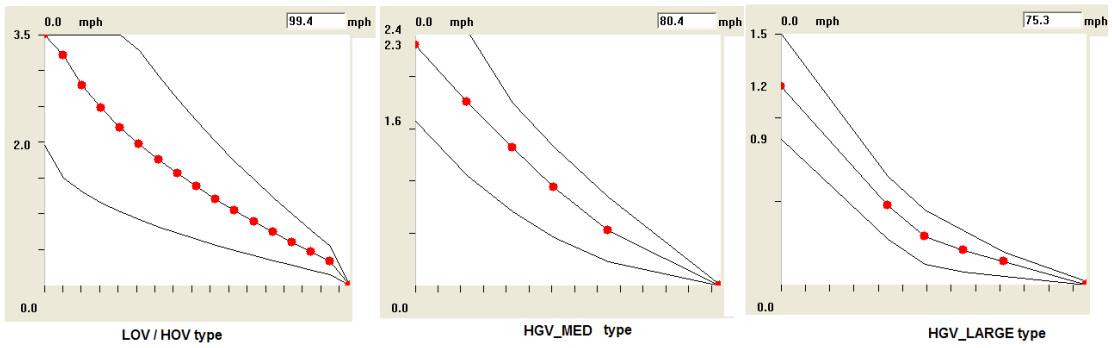


Figure D.4: Maximum acceleration

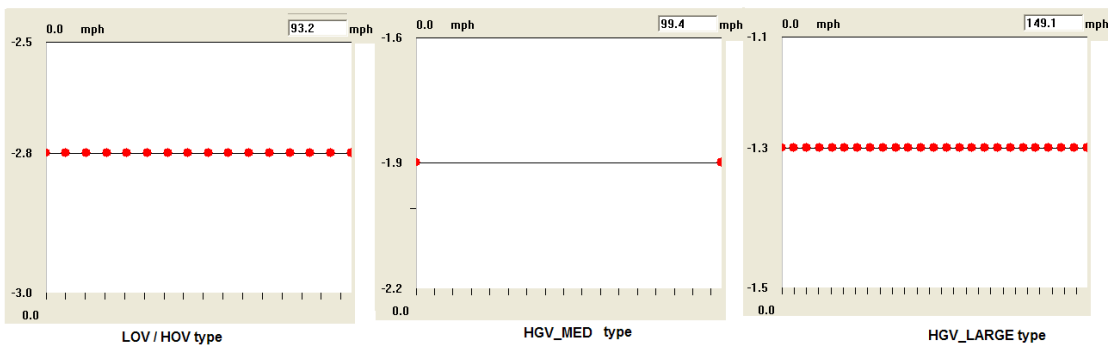


Figure D.5: Desired acceleration

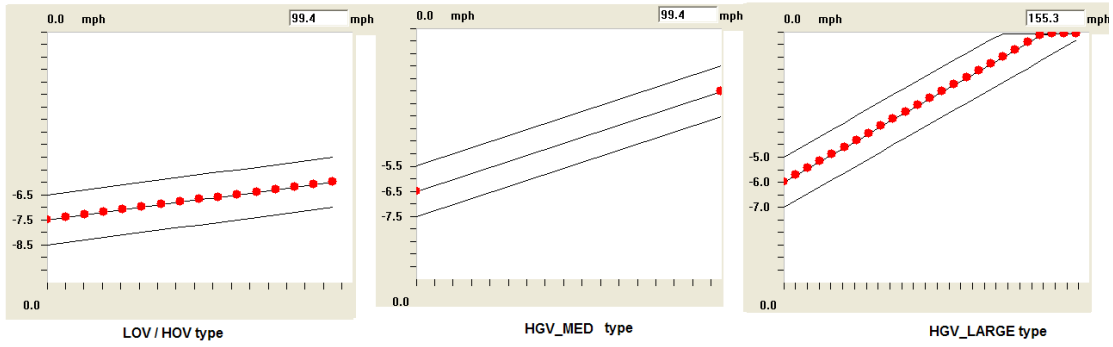


Figure D.6: Maximum deceleration

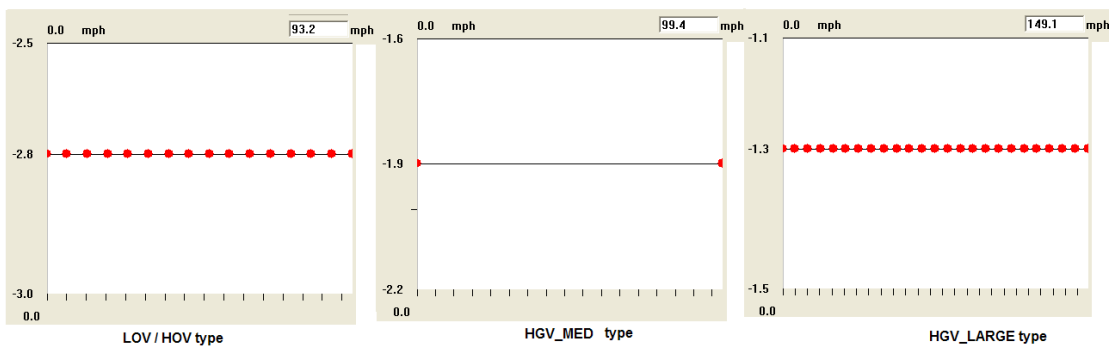


Figure D.7: Desired deceleration

Appendix E

Intermediate Vissim results

	39.159	38.209	38.069	36.589	35.409	34.899	34.049	33.049	32.199	32.019	30.999	30.779	30.139	29.999	29.879	29.17	28.27	28.03	26.8	26.12	25.68	25.5
5:30	63	63	62	63	62	63	63	64	63	63	63	62	63	62	63	63	64	63	64	63	63	64
5:45	63	62	61	63	61	62	63	63	63	63	63	63	63	63	63	64	63	64	64	64	61	64
6:00	63	62	60	63	62	62	63	63	63	62	63	62	62	61	62	63	63	63	63	63	60	64
6:15	63	61	57	63	57	60	62	61	61	60	61	60	62	62	62	63	62	61	63	63	58	63
6:30	63	63	57	63	49	57	60	61	59	57	47	38	57	54	58	61	61	61	62	61	54	62
6:45	63	62	60	63	57	58	61	60	48	37	29	26	56	55	58	61	62	59	61	61	55	62
7:00	63	60	58	63	60	61	62	63	33	24	26	25	56	50	56	61	60	56	60	58	54	62
7:15	63	63	57	63	61	62	63	62	22	28	27	27	47	44	54	59	58	50	61	38	40	62
7:30	63	62	61	63	59	61	62	62	21	23	25	27	29	40	54	60	60	43	29	22	40	61
7:45	63	63	61	64	59	62	63	63	25	26	22	25	36	38	52	58	26	23	21	25	40	62
8:00	63	63	62	64	63	63	64	63	63	52	40	32	26	41	54	33	19	28	27	29	42	61
8:15	63	63	62	64	63	63	64	64	63	63	63	61	58	53	58	43	37	41	35	36	45	61
8:30	63	63	61	64	63	63	64	63	63	61	63	62	63	60	62	63	63	62	59	44	42	61
8:45	63	64	61	64	64	63	64	63	63	63	63	63	63	60	62	63	63	62	63	62	61	64
9:00	64	64	63	64	62	63	63	64	63	62	63	62	63	62	63	63	63	63	63	63	62	64
9:15	63	64	63	64	62	63	63	63	63	63	63	62	63	63	62	63	63	62	63	63	58	64
9:30	64	64	62	64	63	62	63	63	63	63	63	63	62	62	62	63	63	63	63	63	61	63
9:45	64	64	62	64	63	63	64	64	63	63	63	63	62	62	63	64	63	62	63	63	58	64
10:00	63	64	63	64	63	63	63	63	63	63	63	63	64	63	63	64	64	63	63	63	60	64
10:15	63	64	62	64	62	61	63	62	62	61	63	62	63	62	63	63	64	63	63	63	61	64

Figure E.1: Contour plot after adjusting the look back distances

	39.159	38.209	38.069	36.589	35.409	34.899	34.049	33.049	32.199	32.019	30.999	30.779	30.139	29.999	29.879	29.17	28.27	28.03	26.8	26.12	25.68	25.5
5:30	63	63	62	64	63	63	63	63	63	63	63	63	62	63	64	64	63	64	64	63	64	64
5:45	63	63	62	63	61	62	63	63	63	63	63	63	63	63	63	64	64	64	64	64	62	64
6:00	63	63	61	64	62	63	63	63	62	62	63	62	61	61	61	63	63	63	63	63	60	64
6:15	63	61	59	63	58	60	62	62	61	62	60	58	62	62	62	63	63	63	63	63	60	64
6:30	63	63	60	63	56	60	61	61	55	50	49	48	48	47	56	61	62	60	61	61	58	63
6:45	63	63	60	63	60	61	62	61	27	33	27	30	55	53	57	61	61	58	62	62	58	63
7:00	63	63	61	63	61	61	62	63	31	26	28	28	55	44	55	60	62	59	60	61	57	63
7:15	63	63	59	63	60	61	63	59	20	33	23	24	22	41	53	59	61	59	62	52	45	62
7:30	63	63	62	63	61	61	62	31	15	19	19	23	23	41	55	60	61	57	47	23	43	62
7:45	63	63	61	64	63	63	64	16	20	27	23	26	26	41	54	60	58	46	25	28	49	62
8:00	63	63	63	64	63	63	64	52	18	29	23	29	26	42	55	59	58	50	26	29	55	62
8:15	63	63	62	64	63	63	64	64	63	55	45	36	23	42	53	58	61	60	35	30	53	61
8:30	63	63	62	64	63	64	64	63	62	63	63	63	54	55	60	62	62	61	61	37	50	62
8:45	63	64	62	64	63	63	64	64	63	63	63	63	63	61	62	63	63	61	63	62	60	63
9:00	64	64	63	64	63	63	63	64	63	62	63	63	63	62	63	63	63	62	63	63	62	64
9:15	63	64	63	64	63	63	63	63	62	63	63	63	63	62	62	63	63	62	63	63	59	63
9:30	64	64	62	64	63	63	63	63	63	63	63	63	62	62	63	63	63	62	63	63	61	64
9:45	64	64	62	64	63	63	64	64	63	62	63	63	62	62	63	64	63	62	63	63	62	64
10:00	63	64	63	64	63	63	63	63	63	63	63	63	63	63	64	64	63	63	63	63	61	64
10:15	63	64	62	64	63	62	63	63	63	63	63	63	61	61	63	63	63	62	63	63	62	64

Figure E.2: Contour plot after adjusting the waiting time

Appendix F

Onramp response

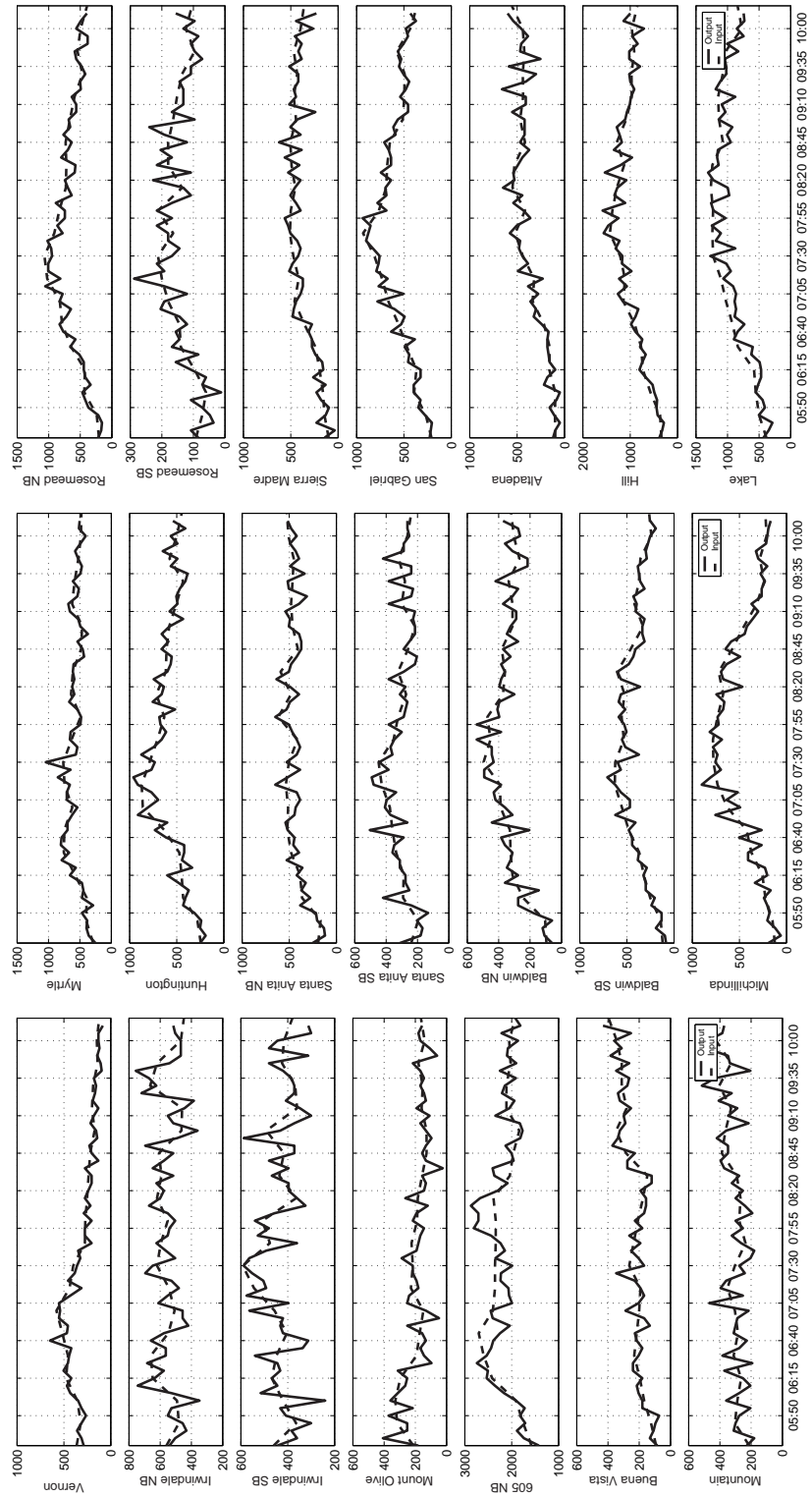


Figure F.1: VISSIM onramp inputs and outputs

Appendix G

Random seed variations

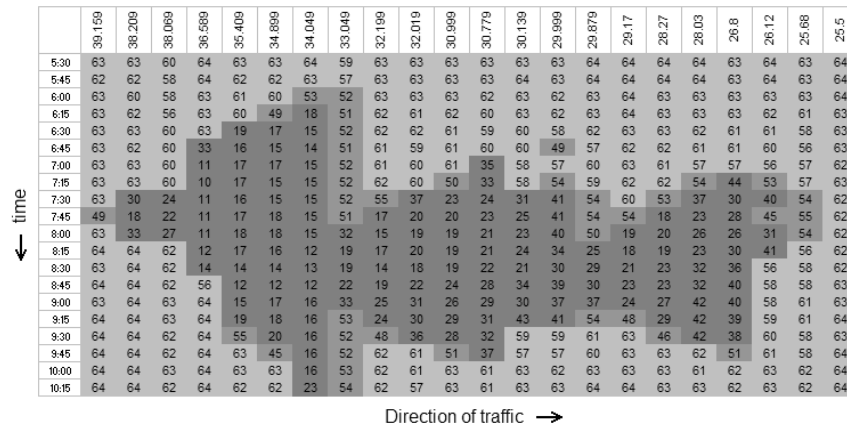


Figure G.1: Random seed = 28

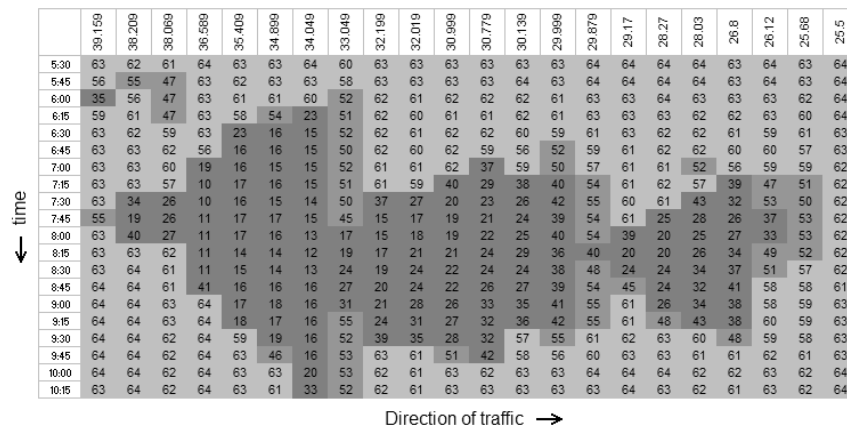


Figure G.2: Random seed = 35

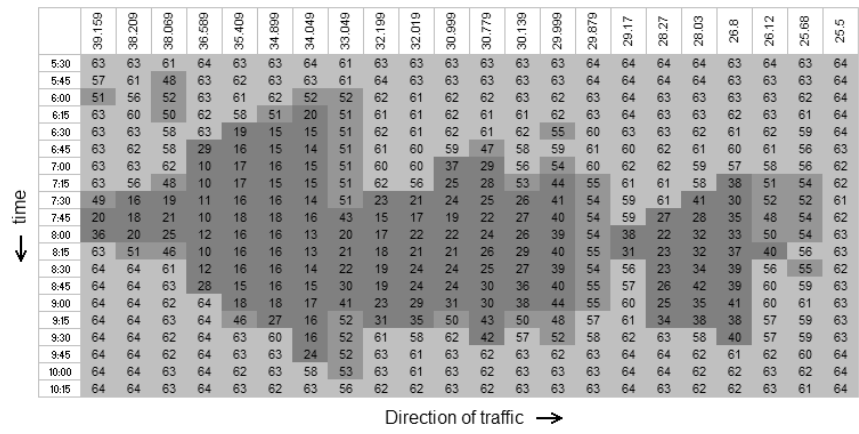


Figure G.3: Random seed = 66

Appendix H

Historically-Averaged Split Ratios

The list of days used to calculate the historically averaged split ratios, along with time-series plots of the split-ratio estimates, are given in Table H.1. Figure H.1 shows the estimated split ratios as a function of time, for each off-ramp in the I-210 test segment. For a description of the procedures used to estimate the split ratios, please see Section 5.4.

FR Index	Postmile	Single/Double	Days Available	Days Used
1	38.209	S	11/27IM, 11/28	11/28/01
2	38	D	11/13, 11/14, 11/15S	11/14/01
3	37	D	11/13, 11/14, 11/15S	11/14/01
4	36	D	11/20IM, 11/21, 11/22IM, 11/27–29	11/21/01
5	35.409	D	11/20IM, 11/21, 11/22IM	11/21/01
6	34.049	S	11/7NF, 11/8IM, 11/13, 11/14, 11/15S, 11/20IM	11/13–14/01
7	33.049	S	11/7NF, 11/8IM, 11/13, 11/14, 11/15S, 11/20IM	11/13–14/01
8	32.019	S	11/7IM, 11/13, 11/22IM, 11/27IM, 11/28, 11/29IM	11/13, 28/01
9	30.779	S	11/1IM, 11/6, 11/7, 11/8, 11/13	11/13/01
10	30.5	S	N/A	11/14/01 (ML), 11/7/01 (FR)
11	29.17	S	N/A	11/13/01 (ML), 11/6/01 (FR)
12	28.27	S	10/3, 10/4, 10/10, 10/11	10/3, 10/4, 10/10, 10/11/01
13	27.64	D	12/13	12/13/01
14	26.8	D	12/13	12/13/01
15	26.12	S	1/10	1/10/02
16	25.68	S	*	1/10/02
17	210 FR	D	*	1/10/02
18	710 FR	D	*	1/10/02

Table H.1: Information used to compute estimated split ratio for each off-ramp in I-210 test segment. First column: off-ramp index (increasing upstream to downstream). Second column: off-ramp postmile or label. Third column: single or paired off-ramp configuration (estimation procedures differ as explained in Section 5.4). Fourth column: Dates for which complete, or mostly complete mainline and off-ramp data was available for use in Eqs. (5.6) or (5.8). IM – incomplete mainline data, NF – no Caltrans off-ramp data for that day, S – flow data contains a spike most likely due to an incident. * – data was taken from the composite set of [24]. Fifth column: Split ratios were ultimately computed for these dates.

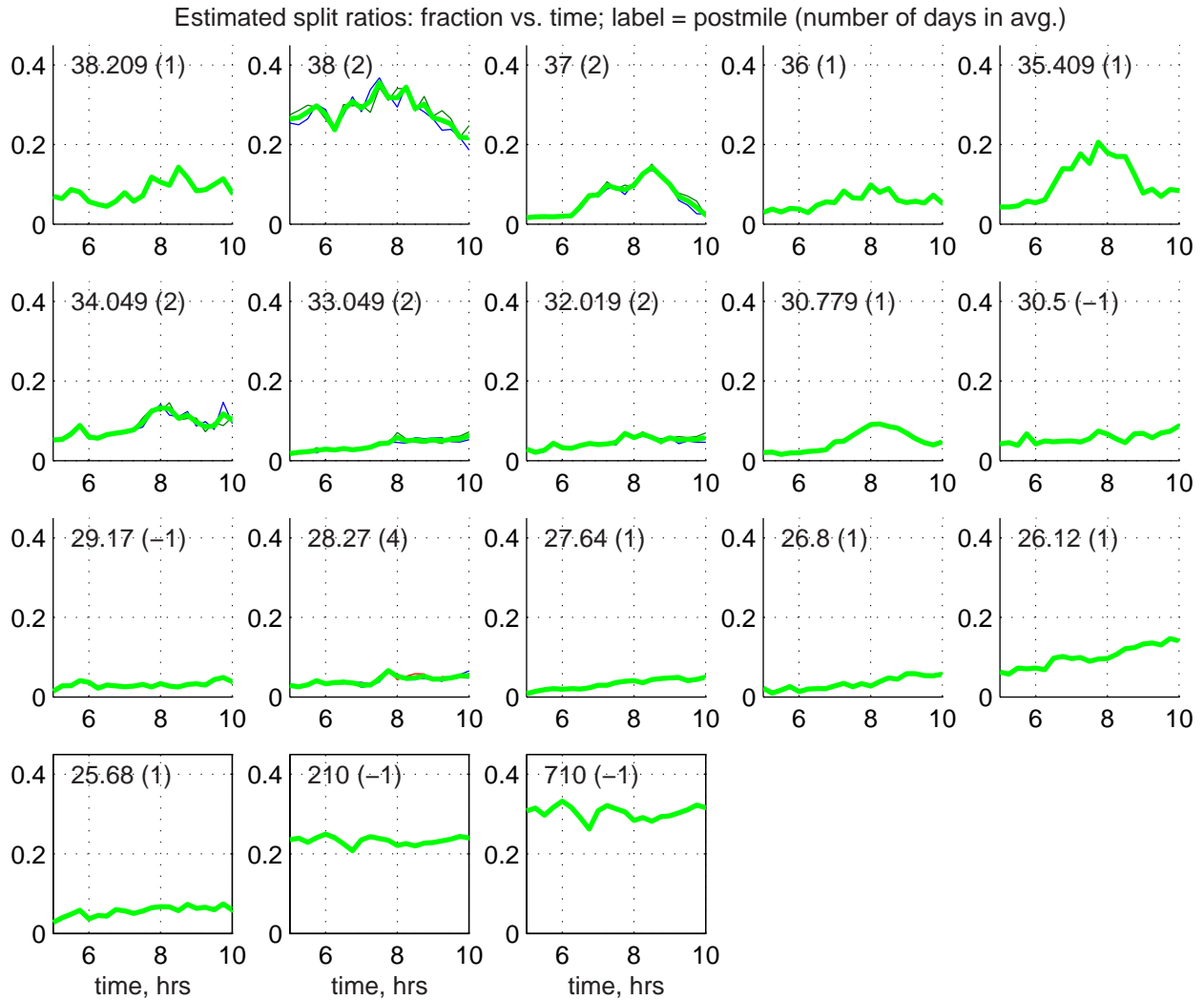


Figure H.1: Estimated 15-minute average split ratios. Each plot contains a text label with the postmile and the number of days used in the historical average in parentheses. “-1” indicates that there was insufficient data to compute a ratio for any individual day, hence a reconstructive procedure was used, as described in Section 5.4. The average value is shown as a bold (green) line, with individual days (if available) as finer lines.